



P248

NASA Contractor Report 189558

**INNOVATIVE FABRICATION PROCESSING OF ADVANCED  
COMPOSITE MATERIALS CONCEPTS FOR PRIMARY AIRCRAFT  
STRUCTURES**

**C. Kassapoglou, A. J. DiNicola, and J. C. Chou**

**UNITED TECHNOLOGIES, SIKORSKY AIRCRAFT DIVISION  
Stratford, Connecticut**

**Contract NAS1-18799  
February 1992**



National Aeronautics and  
Space Administration

**Langley Research Center**  
Hampton, Virginia 23665-5225



Review for general release February 28, 1994

(NASA-CR-189558) INNOVATIVE  
FABRICATION PROCESSING OF ADVANCED  
COMPOSITE MATERIALS CONCEPTS FOR  
PRIMARY AIRCRAFT STRUCTURES Final  
Report (Sikorsky Aircraft) 248 p

N94-32877

Unclas

G3/24 0011951

11/11/11

11/11/11

11/11/11

## FOREWORD

This is the final report of NASA contract NAS1-18799. It was prepared by the Sikorsky Aircraft Division of United Technologies. The work was sponsored by the NASA Langley Research Center. Mr. Jerry W. Deaton was the technical monitor.

The following Sikorsky personnel were instrumental in the successful completion of this phase:

**Program Manager**

S. P. Garbo

**Principal Investigator**

C. Kassapoglou

**Structural Analysis**

A. J. DiNicola

J. C. Chou (now with Pratt & Whitney Florida)

A. L. Dobyns

D. W. Lowry

**Design**

T. C. Harman

**Manufacturing/Tooling**

K. M. Adams (now with Dow-United Technologies Composite Products)

J. Boudreau (now with Dow-United Technologies Composite Products)

M. J. Duda (now with Dow-United Technologies Composite Products)

B. Beatty (now with Dow-United Technologies Composite Products)

R. T. Reavely (now with Dow-United Technologies Composite Products)

D. M. Cournoyer

A. J. Giarratano

P. G. Sanders

D. J. Tuttle

J. C. Gillick

**Testing/Planning/Tool Design**

P. C. Inguanti

**Testing**

K. D. Forbes

H. Rivera

F. M. Gordon

S. Martin

**Weights/Systems**

D. K. Unsworth

**Inspection/Chemical Testing**

L. E. Fabian

C. W. Wright

F. D. Gritsko

L. S. Duh

E. W. Cassidy

D. D. King

## TABLE OF CONTENTS

TITLE	PAGE
1.0 INTRODUCTION AND SUMMARY	1
2.0 THE THERM-X® PROCESS IN AUTOCLAVE APPLICATIONS	4
2.1 Overview	4
2.2 Bagging Sequence	6
2.3 Cure Cycle	8
3.0 DESIGN SELECTION	9
3.1 Selection of Candidate Structural Details	9
3.1.1 Cocured Sandwich Panels	23
3.1.2 Sandwich - Solid Laminate-Sandwich Transition	23
3.1.3 Core Transition	24
3.1.4 Cocured Channel Stiffeners on Panels	27
3.1.5 Corners	30
3.1.6 Skin-Stiffener Combination	32
3.1.7 Cocured Box with Cocured Internal Stiffeners (Ribs/Spars)	37
3.1.8 Beaded Panels	37
3.1.9 Flat Panel Bag Foldover	40
3.1.10 Thick Cylinder	40
3.1.11 Panel with "Continuous" Frames and Stiffeners	44
3.2 Selection Process	49
3.3 Design of Full Scale Panel	52
3.3.1 Governing Equations and Optimization Scheme	52
3.3.2 Results of the Optimization Method and Discussion	67
4.0 BUILDING BLOCK EVALUATION	75
4.1 Test Matrix and Objectives	75
4.2 Test Results	78
4.2.1 ±45 Coupons	78
4.2.2 Skin-Stiffener Separation Specimen	80
4.2.3 Stiffener Crippling Specimen	84
4.2.4 Compression and Shear After Impact Specimens	89
4.2.5 Skin Tearing Specimens	93
4.2.6 Frame-Stiffener Intersection Specimen	101
4.2.6.1 Comparison of Test Results to Finite Element Predictions	103
4.2.6.2 Failure Mode and Prediction of Frame-Stiffener Intersection	108
4.2.6.3 Damage Tolerance of Frame-Stiffener Intersection Specimens	117
4.2.6.4 Conclusions from Frame-Stiffener Intersection Tests and Analysis	121

## TABLE OF CONTENTS (CONT'D)

TITLE	PAGE	
4.3	Summary of Labor Hours Needed for Specimens Made with the THERM-X® Process	125
4.4	Conclusions from Building Block Evaluation	126
4.4.1	Flat Parts	126
4.4.2	Complex Cocured Parts	126
4.4.3	Effectiveness of the Embedded Flange	128
4.4.4	Effectiveness of the Shear Tie	128
4.4.5	Wrinkles and Voids at Radius Regions	128
5.0	FULL-SCALE PANEL	131
5.1	Tooling	131
5.2	Fabrication	134
5.3	Test	140
5.3.1	Static Test	140
5.3.2	Fatigue Test	155
5.4	Correlation of Test Results with Analysis Predictions	170
5.4.1	Finite Element Analysis and Comparison with Test Results	170
5.4.2	Diagonal Tension Analysis and Comparison with Test Results	174
5.4.3	Failure Predictions	185
5.5	Teardown Inspection	197
5.5.1	Void Content and Fiber Volume Measurements	197
5.6	Labor Hours Comparison - THERM-X® Tooling Versus Conventional Layup	212
6.0	CONCLUSIONS AND RECOMMENDATIONS	220
6.1	Conclusions	220
6.2	Recommendations	221
	REFERENCES	222
	APPENDIX: Drawing of Full Scale Panel	224

## LIST OF FIGURES

TITLE	PAGE
2.1 THERM-X® Process	5
2.2 Bagging Sequence for THERM-X® Process	7
3.1 Manufacturing Nonconformities	13
3.2 Near 90 Degree Remps on Sandwich Panels	14
3.3 Cocured Sandwich Panels	14
3.4 Sandwich-Solid Laminate-Sandwich Transition	15
3.5 Corners	15
3.6 Beaded Panels	17
3.7 Skin-Stiffener Combination	17
3.8 Core Transition	18
3.9 Bag Foldover	18
3.10 Core Around a Radius	19
3.11 Cocured Box with Cocured Internal Ribs	19
3.12 Cocured Channel Stiffeners on Panels	21
3.13 Thick Cylinder with Waviness	21
3.14 Continuous Frame-Stiffener Intersections	22
3.15 Allowable Compressive Load as a Function of Facesheet Thickness	26
3.16 Variation of Moment of Inertia with Web Thickness for Various Web Inclinations	28
3.17 Variation of Maximum Bending Stress as a Function of Web Thickness for Various Web Inclinations	29
3.18 Corners - Loading and Geometry Definition	31
3.19 Skin-Stiffener Combination; Defect-Free Manufacture	33
3.20 Skin Stiffener Combination; Manufacture with Defects	35
3.21 Maximum Stress as a Function of Applied Load for Defect-Free and Improper Manufacture	36
3.22 Beaded Panels - Shear Load Versus Bending Stiffness	39
3.23 Flat Panel Bag Foldover - Modelling Idealization	41
3.24 Thick Cylinders - Shear Stress as a Function of Applied Torque	43
3.25 Finite Element Model for Frame in Bending	45
3.26 Geometry Configurations for Frames With and Without Enlarged Mouseholes	46
3.27 Stress (Von Mises) Distribution in the Vicinity of Mousehole Closest to Frame Root	47
3.28 Stress (von Mises) Distribution in the Vicinity of the Mousehole Away from the Frame Root	47
3.29 Cost for Various Structural Details	51
3.30 Curved Stiffened panel as Structural Element	53
3.31 Free Body Diagram of the Post-Buckled Panel	58
3.32 Schematic Representation of Dependence of Cost (Number of Frames and Stiffeners) on Stiffener-to-Frame-Spacing Ratio	62
3.33 Optimization Procedure	68

## LIST OF FIGURES

TITLE	PAGE
3.34 Optimum Geometry Determination for Stiffened Panels - Cost Considerations	71
3.35 Optimum Geometry Determination for Stiffened Panels - Highly Loaded Structure	74
4.1 Building Block Test Specimens and Full-Scale Panel	76
4.2 In-plane Shear ( $\pm 45$ Coupon) Specimen Geometry	79
4.3 Skin-Stiffener Separation Specimen	81
4.4 Skin-Stiffener Separation Specimen - Test Setup	83
4.5 Skin-Stiffener Separation Specimen - Failure Mode	83
4.6 Stiffener Crippling Specimen	85
4.7 Individual Segments of Stiffener Used for Stiffness Analysis	86
4.8 Stiffener Crippling Specimen - Failure Mode	88
4.9 C-Scan of Compression After Impact Specimen	90
4.10 Typical Failures of CAI and SAI Specimens	92
4.11 CAI Strength as a Function of Impact Energy	94
4.12 SAI Strength as a Function of Impact Energy	94
4.13 Internal Damage as Indicated by C-Scan as a Function of Impact Energy	95
4.14 Indentation at Point of Impact as a Function of Impact Energy	96
4.15 Skin Tearing Specimen	97
4.16 Cure-Induced Initial Curvature of Skin Tearing Specimen	100
4.17 (a) Residual Surface Strains Due to Specimen Curvature	102
(b) Strain Distribution after Specimen Straightening	102
(c) Strain Distribution Immediately Prior to Failure	102
4.18 Frame-Stiffener Intersection Specimen	104
4.19 Frame-Stiffener Intersection Detail	105
4.20 Finite Element Mesh for Frame-Stiffener Intersection Specimen	107
4.21 Comparison of Finite Element Predictions to Test Results at Hat Stiffener Center (Shear Strains)	109
4.22 Comparison of Finite Element Predictions to Test Results at Frame-Stiffener Intersection Corner	109
4.23 Comparison of Finite Element Predictions to Test Results at Bay Quarter Point (Shear Strains)	110
4.24 Comparison of Finite Element Predictions to Test Results at Bay Center (Shear Strains)	110
4.25 First Shadow Moire Fringes on Frame-Stiffener Intersection Specimen (2600 lbs of Applied Load)	111
4.26 Shadow Moire Fringes near Failure of Frame-Stiffener Intersection Specimen (20000 lbs)	112
4.27 Comparison of Out-of-Plane Deflection Shape at Bay Center Parallel to Stiffener Axis	113
4.28 Onset of Failure Location - Finite Elements versus Test	115

## LIST OF FIGURES

TITLE	PAGE
4.29 Schematic Failure Mode of Frame-Stiffener Intersection Specimen	116
4.30 Two Impact Locations for the Frame-Stiffener Intersection Specimen No 3	118
4.31 Internal Damage Produced by Varying Levels of Impact Energy	119
4.32 Impact Damaged Specimen Strain Gage Locations	122
4.33 Impact Sites on Frame-Stiffener Intersection Specimen No 3	123
4.34 Delamination Area Prediction of Residual Shear Strength	124
4.35 Indentation Prediction of Residual Shear Strength	124
4.36 Strain Gage Plots for Crippling Specimen CRP-1	127
4.37 Embedded Flange Concept	129
4.38 Stress Concentrations for Embedded and Non-Embedded Flange Designs	129
4.39 Separation of Pressure Medium from Part to be Cured	130
5.1 Full-Scale Panel and Building Block Test Specimens	132
5.2 Aluminum Tool for Full-Scale Article	133
5.3 Full-Scale Panel Layup Procedure	135
5.4 Detail of Assembly During Layup of Full-Scale Panel	138
5.5 Full-Scale Panel No 1	139
5.6 Full-Scale Panel No 1 - Hat Stiffener Detail	141
5.7 Full-Scale Panel No 1 - Frame-Stiffener Intersection Corners	142
5.8 Full-Scale Panel No 1 - Frame End	143
5.9 Full-Scale Test No 3. Applied Load: 12000 lbs (283 lbs/in)	145
5.10 Full-Scale Test No 3. Applied Load: 20680 lbs (487 lbs/in)	147
5.11 Full-Scale Test No 3. Applied Load: 23000 lbs (542 lbs/in)	148
5.12 Full-Scale Test No 3. Applied Load: 23500 lbs (554 lbs/in)	149
5.13 Full-Scale Test No 3. Failure at 25925 lbs (622 lbs/in)	150
5.14 Failed Full-Scale Specimens 1 and 2	152
5.15 Transducer Locations for Collecting Acoustic Emission Data	153
5.16 Acoustic Emission Energy versus Channel (Transducer)	153
5.17 Acoustic Emission Amplitude versus Channel	154
5.18 Acoustic Emission Amplitude versus Load for Transducer No 5	154
5.19 Fatigue Test Panel - Test Parameters Information	157
5.20 Buckled Shape During First Loading Cycle	159
5.21 First Damage - Data up to 10000 Cycles	160
5.22 Corner Delaminations at 37000 and 47000 Cycles	161
5.23 Stiffener Web Failure - 69200 Cycles (Schematic)	162
5.24 Stiffener Web Failure - 69200 Cycles (Photograph)	163
5.25 Buckled Pattern at 69200 Cycles	164
5.26 Damage During Limit Load Cycle after 69200 Cycles	166
5.27 Buckled Pattern During Limit Load Cycle	167
5.28 Damage After 200000 Cycles	168
5.29 Shear Strains at Various Cycle Levels	169



## LIST OF FIGURES

	TITLE	PAGE
5.30	Damage Locations and Extent on Full-Scale Fatigue Test Panel	171
5.31	Full-Scale Panel Finite Element Model	172
5.32	Comparison of Finite Element Predictions to Test Results at Hat Stiffener Center (Shear Strains)	173
5.33	Comparison of Finite Element Predictions to Test Results at Bay Quarter Point (Shear Strains)	175
5.34	Comparison of Finite Element Predictions to Test Results at Bay Center (Strain Along Frame Axis)	176
5.35	Load Versus Deflection Plot at Bay Center (Finite Element Prediction and Test Measurement)	177
5.36	Full-Scale Panel Bay Geometry	178
5.37	Strain Gage Locations in Full-Scale Static Tests	184
5.38	Shear Strain Comparison for Intersection and Full-Scale Tests (Bay Center)	186
5.39	Global Finite Element Model and Local Region of Interest	188
5.40	Local Finite Element Model #1	189
5.41	Deformed Shape of Local Model #1 at 24100 lb of Applied Load	190
5.42	Hoffman Failure Numbers of Local Model #1 at 24100 lb of Applied Load	192
5.43	Local Finite Element Model #2	193
5.44	Deformed Shape of Local Model #2 at 24100 lb of Applied Load	194
5.45	Hoffman Failure Numbers of Local Model #2 at 24100 of Applied Load and Test Specimen Snapshot	195
5.46	Specimens Used for Teardown Inspection (Full-Scale Panel)	198
5.47	Specimens Used for Teardown Inspection (Frame-Stiffener Intersection Specimen)	198
5.48	Void Content Values for Full-Scale Panel No 2	199
5.49	Fiber Volume Values for Full-Scale Panel No 2	200
5.50	Void Content and Fiber Volume Values at Frame-Stiffener Intersection Corner of Full-Scale Panel No 2	202
5.51	Void Content Values for Frame Stiffener Intersection Specimen No 2	203
5.52	Fiber Volume Values for Frame-Stiffener Intersection Specimen No 2	204
5.53	Skin Micrographs from Frame-Stiffener Intersection Specimen	205
5.54	Skin Micrographs from Full-Scale Specimen	207
5.55	Skin Micrographs from Full-Scale Specimen (Left Middle Bay)	208
5.56	Hat Stiffener Cross-Section (Frame-Stiffener Intersection Specimen)	209
5.57	Frame Cross-Section (Frame-Stiffener Intersection Specimen)	210

## LIST OF FIGURES

TITLE	PAGE
5.58 Hat Stiffener Cross Sections Near Frame-Stiffener Intersection Corners	211
5.59 Frame and Stiffener Cross-Sections Near Frame-Stiffener Intersection Corners (Full-Scale Specimen)	213
5.60 Stiffener Cross Sections from Full-Scale Specimen	214
5.61 Labor Hours as a Function of Part Weight for Hand Laid up and THERM-X® Processed Parts (no assembly)	215
5.62 Variation of Labor Hours with Part Weight (Assembly Included)	218

## LIST OF TABLES

	TITLE	PAGE
1.1	Typical Material Costs	1
2.1	Steps in THERM-X® Process	4
2.2	Cure Cycle	8
3.1	Composite Structural Details with Manufacturing Problems	10
3.2	Cocured Sandwich Panels - Weight and Labor Hour Estimates	23
3.3	Sandwich - Solid Laminate - Sandwich Transition - Weight and Labor Hour Estimates	24
3.4	Core Transition - Weight and Labor Hour Estimates	25
3.5	Cocured Channel Stiffeners on Panels - Weight and Labor Hour Estimates	27
3.6	Corners - Weight and Labor Hour Estimates	32
3.7	Skin-Stiffener Combination - Weight and Labor Hour Estimates	34
3.8	Cocured Box with Cocured Internal Stiffeners - Labor Hour Estimates	37
3.9	Beaded Panels - Weight and Labor Hour Estimates	38
3.10	Flat Panel Bag Foldover - Weight and Labor Hour Estimates	40
3.11	Thick Cylinder - Weight and Labor Hour Estimates	42
3.12	Panel with Continuous Frames and Stiffeners - Weight and Labor Hour Estimates	48
3.13	Structural Details - Weight and Labor Hour Comparisons (Estimates) Between THERM-X® Process and Conventional Hand Layup	49
3.14	Structural Details - \$ Cost Estimates for THERM-X® Tooling and % Difference from Standard Manufacture	50
4.1	Test Matrix	77
4.2	In-Plane Shear ( $\pm$ 45 Coupons) Test Results	78
4.3	In-Plane Shear Test Results vs C12K/5225 Qualification Data	80
4.4	Skin-Stiffener Separation Strength for the Skin-Stiffener Specimen	82
4.5	Stiffener Crippling Strength: Experiment Versus Analysis	89
4.6	Impact Testing Summary of Results	91
4.7	Skin Tearing Test Results	98
4.8	Skin Tearing Test Results vs C3K/5225 Qualification Data	99
4.9	Damage Measurements at Impact Locations	120
4.10	Labor Hours Required to Manufacture Building Block Specimens	125
5.1	Labor Hour Breakdown for Full-Scale Panels	137
5.2	Full-Scale Test Failure Loads	155
5.3	Full-Scale Properties Used in the Analysis	182
5.4	Analysis Results for Full-Scale Panel	182
5.5	Measured Strains from Curved panel Tests (Applied Load 22000 lbs)	183
5.6	Labor Hours Comparison - THERM-X® Versus Hand Layup	217



## 1.0 INTRODUCTION AND SUMMARY

Even though significant progress has been made recently in using composites in aircraft structures, their use in primary structure of commercial aircraft has been limited. Two of the reasons for this limited usage are (1) Composite manufacturing of complex structures is in many cases more expensive than the equivalent metal part, and (2) Innovative concepts that improve performance of composites and cost are slow in being implemented in civilian applications.

The cost of manufacturing composite parts can be divided into material cost and labor cost. The material cost for most composite material forms and processes currently used in aircraft manufacturing is at least an order of magnitude higher than equivalent metallic material. Typical ranges for material cost are shown in Table 1.1. Thermoset and thermoplastic materials as well as metals are included for comparison.

Table 1.1  
Typical Material Costs

MATERIAL	COST (\$/LB)
Composite	
Resin transfer molding	12-25
First generation thermoset	50-60
Toughened thermoset	70-100
Fabric commingled w/thermoplastic	90-120
Thermoplastic	120-300
Metal	
Aluminum	3.5
Titanium	6
Steel	1.5-4.5

On the fabrication end, the classical approach has been to manufacture configurations that are based on metal experience. This does not utilize fully the potential of composites for automation especially as that is applied in processes that start from basic constituents (fiber and matrix) and, with minimum scrap and operations, generate complete parts. Only recently have processes such as resin transfer molding and automated tow placement have been widely recognized as viable alternatives to conventional processes. Such new processes, once fully optimized, are expected to offset significant portion of the higher material cost of composites by reducing the labor cost to below that of equivalent metal structure.

A significant part of the cost in many of these processes is tooling. Complex contoured male and female tools are often required to improve consolidation, maintain tolerances and produce the required geometry. Processes that simplify tooling and reduce labor are, therefore, prime candidates for consideration in manufacturing composite aircraft structure.

In addition to cost associated with material and labor, composites possess characteristics that require special attention during design and manufacturing such as sensitivity to impact damage and delamination and low out of plane properties. These concerns have slowed down the introduction of innovative configurations in primary composite structures especially in civilian applications.

The NASA Advanced Composites Technology (ACT) program aims at reducing composites manufacturing cost and speeding up the implementation of new manufacturing processes in aircraft structures. As part of the ACT program innovative structural concepts, manufacturing techniques and analysis methods will be developed that will enable increased usage of composites in primary aircraft structures.

Sikorsky Aircraft's participation in this program has focused on the structural evaluation of complex fuselage structures fabricated using a THERM-X® process. The THERM-X® process is similar to conventional hand layup with one important difference: A flowable polymer is used as the pressure transfer medium between the laid up part and the vacuum bag. Under pressure, the flowable polymer (THERM-X), switches from a powdery solid to a flowing liquid-like material which transmits quasi-hydrostatic pressure directly to the part during cure. The use of a flowable pressure transfer medium simplifies tooling and bagging procedures and improves the quality and definition of parts with complex geometry. As a result, significant cost savings are realized.

The objective of the current program was to design and manufacture parts of complex geometry using the THERM-X® process, quantify structural performance (static and fatigue strength), determine the effect of the process on part quality, and compare the labor hour requirements of this process to conventional hand layup procedures.

The program was divided into three tasks: During Task 1.1 - Design Selection, various structural details common in aircraft structures were evaluated for the applicability of the THERM-X® process. The structural detail with the highest complexity level and potential to show cost savings if THERM-X® tooling were used, a curved panel with cocured frames and stiffeners, was selected. Task 1.2 - Building Block Evaluation went through a building block approach that isolated various failure modes and structural details of the full-scale structural component selected in Task 1.1. Tests and analyses were performed on the details to quantify failure modes, load path integrity and interaction between various subcomponents of the full-scale article. In Task 1.3 - Full-Scale Test, the structural component selected, curved fuselage panel with cocured frames and stiffeners, was manufactured, analyzed and tested (static and fatigue) as the final evaluation of the process.

The breakdown of this report is as follows:

Section 2 contains a brief description of the THERM-X® process as used in an autoclave. Basic tooling requirements and material capabilities are given. The bagging sequence and cure cycle used are also described.

Section 3 describes the work done in Task 1.1 - Design Selection. Structural details of varying complexity are evaluated on the basis of ease of manufacture, potential for minimal manufacturing defects, structural integrity of the resulting part and the effect of using the THERM-X® medium during cure to improve part quality and reduce manufacturing costs.

In Section 4, the work done under Task 1.2 - Building Block Evaluation is described. Correlation of test results with analysis predictions is given and failure modes are discussed. The effect of the process on part quality, investigated through void content and fiber volume tests and micrographs of selected areas, is also presented.

Task 1.3 - Full-Scale Test is described in Section 5. The manufacturing sequence, analysis predictions and test results are given. Part quality is quantified by tearing down one of the test panels (after test) and taking microphotographs of areas of complex geometry. In addition, void content and resin content results from the same locations are reported. A comparison of labor hours needed to manufacture parts using the THERM-X® process versus conventional hand layup labor requirements is included in the same section.

Finally, conclusions and recommendations are given in section 6. The use of the THERM-X® medium is shown in this program to result in high quality parts of relatively high complexity with simplified tooling and reduced labor hours (at least 22%) for the types of parts considered in this program.

## 2.0 THE THERM-X PROCESS IN AUTOCLAVE APPLICATIONS

### 2.1 OVERVIEW

The process is shown schematically in Figure 2.1. The part is laid up in a tool that is surrounded by a box structure that serves as THERM-X container. Once the layup is complete, bleeder and breather plies are added as required by the particular material system used and the box structure is filled with THERM-X® medium. The medium is a silicone-based flowable polymer. Under standard atmospheric conditions, it is in the form of a fine white powder. Under pressure (about 20 psi) it exhibits liquid-like flow characteristics. Used as the pressure transfer medium placed between the vacuum bag and the part, it transmits quasi-hydrostatic pressure over all part surfaces. Once the pressure is removed, the medium reverts to the powder solid state and can be reused in another cure.

The usage of a flowable pressure transfer medium, makes possible the fabrication of parts of complex geometry with tight radii and sharp corners without any additional tooling. In addition, the vacuum bag does not need to conform to the exact geometry of the part since it merely covers and contains the pressure medium. Thus, bagging time is reduced substantially.

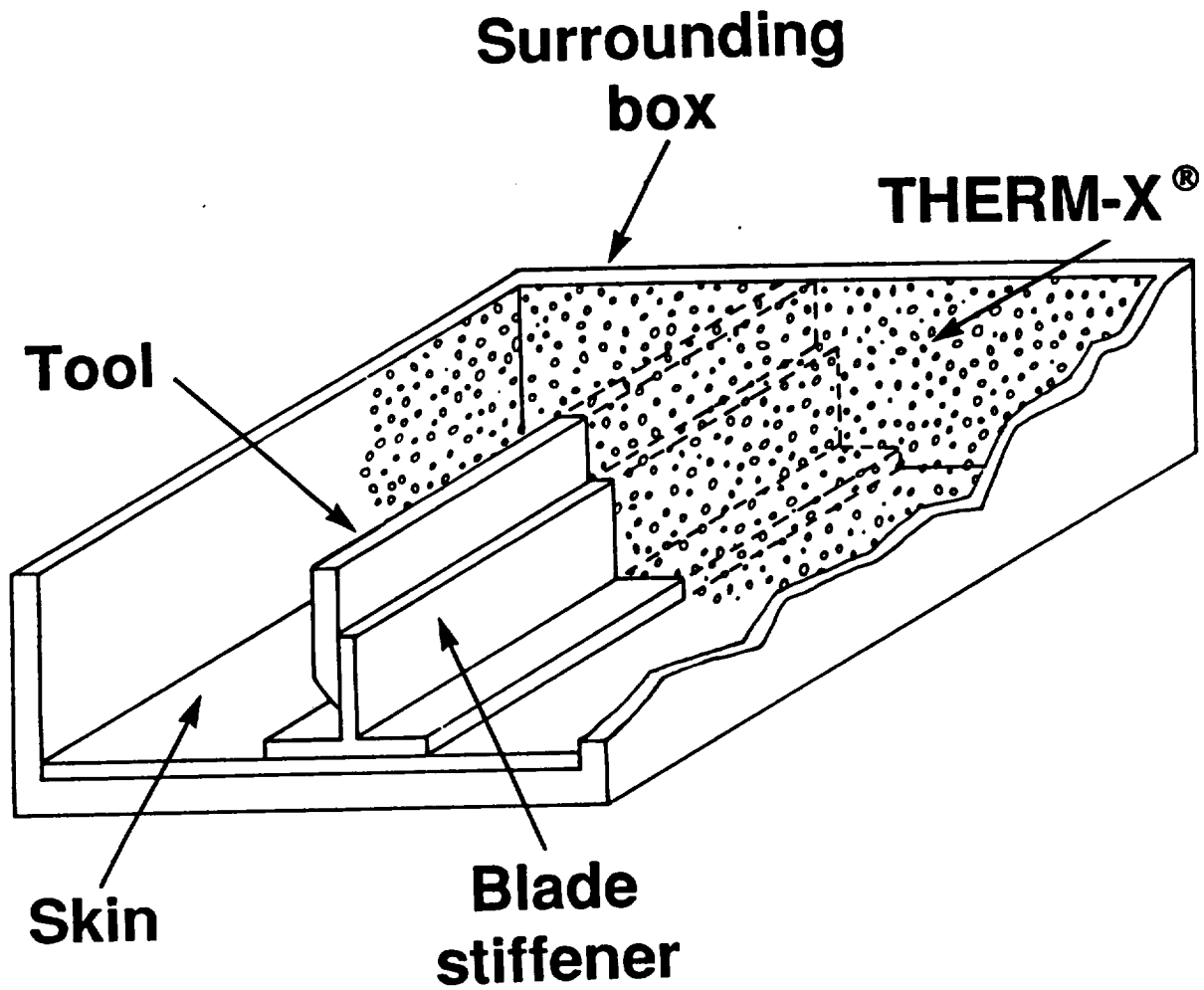
Besides simplified tooling and reduced bagging time, the use of a pressure medium results in more consistent parts that will not depend on the expertise of personnel performing the bagging operation. In addition, within each individual part, the part quality should be more uniform throughout. For example, for a part with many intersecting members, all corners will see the same uniform pressure and will have the same high quality and compaction. This means that the risk of having localized problems in large parts is reduced. Larger parts can be made at lower risk and thus, the reduction in assembly costs can be realized. Another advantage of the uniform pressure at sharp geometry areas is that bridging and wrinkling, problems common to such parts, are minimized. Thus the amount of scrappage, rework and repair is significantly reduced.

The steps to manufacture a part using the THERM-X® process are shown in Table 2.1.

Table 2.1  
Steps in THERM-X® Process

<u>STEP</u>	<u>COMMENT</u>
1. LAYUP PREPREG	Same as in conventional
2. ADD BREATHER AND BLEEDERS AS REQUIRED	layup
3. CLOSE BOX STRUCTURE	For ease of layup box structure is added after layup is complete
4. FILL WITH PRESSURE MEDIUM	Multiple fills may be needed followed by pulling vacuum to insure enough medium is present
5. VACUUM BAG	Over pressure medium and surrounding box; same as conv.





**FIGURE 2.1. THERM-X<sup>®</sup> PROCESS**

The THERM-X® medium can be used for both thermoset and thermoplastic materials. It can be used without any problems in cure cycles up to 750 degrees F and is known to operate effectively for pressures between 40 and 1500 psi. The same batch of material can be reused many times (no limit in the number of times it is used has been found so far).

## 2.2 BAGGING SEQUENCE

There have been internal research experimental programs where the THERM-X® medium was used in direct contact with the part to be cured and no mixing of the medium with the resin was observed. The resulting parts were, in most cases of high quality. There were a few incidents of curing parts in direct contact with THERM-X where patches of oily residue on the part surface were evident after the cure. While this residue was shown not to affect the static properties as measured by short beam shear and flexure tests, it would make secondary bonding very difficult even with the proper surface treatment. For this reason, a separating film of nonporous Teflon (FEP film) was used to isolate the part from the pressure medium. There was no need to have a continuous film over the part as the pressure medium is quite viscous and cannot seep through splices. Thus, the separating film was cut and spliced on an as-necessary basis to minimize bridging.

By being able to overlap pieces of the separating film, any problems associated with regular vacuum bagging which is continuous and must conform exactly to the part being cured (wrinkling, bridging, bag pinching, etc.) were eliminated. The increase in labor hours for adding the separating film was negligible. The bagging sequence used for the parts fabricated in this program is shown in Figure 2.2.

The problem of the oily residue has been traced to defective batches of THERM-X. The problem has been eliminated and other than breathing and bleeding materials that will be necessary for some material systems, THERM-X can be cured directly in contact with the part eliminating the need and the added labor for a separating film.

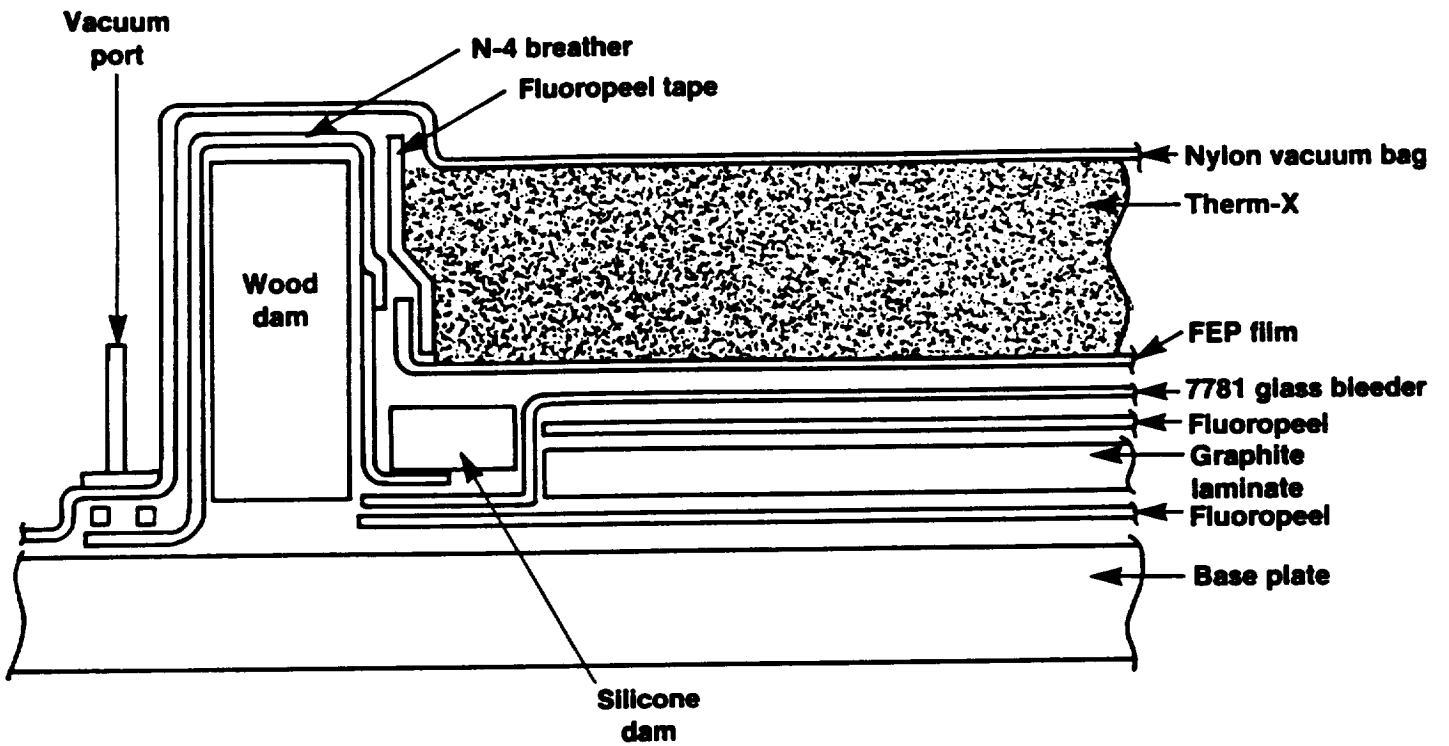


FIGURE 2.2. BAGGING SEQUENCE FOR THERM-X<sup>®</sup> PROCESS

## 2.3 CURE CYCLE

The cure cycle used for the THERM-X® process is the recommended cure cycle for the material to be used. Since the pressure medium has a large range of temperatures and pressures over which it can operate successfully, additional improvements on part quality can be realized by using as high a pressure during cure as the material system and desired resin content will permit. The increased pressure improves compaction and consolidation in the vicinity of corners and intersecting members and eliminates ply waviness common to thicker parts and to areas of ply build-ups.

The cure cycle used in this program is shown in Table 2.2. As an added precaution, a cold pressure check was done at the beginning of the cure cycle at a pressure of 85 psi with vacuum connected. In addition, a one hour hold at 270 degrees was added to the cure cycle at 50 psi. The purpose of that was to allow the resin to gel so that if the bag breaks at 350 degrees and 100 psi pressure, there was a reasonable chance of still obtaining a good part. The material system used was Celion 12K (Gr tape prepreg) or 3K (Gr woven prepreg) with the BASF/NARMCO 5225 resin.

Table 2.2  
Cure Cycle

	Approx Time (min)	Temperature (F)	Pressure (psi)	Comments
Start		70		
Ramp 1	15	100+15	50	
Hold 1	5	100+15	50	Cold
Ramp 2	15	100+15	85	pressure
Hold 2	5	100+15	85	check
Reduce pressure to 50 psi				
Ramp 3	45	160	50	
Hold 3	60	160	50	Soak
Vent vacuum				
Ramp 4	80	270	50	
Hold 4	60	270	50	Gel
Increase pressure to 100 psi				
Ramp 5	80	350	100	
Hold 5	120	350	100	Cure
Ramp 6		150	100	
Reduce pressure to 15 psi				
End				

## 3.0 DESIGN SELECTION

### 3.1 SELECTION OF CANDIDATE STRUCTURAL DETAILS

The previous experience at Sikorsky Aircraft in composite manufacturing (for example, Sikorsky Engineering Reports "Manufacturing Cost Report Vol IV", SER-750039, January 1984 and "Damage Tolerance of Composite Materials", SER-510322, November 1989) was used to isolate problems encountered in composite manufacturing and assess their effect on structural performance. A review of previous programs focused on structural efficiency (low cost and weight for a given loading) of various structural details. Historical problems encountered during manufacturing of these details and their effect on structural performance were investigated. The potential structural efficiency improvements realized in design innovations through use of THERM-X® processing were evaluated.

A list of such structural details is shown in Table 3.1. For each detail, the manufacturing problems associated with hand layup are indicated. The effect on structural performance is described and the possible improvement with the use of THERM-X® medium is assessed.

The second half of Table 3.1 (items 9-12) describes structural details that cannot be produced efficiently using current standard procedures. Complex tooling, additional mandrels and special bagging procedures are needed and still, in some cases, the resulting parts do not have satisfactory load continuity. It is in this second set of structural details that the use of the THERM-X® process was expected to have the most impact by making these parts possible at an acceptable cost.

**Table 3.1**  
**Composite Structural Details with Manufacturing Problems**



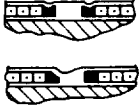

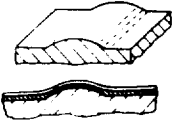



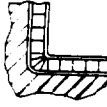
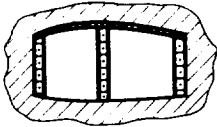
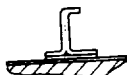
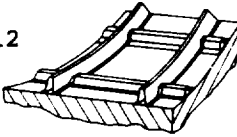
<b>DETAIL</b>	<b>MANUF. PROBLEM</b>	<b>EFFECT ON STRUCT'L PERFORMANCE</b>	<b>IMPROVEMENT USING THERM-X</b>
<p>1</p>  <p>Near 90 Degree Ramps on Sandwich</p>	Facing Wrinkle, Core Crush	Reduced Compression & Bending Performance	Marginal
<p>2</p>  <p>Cocured Sandwich Panels</p>	Wrinkles on Bag Side	Reduced Buckling Loads	Moderate
<p>3</p>  <p>Sandwich-Solid Transition</p>	Wrinkles on Bag Side	Reduced Compression & Bending Performance	Moderate
<p>4</p>  <p>Corners</p>	Voids	Reduced Bending Str Low Fatigue Life	Significant
<p>5</p>  <p>Beaded Panels</p>	Resin Rich Areas, Darting	Reduced Buckling Ld Low Damage Tolerance	Significant
<p>6</p>  <p>Skin-Stiffener Combinations</p>	Wrinkle, Dim. Tolerance	Low Fatigue Life	Significant

Table 3.1 (continued)  
Composite Structural Details with Manufacturing Problems

DETAIL	MANUF. PROBLEM	EFFECT ON STRUCT'L PERFORMANCE	IMPROVEMENT USING THERM-X
7  Core Transition	Step	Reduced Buckling Ld	Moderate
8  Bag Foldover	Wrinkle, Trapped Bag	Reduced Compression Reduced Shear Props.	Significant
9  Core Around a Radius	Cannot Be Done W/Current Methods		Marginal
10  Cocured Box with Cocured Int'l Stiffeners	Cannot Be Done W/Current Methods		Moderate
11  Cocured Channel Stiffeners on Panel	Cannot Be Done W/Current Methods (for certain lip web dimensions)		Significant
12  "Continuous" Frame Stiffener Intersections	Cannot Be Done W/Current Methods		Significant

To assess the importance of the manufacturing problems, their frequency of occurrence in Sikorsky Aircraft composite structures as fractions of the total number of manufacturing non-conformities is shown in the pie chart of Figure 3.1. Cumulatively, wrinkles, core crushing, voids, and resin rich regions add up to 34% of non-conforming parts. To put this in perspective, in a typical composites manufacturing start-up program such as the ACAP, the total number of non-conforming parts is approximately 45% of the total number of parts made. This suggests that significant cost and labor savings can be realized if these types of problems can be drastically reduced or altogether eliminated. The expected results would be reduced disposition and repair times, reduced scrap rates, and improved part quality and integrity.

A discussion of each of the structural details is provided in the following paragraphs.

Near 90° Ramps on Sandwich Panels. This detail is shown in Figure 3.2. For ramp angles higher than 45 degrees, the facesheet that conforms to the ramp angle shows wrinkles and the core under it is locally crushed. An improved manufacturing procedure eliminating wrinkling and, in particular, the core crushing, would result in panels with improved bending and compression properties. THERM-X® technology, as currently envisioned, may not lead to improvements of this situation.

Cocured Sandwich Panels. When cocuring sandwich panels, the facesheet on the bag side is under autoclave pressure and, for facesheets of low to moderate thickness (up to 15 plies), as the resin flows, the facesheet develops dimples that exhibit the "telegraphing" pattern shown in Figure 3.3. The resulting panels have reduced buckling strength and, for design and analysis, cocured knockdown factors must be used which may be as high as 60-70%. It is believed that small improvements may be achieved if THERM-X is used since the pressure distribution on the facesheet will be more uniform than that exerted by the vacuum bag. Still, as the resin flows, the plies next to the core will dimple between the edges of core cells.

Sandwich-Solid Laminate-Sandwich Transition. Often, local reinforcement and attachment requirements necessitate the change from sandwich structure to solid laminate and back to sandwich structure (Figure 3.4). Foaming adhesive at the core splice is used. Around the foaming adhesive, wrinkles and depressions tend to develop. These wrinkles reduce the buckling load for the panel as a whole and act as local stress concentrations. Use of THERM-X may moderately improve the part quality.

Corners. For corners cured on female tools, the inner side is in direct contact with the vacuum bag which cannot conform exactly to the contour especially for corners close to 90 degrees. As a result, the bag "bridges" and insufficient pressure is exerted during curing. Voids are present at the corner (Figure 3.5) and excess resin is found on the inside radius. Delaminations may propagate during fatigue loading and lead to premature failure. This is a structural detail where the use of THERM-X® tooling is expected to improve the quality significantly by ensuring proper compaction.



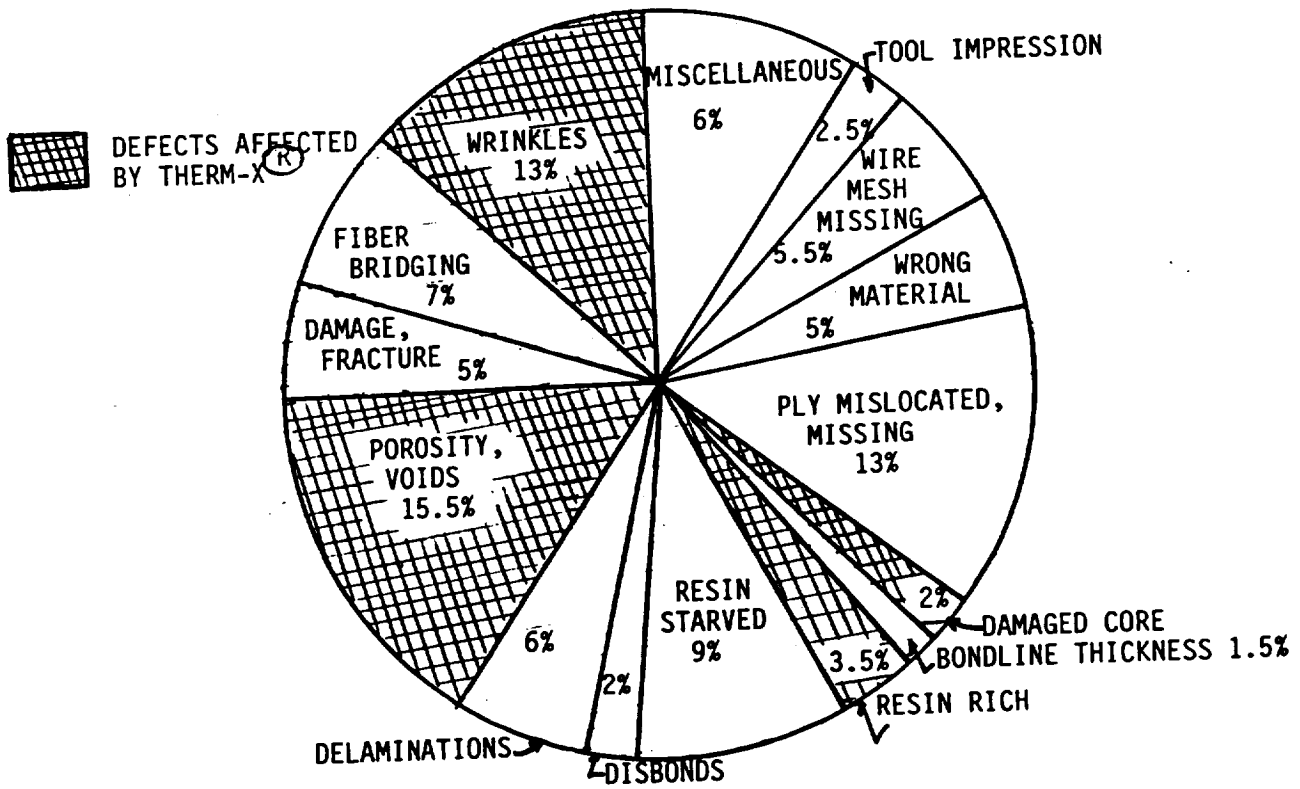


FIGURE 3.1. MANUFACTURING NONCONFORMITIES

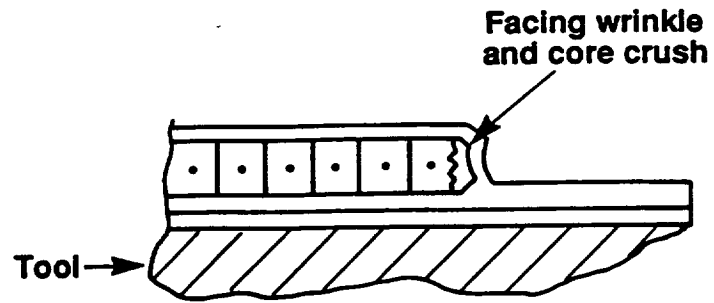


FIGURE 3.2. NEAR 90 DEGREE RAMPS ON SANDWICH PANELS

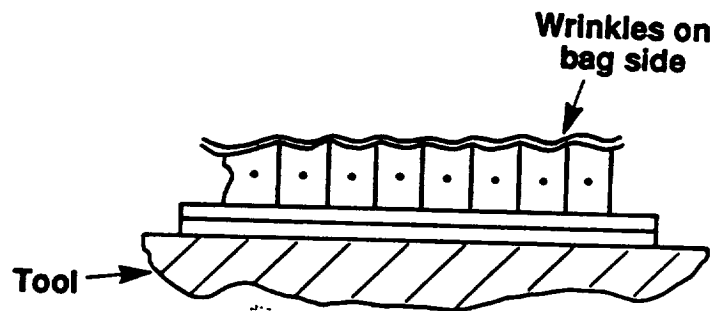


FIGURE 3.3. COCURED SANDWICH PANELS

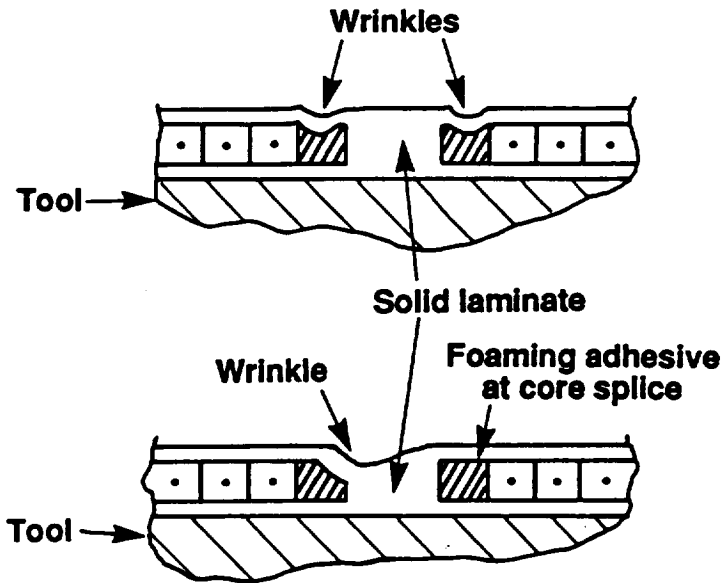


FIGURE 3.4. SANDWICH-SOLID LAMINATE-SANDWICH TRANSITION

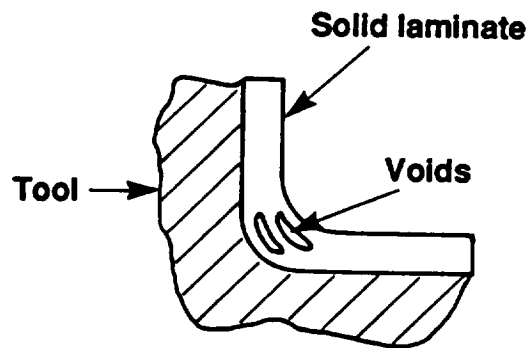


FIGURE 3.5. CORNERS

Beaded Panels. Beaded panels (Figure 3.6) are used for their improved bending performance (considering their manufacturing simplicity). In practice, resin rich regions are almost unavoidable near the curvature changes on the tool side of the panels. In addition, layup of beaded panels requires selective "darting" and splicing which not only increases their cost but reduces their strength because of local stress concentrations. The THERM-X® process is expected to eliminate the resin rich regions.

Skin-Stiffener or Spar-Skin Combinations. The situation is shown schematically in Figure 3.7. Because of the tight radius in the web to flange transition of the stiffener, mandrels are commonly used. These and/or the vacuum bag may shift during curing and create wrinkles and spar webs that are not vertical to the skin panel. This local disruption of load transfer leads to reduced fatigue lives. THERM-X® tooling is expected to significantly improve the situation because equal pressures will be exerted on both sides of the web and over the entire radius regions. In general, no mandrels will be necessary.

Core Transition. As the load requirements change along a structure (for example the bending stiffness requirement decreases along the wing from the root to the tip), cost and weight savings considerations require the change of core from higher to lower density (Figure 3.8). Due to uneven compaction between the two core types, a step may result in the structure. The compression properties will be reduced and the fatigue life will be adversely affected. In addition, low speed impact in the step area will cause significant damage and reduce the damage tolerance of the structure. Moderate improvements are expected if THERM-X® processing is used.

Bag Foldover. When relatively complicated sub-assemblies are cured, in order to ensure proper compaction and leak proof bagging, the bag is pleated or folded over in some locations. This may result in pinching of the laminate and possibly trapping of bag material in the resulting wrinkle (Figure 3.9). The local stress concentration reduces the shear and compression load carrying ability and leads to unsatisfactory damage tolerance. Use of THERM-X eliminates the direct contact between the part and the vacuum bag and no such wrinkles should be present in the structure after curing.

Core Around a Radius. This is a configuration that is not possible with current standard manufacturing techniques. It is shown in Figure 3.10. It is very hard to turn core around sharp radii because of anticlastic curvature effects and the fact that it tends to crush on itself. Successfully manufactured corners of this kind would have reduced requirements on local attachments and shear clips and show increased strength and fatigue life. The current THERM-X® technology is not expected to improve the situation.

Cocured Box Structure with Cocured Internal Ribs. This is another configuration that is extremely difficult and expensive to make using current manufacturing procedures. Such a structure (Figure 3.11) would be more efficient since it would permit reduction of the skin thickness as the internal ribs would take some of the bending loads. Using THERM-X will eliminate a lot of the internal tooling required and should make these structures possible at an affordable cost.

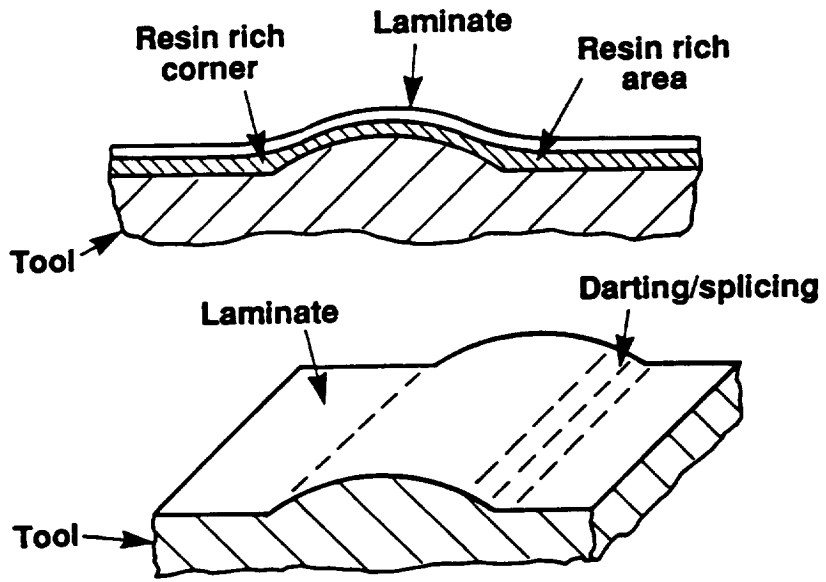


FIGURE 3.6. BEADED PANELS

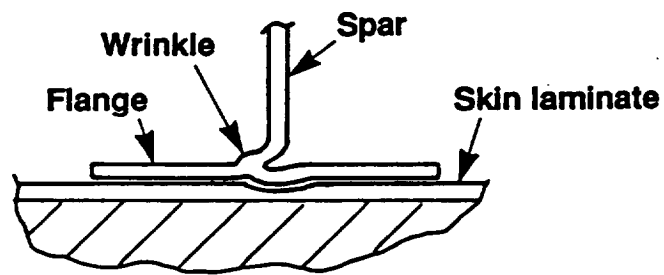


FIGURE 3.7. SKIN-STIFFENER COMBINATION

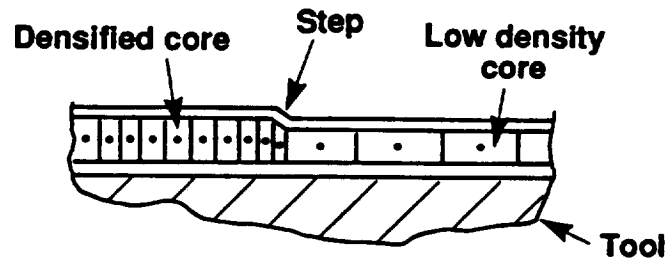


FIGURE 3.8. CORE TRANSITION

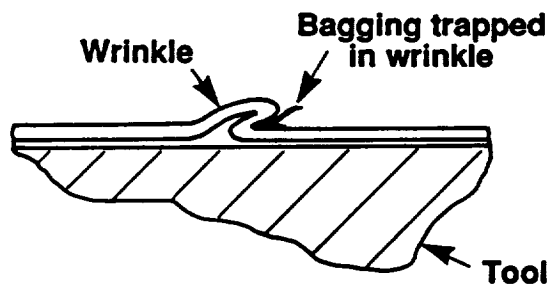


FIGURE 3.9. BAG FOLDOVER

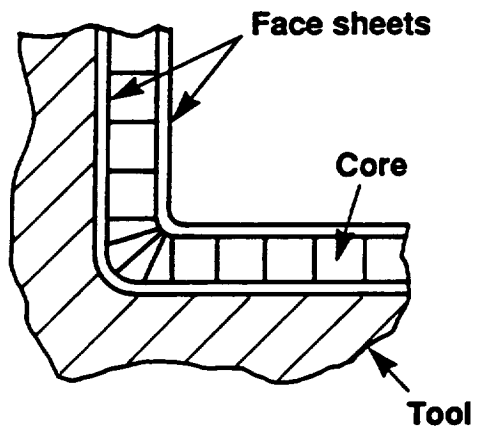


FIGURE 3.10. CORE AROUND A RADIUS

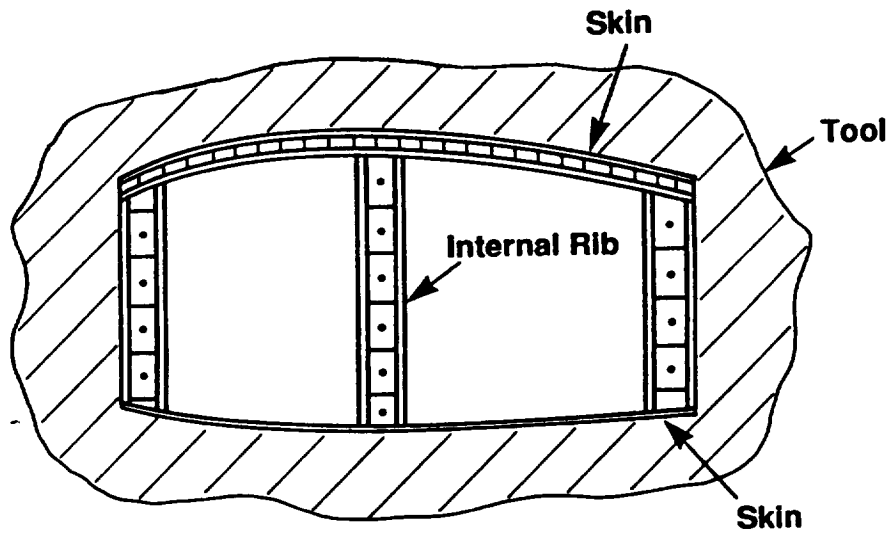


FIGURE 3.11. COCURED BOX WITH COCURED INTERNAL RIBS

Cocured Channel Stiffeners on Panels. The structural detail is shown in Figure 3.12. For small lips, not enough pressure is generated during curing and the advantages of the lip are lost. For large webs, it is very hard to maintain it vertical to the panel (see also the above discussion on the Skin-Stiffener combinations). The THERM-X® medium generates quasi-hydrostatic pressure even at areas of tight radii and is expected to make possible a wider range of geometries.

Thick Cylinders. Used as transmission shafts, thick cylinders exhibit ply waviness resulting from insufficient debulking and non-uniform pressure distribution during layup and cure (Figure 3.13). Significant improvements are expected if THERM-X® tooling is used because of the uniform pressure transmitted to the part.

"Continuous" Frame-Stiffener Intersections. Currently, such configurations (Figure 3.14) are made with cutouts in the frames to accommodate the stiffeners and/or require complex brackets to ensure load continuity at crossover points. THERM-X® tooling will make possible configurations with virtually continuous load paths in both directions and will permit cocuring of shear ties that will transfer load from frames to stiffeners.

Based on the above discussion of the details, a first screening narrowed down the structural details to those that are expected to show the largest improvement if THERM-X® tooling is used. The details selected for further evaluation are (1) Cocured Sandwich Panels, (2) Sandwich-Solid Laminate-Sandwich Transition, (3) Core Transition, (4) Cocured Channel Stiffeners on Panels, (5) Bag Foldovers on Flat Panels, (10) Thick Cylinders, and (11) "Continuous" Frame-Stiffener Intersections. Note that the thick cylinders were added to the original list mainly to address the issue of waviness.

A simple analysis of these details follows. In each case, the typical problem or defect during conventional manufacturing is assumed to be eliminated by using the THERM-X® process. The THERM-X® process is then compared to conventional hand layup and bagging by estimating the additional weight or labor hours needed to make a part made using conventional layup equivalent to a part made using THERM-X® tooling. Labor hours are estimated using data on similar parts made with the two methods. Process documentation, curing, and inspection are not included in the labor hour estimates. For the weight estimates, typical density values were used. For Graphite/Epoxy (C12K or C3K/5225) a value of 0.056 lb/in<sup>3</sup> was used. For 3 lb and 6-8 lb cores the density values were 0.00174 lb/in<sup>3</sup> and 0.00406 lb/in<sup>3</sup> respectively. Adhesive was neglected in the weight estimates as it is a very small fraction of the total weight. For illustration purposes, quasi-isotropic layups were used unless otherwise noted.



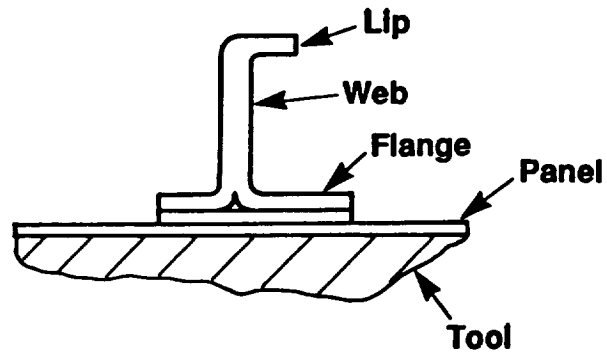


FIGURE 3.12. COCURED CHANNEL STIFFENERS ON PANELS

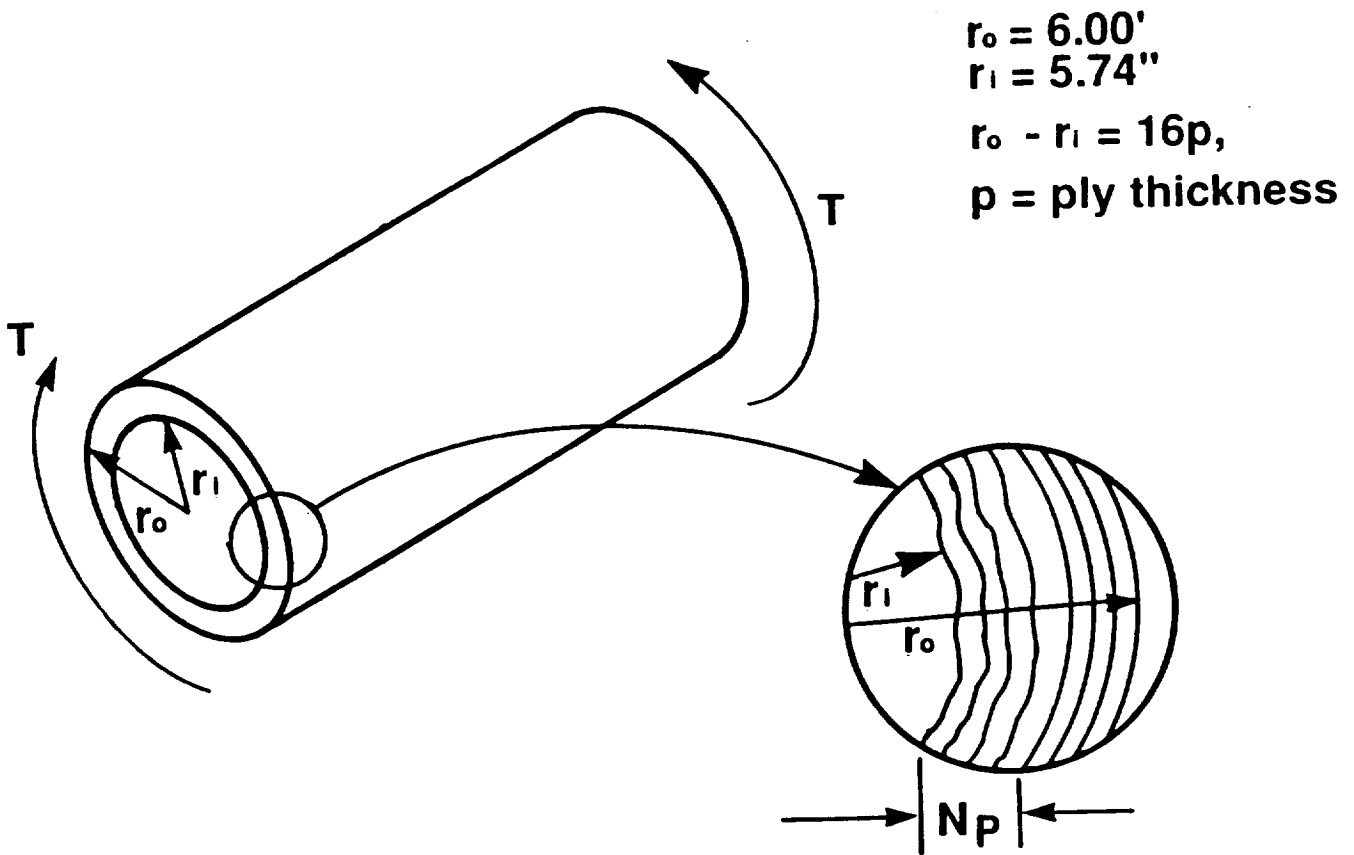
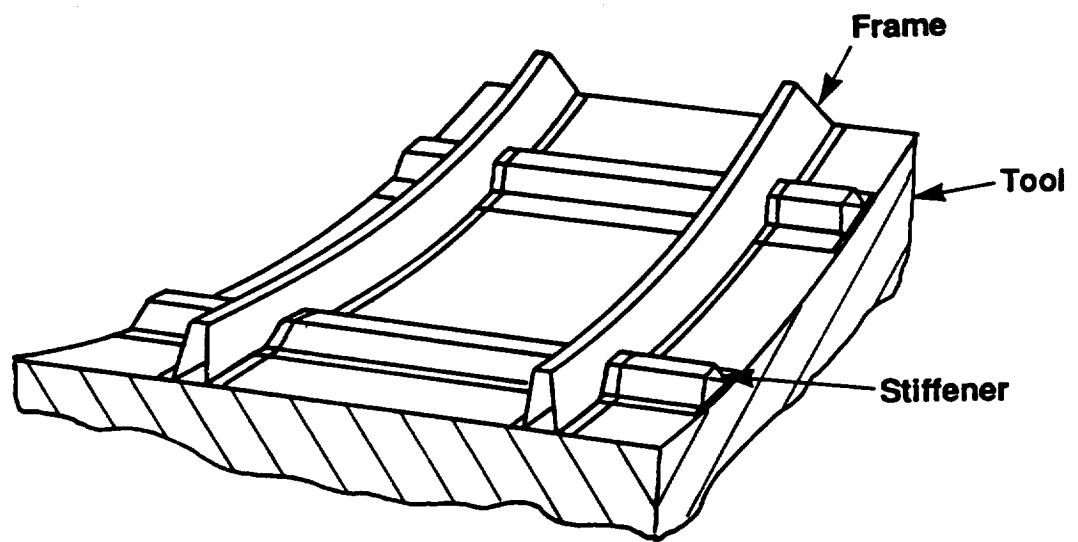


FIGURE 3.13. THICK CYLINDER WITH WAVINESS



**FIGURE 3.14. CONTINUOUS FRAME-STIFFENER INTERSECTIONS**

### 3.1.1 COCURED SANDWICH PANELS

An average cocured knockdown factor of 30% in compression is used as the effect of conventional bagging on cocured sandwich panels. THERM-X® processing is estimated to result in a 20% knockdown factor due to more uniform pressure distribution over the facesheet. Simple classical laminated plate theory with the use of Tsai-Hill first ply failure criterion shows that a 30% knockdown factor for typical unidirectional Graphite/Epoxy results in a 15% increase in thickness for the facesheet compression strength to be the same as for a panel with a 20% knockdown factor. For relatively thin facesheets (up to 7 plies) this translates to one additional ply per facesheet (the ply is added on both facesheets to keep them symmetric). The weight and labor hour estimates for a 24"x24" sandwich panel with 0.75 inch thick honeycomb core are shown in detail in Table 3.2 for both conventional layup and THERM-X® processing.

Table 3.2  
Cocured Sandwich Panels - Weight and Labor Hour Estimates

PROCESS STEP	THERM-X® PROCESS (HRS)	CONVENTIONAL LAYUP (HRS)
PREPARE CORE	0.5	0.5
PREPARE TOOL	0.5	0.5
CUT MATERIAL	0.5	0.6
LAY-UP PANEL	1.5	1.6
VACUUM BAG	1.0	1.0
STRIP & TRIM	2.2	2.0
TOTAL LABOR HRS	6.2	6.2
TOTAL WEIGHT (LBS)	2.69	3.46

### 3.1.2 SANDWICH - SOLID LAMINATE - SANDWICH TRANSITION

A wrinkle, on the order of two ply- to the whole facesheet - thickness deep, appears usually on the bag side in the transition region. It is expected that with THERM-X® processing there will be no wrinkle. For the part conventionally laid up a repair will be needed. The typical repair consists of a two to four ply doubler. Sikorsky Aircraft experience suggests that the time required for the repair (including any reanalysis and disposition) is between 0.5 and 2 hours. Based on this increase in weight and labor hours due to the presence of the doubler, the weight and labor hour estimates for a 24"x24" sandwich panel with 0.75 inch thick honeycomb core are shown in detail in Table 3.3 for the two manufacturing procedures.

Table 3.3  
Sandwich - Solid Laminate - Sandwich Transition  
Weight and Labor Hour Estimates

PROCESS STEP	THERM-X <sup>o</sup> PROCESS (HRS)	CONVENTIONAL LAYUP (HRS)
PREPARE CORE	0.7	0.7
PREPARE TOOL	0.5	0.5
CUT MATERIAL	0.7	0.7
LAY-UP PANEL	1.8	1.8
VACUUM BAG	1.0	1.0
STRIP & TRIM	2.2	2.0
REPAIR	0.0	0.5
<hr/>		
TOTAL LABOR HRS	6.9	7.2
TOTAL WEIGHT (LBS)	5.16	5.21

### 3.1.3 CORE TRANSITION

From previous Sikorsky Aircraft experience with core transitioning from 3 lb density to 6 or 8 lb density, a step may appear at the transition point on the order of a facesheet thickness deep when standard manufacturing procedures are used. In such a case, under compression loading, the adhesive under the step will be loaded in interlaminar peel and shear.

The average peel and shear stresses can be estimated by balancing the forces and moments in the vicinity of the step. In terms of the applied compressive force  $N$  (lb/in) the peel stress  $\sigma$  and the shear stress  $\tau$  are given by:

$$\sigma = \frac{F \sin 2\phi}{\Delta x} \quad (3.1)$$

$$\tau = -\frac{F}{\Delta x} (1 + \cos 2\phi) \quad (3.2)$$

A generalized failure criterion for the adhesive can then be used similar to the quadratic failure criteria used for composites:

$$\frac{\sigma^2}{XX'} + \frac{\tau^2}{S^2} + \left(\frac{1}{X} - \frac{1}{X'}\right) \sigma = 1 \quad (3.3)$$

where X, X', S are tension, compression, and shear allowables for the adhesive. Using equations 3.1 and 3.2 to substitute in 3.3, an expression for the load Ncr to cause failure can be obtained as a function of the adhesive allowables (3000 psi in tension, 7500 psi in compression, and 2000 psi in shear), the step inclination and the step size:

$$N_{cr} = \frac{-\sin 2\phi \left(\frac{1}{X} - \frac{1}{X'}\right) \pm \sqrt{\sin^2 2\phi \left(\frac{1}{X} - \frac{1}{X'}\right)^2 + 4 \left(\frac{\sin^2 2\phi}{XX'} + \frac{(1 + \cos 2\phi)^2}{S^2}\right)}{2 \left[\frac{\sin^2 2\phi}{XX'} + \frac{(1 + \cos 2\phi)^2}{S^2}\right]} \Delta x \quad (3.4)$$

For different step sizes and inclinations, a family of curves can be obtained as shown in Figure 3.15. The continuous curve ( $\phi=90$  degrees) corresponds to a no-step situation which would be the result expected from using THERM-X<sup>®</sup> medium and would correspond to facesheet compression failure (as opposed to adhesive failure). The fact that some adhesive failure lines (such as the H=h/8 line) fall above the no-step line indicates that the adhesive allowables are high enough to preclude adhesive failure for small step sizes. In that case, the facesheet would fail first.

As a typical example, the case of H=h/4 is considered for a sandwich panel with a facesheet thickness of 0.1 inch (quasi-isotropic layup) and no step present (THERM-X<sup>®</sup> processed). Then, from Figure 3.15, to account for the possibility of a step with H=h/4 (conventional layup), the facesheet thickness should be 0.11 inches which corresponds to a thickness increase of 0.01 inches which is about two 0.006 inch tape plies. Based on this increase in thickness, the weight and labor hour estimates for the two manufacturing procedures are shown in Table 3.4.

Table 3.4  
Core Transition - Weight and Labor Hour Estimates

PROCESS STEP	THERM-X <sup>®</sup> PROCESS (HRS)	CONVENTIONAL LAYUP (HRS)
PREPARE CORE	0.7	0.7
PREPARE TOOL	0.5	0.5
CUT MATERIAL	0.5	0.6
LAY-UP PANEL	1.6	1.7
VACUUM BAG	1.0	1.0
STRIP & TRIM	2.2	2.0
TOTAL LABOR HRS	6.5	6.5
TOTAL WEIGHT (LBS)	4.22	5.00

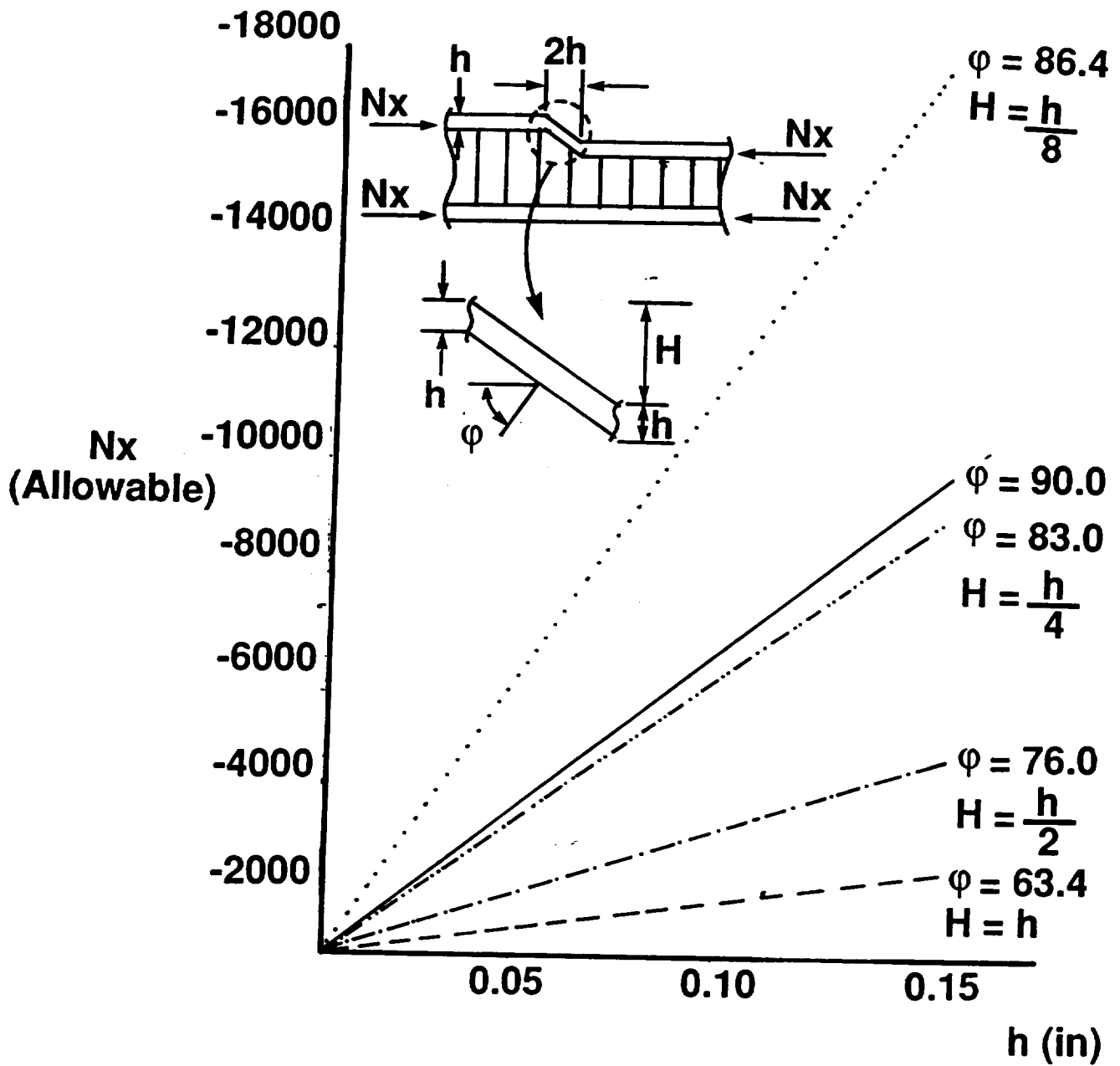


FIGURE 3.15. ALLOWABLE COMPRESSIVE LOAD AS A FUNCTION OF FACESHEET THICKNESS

### 3.1.4 COCURED CHANNEL STIFFENERS ON PANELS

A simple approach to estimate the effect of webs that make an angle  $\theta$  with the vertical direction amounts to finding the moment of inertia  $I$  and the ratio  $c/I$  as a function of this angle. The quantity  $c$  is the distance of the centroid of the cross section from the outer fibers. Thus, a variation in  $I$  would give a measure of the change in buckling load since the buckling load is proportional to the moment of inertia, and the change in  $c/I$  with  $\theta$  will give the change in maximum bending stress. It is assumed that bending occurs about the centroidal axis of the stiffener cross-section.

The moment of inertia  $I$  as a function of the thickness  $h$  ( $4h$  is assumed to be the thickness of the stiffener) for different values of the off-vertical angle, is shown in Figure 3.16. The continuous curve corresponds to a vertical web and is assumed to be representative of a part made with THERM-X<sup>®</sup> tooling. The remaining curves, for various values of  $\theta$ , correspond to defective parts made with current manufacturing procedures. For up to 15 degree angles, the change in moment of inertia from a vertical stiffener web is negligible. For 30 degree off-vertical webs and  $h$  values around .07 inches (corresponding to web thicknesses of .28 inches), an increase from 0.07 to 0.075 inches is required for the defective part to have the same moment of inertia as the non-defective part. This corresponds to a thickness increase for the web of 0.02 ( $\approx 4 \times 0.005$ ) inches which translates to approximately two more 0.012 inch thick tape plies.

A slightly larger weight penalty will be paid for a 30 degree web to result in the same maximum bending stress as a vertical web. This is shown in Figure 3.17 (a 0.28 inch vertical web is again the reference). Since however the two-ply requirement estimated above was slightly more than the thickness needed in that case, it will be assumed that two additional plies will be sufficient.

Based on this conclusion, the weight and labor hours estimates for an 8 inch long stiffener with a 3 inch web, a 0.66 inch lip, and a 1.5 inch flange on an 8 inch x 8 inch skin panel and quasi-isotropic layup are shown in Table 3.5.

Table 3.5  
Cocured Channel Stiffeners on Panels -  
Weight and Labor Hour Estimates

PROCESS STEP	THERM-X <sup>®</sup> PROCESS (HRS)	CONVENTIONAL LAYUP (HRS)
PREPARE TOOLS	0.5	0.5
CUT MATERIAL	0.7	0.8
LAY-UP PANEL	1.6	1.7
VACUUM BAG	1.0	1.5
STRIP & TRIM	2.2	2.0
TOTAL LABOR HRS	6.0	6.5
TOTAL WEIGHT (LBS)	0.23	0.26

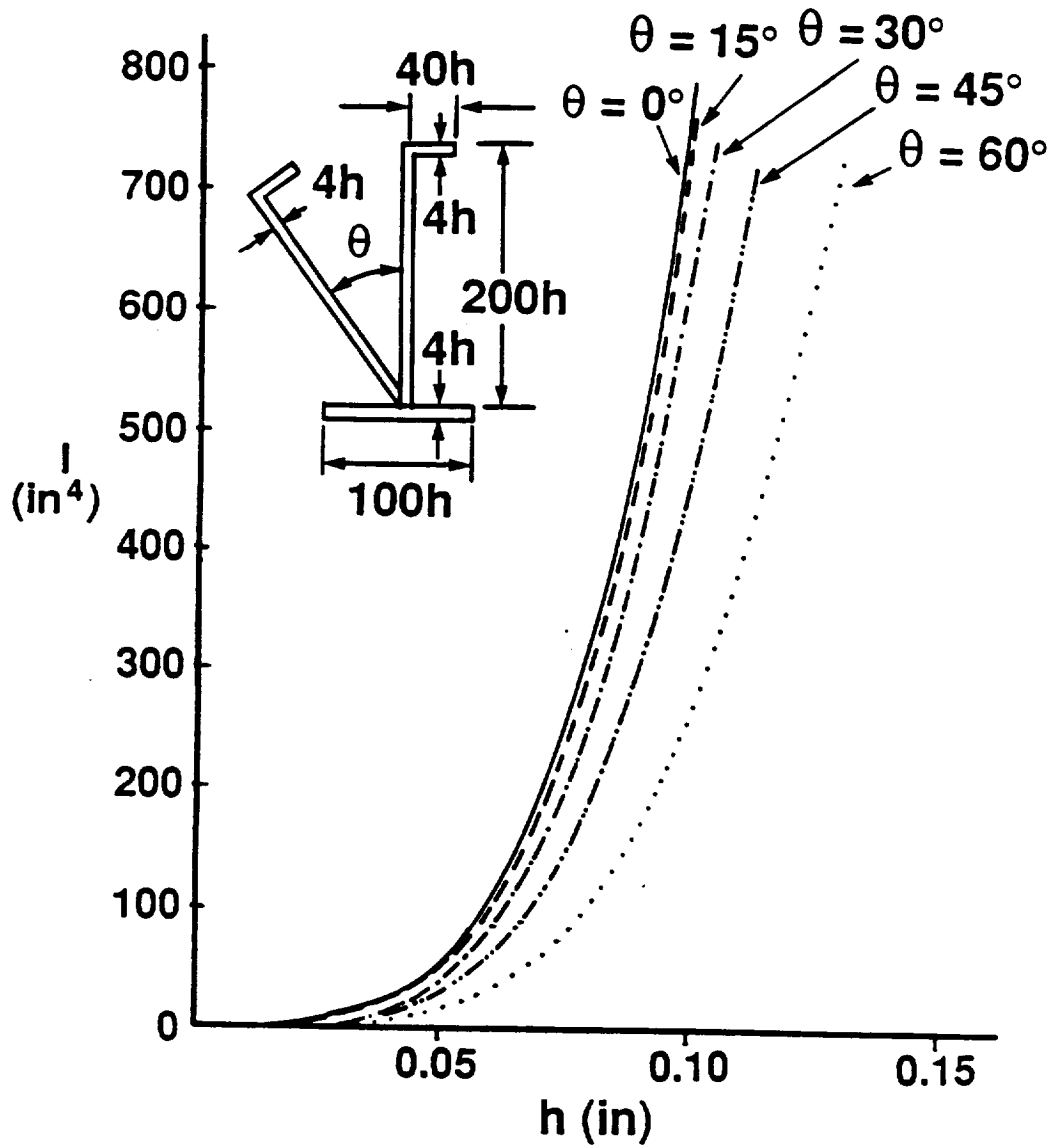


FIGURE 3.16. VARIATION OF MOMENT OF INERTIA WITH WEB THICKNESS FOR VARIOUS WEB INCLINATIONS



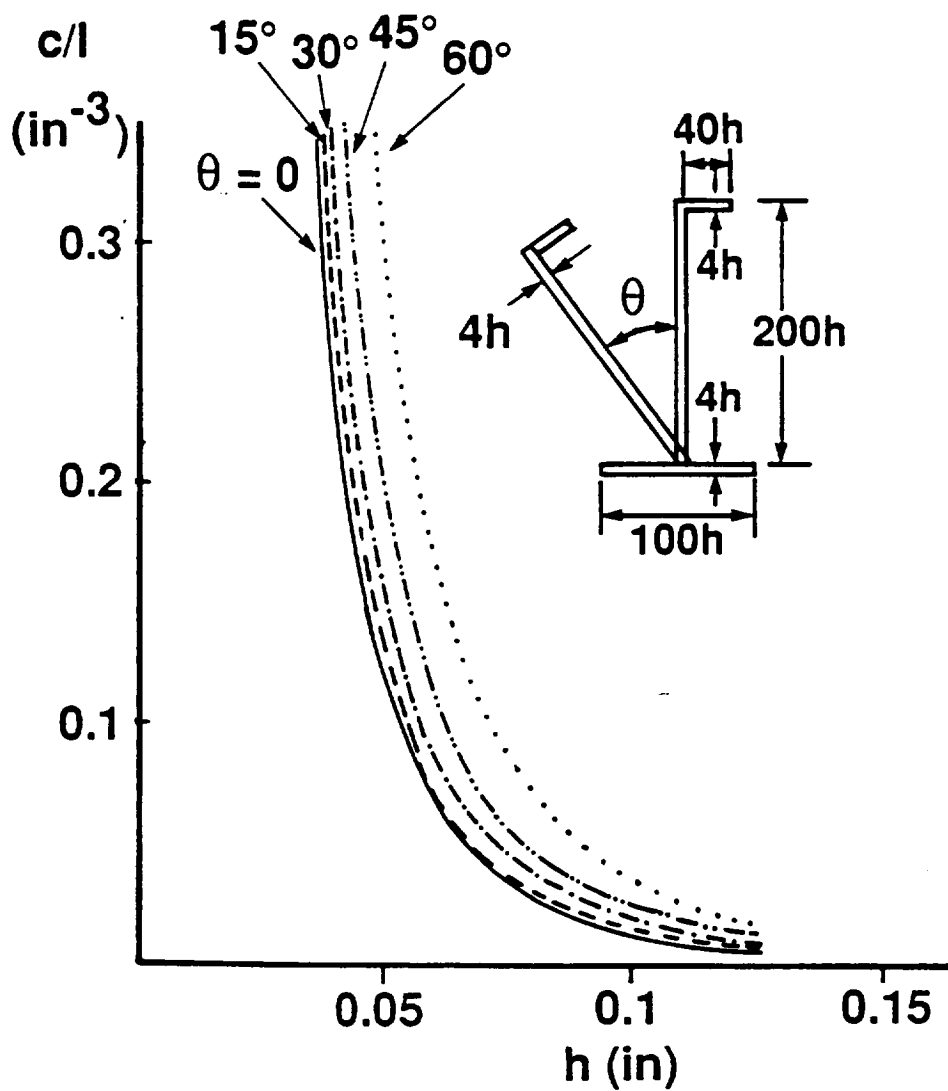


FIGURE 3.17. VARIATION OF MAXIMUM BENDING STRESS AS A FUNCTION OF WEB THICKNESS FOR VARIOUS WEB INCLINATIONS

### 3.1.5 CORNERS

Subsurface anomalies most commonly encountered during the hard tooling manufacture of corner sections are matrix porosity, interply delamination, or a combination of the two. The porosity effects may be analyzed using classical curved beam analyses to approximate the increase in both interlaminar tension and shear stresses resulting from the decrease in effective area. Delaminations are most effectively analyzed using a strain energy release rate approach to compute a critical delamination size associated with unstable crack growth.

Classical isotropic curved beam formulas may be used to approximate the interlaminar tension and shear stress states in a quasi-isotropic corner section. For illustration, these stress components will be calculated at the centerline of the section. The applicable formulas are as below [Reference 3]:

$$\sigma_r = \left\{ \frac{b-h}{t_r A h r} \right\} M \left( \int_{r_i}^b \frac{dA}{r} - \frac{A_r}{b-h} \right) \quad (3.5)$$

$$\tau_{r\theta} = \left\{ \frac{b-h}{t_r A h r^2} \right\} V (b A_r - Q_r) \quad (3.6)$$

$$A_r = \int_{r_i}^b dA \quad (3.7)$$

$$Q_r = \int_{r_i}^b r dA \quad (3.8)$$

where all geometry parameters are defined in Figure 3.18. The contribution of the normal force, N, to the interlaminar stress state is found to be negligible. Substituting appropriate values into the stress equations, the approximate interlaminar stresses for the zero porosity, or "Defect-Free Manufacture", condition are found to be:

$$\sigma_r = 2.68 M \quad (3.9)$$

$$\tau_{r\theta} = 3.90 V \quad (3.10)$$

Assuming that matrix porosity reduces the load carrying area of the section by 10%, but does not decrease the thickness of the component, similar calculations yield interlaminar stress values for the "Defective Manufacture" condition:

$$\sigma_r = 2.98 M \quad (3.11)$$

$$\tau_{r\theta} = 4.33 V \quad (3.12)$$

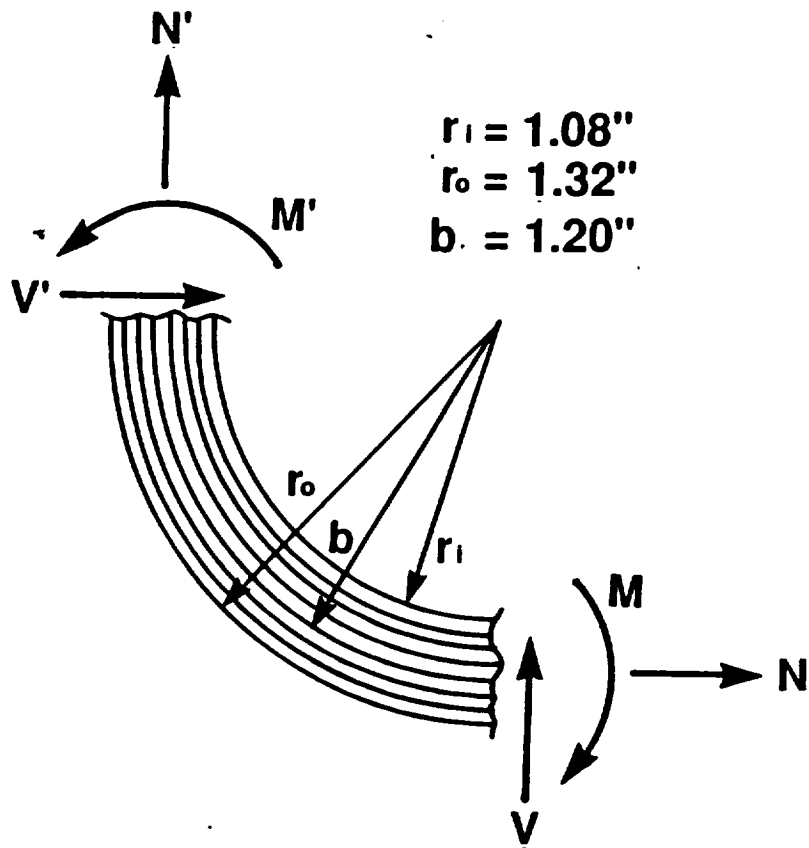


FIGURE 3.18. CORNERS - LOADING AND GEOMETRY DEFINITION

The reduction of section area may be compensated by adding plies to either the inner or outer surface of the corner. In order to reduce the interlaminar stresses, the area of the section must be increased by the factor 1.11 since

$$2.98/2.68 = 4.33/3.90 = 1.11$$

Thus the thickness must be increased (assuming constant width) from 0.240" to 0.266", or by 0.026". Since the nominal ply thickness is taken to be 0.015 inches (for fabric plies), the addition of two plies to the corner should compensate for the 10% porosity level.

As an indication of the cost associated with adding material to "Defective" structure, a comparison to a "Defect-Free" component as produced by the THERM-X<sup>o</sup> process is presented in Table 3.6.

Table 3.6  
Corners - Weight and Labor Hour Estimates

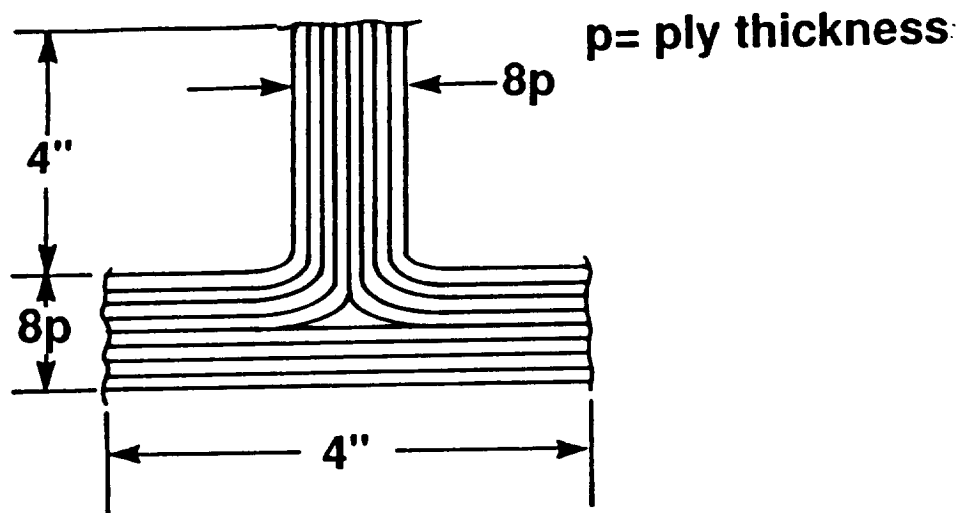
PROCESS STEP	THERM-X <sup>o</sup> PROCESS (HRS)	CONVENTIONAL LAYUP (HRS)
PREPARE TOOLS	0.5	0.5
CUT MATERIAL	0.4	0.4
LAY-UP PANEL	1.0	1.2
VACUUM BAG	1.0	1.2
STRIP & TRIM	2.2	2.0
TOTAL LABOR HRS	5.1	5.3
TOTAL WEIGHT (LBS)	0.97	1.13

### 3.1.6 SKIN-STIFFENER COMBINATION

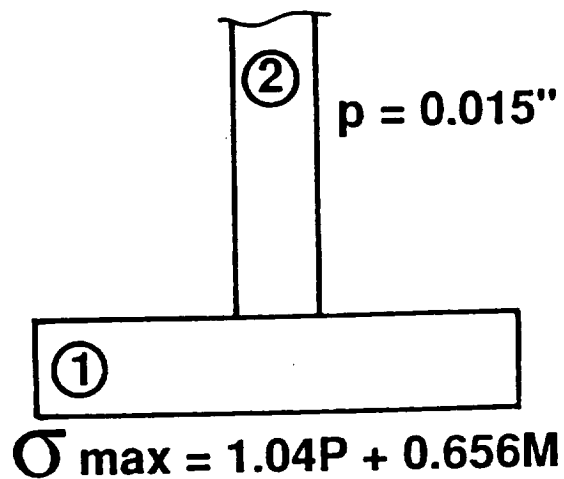
Conventional manufacturing processes for skin-stiffener combinations often result in poor final configurations due to misalignment of the stiffener web relative to its flange. This low quality component adversely affects both the axial and bending load capacity of the structure.

The ideal skin-stiffener combination resulting from "Proper Manufacture" along with its analytical approximation is shown in Figure 3.19. Neglecting contributions of the skin in both axial and bending calculations, and noting that ply thickness  $p$  equals 0.015", the maximum tensile stress developed in the structure is found to be:

$$\sigma_{\max} = 1.04 P + 0.656 M \quad (3.13)$$



**Analysis/Idealization**



**FIGURE 3.19. SKIN-STIFFENER COMBINATION; DEFECT-FREE MANUFACTURE**

A detail of the result of a process that results in defects is shown in Figure 3.20. Note that plies in the vicinity of the web-flange junction are folded over upon themselves, kinked, and otherwise poorly located. It is assumed that the plies in this area are ineffective in reacting both axial and bending loads. The degree of ineffectiveness is illustrated in the analytical idealization of the structure also shown in Figure 3.20. The maximum tensile stress developed in the structure is calculated as

$$\sigma_{\max} = \frac{P}{(0.42+24p')} + \frac{Mk}{(183p'-63kp')} \quad (3.14)$$

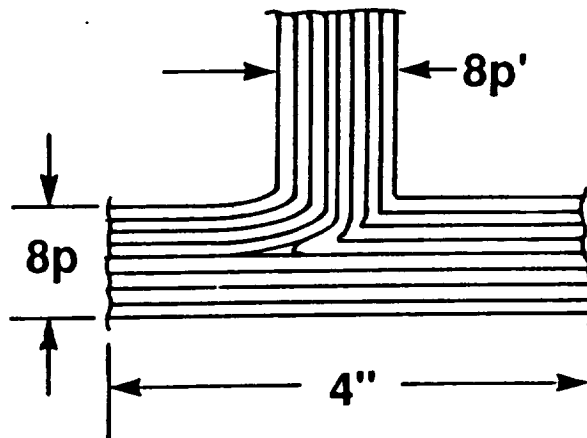
where  $k = (0.0234+63p')/(0.42+24p')$ , and  $p'$  is an unknown ply thickness to be determined. The unknown  $p'$  represents the thickness that must be added to the web and flange in order to produce the same maximum tensile stress as for the "Defect-Free Manufacture" condition.

As an example, consider the design loads  $P=67300$  lb and  $M=0$ . From equation 3.13,  $\sigma_{\max} = 70$  ksi. Substituting  $\sigma_{\max}$  into Eq. 3.14 and solving for  $p'$  yields the result  $p'_{\max} = 0.180$ ", i.e. the web thickness required to produce the same maximum tensile stress as for "Defect-Free Manufacture" is 0.180". Noting that the original thickness is 0.120", adding four plies of 15 mil material will be sufficient to bring the "Mismanufactured" structure up to strength requirements. A graphical representation of the analysis is shown in Figure 3.21.

For both "Defect Free Manufacture" and "Mismanufacture" skin-stiffener combinations analyzed above, a cost breakdown in terms of structural weight and fabrication time is presented in Table 3.7.

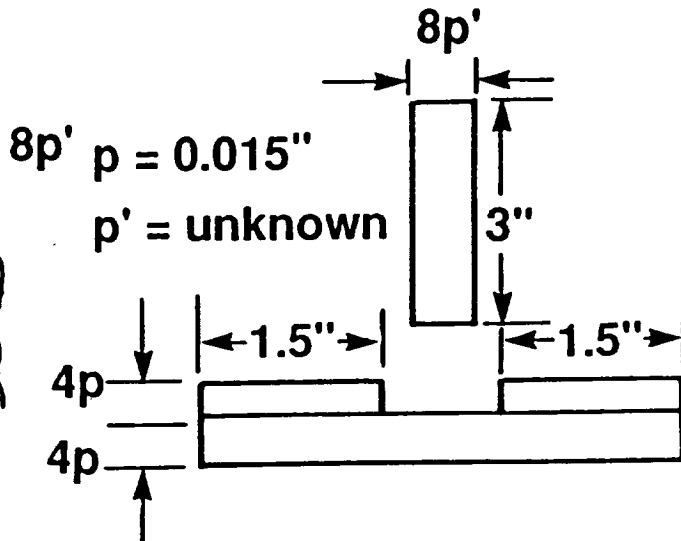
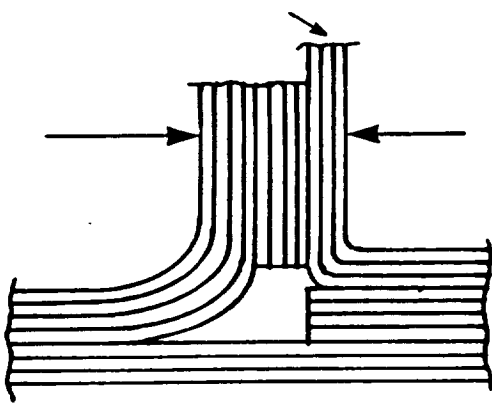
Table 3.7  
Skin-Stiffener Combination-  
Weight and Labor Hour Estimates

PROCESS STEP	THERM-X <sup>o</sup> PROCESS (HRS)	CONVENTIONAL LAYUP (HRS)
PREPARE TOOLS	0.5	0.5
CUT MATERIAL	0.7	0.8
LAY-UP PANEL	2.0	2.0
VACUUM BAG	1.0	1.5
STRIP & TRIM	2.2	2.0
TOTAL LABOR HRS	6.4	6.8
TOTAL WEIGHT (LBS)	0.16	0.20



**Analysis/Idealization**

**Added plies**



$$\sigma_{\max} = \frac{P}{(0.42 + 24p')} + \frac{M\kappa}{0.0234 + 63p'}$$

$$\kappa = \frac{183p' - 63\kappa p'}{0.42 + 24p'}$$

**FIGURE 3.20. SKIN-STIFFENER COMBINATION; MANUFACTURE WITH DEFECTS**

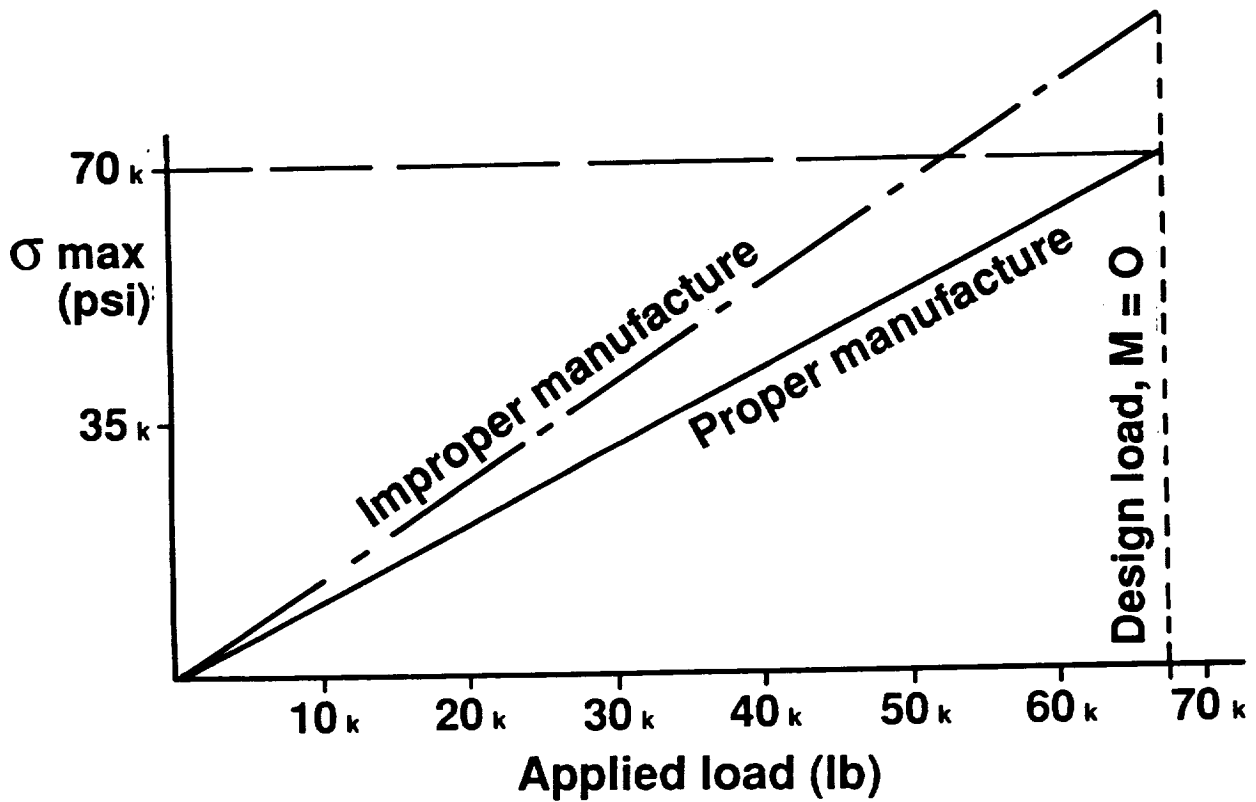
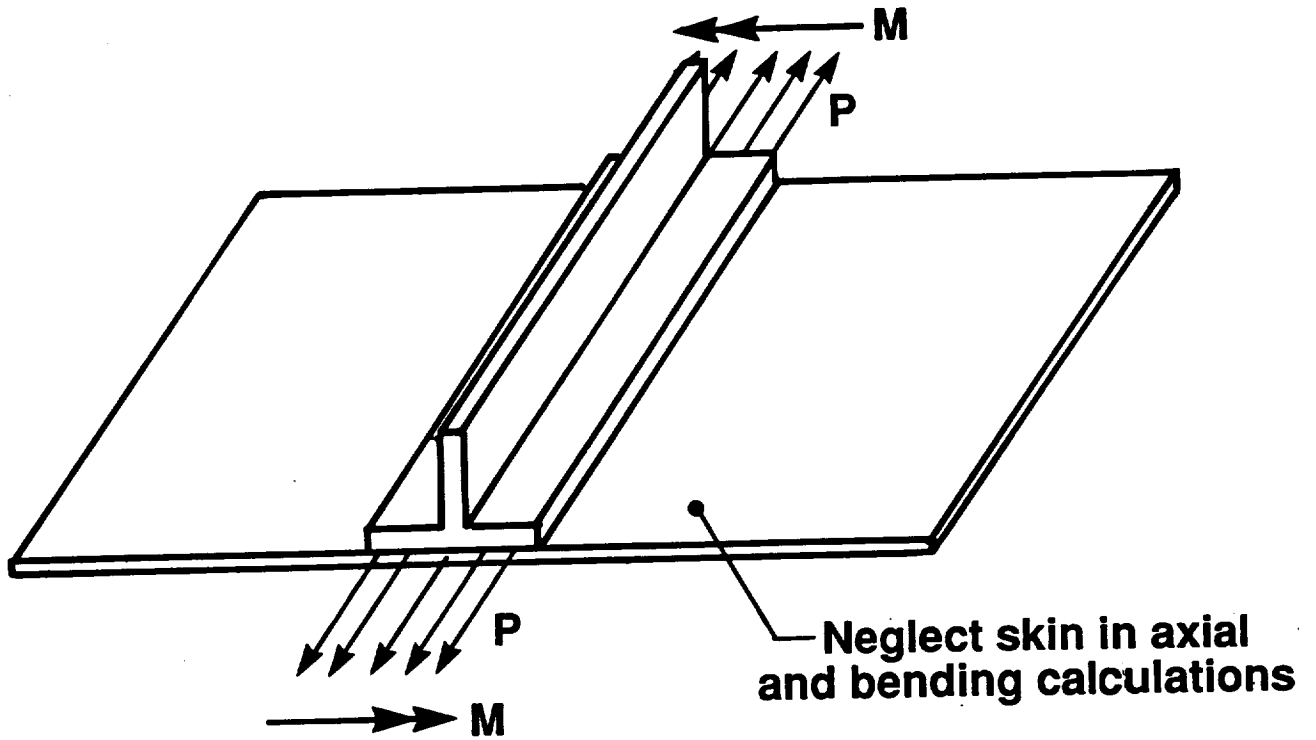


FIGURE 3.21. MAXIMUM STRESS AS A FUNCTION OF APPLIED LOADS FOR DEFECT-FREE AND IMPROPER MANUFACTURE



### 3.1.7 COCURED BOX WITH COCURED INTERNAL STIFFENERS (RIBS/SPARS)

For this structural detail, issues such as different loading types (bending and torsion), continuity of load paths, load transfer at attachment points, the detailed configuration of attachments (shear clips for example) between skin and spars, need a detailed analysis that would account for various failure modes (in-plane and out-of-plane) and would culminate at a finite element analysis of the whole structure. In addition, manufacturing issues such as locating of parts inside the box and maintaining tolerances merit special attention when the structure is to be cocured.

For the reasons mentioned above, no weight estimates are given for this structural detail. An attempt was made to estimate labor hours required to manufacture a small box (36 inch wide by 36 inch long by 12 inches high) based on current production practices and the Sikorsky Aircraft experience with THERM-X\*. These preliminary estimates (shown in Table 3.8) are based on using rigid internal layup tooling with an air bladder. The part is cured with the internal mandrel in place, while pressure is being applied by the bladder to consolidate the layup against the female tool surface on the outside. Unless specially designed THERM-X\* flexible bags are designed there appears to be no advantage (from the point of view of labor hours required, assuming no weight penalties for the conventional manufacturing process) to a THERM-X\* manufacturing procedure.

Table 3.8  
Cocured Box with Cocured Internal Stiffeners-  
Labor Hour Estimates

PROCESS STEP	THERM-X* PROCESS (HRS)	CONVENTIONAL LAYUP (HRS)
PREPARE CORE	4.0	4.0
PREPARE TOOL	1.0	1.0
CUT MATERIAL	2.0	2.0
LAYUP CORE	2.0	2.0
LAY-UP SKIN	2.0	2.0
ASSEMBLE IN TOOL	2.0	2.0
POSITION LOCATORS	0.5	0.5
VACUUM BAG	3.0	3.0
STRIP & TRIM	2.0	2.0
TOTAL LABOR HRS	18.5	18.5

### 3.1.8 BEADED PANELS

When the conventional bagging procedures are used, resin rich regions are normally built up around the beaded panel transition area on the tool side of the panel. In such a case, the bending stiffness of the panel will be reduced. The degree of stiffness reduction is dependent on the depth of resin build-up.

The empirical equation (equation 3.15) for calculating the stability (bead pullout) of the beaded panel was developed for metal structure and orthotropic plate bending relations were incorporated later in order to apply this formula to laminated structure (reference 4).

$$N_{xyo} = 4 \sqrt{\left[ \frac{N_{xy} (1 + \text{min. M.S.})}{t} \right] \text{Deq} \left( 1 - \frac{D_{12}^2}{D_{11} D_{22}} \right) \sqrt{\frac{b}{h^2 - hd + 4d^2}}} \quad (3.15)$$

where  
 $N_{xy}$  - applied running shear load  
 min. M.S. - strength margin of safety under  $N_{xy}$   
 $\text{Deq} = (D_{11} * D_{22})^{.25}$   
 $h$  - height of web  
 $t$  - web thickness  
 $d$  - distance between beads

As a result of excess resin on one side of the laminate, the laminate is treated as an unsymmetric plate with respect to the mid-plane. The reduced bending stiffness matrix  $[D]^*$ , (equation 3.16) was used to calculate the allowable running shear load (equation 3.15). This is analogous to calculating the inertia of a section about an axis other than the neutral axis and then applying the parallel-axis theorem to calculate the inertia about the neutral axis. Figure 3.22 shows the plot of normalized running shear load versus normalized equivalent bending stiffness. The subscripts r.r and b.l. correspond to resin rich, and base line respectively.

$$[D]^* = [D] - [B][A]^{-1}[B] \quad (3.16)$$

For a three-ply beaded panel with fabric material and quasi-isotropic layup, an extra ply is required to compensate for the loss of bending stiffness around the beaded panel transition region. This calculation is done assuming a 0.0075 inch resin rich region and calculating the resulting equivalent bending stiffness by adding plies that will restore the original bending stiffness. The weight and labor hour estimates for a three-beaded 12"x12" panel are shown in detail in Table 3.9 for conventional layup and Therm-X® tooling procedures.

Table 3.9  
 Beaded Panels - Weight and Labor Hour Estimates

PROCESS STEP	THERM-X® PROCESS (HRS)	CONVENTIONAL LAYUP (HRS)
PREPARE TOOL	0.5	0.5
CUT MATERIAL	0.5	0.6
LAY-UP PANEL	2.0	2.0
VACUUM BAG	1.0	1.5
STRIP & TRIM	2.2	2.0
TOTAL LABOR HRS	6.2	6.6
TOTAL WEIGHT (LBS)	0.18	0.24

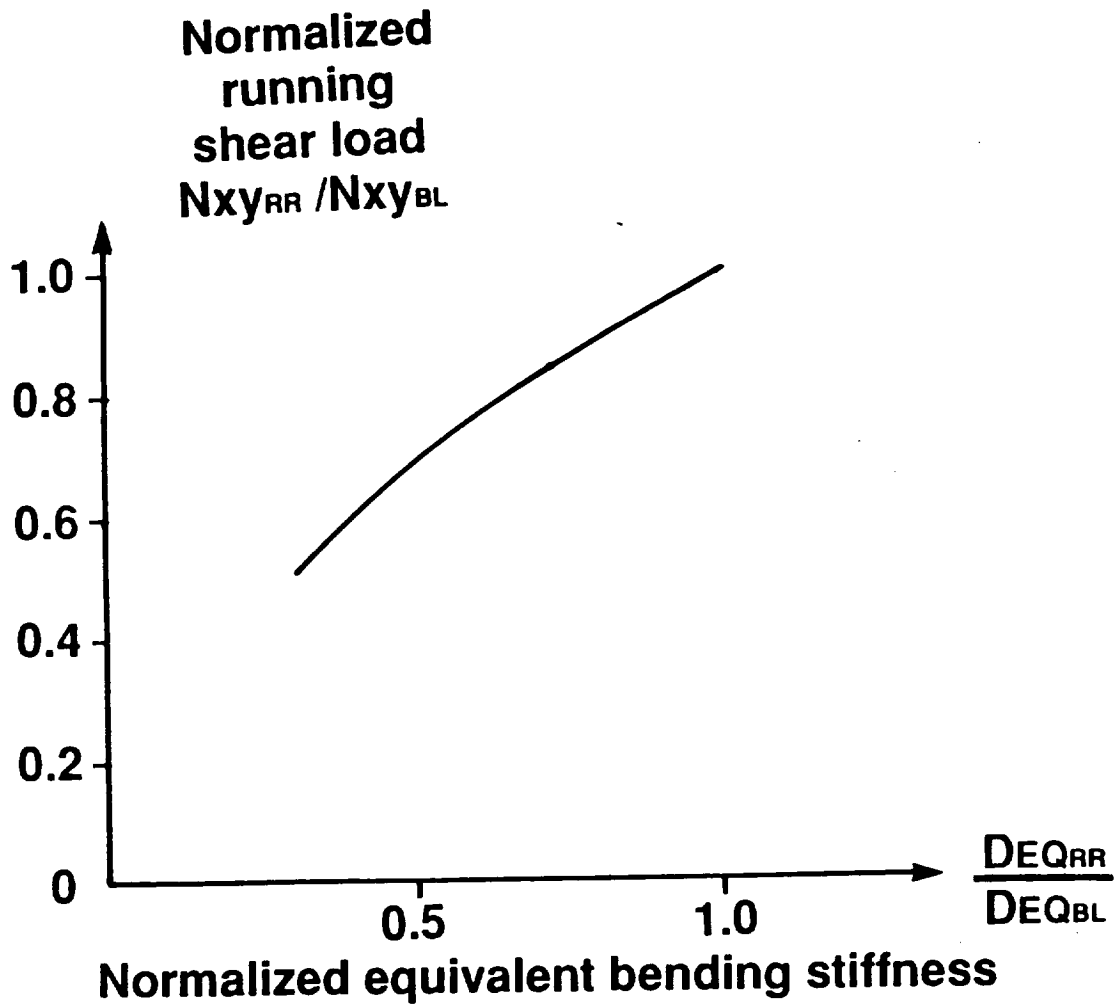


FIGURE 3.22. BEADED PANELS - SHEAR LOAD VERSUS BENDING STIFFNESS

### 3.1.9 FLAT PANEL BAG FOLDOVER

Bag foldovers (pinching) typically result in wrinkles. Analysis of a panel with such a wrinkle loaded in compression requires solution of non-linear equations and no closed-form expressions describing the response can be obtained. The problem was simplified by modelling it as a beam loaded eccentrically, as shown in Figure 3.23. The bending moment at any section is  $-P(v + e)$  where  $e$  is the eccentricity. Depending on the size of the eccentricity, the strength lost because of the wrinkle can be recovered by adding plies locally. Typically, for  $e$  values less than two ply thicknesses, one-ply doublers on both sides of the panel would work.

The detailed weight and cost penalty, based on this assumption, for a 8"x4" panel manufactured by the conventional bagging procedure and THERM-X<sup>o</sup> processing is shown in Table 3.10.

Table 3.10  
Flat Panel Bag Foldover - Weight and Labor Hour Estimates

PROCESS STEP	THERM-X <sup>o</sup> PROCESS (HRS)	CONVENTIONAL LAYUP (HRS)
PREPARE TOOL	0.5	0.5
CUT MATERIAL	0.4	0.5
LAY-UP PANEL	1.0	1.2
VACUUM BAG	1.0	1.5
STRIP & TRIM	2.2	2.0
TOTAL LABOR HRS	5.1	5.7
TOTAL WEIGHT (LBS)	0.04	0.06

### 3.1.10 THICK CYLINDER

Conventional manufacture of a cylindrical tube is accomplished by filament winding on a male mandrel and vacuum bagging the outer surface. As a consequence of the relatively uneven pressure exerted by the vacuum procedure, excessive ply waviness is often observed near the inner radius after the cure has been completed. The waviness of the plies reduces the torsional capacity of the tube and, as a result, increases the maximum shear stress in the component for a given torque load. Processing with THERM-X<sup>o</sup> (in combination with the proper debulking cycles) is not expected to produce waviness since hydrostatic pressure is applied to the part during bagging and cure.

Classical analysis of the unflawed tube results in the maximum shear stress

$$\tau_{\max} = \frac{Tr}{J} \quad (3.17)$$

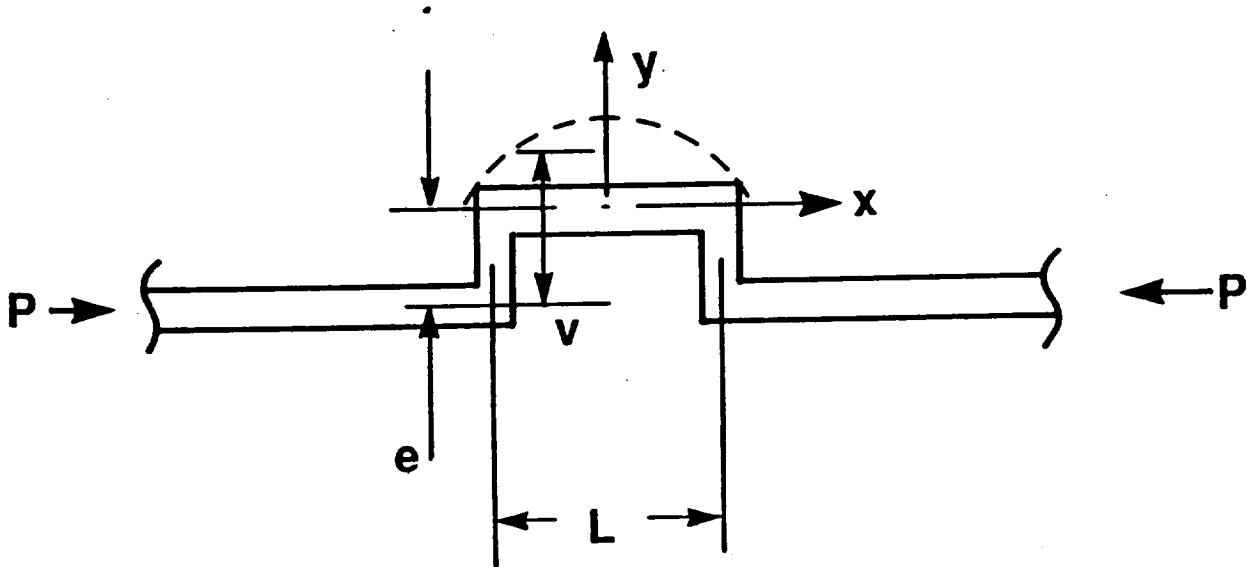


FIGURE 3.23. FLAT PANEL BAG FOLDOVER - MODELING IDEALIZATION

where J is the polar moment of inertia of the tube. Assuming that waviness is of such a degree as to render a number of plies N unable to react torque loads, the reduced section J must be compensated by adding plies to the outer surface. In this way, the design torsional load will produce the same maximum shear stress in the tube. The tube with waviness is analyzed using

$$\tau_{\max} = \frac{2 T r'_o}{\pi(r'_o{}^4 - r'_i{}^4)} \quad (3.18)$$

where  $r' = r + Np$ , N equals the number of wavy plies, p is ply thickness. The equation will be solved for  $r'$  which will produce the same maximum shear stress as in the tube without waviness.

Results of such analysis for various values of N are shown in Figure 3.24. Due to the large r/t ratio, the presence of N wavy plies requires approximately N plies to be added to the outer surface in order to yield the same maximum shear stress.

Cost analyses of structural weight and fabrication time are presented in Table 3.11 for a 30 ft long tube with 12 in. outer diameter and 11.5 in. inner diameter. Although THERM-X<sup>®</sup> processing is estimated to produce a lower weight component (15%), fabrication time penalties are associated with filament winding and THERM-X<sup>®</sup> tooling. Since tubular structure is typically wound over a male mandrel which is not removed until curing has been completed, removal of the mandrel and implementation of THERM-X<sup>®</sup> tooling accounts for the additional fabrication time required.

Table 3.11  
Thick Cylinder - Weight and Labor Hour Estimates

PROCESS STEP	THERM-X <sup>®</sup> PROCESS (HRS)	CONVENTIONAL LAYUP (HRS)
PREPARE TOOL	0.5	0.5
PROGRAM WINDER	2.0	2.0
WIND MANDREL	2.0	2.0
VACUUM BAG	2.0	1.0
STRIP & TRIM	2.2	2.0
TOTAL LABOR HRS	8.7	7.5
TOTAL WEIGHT (LBS)	16.0	18.73

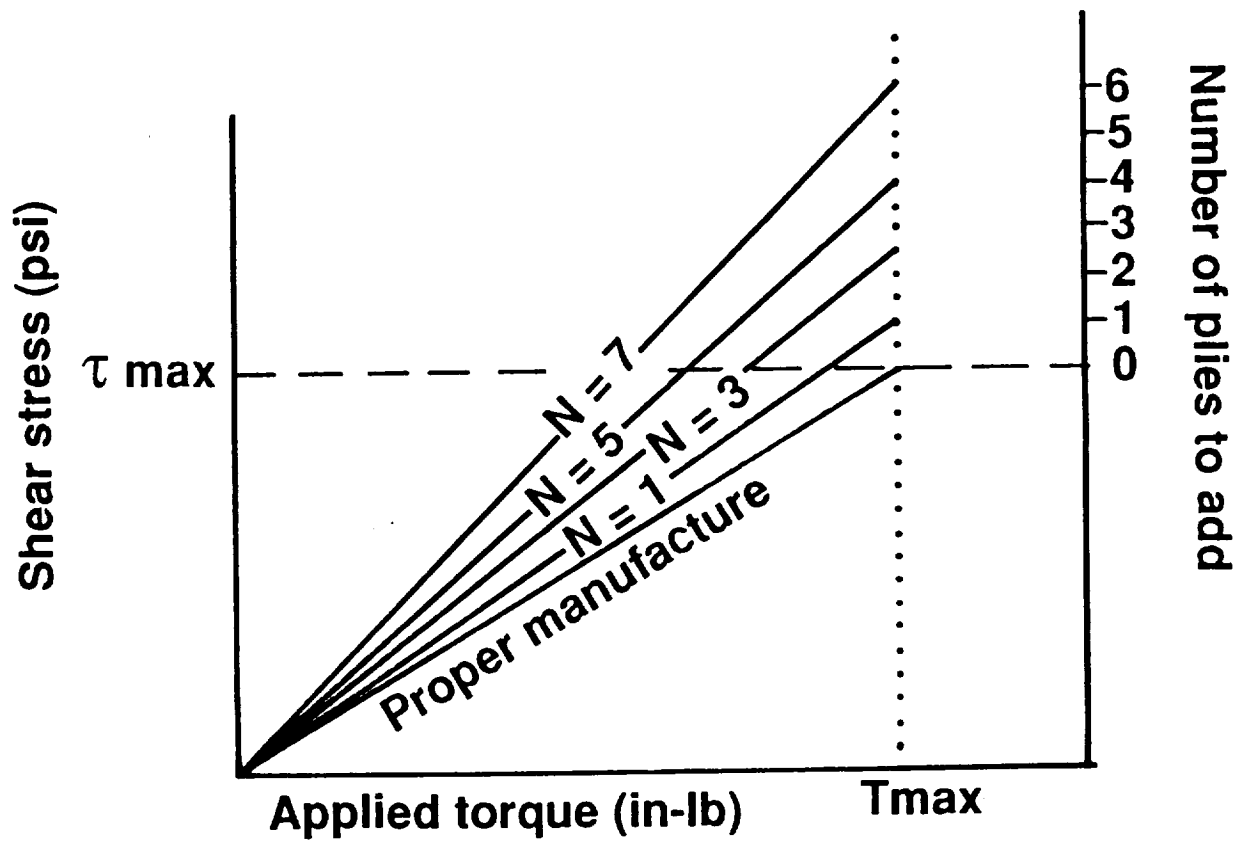


FIGURE 3.24. THICK CYLINDERS - SHEAR STRESS AS A FUNCTION OF APPLIED TORQUE

### 3.1.11 PANEL WITH "CONTINUOUS" FRAMES AND STIFFENERS

The main goal with this type of construction is to create a continuous load path both along the stiffeners and along the frames. With current manufacturing procedures, a cutout (mousehole) is made in the frames to accommodate the stiffeners. It is believed that with THERM-X® tooling generating quasi-hydrostatic pressure even at sharp corners, the mousehole would be much smaller and the incorporation of shear ties would be significantly easier. The loads in the vicinity of the frame/stiffener crossing should therefore be drastically reduced.

To assess this effect, a finite element model of one of the frames was constructed using NASTRAN with CQUAD4 and CBAR elements. For simplicity, any curvature in the frame is neglected. To model the case of a THERM-X® processed part, the two cutouts for the stiffeners were matching exactly the stiffener outer cross-section and the load was assumed to be transferred from the frames to the stiffeners without ply buildup in the region. At the edges of each cutout, bar elements with properties representative of the stiffener were positioned. The finite element mesh is shown in Figure 3.25. A shear force  $V$  of 100 lbs was applied at one end of the frame and the other end was fixed. The frame and stiffener layups were assumed to be quasi-isotropic with a stiffness of 10 msi and a Poisson's ratio of 0.3. the frame thickness was 0.06 inches and the bar elements had a cross sectional area of 0.06 square inches and a moment of inertia of  $1.8 \times 10^{-5}$  in<sup>4</sup>. To model the case of a part manufactured using conventional layup, the bar elements around the mouseholes of the previous model were removed (except for the ones along the flange) and the row of QUAD elements next to the cutout was removed resulting in a 0.5 inch gap. The dimensions and geometric configurations for the two cases are given in Figure 3.26.

The results are shown in Figures 3.27 and 3.28 for the stress distributions in the vicinity of the two stiffeners. The Von Mises stress was chosen as the differentiating parameter. The conclusion does not change if another stress is used. In each plot, the stress distribution for a matching mousehole and an enlarged mousehole (with approximately 0.5 inches of material removed all around the previous cutout) is shown. The stress magnitudes are not important since they are applicable to the particular configuration and loading used for the finite element model. The relative magnitudes, however, are quite significant as they give insight to the local stress concentrations. The stresses around the stiffener in the frame with enlarged mouseholes are much higher than in the frame with mouseholes matching the stiffener contour and improved load transfer by as much as a factor of 2.2 for the stiffener closer to the frame root. This factor is used to estimate the weight penalty that will make the frame with enlarged mouseholes structurally equivalent to the frame with matching mouseholes.



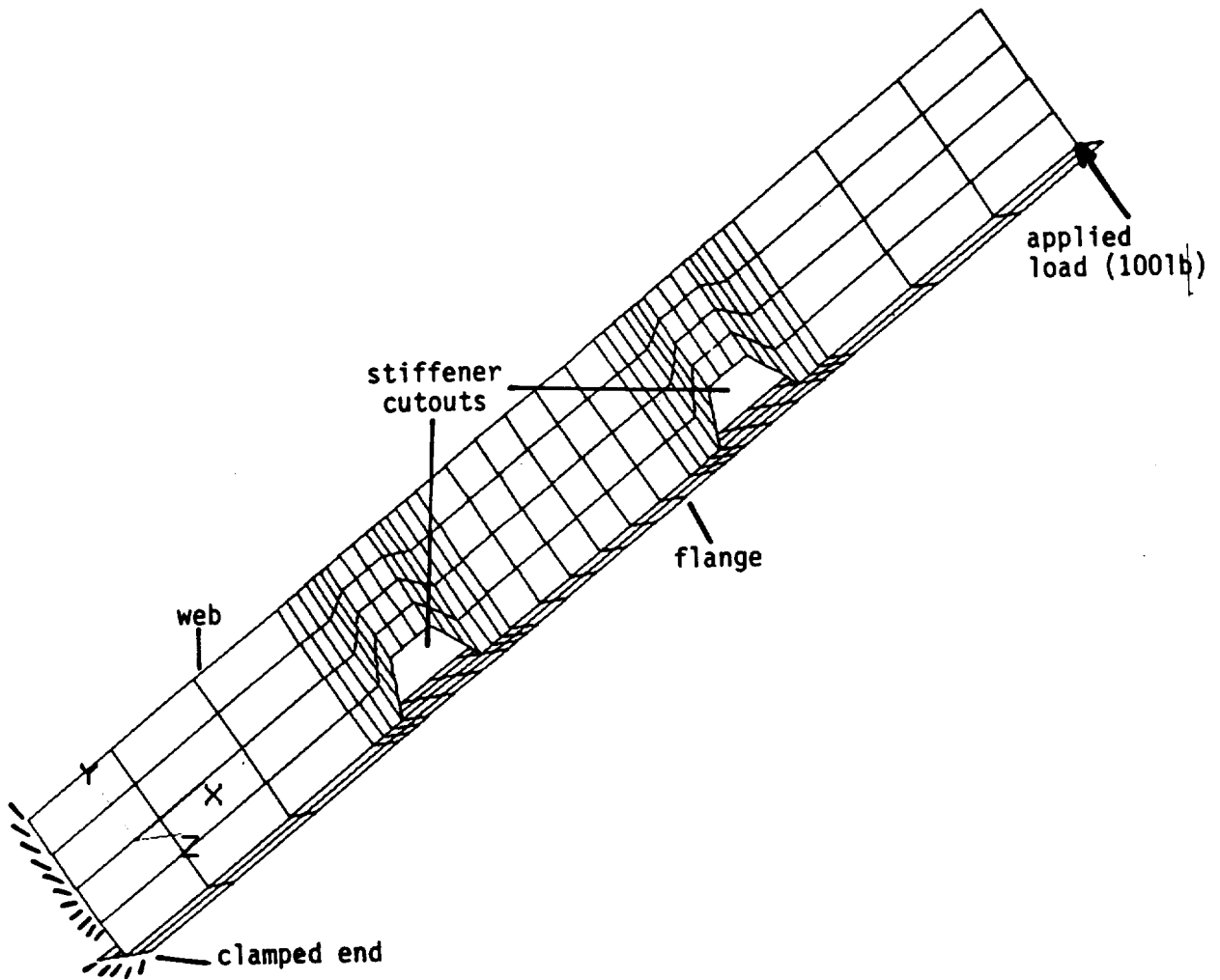


FIGURE 3.25. FINITE ELEMENT MODEL FOR FRAME IN BENDING

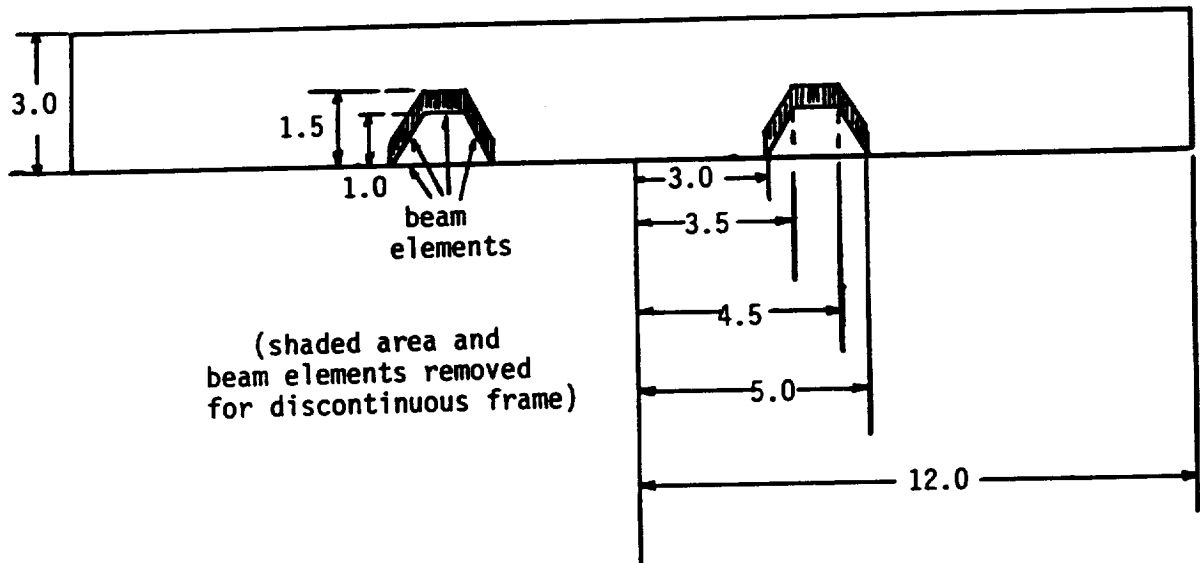


FIGURE 3.26. GEOMETRY CONFIGURATIONS FOR FRAMES WITH AND WITHOUT ENLARGED MOUSEHOLES

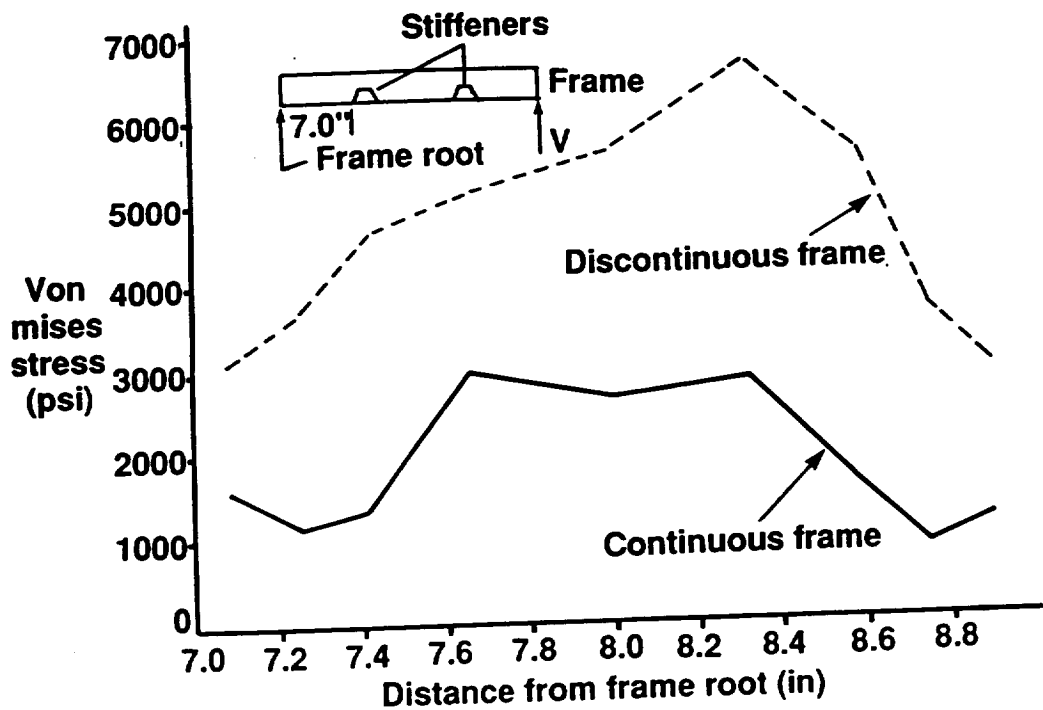


FIGURE 3.27. STRESS (VON MISES) DISTRIBUTION IN THE VICINITY OF MOUSEHOLE CLOSEST TO FRAME ROOT

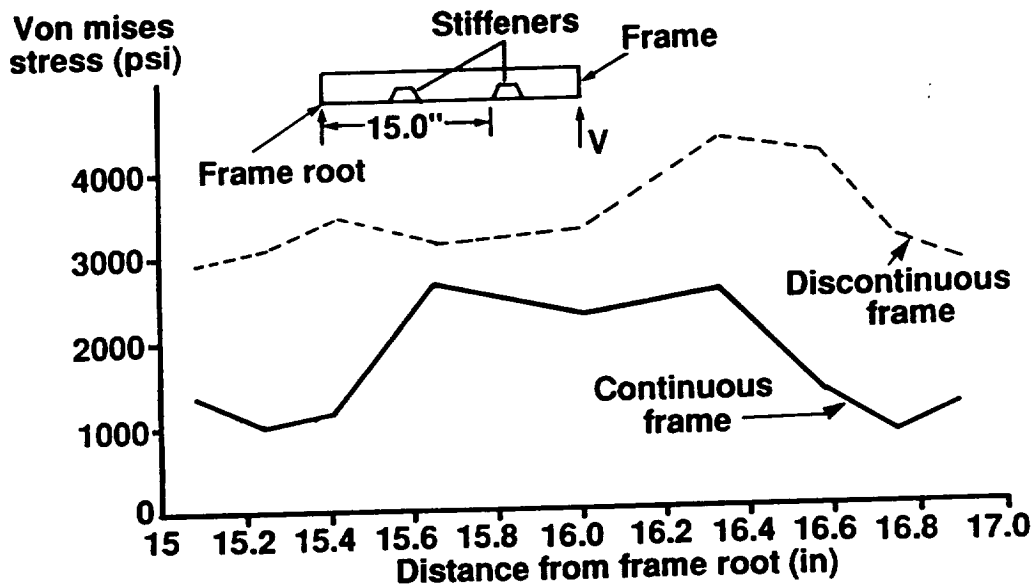


FIGURE 3.28. STRESS (VON MISES) DISTRIBUTION IN THE VICINITY OF THE MOUSEHOLE AWAY FROM THE FRAME ROOT

For a frame in bending, the maximum bending stress is inversely proportional to the thickness and inversely proportional to the square of the depth of the frame where the maximum stress

$$\sigma = \frac{6M}{bh^2} \quad (3.19)$$

expression is used with b the frame thickness and h the frame depth. Thus, to accommodate a 2.2 increase in stress, either the frame thickness must be increased locally by that amount, or the frame depth must increase by a factor of 1.48 ( $\sqrt{2.2}$ ). The thickness increase was chosen since it can be achieved by selective reinforcement in the area around the stiffener cutout while the depth increase would have to be either all along the frame resulting in a heavier structure or, local to the cutout area requiring increased labor hours. The weight and labor hour estimates for a 30 inch by 24 inch curved panel with 24 inch radius of curvature, with two frames (blade shaped with 2 inch webs) and two stiffeners (hat shaped with height of 1 inch aligned with the long panel dimension) and layups  $[(\pm 45)_0/(\pm 45)]$  for the skin and stiffeners and  $[(\pm 45)_0/(\pm 45)]_s$  for the frames are shown in Table 3.12. Ply orientations in parentheses indicate plain weave material. No parentheses indicate unidirectional tape. The part made with standard procedures has at each frame cutout a 2 inch by 2 inch doubler on each side of the frame of thickness equal to the frame thickness and layup the same as the frame layup. These doublers have to be made separately because, if placed in position uncured, the pressure during curing will force them to slide away from their proper position.

Table 3.12  
Panel with Continuous Frames and Stiffeners -  
Weight and Labor Hour Estimates

PROCESS STEP	THERM-X <sup>o</sup> PROCESS (HRS)	CONVENTIONAL LAYUP (HRS)
PREPARE TOOLING AIDS	1.5	1.5
PREPARE TOOLS	1.0	1.0
CUT MATERIAL	1.6	2.6
LAY-UP SKIN, STIFF, FRAMES	5.0	5.0
VACUUM BAG	3.5	1.5
STRIP & TRIM	2.0	2.0
FABRICATE DOUBLERS	0.0	5.0
CUT, FIT, BOND DBRS	0.0	3.0
TOTAL LABOR HRS	14.6	21.6
TOTAL WEIGHT (LBS)	1.96	2.0

### 3.2 SELECTION PROCESS

While the above estimates are by no means complete in accounting for all pertinent factors, they are expected to give correct basic trends. Based on the weight and labor hour estimates of the previous section, the structural details examined can be rated so that the ones where the use of THERM-X® medium is most promising can be determined. The labor hours and weights for a THERM-X® process are shown in Table 3.13 along with the percentage difference from conventional layup. For both process types, the resulting parts are structurally equivalent.

Table 3.13  
Structural Details - Weight and Labor Hour Comparisons (Estimates)  
Between THERM-X® Process and Conventional Hand Layup

DETAIL	WEIGHT (LBS)	%CHANGE FROM HAND LAYUP	LABOR HOURS	%CHANGE FROM HAND LAYUP
COCURED SANDWICH	2.69	-22.4	6.2	0.0
SOLID-SAND TRANSITION	5.16	-1.0	6.9	-4.2
CORE TRANSITION	4.22	-15.6	6.5	0.0
COC'D STIFF'R ON PANEL	0.23	-11.5	6.0	-7.7
CORNER	0.97	-14.2	5.1	-3.8
SKIN/STIFF'R COMB'N	0.16	-20.0	6.4	-5.9
COCURED BOX	---	---	18.5	0.0
BEADED PANELS	0.18	-25.0	6.2	-6.0
BAG FOLDOVER	0.04	-33.3	5.1	-10.5
THICK CYLINDER	16.00	-14.6	8.7	+16.0
PANEL W/CONTINUOUS FRAMES & STIFFENERS	1.96	-2.0	14.6	-32.4

It should be noted that the labor hour estimates account for multiple THERM-X fills and the possible use of a separating membrane between the part and THERM-X® medium to avoid any contamination. (This latter issue has now been resolved and no separating film is needed). The vacuum bagging estimates, therefore, presented in the previous section for THERM-X® tooling, are conservative and as a result tend to increase the total labor hour estimates for the process.

There are no entries for the weight of the Cocured Box because a reasonable estimate would require analysis beyond the scope of this contract (see discussion in section 3.1.7).

As is seen from Table 3.13, THERM-X® tooling results in a lighter (or of equal weight) part for all structural configurations. This is mainly because it was assumed that, for this type of structural details, THERM-X® tooling would produce virtually defect-free parts and thus no doublers and/or additional plies are needed to account for the presence of defects. The biggest savings in weight are for Flat Panels with Bag Foldovers, Beaded Panels, and Cocured Sandwich Panels.

In terms of labor hours required to produce these parts, THERM-X® tooling shows gains for all details except for Thick Cylinders. The labor hour savings are largest for the Panel with Continuous Frames and Stiffeners which is estimated to require 32.4% less labor hours than hand layup.

A way to include both labor hours and weight in a single evaluation is to estimate the cost of these structural details. Assuming typical values of \$ 50.0/lb of Graphite/Epoxy, \$62.8/lb of 3lb core and \$47.0/lb of 6-8lb core, and \$30.0 per labor hour of manufacturing the \$ cost of these parts is estimated (weight x price per lb of material + labor hours x \$ cost/labor hour). It is shown in Table 3.14 for THERM-X® process along with the percent difference from conventional hand layup.

Table 3.14  
Structural Details - \$ Cost Estimates for  
THERM-X® Tooling and % Difference from Standard Manufacture

DETAIL	COST (\$)	%CHANGE FROM CONV. LAYUP
COCURED SANDWICH	329	-10.8
SOLID-SAND TRANSITION	474	-2.2
CORE TRANSITION	421	-8.3
COC'D STIFF'R ON PANEL	203	-6.4
CORNER	201	-6.5
SKIN/STIFF'R COMB'N	200	-6.5
COCURED BOX	---	---
BEADED PANELS	195	-7.1
BAG FOLDOVER	155	-10.9
THICK CYLINDER	1061	-8.5
PANEL WITH CONTINUOUS FRAMES & STIFFENERS	536	-28.3

No estimates are given for the "Cocured Box" for reasons explained above and in section 3.1.7.

In all cases, THERM-X® tooling results in a less expensive part. The largest savings is realized for a "Continuous" Frame/Stiffener Combination (THERM-X® processing is 28% less expensive). The comparison between the two manufacturing processes for all structural details (except the Cocured Box) is shown in graphical form in Figure 3.29. If the two manufacturing procedures were equivalent, all the data points would fall along the 45 degree line. Data points above the 45 degree line indicate that the conventional manufacturing procedure is more expensive. The excess cost is measured as the difference of each datum point from the 45 degree line.

COST (\$) CONVENTIONAL LAY-UP

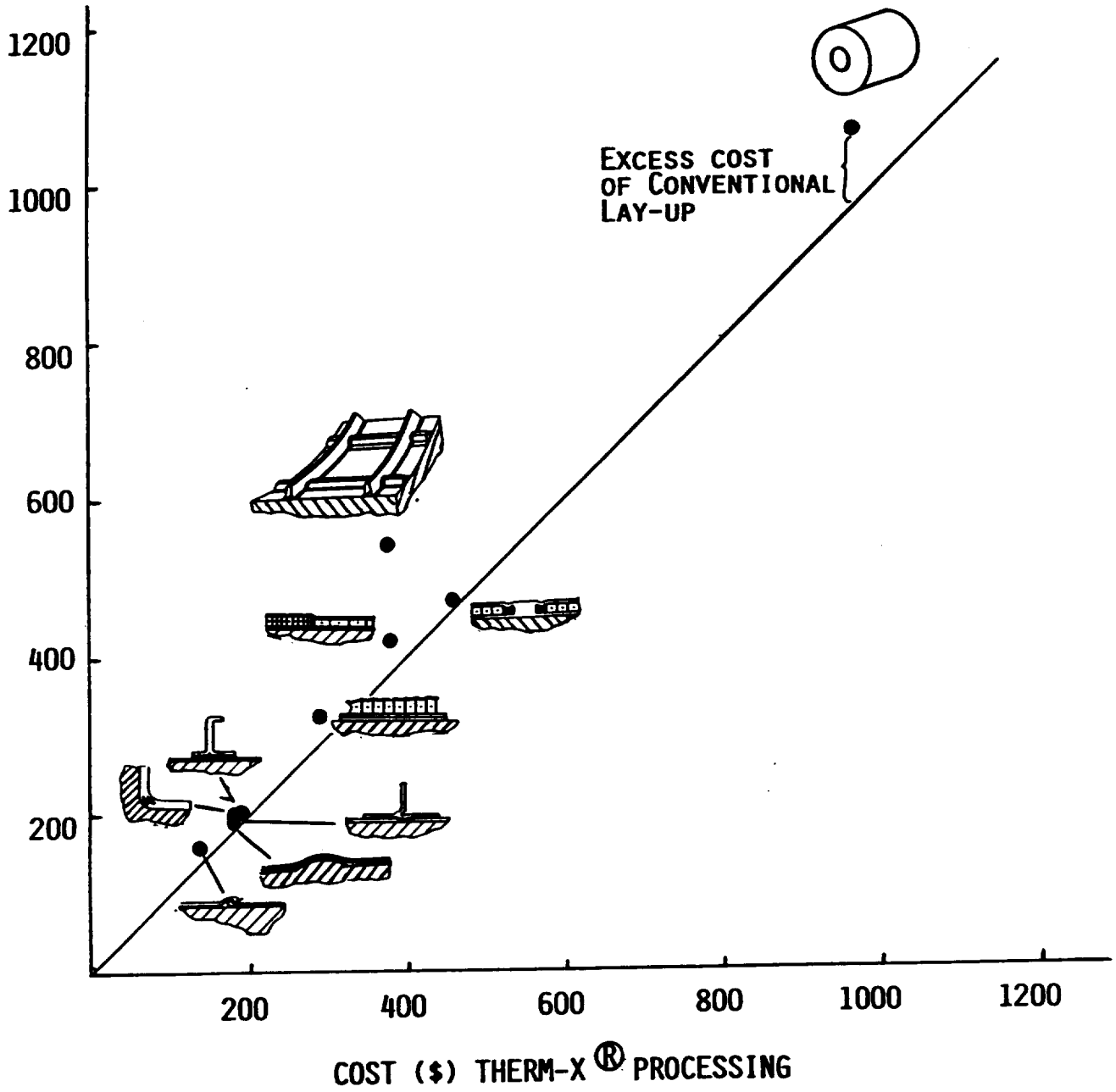


FIGURE 3.29. COST FOR VARIOUS STRUCTURAL DETAILS

Based on this selection procedure, the Panel with "Continuous" Frames and Stiffeners appears to be the structural detail that would show the biggest advantage if THERM-X<sup>®</sup> tooling were used. This structural detail being one very frequently used in primary fuselage structure, was selected as the focus of this program. The following section describes the procedure used to design and optimize this structural detail that was selected as the full scale panel for evaluation in this program.

### 3.3 DESIGN OF FULL SCALE PANEL

The procedure used to determine the geometry of the curved stiffened panel that was used as the full-scale article is described in this section. The panel was assumed to be under compression and shear and the stiffener and frame properties were selected so that weight was minimized.

#### 3.3.1 GOVERNING EQUATIONS AND OPTIMIZATION SCHEME

Fixed wing fuselage and wing skins or helicopter tailcones usually consist of stiffened panels where the skin is used to take the shear loads due to twisting and the stiffeners are used to take the compression loads due to bending. An example of such a panel is shown in Figure 3.30. The loading is in-plane shear  $N_{xy}$  and compression  $N_x$ . Quantities with a subscript "s" refer to the stiffeners and quantities with a subscript "f" refer to the frames. Quantities with no subscripts refer to the skin.

The optimization procedure aims at minimizing the panel weight subject to a series of constraints related to the loading and expected failure modes. The optimum design would correspond to a case where all failure modes occur simultaneously since, in that case, the panel would not be overdesigned for any of the failure modes.

A method to minimize the panel weight and cost is sought subject to a set of constraints: (1) Buckling of the panel as a whole at a predetermined load intensity, (2) Buckling of each individual bay at the same load intensity as buckling for the whole panel, (3) Failure of the post-buckled skin at a predetermined load intensity (ultimate) which is higher than the buckling load, (4) No failure of frames and stiffeners under compression and shear until the ultimate load is reached, and (5) No material used is below minimum gage.

Condition (5) consists of a simple check of the resulting panel geometry. If any thickness value is found to be below minimum gage, the smallest value is set equal to minimum gage and the weight is minimized subject to constraints (1) and (2). In general, in such a case, the resulting skin thickness and frame and stiffener cross-sectional areas are higher than what is required to cause failure at ultimate load and thus, conditions (3) and (4) are satisfied in the sense that no failure occurs at ultimate load. For simplicity, the panel was assumed flat.



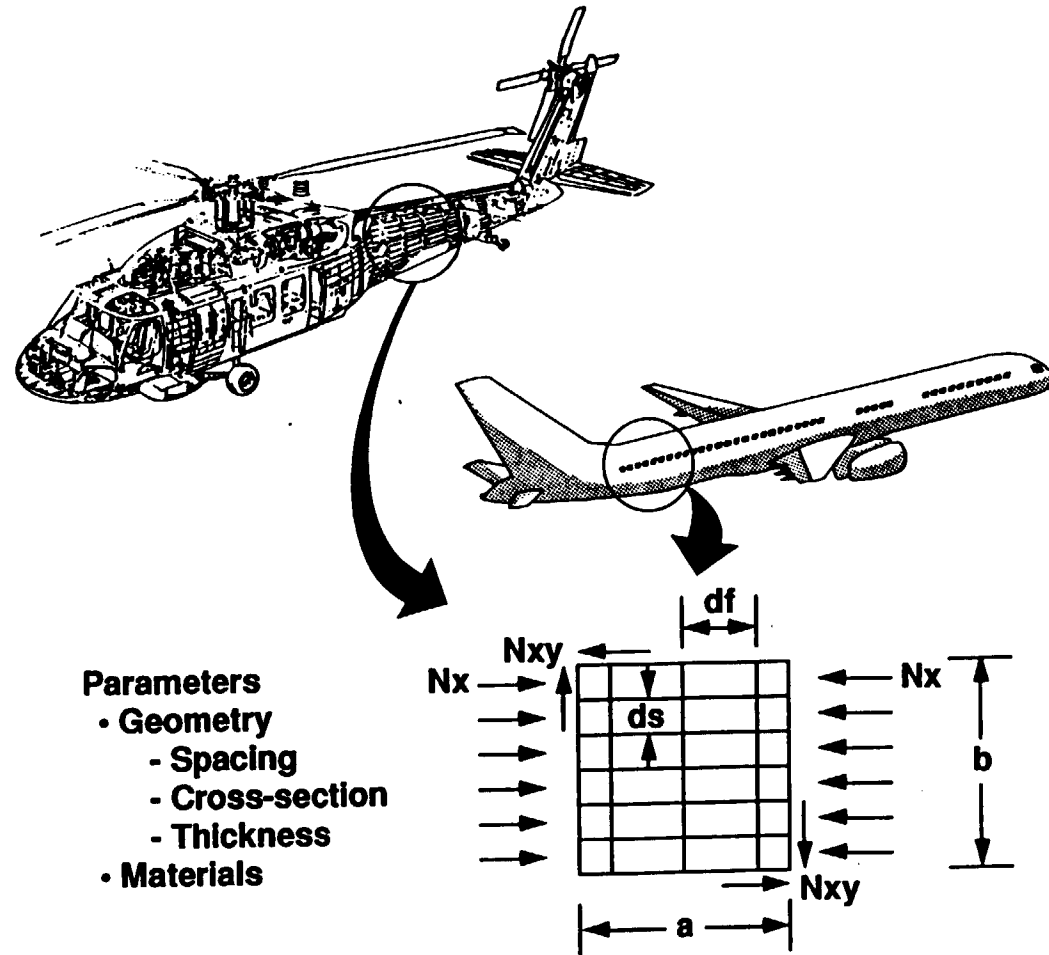


FIGURE 3.30. CURVED STIFFENED PANEL AS STRUCTURAL ELEMENT

The weight of the stiffened panel is given as the weight of the skin, the weight of the stiffeners, and the weight of the frames. Assuming the same density  $\rho$  for all parts (skin, stiffeners, and frames) the following expression is obtained:

$$W = \rho abt + \rho A_s a n_s + \rho A_f b n_f \quad (3.20)$$

where  $n_f$  and  $n_s$  are the number of frames and stiffeners respectively. These can be expressed as  $a/df$  and  $b/ds$  where  $df$  and  $ds$  are the frame and stiffener spacing respectively. Thus,

$$W = \rho ab \left( t + \frac{A_s}{ds} + \frac{A_f}{df} \right) \quad (3.21)$$

It can be seen that for a panel with fixed dimensions and material, the weight is only a function of the skin thickness  $t$ , the frame area to spacing ratio  $A_f/df$  and the stiffener area to spacing ratio  $A_s/ds$ .

The bending stiffnesses of the panel as a whole, including the frames and stiffeners are given by:

$$\begin{aligned} \tilde{D}_{11} &= \frac{E_x t^3}{12(1-\nu_{xy}\nu_{yx})} + \frac{E_s I_s}{ds} \\ \tilde{D}_{22} &= \frac{E_y t^3}{12(1-\nu_{xy}\nu_{yx})} + \frac{E_f I_f}{df} \\ \tilde{D}_{12} &= \frac{E_x \nu_{yx} t^3}{12(1-\nu_{xy}\nu_{yx})} \\ \tilde{D}_{66} &= \frac{G_{xy} t^3}{12} + \frac{G_s J_s}{2ds} + \frac{G_f J_f}{2df} \end{aligned} \quad (3.22)$$

where  $I$  and  $J$  are the bending and polar moments of inertia and the bending engineering constants  $E_x$ ,  $E_y$ ,  $G_{xy}$ ,  $\nu_{xy}$  and  $\nu_{yx}$  (for the skin),  $E_s$ ,  $G_s$  (for the stiffeners) and  $E_f$ ,  $G_f$  (for the frames) are to be chosen, as buckling and postbuckling involve mostly bending of the structural members involved. The panel is assumed to be orthotropic and the frame and stiffener contributions are obtained from reference 5. The first term in each of the above equations is the standard bending stiffness contribution.

For simplicity, it will be assumed that the frames and stiffeners have solid rectangular cross-sections. This is not as limiting as it appears since once the optimization is carried out, other geometries can be selected that match the area and moment of inertia of the rectangular stiffeners. These alternative designs will not be optimal (either lighter or heavier than the rectangular cross section design) but will be close to the optimum point. This is because by setting  $\beta_s = \beta_f = 0$ , the optimization procedure can be completed using  $b_s$  and  $h_s$  (and  $b_f$  and  $h_f$ ) as the quantities describing the cross-section of the stiffeners

and frames i.e. two variables per cross section. This is entirely equivalent to using  $A_s$  and  $I_s$  (and  $A_f$  and  $I_f$ ) as the pertinent quantities since they completely define the cross sections also and assuming zero torsional rigidity for the stiffening members. So the difference in the panel weight will be due to the effect of the torsional rigidity of the frames and stiffeners which, for most cross sections (that are open) is very small.

The area, bending moment of inertia, and polar moment of inertia for a stiffener are given by

$$\begin{aligned} A_s &= b_s h_s \\ I_s &= \frac{b_s h_s^3}{12} \\ J_s &= \beta_s b_s h_s^3 \end{aligned} \quad (3.23)$$

where  $b_s$  and  $h_s$  are the width and height of the stiffener and  $\beta_s$  is a coefficient that depends on the aspect ratio of the cross-section and is given in reference 6. Similar expressions describe the frame quantities. The only difference is the subscript.

Assuming the panel is simply supported at its edges, the condition for buckling under combined loading has the form [7]:

$$1 = \frac{\tilde{D}_{11} \left(\frac{m\pi}{a}\right)^4 + 2(\tilde{D}_{12} + 2\tilde{D}_{66}) \left(\frac{m\pi}{a}\right)^2 \left(\frac{n\pi}{b}\right)^2 + \tilde{D}_{22} \left(\frac{n\pi}{b}\right)^4}{2 N_{xy} \left(\frac{m\pi}{a}\right) \left(\frac{n\pi}{b}\right) - N_x \left(\frac{m\pi}{a}\right)^2} \quad (3.24)$$

where  $m$  and  $n$  are the number of half waves along  $a$  and  $b$  respectively. Equation 3.24 assumes that buckling occurs at the loads  $N_x$  and  $N_{xy}$  which can be selected to equal any predetermined level. The values of  $m$  and  $n$  are selected such that the right hand side of equation 3.24 is minimized. Experimental evidence and analysis [8] show that at least one of the two ( $m$  or  $n$ ) will equal 1 for simply supported edges. This simplifies the search for the values of  $m$  and  $n$  that minimize equation 3.24.

Using equations 3.22 and 3.23 to substitute in 3.24 and solving for the ratio  $A_f/d_f$ , the following expression is obtained:

$$\begin{aligned} \frac{A_f}{d_f} &= \left(\frac{m^2}{n^2} AR \left[ \left(\frac{2N_{xy}}{m} - \frac{N_x AR}{n}\right) \frac{1}{n\pi^2} \frac{b^2}{t^2} \frac{t^2}{hf^2} - AR \left(\frac{m^2}{n^2} \frac{AR^2 E_x t}{12(1-\nu_{xy}\nu_{yx})} \left(\frac{t}{hf}\right)^2 + \right. \right. \right. \\ &\quad \left. \left. \frac{m^2}{n^2} \frac{AR^2 E_s}{12} \frac{h_s^2}{hf^2} \frac{A_s}{ds} + \frac{E_x \nu_{yx} t}{6(1-\nu_{xy}\nu_{yx})} \frac{t^2}{hf^2} + \frac{G_{xy}}{3} \frac{t t^2}{hf^2} + \right. \right. \\ &\quad \left. \left. 2G_s \beta_s \frac{A_s}{ds} \frac{h_s^2}{hf^2} \right] - \frac{E_y t}{12(1-\nu_{yx}\nu_{yx})} \frac{t^2}{hf^2} \right) / \left( \frac{E_f}{12} + \frac{m^2}{n^2} AR^2 2G_f \beta_f \right) \end{aligned} \quad (3.25)$$

where  $AR$  is the aspect ratio  $b/a$  of the entire panel.

By letting

$$\begin{aligned}
 Q_1 &= \frac{E_f}{12} + \frac{m^2}{n^2} AR^2 2G_f \beta_f \\
 P_2 &= \frac{m^2}{n^3} \frac{AR}{\pi^2} \left( \frac{2N_{xy}}{m} - \frac{N_x AR}{n} \right) / Q_1 \\
 P_3 &= \left( \frac{m^2}{n^2} AR^2 \left( \frac{m^2}{n^2} \frac{AR^2 E_x}{12(1-\nu_{xy}\nu_{yx})} + \frac{E_x \nu_{yx}}{6(1-\nu_{xy}\nu_{yx})} + \frac{G_{xy}}{3} \right) + \frac{E_y}{12(1-\nu_{xy}\nu_{yx})} \right) / Q_1 \quad (3.26) \\
 P_4 &= \frac{m^2}{n^2} AR^2 \left( \frac{m^2}{n^2} AR^2 \frac{E_s}{12} + 2G_s \beta_s \right) / Q_1
 \end{aligned}$$

Af/df is rewritten as:

$$\frac{A_f}{d_f} = P_2 \left( \frac{b}{t} \right)^2 \left( \frac{t}{h_f} \right)^2 - P_3 t \left( \frac{t}{h_f} \right)^2 - P_4 \left( \frac{A_s}{d_s} \right) \left( \frac{h_s}{h_f} \right)^2 \quad (3.27)$$

Condition number (2) that requires bay buckling to occur at the same load intensity as overall panel buckling is now imposed. The compressive forces on the stiffeners and the skin will be different. They can be determined by realizing that their sum is the total compressive force  $-N_x$  (where  $N_x$  is negative indicating compression) and that the compressive strains in the skin and stiffeners are equal up to buckling. So

$$F_{st} = (-N_x) b - F_{skin}$$

and (strain equality)

$$\frac{F_{skin}}{E_{xt} b} = \frac{F_{st}}{n_s E_s b_s h_s}$$

Solving for  $F_{st}$  and  $F_{skin}$ ,

$$F_{st} = N_x d_s \frac{\frac{E_s}{E_{xt}} \frac{A_s}{d_s}}{\frac{E_s}{E_{xt}} \frac{A_s}{d_s} + 1} \quad (3.28)$$

$$F_{skin} = N_x b d_s \frac{\frac{E_{xt}}{E_s b_s h_s} + \frac{E_{xt} d_s}{E_s \frac{A_s}{d_s}}}{\frac{E_{xt}}{E_s b_s h_s} + \frac{E_{xt} d_s}{E_s \frac{A_s}{d_s}}} = \frac{N_x b E_{xt}}{E_s \frac{A_s}{d_s} + E_{xt}} \quad (3.29)$$

For buckling of the skin within each bay, the compressive force on the skin will be  $F_{skin}/b$  and the buckling equation 3.24 can be used provided the bending stiffnesses  $D_{ij}$  are for the skin only and do not include the contributions of the frames and the stiffeners. Thus, only the first term in the right hand side of equation 3.22 need be used. It should be noted that the values of  $m$  and  $n$  will be different than for overall buckling of the panel and have to be determined by finding the  $m, n$  pair that minimizes equation 3.24. Again, since the edges of the bay are assumed simply supported either  $m$  or  $n$  (or both) will equal 1.

Substituting in equation 3.24 and rearranging,

$$ds^2 = \frac{t^3 \left( E_x \left( \frac{m^4 \pi^2}{12} \left( \frac{ds}{df} \right)^4 + \frac{\nu_{yx}}{6} m^2 n^2 \pi^2 \left( \frac{ds}{df} \right)^2 + \frac{G_{xy}(1-\nu_{xy}\nu_{yx})}{3} m^2 n^2 \pi^2 \left( \frac{ds}{df} \right)^2 + \frac{E_y}{12} n^4 \pi^2 \right)}{(1-\nu_{xy}\nu_{yx}) m \frac{ds}{df} \left( 2N_{xy} n - \frac{N_x Ext}{E_s A_s + Ext} m \frac{ds}{df} \right)} \quad (3.30)$$

Equations 3.27 and 3.30 cover the first two conditions, buckling of the whole panel and bay buckling. For the postbuckling response, it is assumed that the skin carries no compressive load. The excess compressive load beyond buckling is taken by the stiffening members in the panel. Diagonal tension loads will be carried by the skin however. This situation is shown in Figure 3.31. Only the repeating portion of the panel is shown, which corresponds to a single bay of the complete panel. By letting  $N_{xy}$  denote shear loads on the skin and using the superscript  $b$  to denote loads at buckling, the two stresses  $\sigma_1$  and  $\sigma_2$  on adjacent sides of the bay in Figure 3.31 can be determined by applying force and moment equilibrium of the structure. Thus:

$$\sigma_1 = \frac{\tilde{N}_{xy} - \tilde{N}_{xy}^b}{t} \frac{(2 \cos \alpha \frac{ds}{df} - \sin \alpha)}{\sin \alpha \cos \alpha (\sin \alpha + \cos \alpha \frac{ds}{df})} \quad (3.31)$$

$$\sigma_2 = \frac{\tilde{N}_{xy} - \tilde{N}_{xy}^b}{t} \frac{ds}{df} \frac{(2 \sin \alpha - \cos \alpha \frac{ds}{df})}{\sin^2 \alpha (\sin \alpha + \cos \alpha \frac{ds}{df})} \quad (3.32)$$

where  $\alpha$  denotes the post-buckling angle.

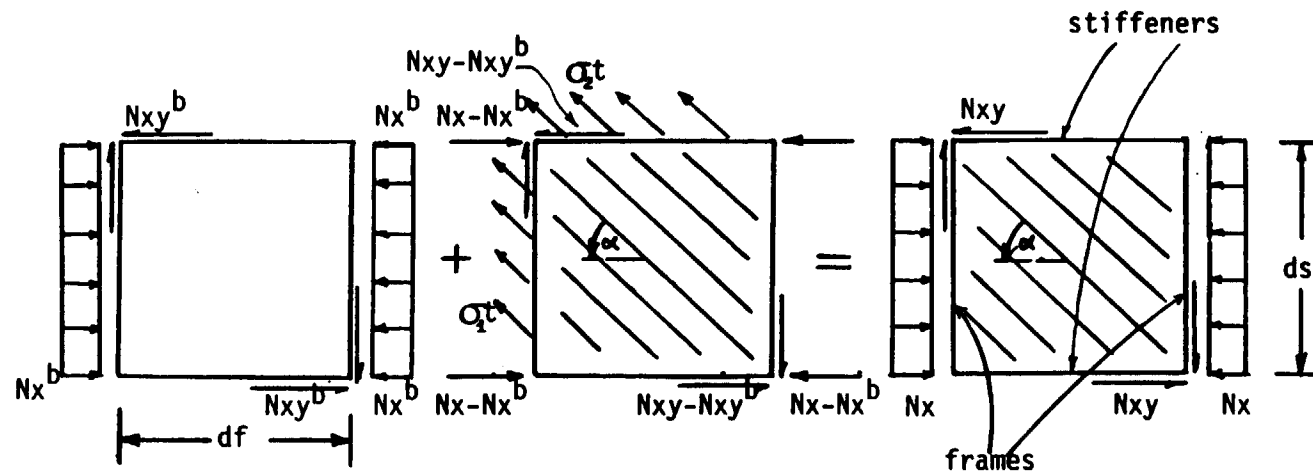


FIGURE 3.31. FREE BODY DIAGRAM OF THE POST-BUCKLED PANEL

It should be noted that the two stress values  $\sigma_1$  and  $\sigma_2$  will not necessarily be the same since the amount of compression and shear load taken by the stiffeners is different from that taken by the frames (due to respective differences in cross sectional properties). Using simple beam theory to calculate the shear stress on each frame and stiffener, the shear load in the skin can be calculated as a function of the total applied shear load:

$$\tilde{N}_{xy} = N_{xy} \left( 1 - \frac{3 - \frac{bs}{ds}}{6 \left( 1 - \frac{bs}{ds} + \frac{1}{3} \frac{bs^2}{ds^2} + \frac{tds}{3As} \right)} \right) \quad (3.33)$$

along the side perpendicular to the stiffeners, and

$$\tilde{N}_{xy} = N_{xy} \left( 1 - \frac{3 - \frac{bf}{df}}{6 \left( 1 - \frac{bf}{df} + \frac{1}{3} \frac{bf^2}{df^2} + \frac{tdf}{3Af} \right)} \right) \quad (3.34)$$

along the side perpendicular to the frames. The quantities,  $bs$ ,  $hs$ ,  $bf$ ,  $hf$  denote width and height of the stiffeners and frames respectively.

Equations 3.33 and 3.34 can be used to substitute in equations 3.31 and 3.32. The resulting expressions for the post-buckling shear stresses are

$$\sigma_1 = \frac{(N_{xy} - \frac{b}{t} N_{xy})}{t} \left( 1 - \frac{3 - \frac{bs}{ds}}{6 \left( 1 - \frac{bs}{ds} + \frac{1}{3} \frac{bs^2}{ds^2} + \frac{tds}{3As} \right)} \right) \frac{(2\cos\alpha \frac{ds}{df} - \sin\alpha)}{\sin\alpha \cos\alpha (\sin\alpha + \cos\alpha \frac{ds}{df})} \quad (3.35)$$

along the side perpendicular to the stiffeners, and

$$\sigma_2 = \frac{(N_{xy} - \frac{b}{t} N_{xy})}{t} \left( 1 - \frac{3 - \frac{bf}{df}}{6 \left( 1 - \frac{bf}{df} + \frac{1}{3} \frac{bf^2}{df^2} + \frac{tdf}{3Af} \right)} \right) \frac{ds}{df} \frac{(2\sin\alpha - \cos\alpha \frac{ds}{df})}{\sin^2\alpha (\sin\alpha + \cos\alpha \frac{ds}{df})} \quad (3.36)$$

along the side perpendicular to the frames

To these, the shear stress exerted on the skin at buckling should be added (which is assumed to equal  $N_{xy}b/t$  for both sides of the panel) and the compression stress due to the compressive load  $N_{xb}$  at buckling which equals  $F_{skin}/(tb)$  with  $F_{skin}$  as calculated by equation 3.29. For optimum design, failure of the skin should occur when the applied shear and compression reach ultimate load. The skin would then be under combined compression and shear and an interaction failure criterion would be needed. This criterion is usually of the form [9]:

$$R_s^p + R_c^q = 1 \quad (3.37)$$

where p and q are exponents determined experimentally and  $R_c$ ,  $R_s$  denote ratios of the applied compression and shear stresses respectively normalized by the corresponding allowable for single loading situations. For simplicity, p and q are set equal to 1 which is conservative. Then, using equations 3.35 and 3.36 to substitute in 3.37 and including the contribution of the buckling stresses, the failure condition has the form

$$\begin{aligned} & \frac{N_{xy} - N_{xy}^b}{t F_{su}} \left( 1 - \frac{3 - \frac{bs}{ds}}{6 \left( 1 - \frac{bs}{ds} + \frac{1}{3} \left( \frac{bs}{ds} \right)^2 + \frac{t}{3 \frac{As}{ds}} \right)} \right) \frac{2 \cos \alpha \frac{ds}{df} - \sin \alpha + \sin \alpha + \cos \alpha \frac{ds}{df}}{df} \\ & + \frac{N_{xy}^b}{t F_{su}} + \frac{N_x^b}{t F_{cu}} \frac{1}{1 + \frac{E_s}{E_{xt}} \frac{As}{ds}} = 1 \end{aligned} \quad (3.38a)$$

along the side perpendicular to the stiffeners, and

$$\begin{aligned} & \frac{N_{xy} - N_{xy}^b}{t F_{su}} \left( 1 - \frac{3 - \frac{bf}{df}}{6 \left( 1 - \frac{bf}{df} + \frac{1}{3} \left( \frac{bf}{df} \right)^2 + \frac{t}{3 \frac{Af}{df}} \right)} \right) \frac{ds}{df} \frac{2 \sin \alpha \cos \alpha - \cos^2 \alpha \frac{ds}{df}}{\sin^2 \alpha + \sin \alpha \cos \alpha \frac{ds}{df}} + \\ & + \frac{N_{xy}^b}{t F_{su}} = 1 \end{aligned} \quad (3.38b)$$

along the side perpendicular to the frames.

The quantities  $F_{su}$  and  $F_{cu}$  denote shear and compression allowables for the skin material. If composites are used,  $F_{su}$  and  $F_{cu}$  can be taken to represent the stresses at which first ply failure of the skin occurs.

In a similar manner, the failure conditions for the stiffeners which are under compression and shear, and the frames which are primarily under shear, can be written in the form:

$$\frac{N_x^b}{(F_{cu})_s} \frac{E_s}{E_{xt}} + \frac{N_x - N_x^b}{t (F_{cu})_s} + \frac{3 - \frac{bs}{ds}}{12 \left( 1 - \frac{bs}{ds} + \frac{1}{3} \left( \frac{bs}{ds} \right)^2 + \frac{t}{3 \frac{As}{ds}} \right)} \frac{N_{xy}}{(F_{su})_s h_s} = 1 \quad (3.39)$$

for stiffener failure, and

$$\frac{3 - \frac{bf}{df}}{12 \left( 1 - \frac{bf}{df} + \frac{1}{3} \left( \frac{bf}{df} \right)^2 + \frac{t}{3 \frac{Af}{df}} \right)} \frac{N_{xy}}{(F_{su})_f h_f} = 1 \quad (3.40)$$

for frame failure.



Equations 3.38 through 3.40 are the failure conditions (3) and (4) at ultimate load. The next step is to minimize panel weight and cost. Some cost considerations can help eliminate the ratio of the stiffener spacing to frame spacing  $ds/df$  from the list of unknown quantities.

The cost of the stiffened panel will depend strongly on the number of frames and stiffeners used. As that number increases, the labor hours for assembly increase and the amount of material used increases. At the same time the skin thickness decreases but not enough to offset the increased costs of the additional stiffeners. Thus, to minimize cost, the number of frames and stiffeners must be minimized. The number of frames and stiffeners can be written as:

$$C = \frac{b}{ds} + \frac{a}{df} \quad (3.41)$$

or rearranging:

$$C = \frac{1}{ds} \left( b + a \frac{ds}{df} \right) \quad (3.42)$$

Now the stiffener spacing can be expressed in terms of the stiffener to frame spacing ratio through the bay buckling equation 3.30. Thus,

$$C = (b + a \frac{ds}{df}) / \left[ \frac{t^3 \left( E_x \frac{m^4 \pi^2}{12} \left( \frac{ds}{df} \right)^4 + \frac{v_{yx} m^2 n^2 \pi^2}{6} \left( \frac{ds}{df} \right)^2 + \frac{G_{xy}(1-v_{xy}v_{yx}) m^2 n^2 \pi^2}{3} \left( \frac{ds}{df} \right)^2 + \frac{E_y n^4 \pi^2}{12} \right)^{1/2}}{(1-v_{xy}v_{yx}) m \frac{ds}{df} (2N_{xy} n - \frac{N_x E_{xt}}{E_s A_s + E_{xt}} m \frac{ds}{df})} \right] \quad (3.43)$$

It can be seen from that expression that as  $ds/df$  tends to zero,  $C$  (the number of frames and stiffeners) tends to zero. For large  $ds/df$ ,  $C$  tends to a constant number:

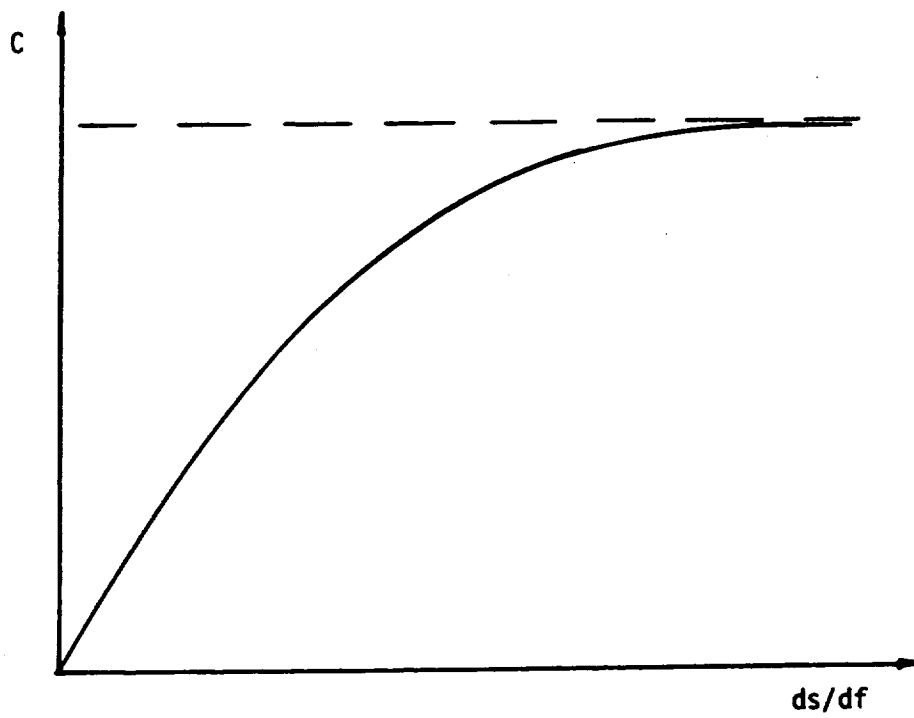
$$\frac{a \sqrt{12(1 - v_{xy}v_{yx})} |N_x b|}{\sqrt{t^3 m^2 \pi^2} E_x \left( \frac{E_s A_s}{E_{xt}} \frac{ds}{ds} + 1 \right)}$$

Therefore, a plot of  $C$  versus  $ds/df$  will have the form shown schematically in Figure 3.32. This implies that for low cost,  $ds/df$  must be kept as low as possible. Upper and lower bounds on  $ds/df$  can be obtained by considering the skin failure conditions 3.38.

Equations 3.38a and 3.38b can be rearranged as follows:

$$\frac{N_{xy} - N_{xy}^b}{t F_{su}} \left( 1 - \frac{3 - \frac{bs}{ds}}{6 \left( 1 - \frac{bs}{ds} + \frac{1}{3} \left( \frac{bs}{ds} \right)^2 + \frac{t}{3 \frac{As}{ds}} \right)} \right) \frac{2 \cos \alpha \frac{ds}{df} - \sin \alpha + \sin \alpha + \cos \alpha \frac{ds}{df}}{ds} = 1 - \quad (3.44a)$$

$$- \frac{N_{xy}^b}{t F_{su}} - \frac{N_x^b}{t F_{cu}} \frac{1}{1 + \frac{E_s A_s}{E_{xt} ds}}$$



**FIGURE 3.32. SCHEMATIC REPRESENTATION OF DEPENDENCE OF COST (NUMBER OF FRAMES AND STIFFENERS) ON STIFFENER-TO-FRAME-SPACING RATIO**

$$\frac{N_{xy} - N_{xy}^b}{t F_{su}} \left( 1 - \frac{3 - \frac{bf}{df}}{6 \left( 1 - \frac{bf}{df} + \frac{1}{3} \left( \frac{bf}{df} \right)^2 + \frac{t}{3 \frac{Af}{df}} \right)} \right) \frac{ds}{df} \frac{2 \sin \alpha \cos \alpha - \cos^2 \alpha \frac{ds}{df}}{\sin^2 \alpha + \sin \alpha \cos \alpha \frac{ds}{df}} =$$

$$1 - \frac{N_{xy}^b}{t F_{su}} \tag{3.44b}$$

The right hand sides of 3.44a and 3.44b are positive for sufficiently small applied loads (which is the case of interest). Then, the quantities involving the post-buckling angle  $\alpha$  in the left hand side of each equation must be positive. Thus, from equation 3.44a,

$$2 \cos \alpha \frac{ds}{df} - \sin \alpha > 0 \tag{3.45a}$$

and from 3.44b,

$$2 \sin \alpha \cos \alpha - \cos^2 \alpha \frac{ds}{df} > 0 \tag{3.45b}$$

which can be combined to the single relation

$$\frac{\tan \alpha}{2} < \frac{ds}{df} < 2 \tan \alpha \tag{3.46}$$

which gives the range of permissible values of  $ds/df$ . Since, for low cost,  $ds/df$  must be as low as possible, (see Figure 3.32), it should be, at most, slightly larger than  $1/2(\tan \alpha)$ . Arbitrarily,  $ds/df$  is set to be 5% larger than that value:

$$\frac{ds}{df} = 1.05 \frac{\tan \alpha}{2} \tag{3.47}$$

The final condition is weight minimization. Using equation 3.27 to substitute in the expression for the panel weight (equation 3.21),

$$\frac{W}{\rho ab} = \frac{A_s}{ds} - P_4 \frac{A_s}{ds} \left( \frac{hs}{hf} \right)^2 + \left( 1 - P_3 \left( \frac{t}{hf} \right)^2 \right) t + \frac{P_2 b^2}{t^2} \left( \frac{t}{hf} \right)^2 \tag{3.48}$$

At the limiting case of zero skin thickness ( $t \rightarrow 0$ ) the right hand side of equation 3.48 tends to positive infinity. At the limiting case of large skin thickness ( $t \rightarrow \infty$ ), the right hand side of equation 3.48 also goes to positive infinity provided that:

$$1 - P_3 \left( \frac{t}{hf} \right)^2 > 0 \quad (3.49)$$

The two limiting values of positive infinity for the normalized weight expression 3.48 imply that there is a value of  $t$  for which the panel weight is minimized. That value can be determined by differentiating the right hand side of equation 3.48 with respect to  $t$  and setting the resulting expression equal to zero. This leads to

$$t = \left[ \frac{2P_2 b^2 \left( \frac{t}{hf} \right)^2}{1 - P_3 \left( \frac{t}{hf} \right)^2} \right]^{1/3} \quad (3.50)$$

which can be used either to calculate  $t$  knowing  $t/hf$ , or calculate  $t/hf$ , knowing  $t$ .

To establish an iterative procedure, a corrected value of the skin thickness must be determined (see also step 13 of optimization procedure below). For that, equation 3.38a can be used. Rearranging equation 3.38a the following fourth order equation is obtained for the skin thickness  $t$ :

$$T13 t^4 + T14 t^3 + T15 t^2 + T16 t + T17 = 0 \quad (3.51)$$

where

$$T13 = - \frac{2}{0.508} \frac{Fsu}{(N_{xy} - N_x^b) \frac{Af}{df}}$$

$$T14 = \frac{2}{\frac{Af}{df}} + \frac{2}{\frac{Af}{df}} \frac{N_{xy}^b}{0.508(N_{xy} - N_{xy}^b)} - \frac{6 Fsu}{0.508(N_{xy} - N_{xy}^b)}$$

$$T15 = 3 + \frac{6}{0.508} \frac{Fsu}{N_{xy} - N_{xy}^b} \frac{Af}{df} \frac{t}{hf} + \frac{6}{0.508} \frac{N_{xy}^b}{(N_{xy} - N_{xy}^b)}$$

$$T16 = \frac{Af}{df} \frac{t}{hf} \left[ - \frac{2}{0.508} \frac{Fsu}{N_{xy} - N_{xy}^b} \frac{Af}{df} \frac{t}{hf} - 5 - \frac{6}{0.508} \frac{N_{xy}^b}{(N_{xy} - N_{xy}^b)} \right]$$

$$T17 = 2 \left( \frac{Af}{df} \right)^2 \left( \frac{t}{hf} \right)^2 \left[ 1 + \frac{N_{xy}^b}{0.508(N_{xy} - N_{xy}^b)} \right]$$

This equation is solved by iteration using a Newton-Raphson method.

Finally, the postbuckling angle  $\alpha$  must be determined. For that, the expression developed by Kuhn et al [10] is used. This expression is approximate (valid for complete diagonal tension) but of sufficient accuracy for the purposes of the current analysis which aims at determining basic trends:

$$\tan^4 \alpha = \frac{1 + \frac{t}{2 \frac{A_s}{d_s}}}{1 + \frac{t(1 + 3(\frac{t}{h_f} + 1)^2)}{\frac{A_f}{d_f}}} \quad (3.52)$$

The optimization procedure then involves the following steps:

1. Assume a starting value of post-buckling angle  $\alpha$ .
2. Assume  $A_s/d_s$  and  $A_f/d_f$  ratios.
3. Use equation 3.47 to calculate  $d_s/d_f$ .
4. Assume starting values for polar moment of inertia constants ( $\beta_s$ ,  $\beta_f$ ) which are used in:  $J = \beta b h^3$ .
5. Assume a starting value of  $t$  and use equation 3.30 to calculate  $d_s$ .
6. Use  $d_s$  and  $d_s/d_f$  found in step 3 to calculate  $d_f$ .
7. Use equations 3.26 to calculate  $P_2$ ,  $P_3$ ,  $P_4$ , and  $Q_1$ . Then use equation 3.50 and the value of  $t$  assumed in step 5 to find  $t/h_f$ .
8. Use equation 3.27 (overall buckling) to calculate  $h_s/h_f$ . Note: for some  $t$ ,  $t/h_f$  values, equation 3.27 will give imaginary  $h_s/h_f$  values. The reason for that is that the assumed value of  $A_f/d_f$  in step 2 is too high. Return to step 2 and repeat procedure with a lower value of  $A_f/d_f$ .
9. Use  $t$  from step 5 and  $t/h_f$  from step 7 to find  $h_f$ .
10. Use  $h_f$  from step 9 and  $h_s/h_f$  from step 8 to find  $h_s$ .
11. Use  $A_s/d_s$  from step 2 and  $d_s$  from step 5 to find  $A_s$ . Use  $h_s$  from step 10 to find  $b_s$ . Use  $A_f/d_f$  from step 2 and  $d_f$  from step 6 to calculate  $A_f$ . Use  $h_f$  from step 9 to calculate  $b_f$ .
12. Use the overall buckling and bay buckling equations (3.27 and 3.30) to iterate on the number of half-waves  $m$  and  $n$  over the whole panel and each bay. The  $m, n$  pairs that give the lowest buckling loads are selected. If these are not the same as used in steps 5 and 7, repeat procedure starting from step 5.
13. Correct for the value of  $t$  by using equation 3.51. If it is sufficiently close to the value used in step 5 (within 1%) proceed to the next step. Otherwise return to step 5 and repeat the procedure.
14. Based on the values of  $b_s$ ,  $h_s$ ,  $b_f$ ,  $h_f$  (from steps 11 and 9) calculate torsional stiffness parameters  $\beta_s$  and  $\beta_f$ . Compare with the values assumed in step 4. If they are not sufficiently close (within 1%) return to step 4 and repeat the procedure.

15. If there are no thicknesses (skin, frame, or stiffener) below minimum gage, perform a strength test for the frames and the stiffeners using equations 3.40 and 3.39. If there are thicknesses below minimum gage, or stiffener or frame failure occurs, follow the alternative procedure described below.
16. Use equation 3.52 to calculate the new postbuckling angle  $\alpha$ . If it is not within 1% of the assumed value in step 1, use the new value as a starting value and go to step 1. If it is within 1%, the optimization is complete.

The above procedure minimizes the weight of a stiffened panel permitting postbuckling and ensuring material failure when ultimate load is reached. If, however, the resulting configuration involves material thicknesses below minimum gage, that material must be replaced with minimum gage material. This implies that the material failure condition will no longer occur at ultimate load and the panel could take ultimate load without failing. As a result, equation 3.38a (or its modification 3.51) can no longer be used since they impose skin failure. The optimization procedure is modified as follows:

### CASE 1. STIFFENER BELOW MINIMUM GAGE

The value of  $b_s$  is assumed (equal to minimum gage). Remove step 10. Replace steps 5, 7, 9, 11 and 13 of general procedure above with:

5. Assume  $t/h_f$ .
7. Use equations 3.26 to calculate  $P_2$ ,  $P_3$ ,  $P_4$ , and  $Q_1$ . Then use equation 3.50 and the value of  $t/h_f$  assumed (step 5) to find  $t$ .
- 7a. Use equation 3.30 on bay buckling to calculate  $d_s$ . Assume stiffener thickness  $b_s$  equal to minimum gage.
9. Use  $t$ ,  $t/h_f$  from steps 7 and 5 to calculate  $h_f$ .
11. Use  $A_s/d_s$  from step 2 and  $d_s$  from step 7a to find  $A_s$ . Use assumed value of  $b_s$  to find  $h_s$ . Use  $A_f/d_f$  from step 2 and  $d_f$  from step 6 to calculate  $A_f$ . Use  $h_f$  (step 9) to calculate  $b_f$ .
13. Use  $h_f$  from step 9 and  $t$  from step 7 to correct value of  $t/h_f$ . Return to step 5 and repeat procedure unless the new  $t/h_f$  value is within 1% of the previous  $t/h_f$  value.

## CASE 2. FRAME BELOW MINIMUM GAGE

The value of  $bf$  is assumed. Remove step 13. Replace steps 5, 7, 9, and 11 of general procedure above with the following:

5. Assume  $t/hf$ .
7. Use equations 3.26 to calculate  $P2$ ,  $P3$ ,  $P4$ , and  $Q1$ . Then use equation 3.50 and the value of  $t/hf$  assumed (step 5) to find  $t$ .
- 7a. Use  $t$  (step 7) and bay buckling equation 3.30 to calculate  $ds$ .
- 7b. Use  $Af/df$  from step 2 and value of  $df$  from step 6 to find  $Af$ .
9. Use  $Af$  from step 7b and assumed value of  $bf$  to find  $hf$
- 9a. Use  $hf$  from step 9 above and  $t$  from step 7 to correct  $t/hf$  value. Repeat procedure from step 5 on, unless the successive  $t/hf$  values differ by less than 1%.
11. Use  $As/ds$  from step 2 and  $ds$  from step 7a to find  $As$ . Use  $hs$  from step 10 to find  $bs$ . Use  $hf$  from step 9 and  $Af$  from step 7b to calculate  $bf$ .

The basic optimization procedure and the two alternative procedures in case of minimum gage material are shown schematically in Figure 3.33. It should be noted that the variable  $As/ds$  is assumed at the beginning of the optimization and the resulting configuration is optimum for this assumed value of  $As/ds$ . To complete the process, various values of  $As/ds$  should be assumed and the resulting optimum configurations compared, to find the one that results in minimum weight and cost. The assumed values of  $As/ds$  should be as low as possible because, as can be seen from equation 3.21, the smaller the values of  $As/ds$  and  $Af/df$  the lower the weight.

### 3.3.2 RESULTS OF THE OPTIMIZATION METHOD AND DISCUSSION

The procedure outlined in the previous section was used to optimize the UH-60 (Blackhawk) tailcone panels. The geometry resulting from this optimization will help define the geometry of the full-scale panel selected for this program.

The shear ( $N_{xy}$ ) and compression ( $N_x$ ) loads at ultimate were assumed to equal 250 lb/in (for both types of loading). The postbuckling ratio (ultimate/ buckling load) was taken to be 2.5. Because these loads are very low compared to the material allowables, the resulting thicknesses were below minimum gage. The alternative optimization approaches were used.

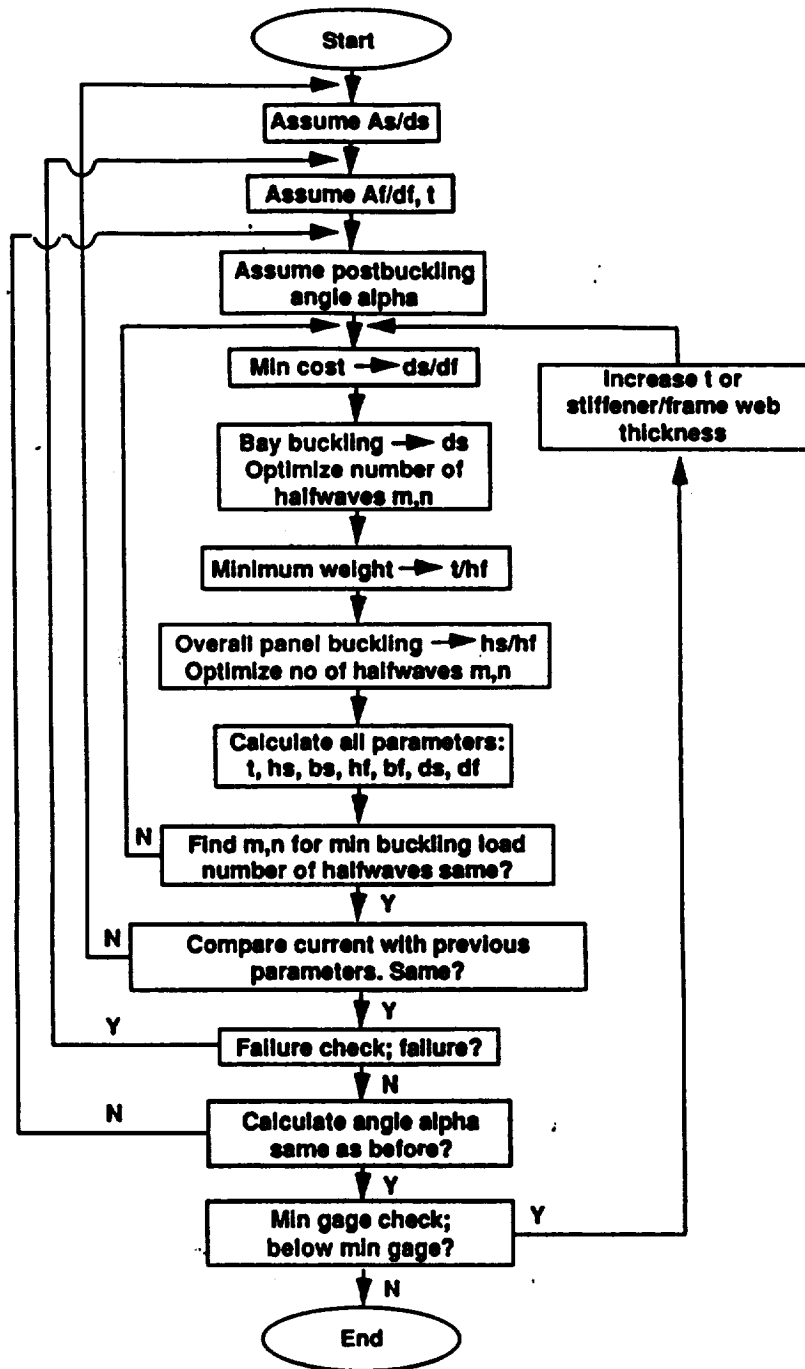


FIGURE 3.33. OPTIMIZATION PROCEDURE



The following properties were used for the panel material. The skin and stiffeners were predominantly 45 degree plies (relative to the axis of application of the compression load), and the frames consisted predominantly of 0 degree plies (perpendicular to the compression load axis):

Skin:  $E_x = 2.7$  msi    Stiffeners:  $E_s = 3.12$  msi    Frames:  $E_f = 10.22$  msi  
 $E_y = 2.7$  msi                       $G_s = 4.45$  msi                       $G_f = 2.79$  msi  
 $G_{xy} = 4.55$  msi  
 $\nu_{xy} = 0.7313$   
 $\nu_{yx} = 0.7313$

For the stiffeners and frames where the webs and flanges had different layouts, the moduli were obtained as weighted averages over the corresponding member cross-sectional areas.

The shear and compression allowables for the skin and the compression allowable for the stiffeners were determined using the Tsai-Hill first ply failure criterion for shear and compression applied individually. The shear allowables for the stiffeners and frames were taken to be equal to the short beam shear values for the material (values in psi):

Skin:  $F_{su} = 60333$     Stiffeners:  $(F_{su})_s = 15000$     Frames:  $(F_{su})_f = 15000$   
 $F_{cu} = 24333$                        $(F_{cu})_s = 24000$

The minimum gage cutoff was selected to correspond to stiffeners or frames made up of no less than two plies.

For pure shear loading, the optimization scheme shows that no stiffeners are needed as should be expected. The combined load case of  $N_x = 250$  lb/in compression and  $N_{xy} = 250$  lb/in shear is more interesting and more realistic of loading situations in aircraft structures. For that reason it is used to design the full-scale panel in what follows.

A simple way to introduce manufacturing cost in the optimization over and beyond what was discussed in the previous section where the number of frames and stiffeners was minimized, is to estimate the increase in cost for every additional stiffener or frame beyond a baseline configuration for which the cost is estimated as accurately as possible. For a panel manufactured using conventional methods, this increase is estimated to be 13.2% of the cost of a three-stiffener, two-frame 30 inch by 30 inch panel for each stiffening member added. For a panel manufactured with THERM-X® tooling, the corresponding increase is 8.64%. These estimates were computed using previous Sikorsky Aircraft data on manufacturing panels with the two fabrication methods.

Given the loading intensity and assuming a square panel 30 inches on each side, the skin thickness, frame and stiffener cross-sectional areas and spacing are determined using the optimization procedure described in the previous section. By varying  $A_s/d_s$ , other optimum configurations are obtained. For each configuration, the amount of material needed is found and multiplied by a typical cost of \$50/lb.

The labor hours required to manufacture a panel with three stiffeners and two frames (used as baseline) 30x30 inches in size with thicknesses and heights as determined by the optimization are estimated in a manner similar to that in section 3.1.11 (based on previous Sikorsky Aircraft experience). To this, the added percentage cost (13.2% for conventional and 8.64 for THERM-X® tooling per frame or stiffener beyond the baseline numbers of two frames and three stiffeners) is added. This gives the total labor hours which are translated to cost assuming a typical value of \$30/hr. The total cost for each configuration then is given as the sum of the material cost and labor cost.

Two cost curves, one for each manufacturing process are shown in Figure 3.34. The different configurations correspond to different cost values as the stiffener or frame spacing are varied. In all cases, the THERM-X® process is less expensive than conventional layup. The savings vary with stiffener spacing decreasing as stiffener spacing increases. It should be noted that for stiffener spacings larger than the ones shown in Figure 3.34, the cost curves turn back up. This is addressed in the discussion for Figure 3.35.

The effect of weight is incorporated in Figure 3.34 through the improved performance curves. These curves are obtained by taking the weight for each configuration and subtracting from it the weight of the minimum weight configuration that can meet the applied loads. The minimum weight configuration for this application corresponds to the minimum gage configuration for both manufacturing approaches. This difference in weight then corresponds to potential weight savings (improved performance) that could be achieved with each configuration had the designer chosen to change the frame and stiffener spacing to the minimum weight configuration values. This weight is translated to improved performance cost values by multiplying it by the premium value of \$/lb that the customer or manufacturer is willing to pay to save a lb of weight off the structure. The premium value varies with the application and the type of aircraft (helicopter versus fixed wing, military versus civil, etc) and is usually determined from a life-cycle cost analysis for the vehicle.

Various improved performance curves are shown in Figure 3.34 each corresponding to a different premium value in the range of 300 to 1000\$/lb. The intersection points between the improved performance curves and the manufacturing/material cost curves are of some interest. Given a premium value, (say \$750/lb which is a value typical of a military helicopter) selecting a stiffener spacing (and its associated panel configuration) would lock in a cost value. For example a stiffener spacing of 4 inches corresponds to a cost (conventional layup) of \$900 per panel. For the same spacing however, the \$750/lb premium value curve indicates potential gains (value of improved performance) of \$1400 if the

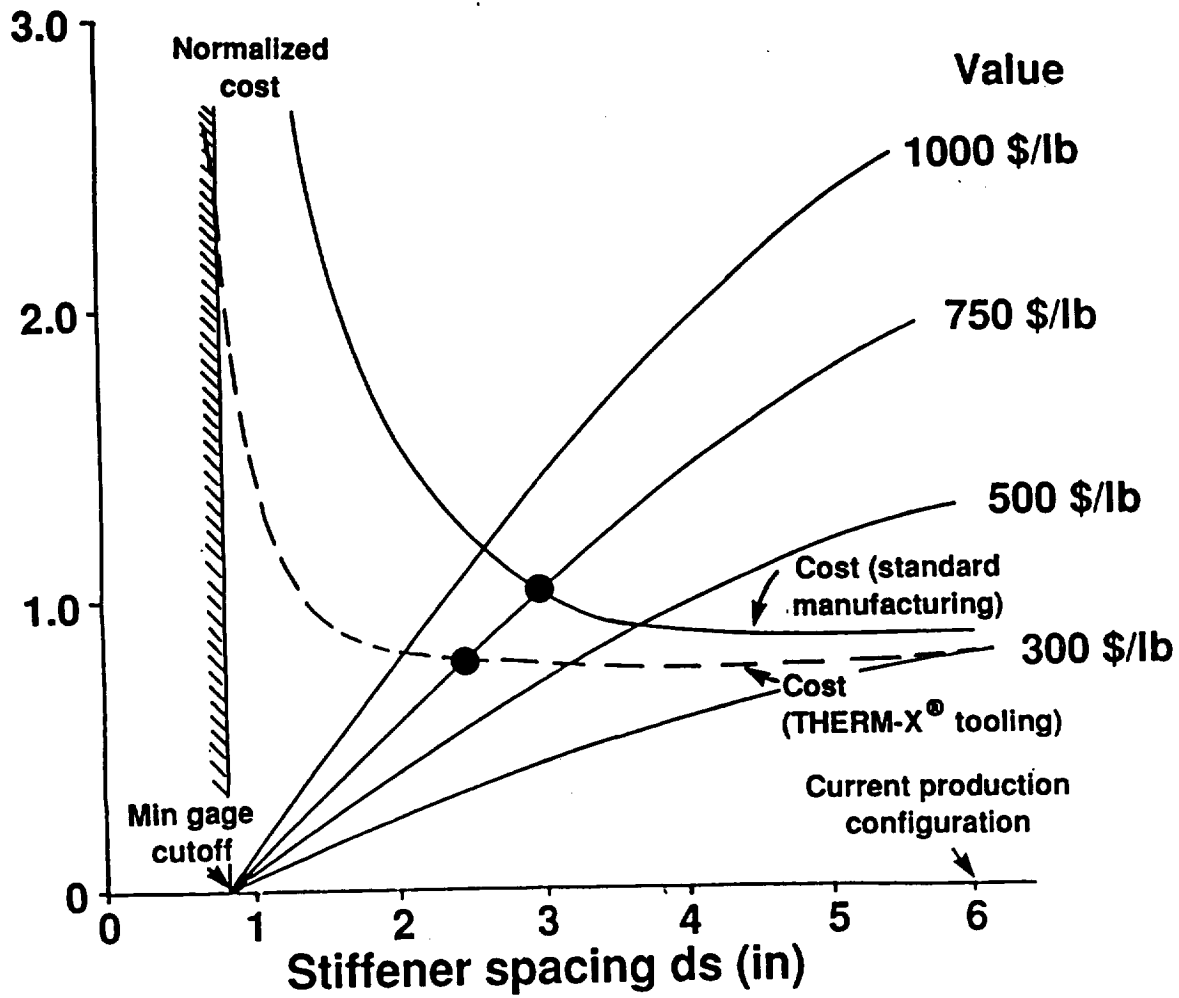


FIGURE 3.34. OPTIMUM GEOMETRY DETERMINATION FOR STIFFENED PANELS - COST CONSIDERATIONS

configuration were to change from the current  $d_s$  value of 4 inches to the minimum weight configuration of about 1 inch. Therefore, at each configuration, there are two opposing tendencies. If the stiffener spacing is too high, the cost is low but the panel is heavy and there is the possibility of significant savings in weight by switching to lower spacings. On the other hand, if the stiffener spacing is low, the cost is high but the weight is low. This cost-weight tradeoff is balanced at the intersection points between the cost curves and the improved performance (potential savings) curves. Away from these intersections, either the cost is too high or the weight is too high.

For the specific example of a premium value of \$750/lb, the optimum point for conventional layup corresponds to stiffener spacing of 3 inches and frame spacing of 9.5 inches. For THERM-X® tooling, the corresponding values are  $d_s=2.5$  inches and  $d_f=7.9$  inches. Comparing the optimum points, the THERM-X processed panel shows 22% savings (\$800 versus \$1030) over the conventional layup panel.

It is interesting to note that the optimum stiffener and frame spacing (2.5" by 7.92" for THERM-X panel) has the same  $d_s/d_f$  ratio as the 6/20 used as the standard configuration for stiffened panels in aerospace applications. The actual values are a little less than half those currently used by industry. This is partly due to the premium value of 750\$ per lb of weight saved that was used in this analysis. If that is removed from the analysis, an additional constraint would have to be added (for example absolute cost rather than cost as a tradeoff of weight saved). In such a case, larger stiffener spacings are favored and, as is shown in Figure 3.34, one of the possible configurations is 6 inches by 19.02 inches, which is very close to production configurations of 6 inches by 20 inches.

This latter configuration of 6 by 19 inches corresponds to a premium value of \$300/lb which is closer to fixed wing civil aircraft premium values. Thus, to make the full-scale panel of this program applicable to a wider range of applications, a configuration close to that should be chosen. In addition, the geometry is very close to standard stiffened panel configurations and thus will make cost comparisons with conventional configurations easier. For these reasons, the configuration 6.5 inches (stiffener spacing) and 20 inches (frame spacing) was chosen as the test configuration for this program.

The remainder of the geometry for the panel is given by the optimization process. The only difference is that rather than rectangular stiffener and frame cross-sections, hat and inverted "tee" (blades) were used respectively. Hat stiffeners are used because of their increased torsional stiffness which reduces the tendency of the stiffeners to pull off the skin under repeated loads. The blade configuration for the frames was chosen because of its simplicity and the fact that significant amount of manufacturing data are available at Sikorsky.

As Figure 3.34 shows, for the selected configuration of 6.5 inches by 20 inches, THERM-X® tooling would be expected to show only 11% savings over conventional layup. This is only an estimate at this point. Actual comparisons will be made in section 5.

To show how the predictions of the optimization process change with various factors, the case of a highly loaded panel was examined. The (ultimate) loads  $N_x = -2500$  lb/in and  $N_{xy} = 1250$  lb/in are typical of fuselage transport. A postbuckling factor of 2.5 was used. The variation of weight and cost with stiffener or frame spacing is shown in Figure 3.35. The compression allowable for the hat stiffeners which is the limiting factor in this case was assumed to be 36000 psi. Again, a 30 inch by 30 inch flat panel is considered.

The cutoff point at low stiffener spacings corresponds to 3.5 inches and is the geometry at which the stiffeners fail in compression. The cutoff point at high stiffener spacings corresponds to 7.0 inches. At that point the frame spacing becomes larger than the assumed dimension of the panel.

Instead of using premium values, the weight for both conventional layup and THERM-X® tooling is plotted as a dotted line. The two cost lines are also shown. In this case the minimum weight configuration corresponds to the minimum allowable stiffener spacing of 3.5 inches. The minimum cost however, corresponds to a  $d_s$  value of 3.75 inches for THERM-X process panel and 4.75 inches for conventional layup. The configuration to be selected would then depend on whether weight or cost are the driver or on the exact premium value (\$/lb of weight saved) used.

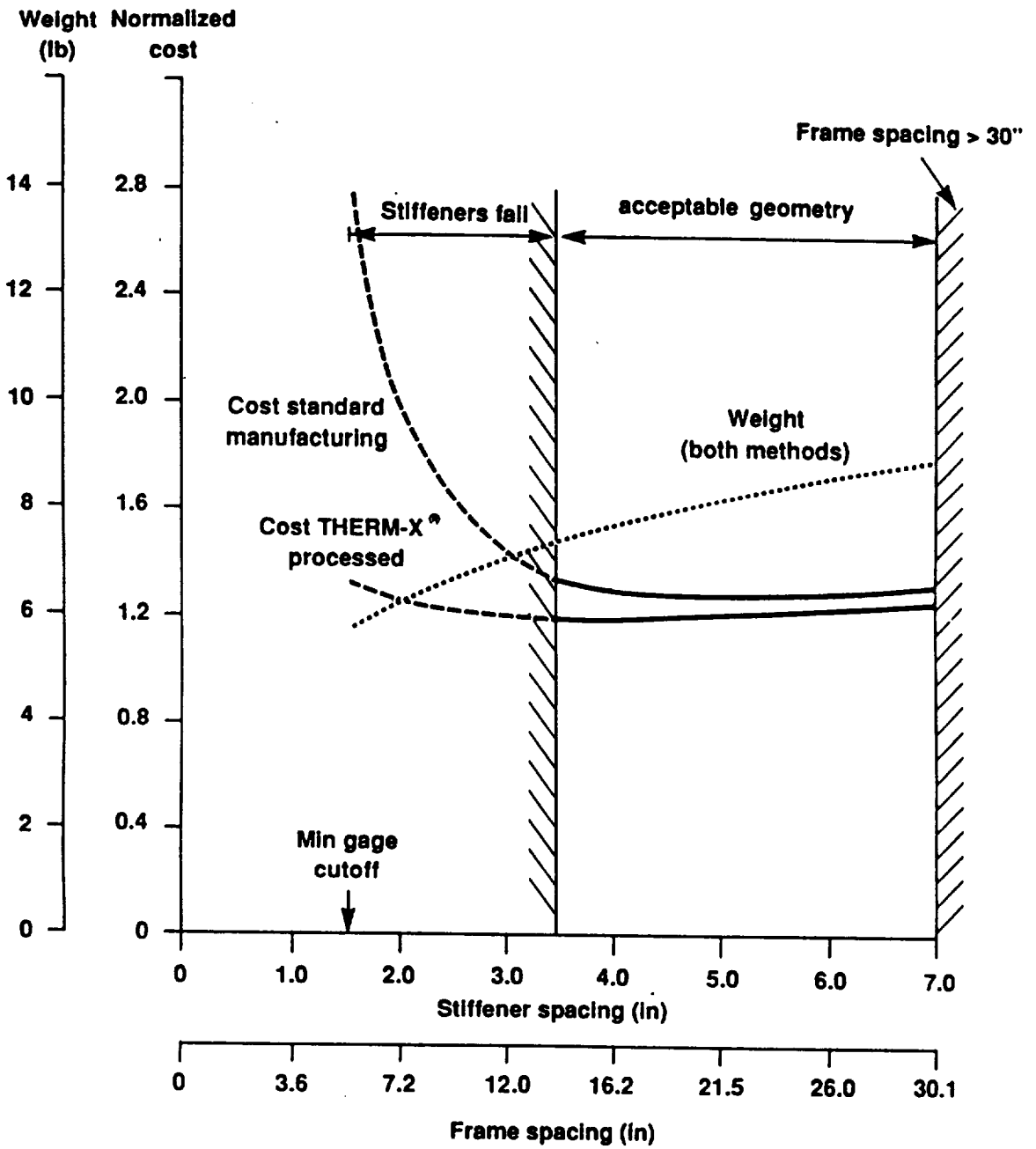


FIGURE 3.35. OPTIMUM GEOMETRY DETERMINATION FOR STIFFENED PANELS - HIGHLY LOADED STRUCTURE

## 4.0 BUILDING BLOCK EVALUATION

### 4.1 TEST MATRIX AND OBJECTIVES

The building block approach provided data that quantified material behavior and failure. It also helped isolate critical areas of the full scale panel and verified analysis methods and predictions. In addition, the test results provided a direct comparison of strength and stiffness properties of parts made using THERM-X® tooling to structure manufactured with conventional autoclave tooling. Manufacturing issues were also addressed throughout the building block approach. Problems such as wrinkles and high void contents encountered during early stages of the building block evaluation pointed at portions of the design and fabrication process that needed modification so that high quality full scale panels could be made.

For all tests, MTS testing machines with hydraulic grips were used. For each test, load versus head displacement plots were obtained. Specimens were dried at 120 F for 24 hours prior to testing. Strains were continuously recorded during each test. Failure loads and failure strains were also recorded. Representative photographs of specimens during testing were taken. All testing was done at room temperature ambient conditions.

The material system used was the BASF/NARMCO 5225 resin and the Celion C12K (for tape) and C3K (for fabric) fiber. This material was chosen because it has been used extensively at Sikorsky in production programs (e.g., CH-53 fuel sponson and S-76 tail rotor spars). As this is a material previously qualified and a statistically significant data base on stiffness and strength properties was available for numerous environmental conditions, no qualification testing was needed for the material itself.

There was, however, the question of whether or not the autoclave THERM-X® process affected the basic properties of the material system. Fiber dominated properties, such as tension compression strength, were assumed to be uninfluenced by THERM-X® processing. Matrix dominated properties such as in-plane shear strength, were judged to potentially demonstrate an influence attributable to processing due to the more uniform pressure distribution and better compaction expected from the THERM-X® application. This latter issue was addressed with straight-sided in-plane shear coupon specimens (ASTM D3519). The remaining specimens addressed damage tolerance and tested specific structural details of the full-scale panel. The relation of test specimens to the full-scale article is graphically overviewed in Figure 4.1.

The complete test matrix and the objectives accomplished with each test during this test program are shown in Table 4.1. Results specific to each test are given in the following section. A summary of labor hour results is given in Section 4.3. Conclusions of the building block evaluation are given in Section 4.4.

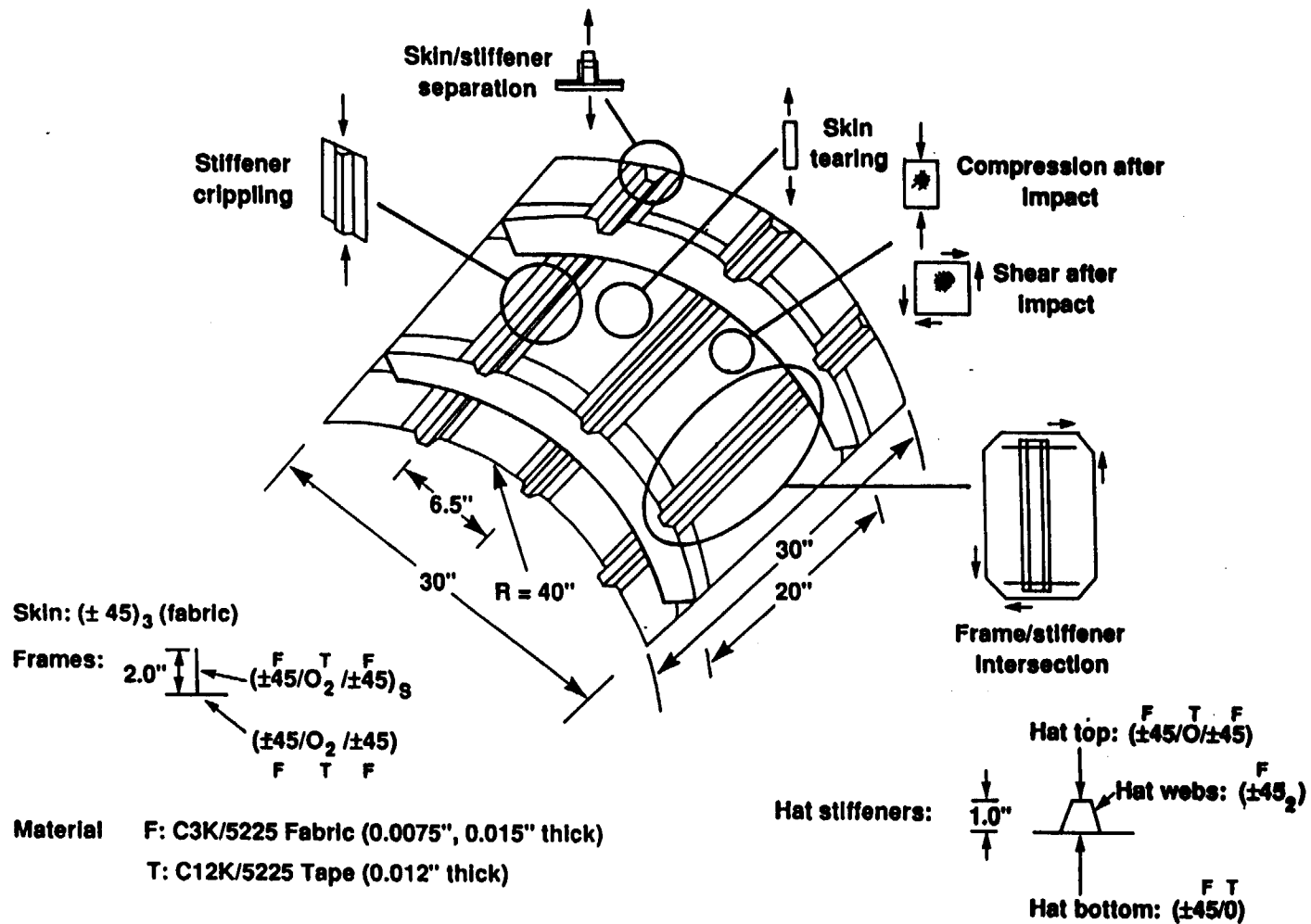


FIGURE 4.1 BUILDING BLOCK TEST SPECIMENS AND FULL-SCALE PANEL



Table 4.1 Test Matrix (Phase I)

SPECIMEN TYPE	NUMBER OF SPECIMENS	LOADING	ENVIRONMENTAL CONDITION	INSPECTION	OBJECTIVE OF TEST
±45 Laminate In-plane Shear Coupons	8	Tension	RTA	Visual, C-Scan, micrographs, Void content	Assess effect of THERM-X® on basic material (resin-dominated) properties. Obtain strength value.
Skin-Stiffener separation	5	Tension	RTA	Visual, C-scan	Determine out-of-plane (peel) strength of skin-stiffener bond.
Stiffener Crippling	6	Compression	RTA	Visual, Micrographs	Determine crippling strength of stiffeners. Assess efficiency/quality of THERM-X® fabricated parts having sharp corners and angles.
Compression after impact	10	Compression	RTA	Visual, C-scan (before and after impact)	Impact resistance and residual compr. strength of THERM-X® fabricated panels. Obtain data to compare with baseline.
Shear after impact	5	Shear	RTA	Visual, C-scan (before and after impact)	Impact resistance and residual shear strength of THERM-X® panels. Obtain data useful for residual test of runout fatigue specimen.
Skin tearing	8	Tension	RTA	Visual, C-scan, micrographs, void content	Examine porosity levels on thin parts made using THERM-X®. Provide failure strength data, verify failure analysis
Frame-stiffener intersection (flat)	3	Shear	RTA	Visual, C-scan, micrographs, void content	Assess quality of shear tie between frame and stiffener. Quantify load transfer and strength at corners.
Full-scale curved stiffened panel (static)	3	Shear	RTA	Visual, C-scan, micrographs, void content.	Assess structural efficiency of composite structures made with THERM-X®.
Full-scale curved stiffened panel (fatigue)	1	Shear	RTA	Visual, C-scan, micrographs, void content.	Assess fatigue behavior of composite structures made using THERM-X®.

RTA: Room Temperature Ambient condition

## 4.2 TEST RESULTS

### 4.2.1 + 45 Laminate In-Plane Shear Coupons

The ±45 coupons served to quantify any effects of the THERM-X® process on the basic material properties, in particular matrix dominated properties. The nominal dimensions of the In-Plane Shear specimens are shown in Figure 4.2. A C-Scan evaluation of the laminate was performed prior to testing. The quality of the laminate was judged to be excellent with only a very few minute anomalies (smaller than 0.1 inch in diameter) evidenced in the specimen gage section of the panel. Experimental results are presented in Table 4.2.

Table 4.2  
In-Plane Shear (±45 Laminate Coupons) Test Results

Specimen Number	UNNORMALIZED	
	Shear Strength (ksi)	Shear Modulus (msi)
1	9.50	0.685
2	9.56	0.697
3	9.54	0.733
4	9.57	0.733
5	9.64	0.768
6	9.87	0.731
7	9.71	0.713
8	9.59	0.702
Mean	9.62	0.720
Sample Std. Deviation	0.119	0.0264
% Coeff. of Variation (CV)	1.23	3.67

A comparison to test results obtained for coupons manufactured using conventional layup is given in Table 4.3. Shear modulus single batch means from the qualification database for C12K/5225, range from 0.71 msi to 0.75 msi with %CV ranging from 3.6% to 10.4%. The five batch mean is 0.731 msi and %CV is 6.2%. Since THERM-X® processing was expected to influence primarily matrix properties, these results were encouraging in that they demonstrate that the flowable polymer process can yield components of comparable shear stiffness and strength with, in some cases, significantly smaller scatter, as is shown in Table 4.3. The results for conventional layup are reported for both three-rail shear tests and ±45 laminate coupon specimens.

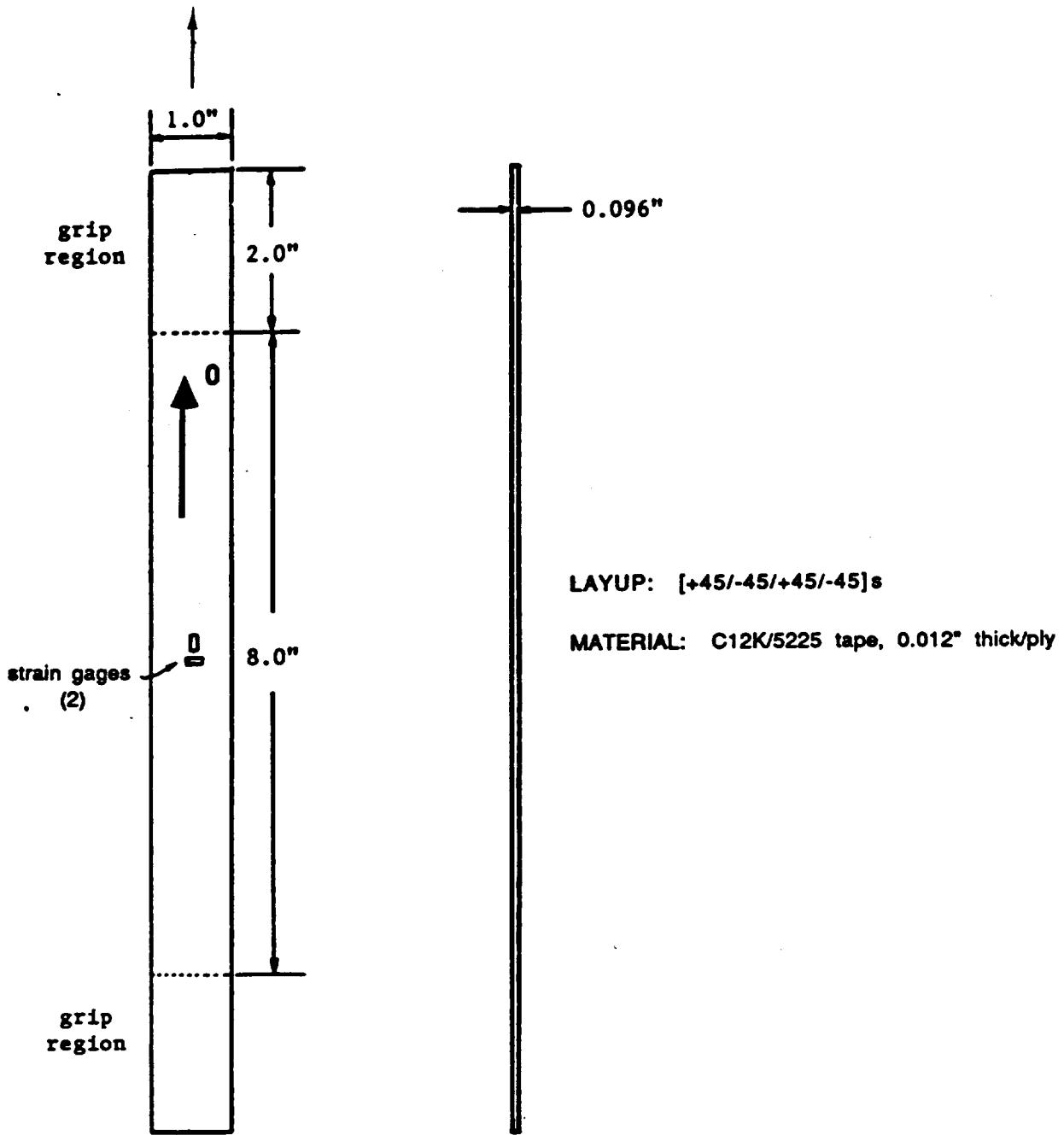


FIGURE 4.2. IN-PLANE SHEAR ( $\pm 45$  COUPON) SPECIMEN GEOMETRY

Table 4.3  
In-Plane Shear Test Results vs C12K/5225 Qualification Data

Experimental Quantity	Present Study Single Batch Mean	C O N V E N T I O N A L L A Y U P (3-rail shear)			
		Single Batch Mean Ranges		5 Batch Mean	±45 coupon Single Batch Mean
		Low	High		
Shear Modulus (msi)	0.72	0.71	0.75	0.73	0.71
% CV	3.7%	3.6%	10.4%	6.2%	10.4%
Shear Strength (ksi)	9.6	9.5	10.2	10.0	9.1
% CV	1.23%	3.4%	5.4%	4.9%	0.53%

Fiber volume and void volume of the in-plane shear specimen panel were determined to be 58.2% and 0.4%, respectively. Both of these values indicate excellent laminate consolidation by falling well within Sikorsky guidelines of 2% or less void content and fiber volume between 55 and 61%.

The results on ±45 laminate coupons show that the THERM-X® process produces flat parts of comparable if not better (in terms of lower scatter on shear strength) properties as conventional layup.

#### 4.2.2 SKIN-STIFFENER SEPARATION SPECIMEN

The skin stiffener separation specimen was used to obtain the pull-off strength of the skin stiffener bond in the full-scale panel. Pull-off of stiffeners in the postbuckling regime is a common failure mode for cocured stiffened composite panels. In addition, this test also was used to evaluate the effectiveness of an embedded flange design concept where the flanges of the stiffeners (and frames) were covered by the top skin ply to delay the skin-stiffener separation failure mode.

The nominal dimensions of the Skin-Stiffener Separation specimen are shown in Figure 4.3. Ultrasonic C-Scan inspection of the specimen panel was performed prior to static testing. The quality of the laminate was judged to be excellent throughout the flat portion of the panel. No C-scan record was possible at the radius region of the specimen. Some small local anomalies (resin starvation and wrinkles) were observed in the fillet transition areas between the web and flange. These were traced to bridging of the breather and bleeder plies and were corrected in subsequent parts.

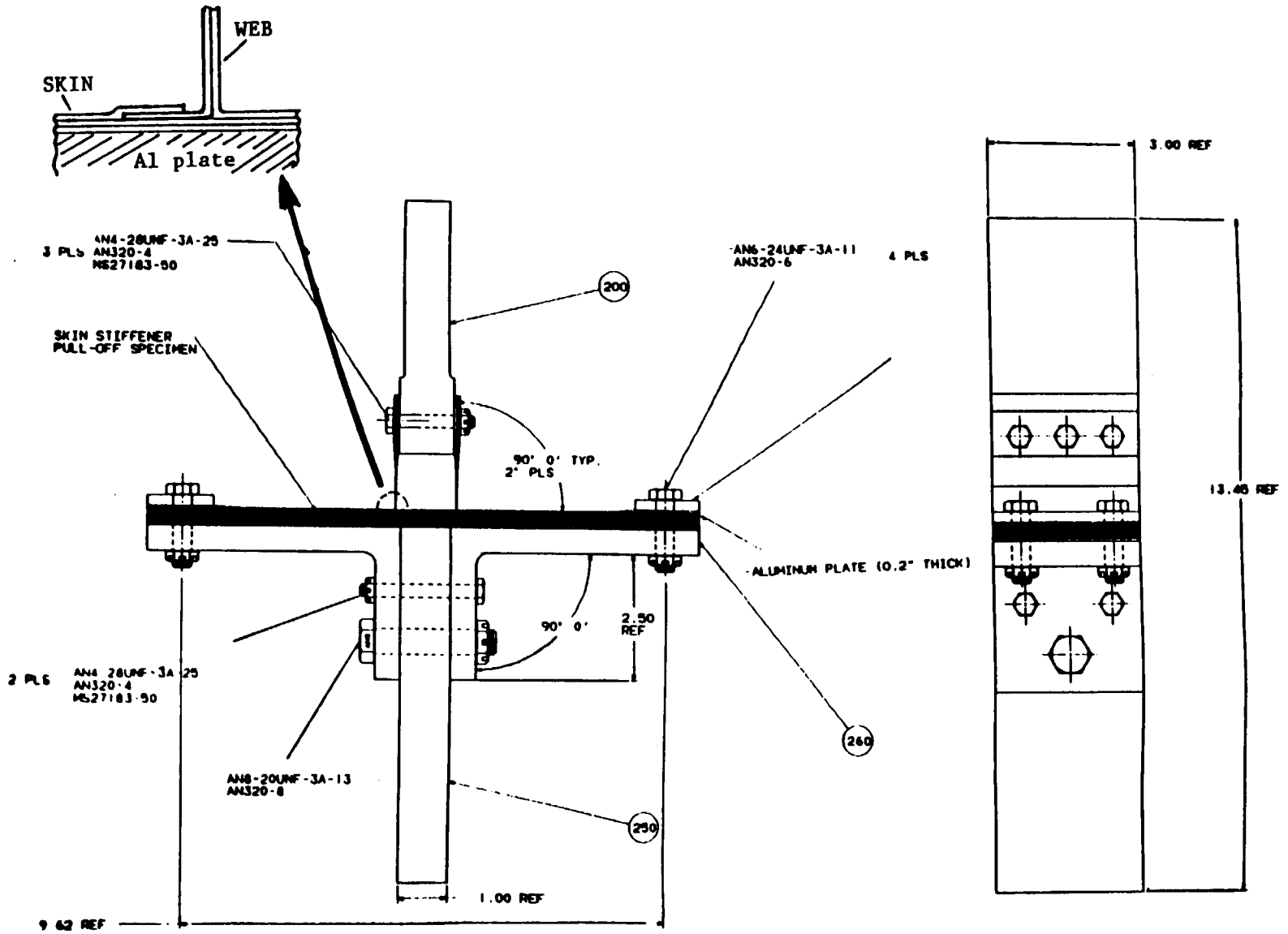


FIGURE 4.3. SKIN-STIFFENER SEPARATION SPECIMEN

Experimentally determined interfacial pull-off loads per unit width along the edge of the skin stiffener interface are reported in Table 4.4. The pull-off specimen test performed very well exhibiting the expected failure modes. The mean pull off strength of 90.5 lb/in is much higher than assumed value of 35 lb/in reported in reference 11. The latter value represents an approximate average from available industry test data. This indicates that the THERM-X® process worked well and also that the embedded flange design delays the skin-stiffener failure mode.

The failure of the skin stiffener pull-off specimen initiated at the web/flange fillet transition area as resin cracking, followed by crack propagation along the flange/skin interface to the final separation of the flange and skin. The failure strength (avg. failure load divided by the cross sectional area of the web) of 6100 psi approaches 5225 epoxy resin tension strength of 7600 psi. The measured value of 6100 psi is expected to be smaller than the mean value since local stress concentrations due to the fillet radius will lead to lower failure loads. The test setup and failure mode for this specimen are shown in Figures 4.4 and 4.5.

Table 4.4  
Skin-Stiffener Separation Strength for the Skin-Stiffener Specimen

Specimen No.	Max. Test Load (lbs) P	Max. Test Load per Flange (lbs) P/2	Width of Flange (inch) W	Pull-off Load/Flange (lb/in) P/2W
STF-1	514	257	3.1	83
PF1	647	324	3.0	108
PF2	581	291	3.08	96
PF3	467	234	3.15	75
PF4	541	271	3.0	90
Mean				90.5
Sample Std. Deviation				12.4
Per Cent Coefficient of Variation (CV)				13.7

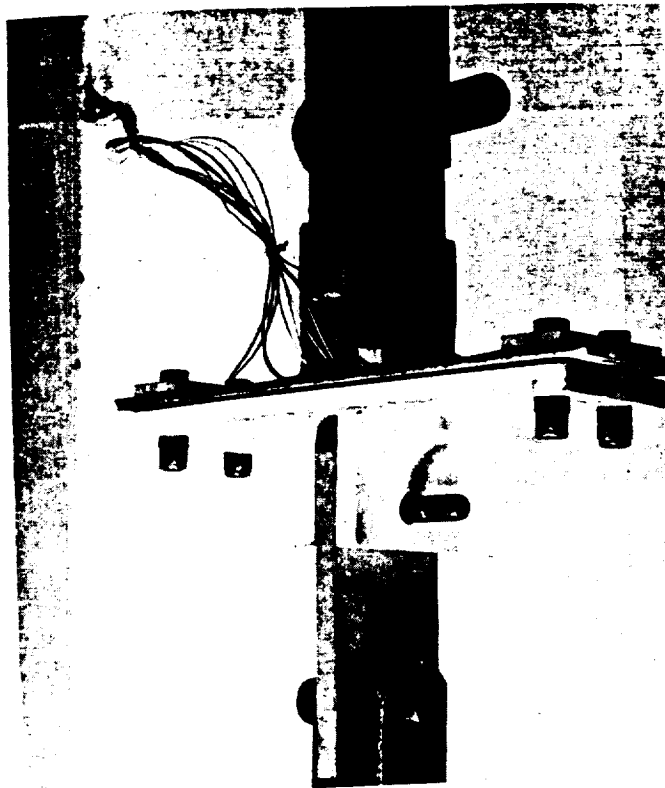


FIGURE 4.4. SKIN-STIFFENER SEPARATION SPECIMEN - TEST SETUP

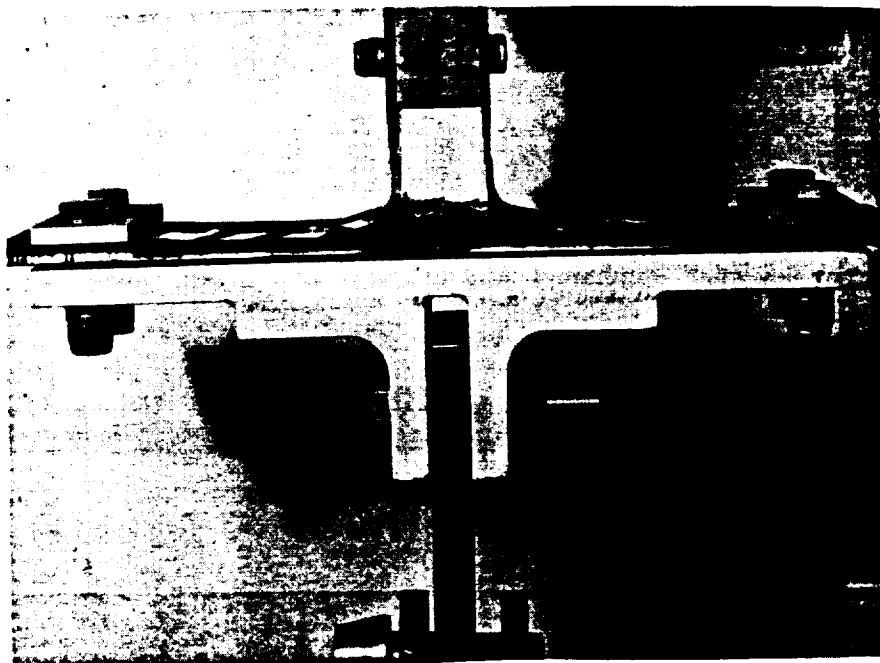


FIGURE 4.5. SKIN-STIFFENER SEPARATION SPECIMEN - FAILURE MODE

### 4.2.3 STIFFENER CRIPPLING SPECIMEN

The stiffener crippling specimen tested the crippling strength of the hat stiffeners of the full-scale panel. In the postbuckling regime, the hat stiffeners are under compression and, in some cases, the webs or the hat top may buckle locally (short wavelength buckle) and fail (crippling) since they have low postbuckling ability. The stiffener crippling evaluation was designed to provide insight on the hat stiffener web failure to be expected in the full-scale panel.

The nominal dimensions of the Stiffener Crippling specimen are shown in Figure 4.6. Ultrasonic C-Scan inspection of the specimen panel (all specimens were cut from a single panel) was performed prior to static testing. The quality of the laminate was judged to be good throughout the panel, but some local anomalies (resin starvation and wrinkles) were observed in fillet transition areas of the web/flange interface. This was the same problem as for the skin-stiffener separation specimens and was resolved in the fabrication of the intersection specimen and full-scale panel.

Void content and fiber volume measurements were taken at various locations of the stiffener caps, bases, and webs. The mean void content value of 2.6% exceeded the SA cutoff limit of 2%. The webs showed consistently higher void contents than the hat tops and bases. The reason for this is the low thickness of the webs compared to the hat tops and bases and the low bleeding of the 5225 resin. A more detailed discussion of this issue is given along with the tear-down inspection results in Section 5. Given the breather/bleeder bridging mentioned in the previous section and the low thickness of the specimens (0.015 inches for the hat webs) this value is not alarming.

Additional void content measurements were taken from the web/flange fillet interface. The average void content was 7.2% which, being high, led to a modification of the web/flange fillet interface design for the frame/stiffener intersection and full scale specimens. The fillet radius was increased to 3/16" (from the original of 1/8") and the local laminate quality was improved by inserting graphite tape in the resin rich pocket area between fillets. These modifications and the modification introduced in splicing the breather and bleeder material (see Section 4.4.5 below) eliminated these problems.

The average fiber volume for the hat top, base, and webs was 58.4% (typical acceptable SA value is 55%) which was considered very good given the geometric complexity of the part. The average fiber volume for the fillet area was 51.8%, below the minimum acceptable value again pointing to inadequate compaction in this area.

For the purpose of analysis, the specimen cross-section was approximated by several distinct segments shown in Figure 4.7. The overall stiffness EA is derived by summing the products of modulus (calculated from classical laminated plate theory for the particular segment), thickness, and width for each segment.



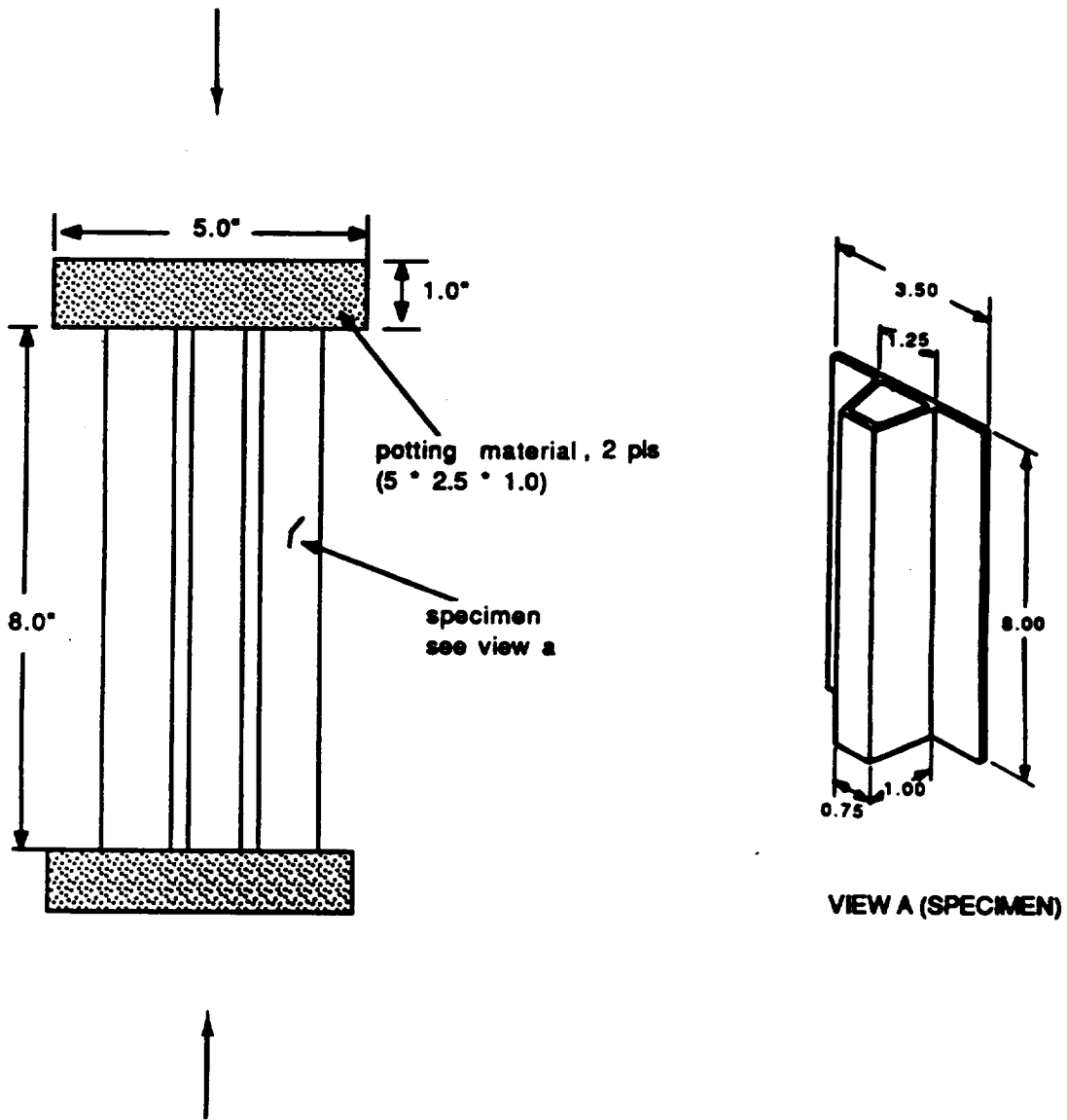
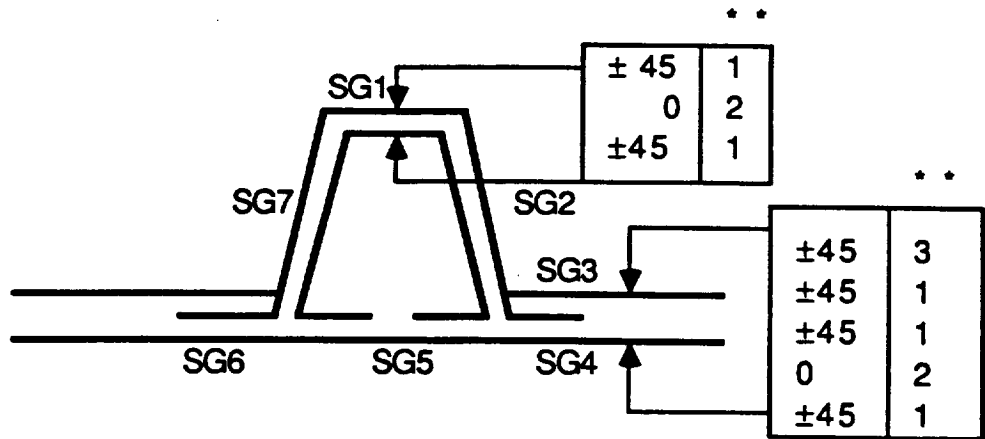


FIGURE 4.6. STIFFENER CRIPPLING SPECIMEN

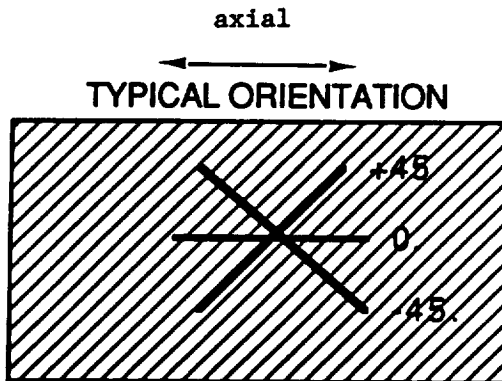
*C-2*



**LEGENDS:**

- SG1 : TOP CAP
- SG2 , SG7 : WEB
- SG3 , SG4 : FLANGE
- SG5 : BOTTOM CAP
- SG6 : FLANGES

- •
- 1 - C3 K/5225 FABRIC, t ply = 0.0075 in
- 2 - C12K/5225 TAPE, t ply = 0.012 in.
- 3 - C3 K/5225 FABRIC, t ply = 0.015 in.



**FIGURE 4.7. INDIVIDUAL SEGMENTS OF STIFFENER USED FOR STIFFNESS ANALYSIS**

This value was compared to the measured EA value. The measured EA value was obtained using the strain gage (SG) values. The strain gage readings were taken at low loads, in the linear portion of a test. The following formula was used to compare the average axial stiffness of the entire test specimen with the predicted stiffness [12]:

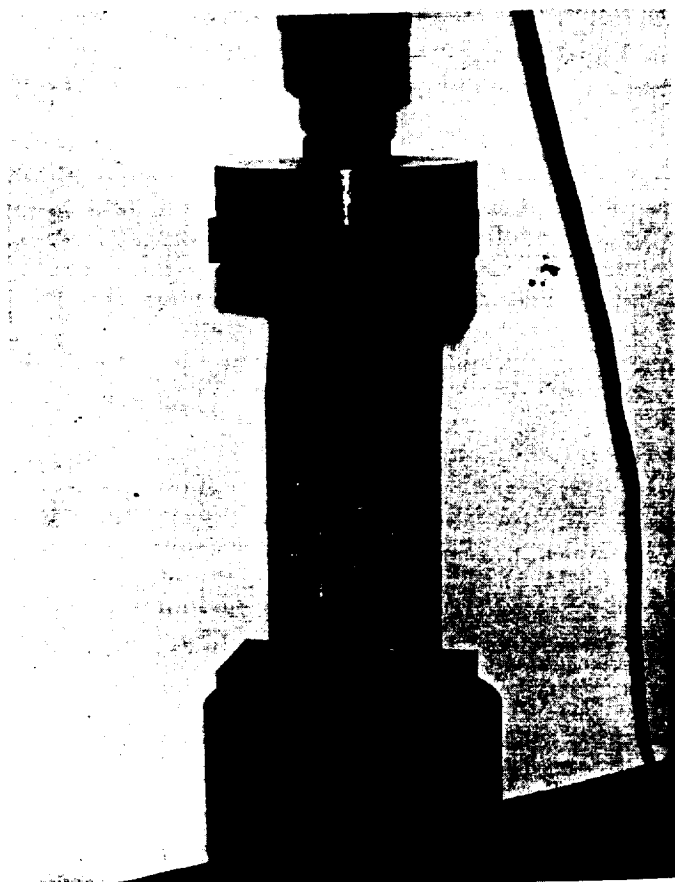
$$\text{Nominal Stiffness} = \text{Load} / \left( \text{SG1} + \text{SG2} + \text{SG5} + \text{SG7} + \frac{2 * (\text{SG3} + \text{SG4} + \text{SG6})}{3} \right) / 7$$

where, Load is the applied load and SG is the individual strain gage reading. The mean measured value for EA of 1.1 million pounds was only 10% higher than the predicted value of 1.0 million pounds.

For typical failures, the hat stiffener flange buckled first, followed by local crippling of the hat stiffener (webs and hat top) and crushing. Little delamination and splitting was found at the skin stiffener interface. The hat stiffener flange also exhibited local buckling. The local buckling and crippling of the hat webs is quite important as it was subsequently found to trigger failure of the full scale panel (see Section 5). A typical failure mode is shown in Figure 4.8.

Failure predictions for the crippling specimens were obtained using the Needham method [12]. The Needham method is a summation technique which adds the load carrying capability of each segment of the hat stiffener to obtain an overall crippling load. The hat stiffener is divided into six segments: the top cap, bottom cap, two webs, and the two flanges as shown in Figure 4.6. The edge conditions of these segments can be categorized further into one-edge free (the flanges) or no edge free (the top and bottom cap, and two webs). The crippling strain curve is derived empirically. The database, from which the crippling curves were fitted, was generated from a series of tests conducted on graphite/epoxy angles and channels to determine the crippling strengths of one-edge-free and no-edge-free segments, respectively. T300/5208 and AS/3501 graphite/epoxy materials were used in the evaluation with laminates using  $\pm 45$ , 0 and 90 degree orientations. These empirical curves were found to be applicable to C3K/5225 material in reference 12. The comparison of the predicted and experimental failure loads is given in Table 4.5. The constrained curvature prediction is 15% lower than the experimental mean value and is considered satisfactory.

The crippling specimen results provided valuable information for the structural and fabrication aspects of the next complexity level specimens in the building block approach (frame-stiffener intersection specimen) and the full-scale panel. Besides the crippling strength, and the failure mode which showed significant damage in the hat webs thus pointing to a candidate location where failure should be expected in the intersection specimen and full-scale panel, it showed that some modifications in the design and layup and bagging procedure were necessary to improve consolidation, reduce void contents and eliminate small wrinkles that were present at the web/skin interface of the hat stiffeners.



**FIGURE 4.8. STIFFENER CRIPPLING SPECIMEN - FAILURE MODE**

Table 4.5  
Stiffener Crippling Strength: Experiment Versus Analysis

Stiffener Crippling Strength (lbs)	Boundary Conditions	Needham Crippling Mean Load (lbs)
2550		
2560	Unconstrained Curvature	762 lbs
3080		
2590		
2625	Constrained Curvature	2264 lbs
2590		
<hr/>		
2666 (MEAN)		
204.6 (SD)		
7.7% (CV)		

#### **4.2.4 COMPRESSION AND SHEAR AFTER IMPACT SPECIMENS**

Damage tolerance of THERM-X® processed panels was assessed with compression and shear after impact specimens. Shear after impact is not usually done as part of a damage tolerance evaluation of a manufacturing process but was included here since the loading of the full-scale panel involved shear.

The geometry and layup of Compression After Impact Specimens was the same as in NASA Reference Publication 1092 [13]. The specimens were C-scanned before and after impact. The C-scan records before impact indicated excellent part quality without any defects.

Fiber volume and void content measurements also showed excellent part quality and consolidation. The fiber volume values were all above the minimum acceptable of 55% averaging 56.3% and the void content values were well below the maximum acceptable of 2% averaging 1.0% void content.

Three impact energies were used with a drop-weight impactor. Five ft-lbs (Compression After Impact only), 10 ft-lbs (which was threshold of visual detectability), and 20 ft-lbs which is the energy level suggested in reference 13. Typical C-scan records of impacted specimens are shown in Figure 4.9. For each specimen, the frontside indentation at the impact site was measured along with the C-scan indicated damage area, and the backside fiber breakage. These results are shown in Table 4.6 for 10 and 20 ft-lb energies. The results were well within the ranges established for the same impact energies for parts fabricated using conventional layup.

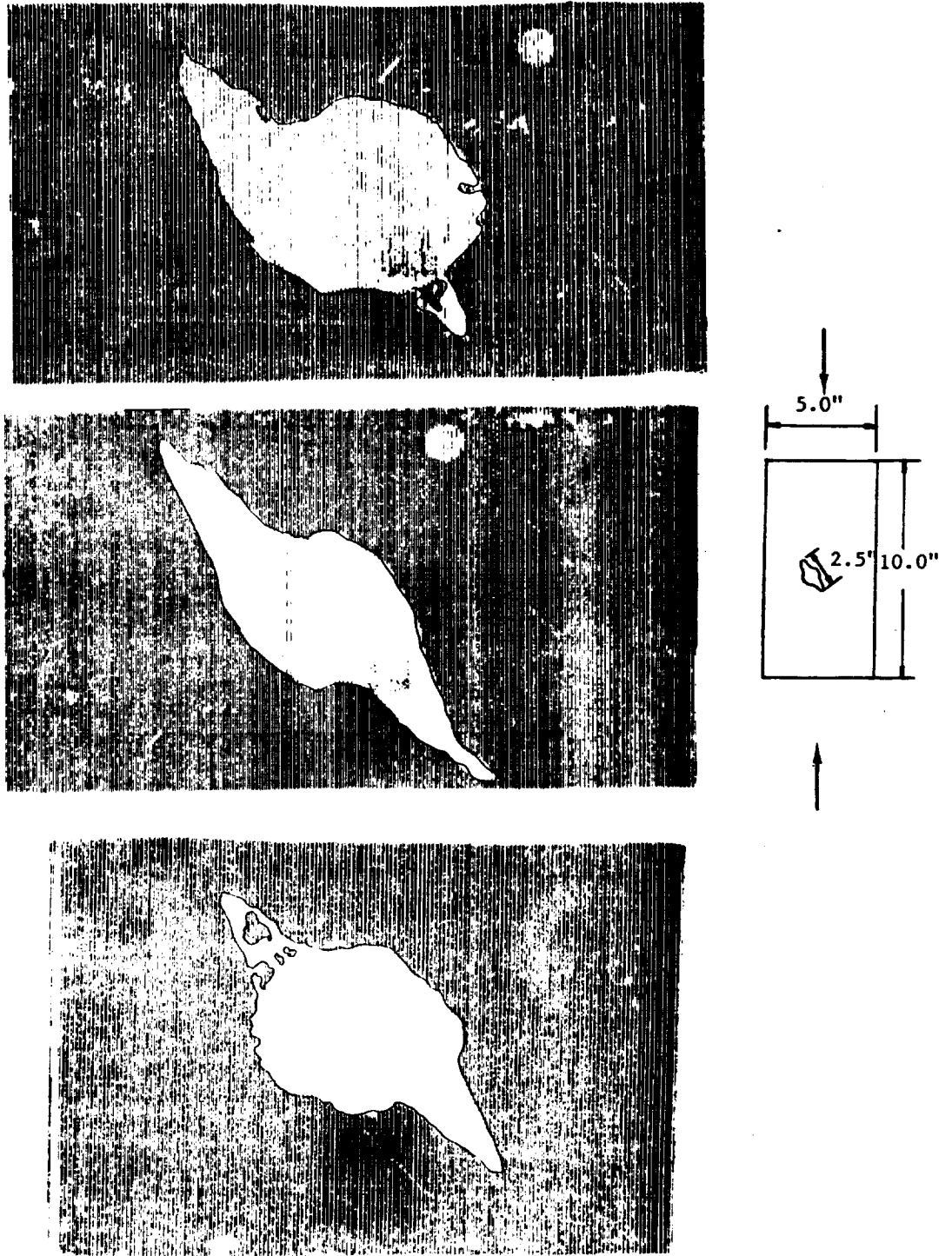


FIGURE 4.9. C-SCAN OF COMPRESSION AFTER IMPACT SPECIMEN

In addition to drop-weight impacts, additional tests were performed on identical specimens impacted at the same energy levels but with an airgun with aluminum bullets. These tests were done at NASA Langley. The impactor speeds in this case are much higher (312 ft/sec for 10 ft-lbs and 441 ft/sec for 20 ft-lbs energy) and the extent of damage is 2 to 3 times larger. This effect of high impactor speed for the same low impact energy has been documented by, among others, Morton and Godwin [14].

Typical failed specimens of compression and shear after impact tests are shown in Figure 4.10. The compression after impact specimen failure is the same as that observed on specimen of conventional layup. The shear after impact specimen failure appears to be a shear failure of the 0 degree plies. No similar tests on conventionally laid up specimens were available for comparison.

Table 4.6  
Impact Testing Summary of Results  
(FROM DROP-WEIGHT IMPACT DAMAGE)

Specimen Fiber Designation	Impact Kinetic Energy, T (ft-lb)	C-Scan Area (in**2)	Frontside Indentation (in)	Backside Breakage (in)
CAI-TOVD				
-1	10.8	3.4	0.019	3.0
-2	10.8	4.1	0.017	3.5
-3	10.8	4.2	0.018	3.0
SAI-TOVD				
-1	10.2	3.6	0.017	3.5
-2	10.4	3.6	0.017	3.0
-3	10.2	2.9	0.016	3.0
CAI-20FT-LB				
-1	19.0	4.7	0.039	5.0
-2	20.7	3.9	0.042	6.0
-3	19.5	6.6	0.033	5.0
SAI-20FT-LB				
-1	19.4	4.3	0.046	5.0
-2	19.5	3.6	0.038	6.0
-3	19.1	4.5	0.032	5.5

Impacted in accordance with NASA Technical Reference 1092,  
ST-1

$$T = (W/2g)*(V_i)^2$$

$V_i$  = velocity of weight at impact measured experimentally

Impactor weight,  $W = 10.33$  lb

Impactor tip diameter = 0.5 in

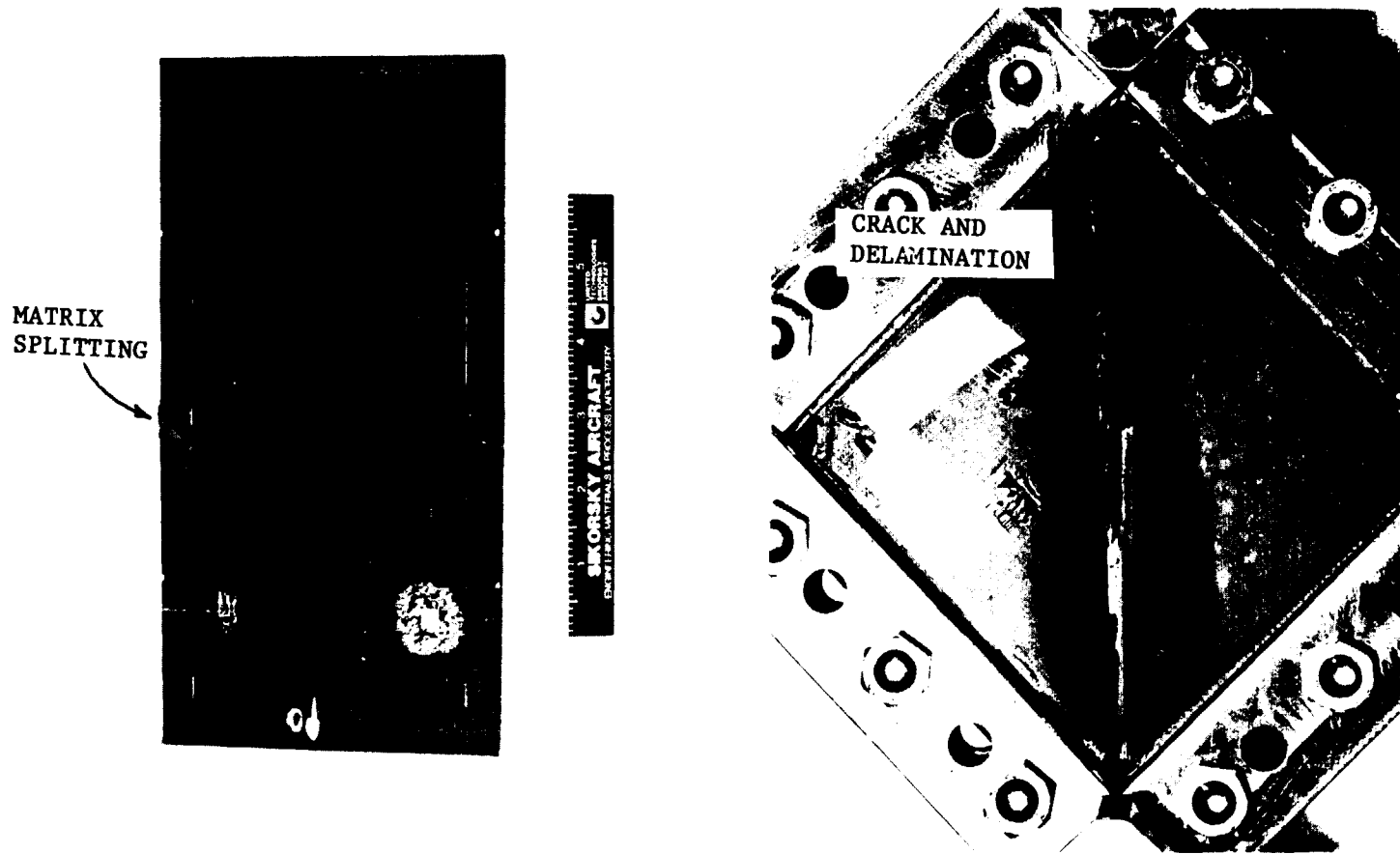


FIGURE 4.10. TYPICAL FAILURES OF CAI AND SAI SPECIMEN



A plot of the compression after impact strength as a function of impact energy is shown in Figure 4.11. Both low velocity (drop weight) and high velocity (air gun) results are included. There is little effect of impactor velocity on residual strength. In the same plot the results obtained on panels with the same configuration and manufactured using conventional layup are included. While at high energies there is no discernible difference in residual strength between conventional layup and THERM-X® tooling, at intermediate energies (around 10 ft-lbs or 600 in-lb/in) the conventional layup specimens show moderately higher strength (15%) than the specimens fabricated with THERM-X® tooling. This difference is believed to be within statistical scatter. Only 3 specimens were tested per energy level per velocity per manufacturing condition which are not enough to yield results with statistical significance.

The shear after impact strength as a function of energy level is shown in Figure 4.12. Only THERM-X® tooling data were available and only after drop-weight impact. Although there is significant scatter, it appears that the knockdown in strength for impacted panels under shear loading is significantly less than the compression after impact strength knockdown for the same energy level.

The extent of damage as measured by C-scan indicated delamination area is shown in Figure 4.13 as a function of impact energy. The air gun impacted specimens show as much as 50% higher damage area than the drop weight impacted specimens. Conventional and THERM-X® specimens show no differences. Compression and shear specimens are pooled together since the specimen layup and impacting procedure are identical.

The indentation at the point of impact for the same specimens is shown in Figure 4.14. In this case, the high speed (air gun) and low speed (drop weight) impacts are close together. In addition, THERM-X® processed and conventional autoclave tooled specimens show no significant differences. A single curve then can be used to describe the trend rather than the two curves of Figure 4.13. This suggests that indentation at the point of impact appears to correlate better with impact energy and thus to residual strength. Indentation then can be used as a means to estimate residual strength after impact by correlating measured indentation to energy level through Figure 4.14 and energy level to residual strength through Figure 4.11. Of course, this can only be viewed as a rough estimate since impactor size and type, specimen layup, type and location of damage are not taken into account.

#### **4.2.5 SKIN TEARING SPECIMENS**

The skin tearing specimens represent the skin of the full-scale panel. They are tested in tension to simulate the tension field in the postbuckled configuration of the full-scale panel. The skin layup was chosen to be 45 degree fabric plies of thickness equal to that indicated by the optimization method of Section 3 (resulting skin thickness 0.03 inches). Since the postbuckled skin is in diagonal tension, the skin tearing specimens were (0/90)<sub>3</sub> coupons tested in tension. The specimen dimensions and configuration are shown in Figure 4.15.

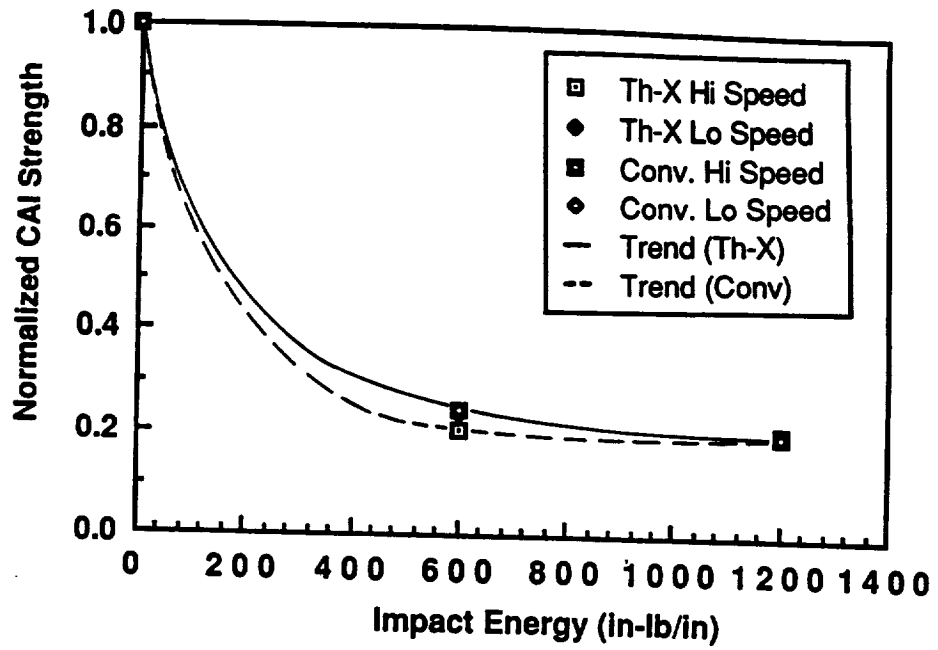


FIGURE 4.11. CAI STRENGTH AS A FUNCTION OF IMPACT ENERGY

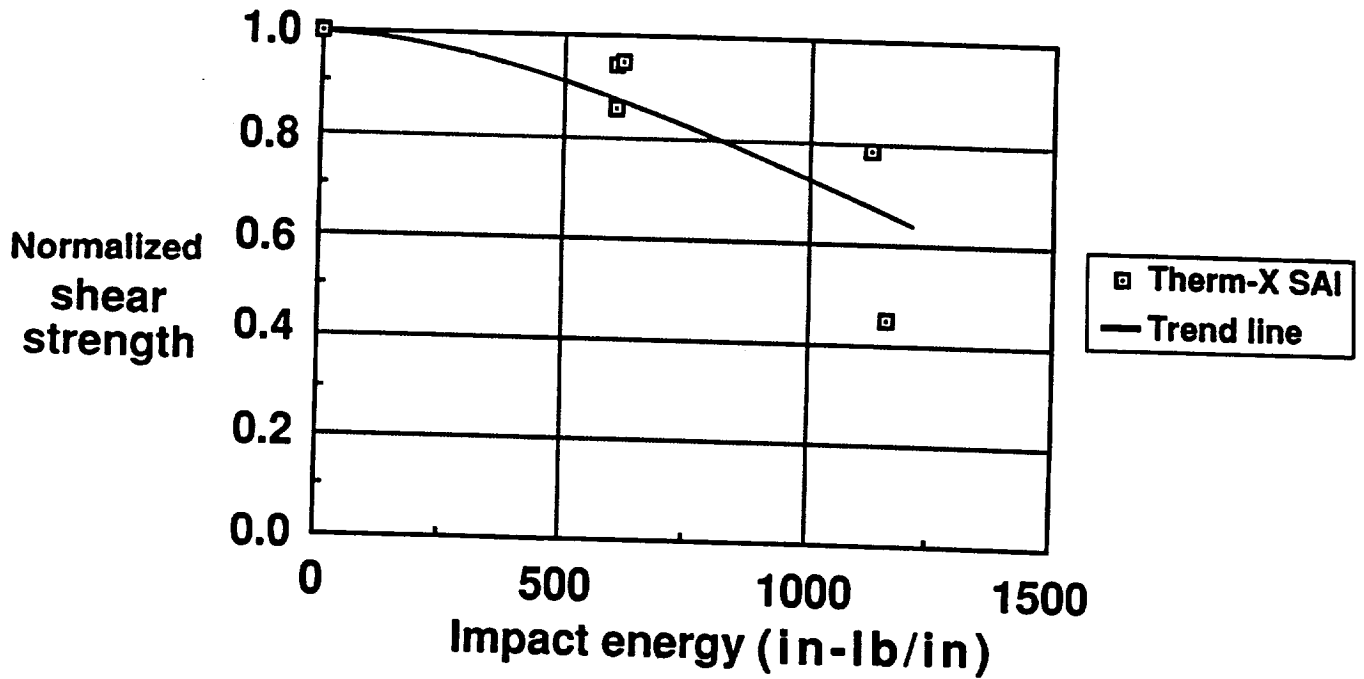


FIGURE 4.12. SAI STRENGTH AS A FUNCTION OF IMPACT ENERGY

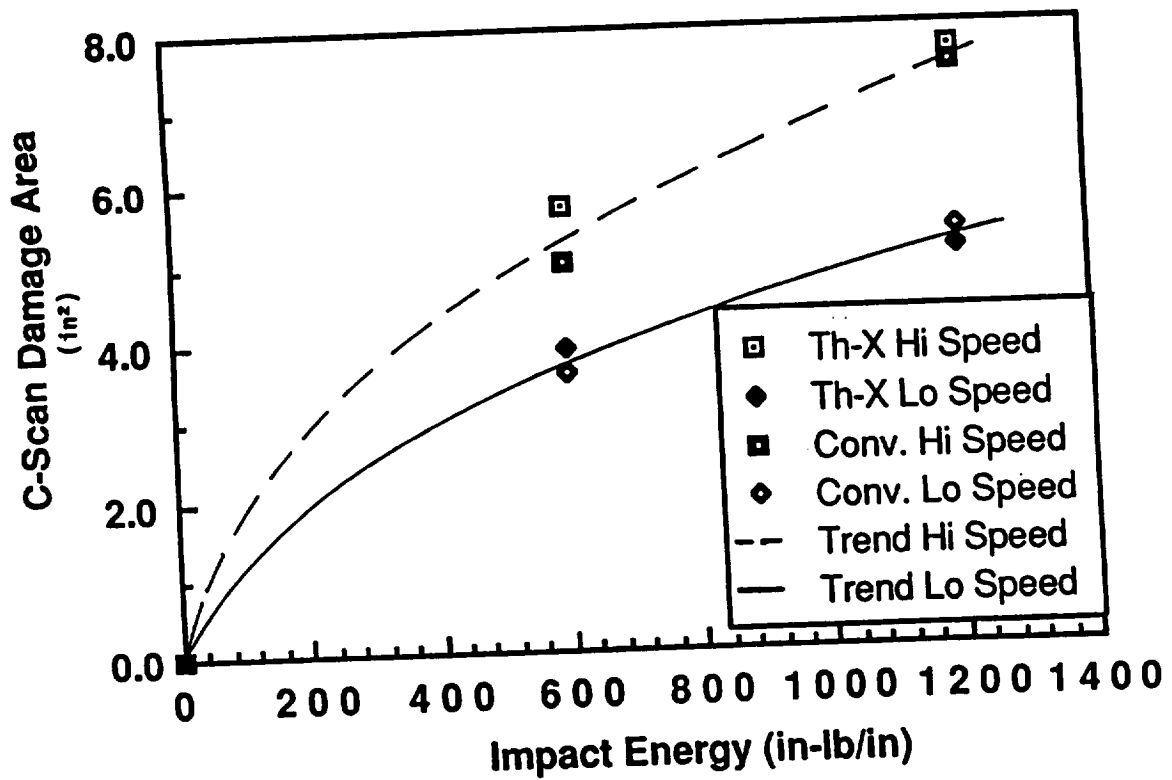


FIGURE 4.13. INTERNAL DAMAGE AS INDICATED BY C-SCAN AS A FUNCTION OF IMPACT ENERGY

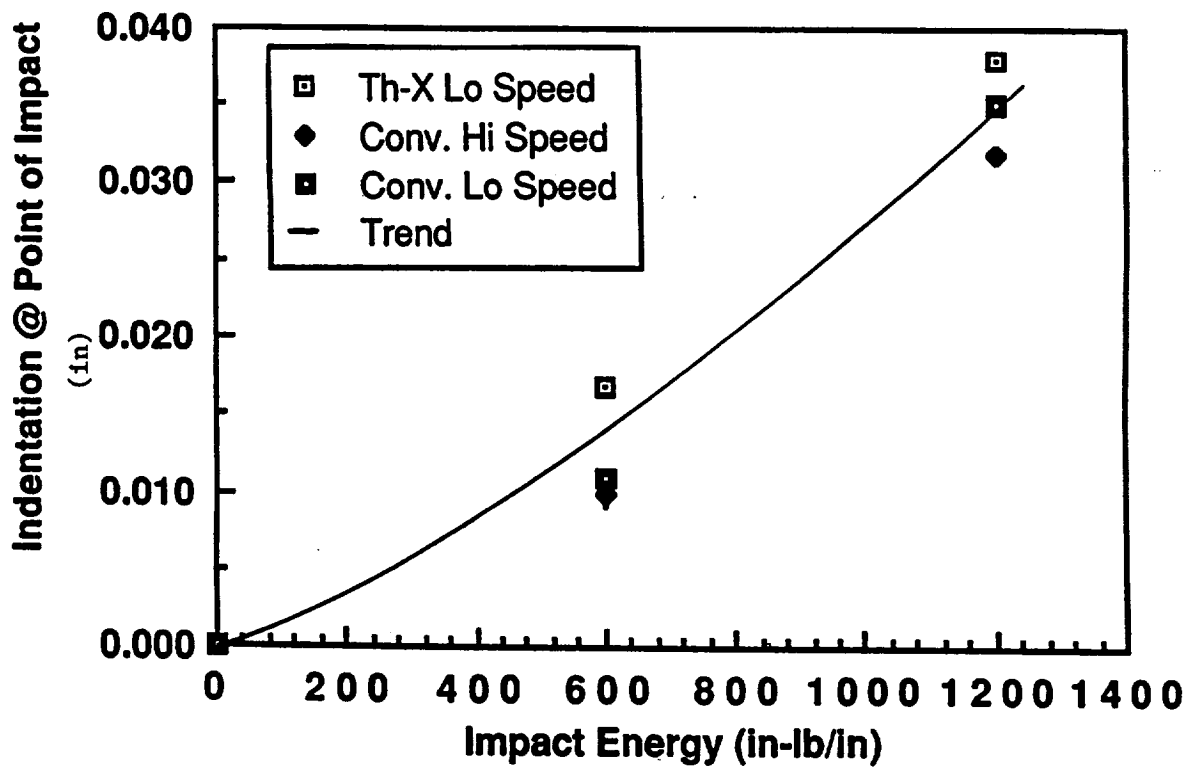


FIGURE 4.14. INDENTATION AT POINT OF IMPACT AS A FUNCTION OF IMPACT ENERGY

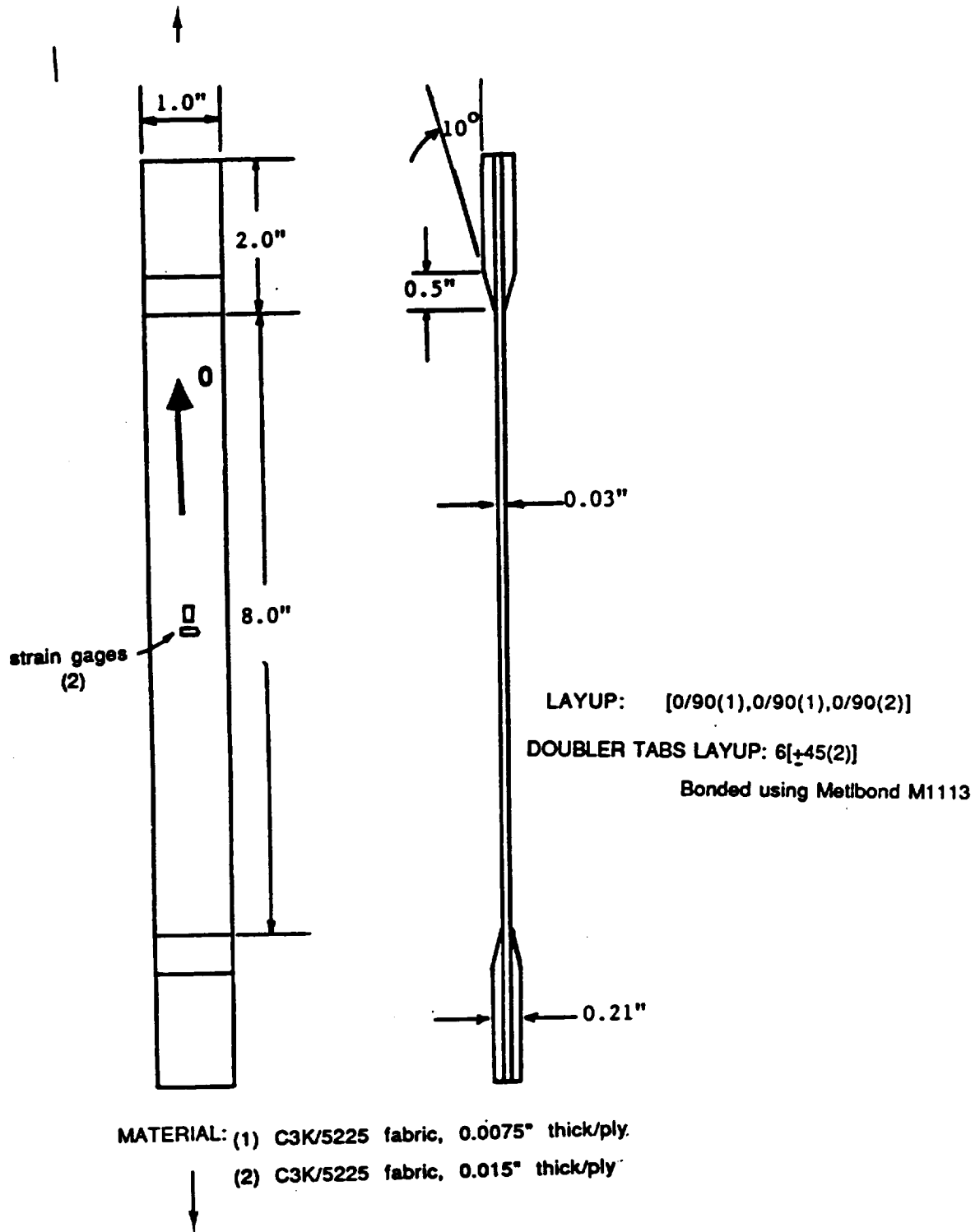


FIGURE 4.15. SKIN TEARING SPECIMEN

Fiber volume data for these specimens averaged 56.4% with the lowest and highest values being 55.0% and 57.3%, all well within the allowable limits of 55% and 61%. The void content values averaged slightly higher (2.7%) than the minimum allowable of 2% with minimum and maximum values 2.0% and 3.3% respectively. These being the first specimens manufactured in the program, the cure pressure used was 45 psi (fabrication details were still being smoothed out) instead of 100 psi as indicated in Section 2. The low pressure is considered to be responsible for the moderately high void content values.

The panel out of which the coupons were cut was C-scanned. Small (up to 0.1 inches in diameter) isolated voids were present at the edges of the panel. The panel was trimmed to remove these areas and the specimens subsequently cut so that areas of voids and porosity were avoided.

Thickness normalized tension strength and modulus values are reported in Table 4.7. In addition, the analytically corrected maximum ply strain at failure is shown. This value accounts for initial specimen curvature that resulted from slight unbalance in the specimen stacking sequence. To meet the full-scale panel requirement of skin thickness of 0.03 inch, two plane weave plies (0.0075 inch thick each) and one eight harness satin ply (0.015 inch thick) were used. The eight harness satin ply was laid up on the outside. This made the sequence unbalanced and resulted in slightly curved specimens. The reason for that was that the resulting specimen radius of curvature was 40 inches which is exactly the radius of curvature for the full-scale panel. For flat specimens however, this radius of curvature implies residual strains stored in the specimen.

Table 4.7  
Skin Tearing Test Results

Specimen Number	UNNORMALIZED		NORMALIZED		Poisson's Ratio	Maximum Ply Strain [E-6]
	Tensile Strength (ksi)	Tensile Modulus (msi)	Tensile Strength (ksi)	Tensile Modulus (msi)		
1	82.6	8.82	91.7	9.79	-----	10400
2	76.9	9.02	85.1	9.99	0.03	9500
3	75.8	8.85	84.4	9.85	0.03	9500
4	86.6	8.77	96.4	9.76	0.04	10600
5	80.6	9.17	87.9	10.0	0.04	10300
6	88.5	9.38	96.5	10.2	0.06	10500
7	72.5	9.29	79.3	10.2	0.03	8500
8	82.7	9.29	89.6	10.1	0.05	9600
Mean	80.8	9.07	88.9	9.99	0.04	9900
Sample Std. Deviation	5.46	0.241	5.98	0.174	0.01	700
% Coeff. of Variation	6.76	2.66	6.73	1.75	26.5	7.3

Notes: 1) Normalization performed for laminate thickness of 0.030"  
2) Maximum Ply Strain based on analysis below to account for specimen curvature

A comparison with the material qualification data for the same specimen configuration but with all plies being of plane weave and conventional hand layup is shown in Table 4.8. Both the uncorrected and the curvature-corrected strength values are shown for the THERM-X processed specimens. A brief description of the method used to correct the strength values for the initial specimen curvature follows.

Table 4.8  
Skin Tearing Test Results vs C3K/5225 Qualification Data

Experimental Quantity	Present Study Single Batch Mean	Single Batch Mean Ranges		5 Batch Mean
		Low	High	
Normalized Tensile Modulus (msi)	9.99	9.76	10.2	9.87
% CV	1.75%	1.16%	2.80%	2.09%
Poisson's Ratio	0.04	0.04	0.05	0.05
% CV	26.5%	9.20%	34.4%	24.8%
Normalized Tensile Strength (ksi)	88.9			
% CV	6.73%			
Normalized Curvature- Corrected Tensile Strength (ksi)	98.6	102	109	104
% CV	6.79%	3.00%	8.10%	4.70%

Since the specimen layup was slightly unbalanced (with one eight harness satin ply on the outside), as dictated by the configuration of the full-scale test article, an initial curvature resulted from the panel's cure cycle, see Figure 4.16. The initial radius of curvature was measured to be 40.3 inches. Maximum residual strain (due to curing) in the surface plies of the panel was thus calculated to be,

$$\epsilon_{res} = \pm \left(\frac{t}{2}\right) \frac{1}{\rho} = \pm 409\mu s \quad (4.1)$$

where  $t$  = average specimen thickness, 0.033", and,  
 $\rho$  = radius of curvature, 40.3 inches.

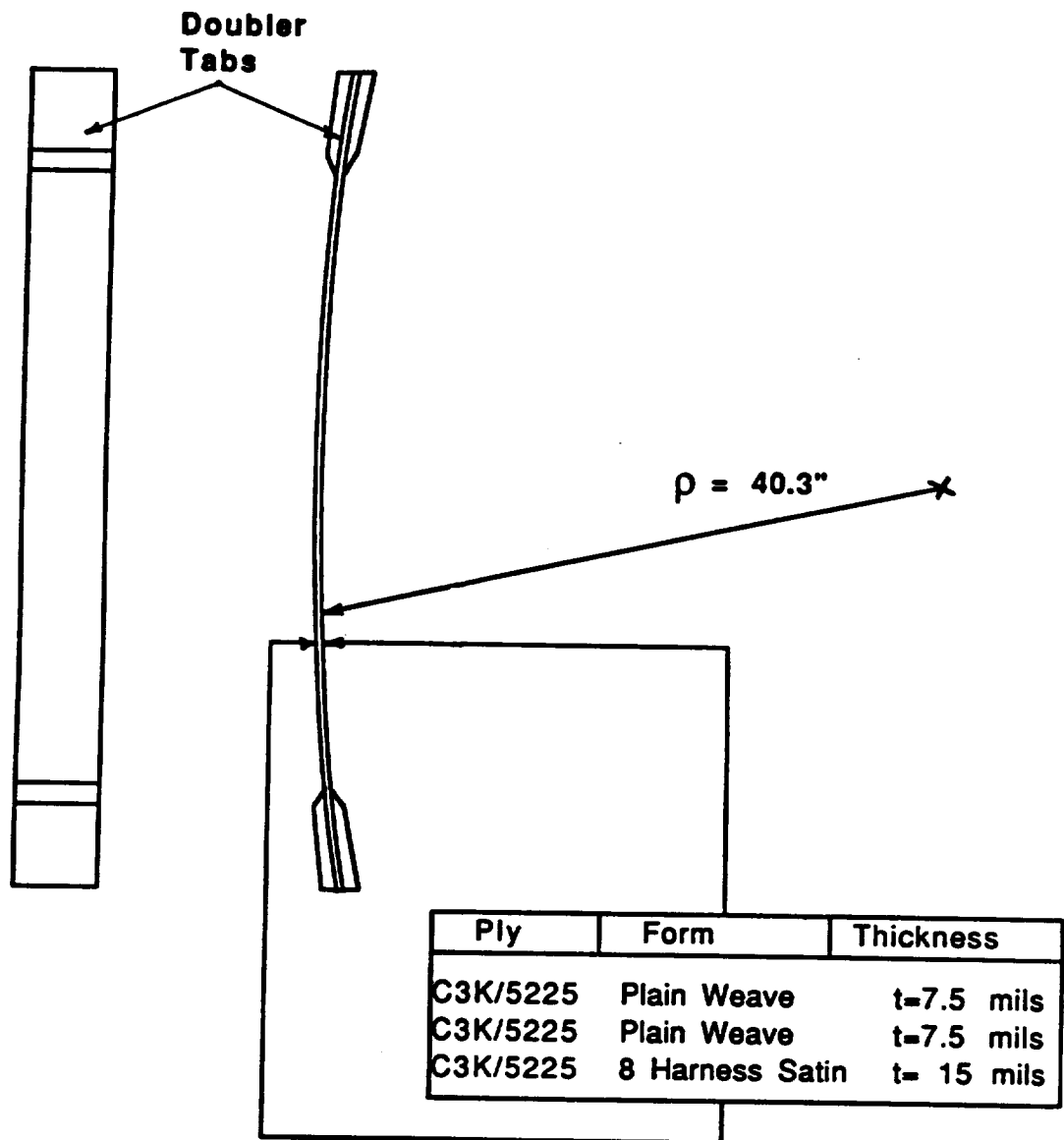


FIGURE 4.16. CURE-INDUCED INITIAL CURVATURE OF SKIN TEARING SPECIMEN



The distribution of the cure induced strains through the thickness of the specimen is shown in Figure 4.17a. Subsequently, strain gages were applied to all specimens while in the curved condition. As a result, the residual strain of equation 4.1 was not indicated by gages. Upon loading, the specimen straightened, thereby imposing the strain distribution shown in Figure 4.17b. Further tensile loading imposed uniform extension on the specimen cross section, (see Figure 4.17c). The maximum ply strain at failure then was calculated to be the gage indicated strain plus the tensile residual strain, or,

$$\epsilon_{\max} = \epsilon_{\text{gage}} + \epsilon_{\text{res}} = \epsilon_{\text{gage}} + 409 \mu\text{s} \quad (4.2)$$

Maximum ply strains calculated using this expression were reported in the rightmost column of Table 4.7.

Using maximum ply strains in conjunction with the uniaxial Hooke's Law, a correction to measured failure stresses may be calculated by,

$$\sigma_{\max,n} = E_n \epsilon_{\max,n} \quad (4.3)$$

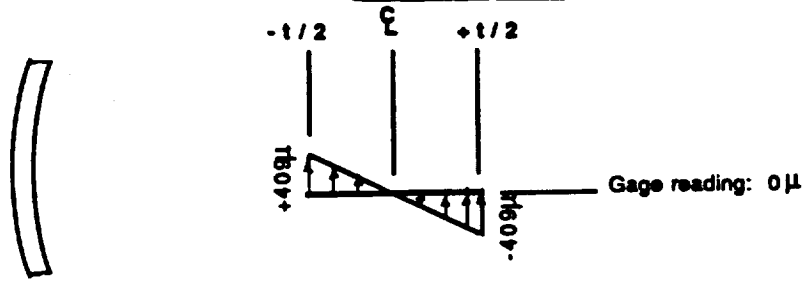
where  $E_n$  = extensional modulus of specimen n, and,  
 $\epsilon_{\max,n}$  = maximum strain of specimen n

The comparison in Table 4.8 shows that the modulus of parts made with THERM-X® tooling is slightly higher than for conventional layup with very low scatter. The Poisson's ratio is slightly lower with slightly more scatter. The corrected strength value is slightly lower with scatter well within the range of scatter values found among batches during the material qualification program (conventional layup). The results from this building block test suggest that when material forms are mixed (plain weave with eight harness satin) the resulting parts may have differences from the equivalent single form layups. Building block tests like this one are useful in quantifying these differences. For the material configurations used in the current program, these differences appear to be very small.

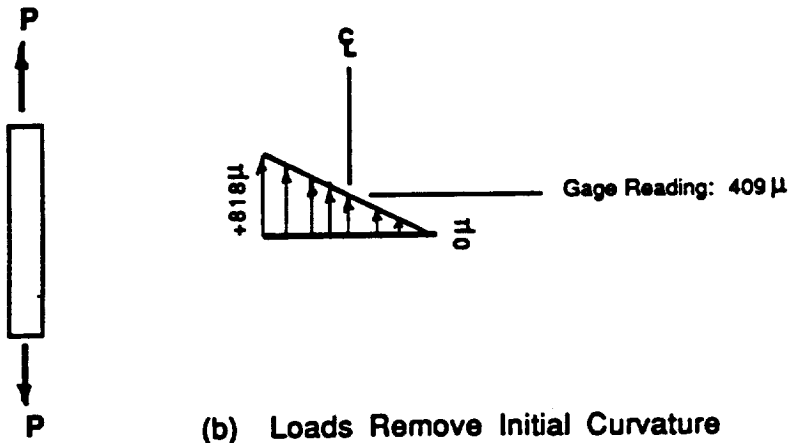
#### 4.2.6 FRAME-STIFFENER INTERSECTION SPECIMEN

The Frame-Stiffener Intersection Specimen (Figure 4.18) was the last specimen of the building block evaluation. It is at the third and highest level of specimen complexity, the first level being the flat specimens and the second being the Crippling and Skin-Stiffener Separation specimens. This specimen integrated the results and findings of the building block evaluation up to that point in terms of design changes and layup and fabrication procedure modifications. It was meant to test the basic structural details of the full-scale panel such as

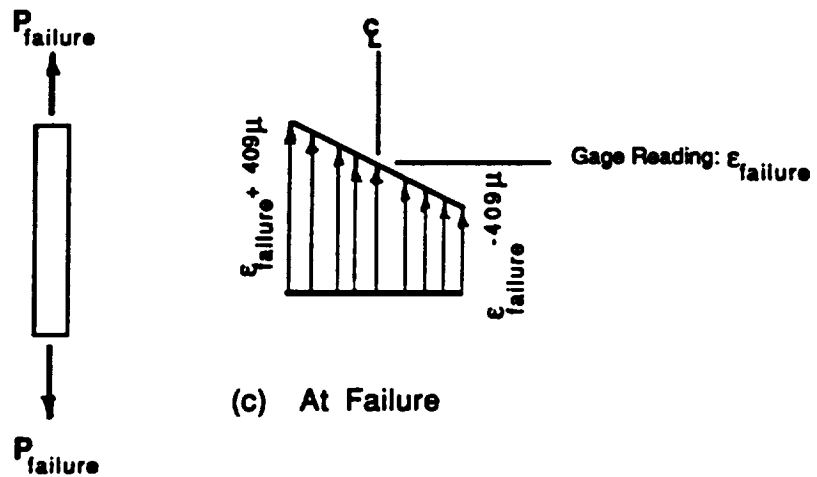
**SPECIMEN DEFORMATION      THROUGH-THICKNESS  
STRAIN DISTRIBUTION**



(a) Residual Strain



(b) Loads Remove Initial Curvature



(c) At Failure

**FIGURE 4.17. (A) RESIDUAL SURFACE STRAINS DUE TO SPECIMEN CURVATURE  
(B) STRAIN DISTRIBUTION AFTER SPECIMEN STRAIGHTENING  
(C) STRAIN DISTRIBUTION IMMEDIATELY PRIOR TO FAILURE**

stiffeners, frames and skin, under loading very similar to the postbuckled configuration of the full scale panel. In addition, this specimen addressed the most complex structural detail of the full-scale panel, the frame-stiffener intersection corner and the built-in shear ties for load transfer between frames and stiffeners.

From the manufacturing point of view, the specimen finalized the manufacturing procedure, gave an accurate indication of the quality of part to be expected for the full-scale panel in particular near areas of sharp radii, geometry changes and intersecting parts. The manufacturing procedure was identical to that used for the full-scale panel, only a smaller tool was used. For a detailed discussion of the manufacturing procedure see section 5 where the full-scale panel fabrication is discussed. The specimen was flat to avoid the complexities introduced by curvature and consisted of two adjacent bays of the full-scale panel.

The specimen configuration is shown in Figure 4.18. The doublers on both sides of the specimen were cocured directly onto the specimen. This was made possible by machining the tool for the specimen to have staggered steps all around to accommodate the extra plies for the doublers. C-scan records of fabricated specimens showed excellent quality. Preliminary void content and fiber volume measurements (from specimens cut off the skin and frame corners) were also excellent, with void content well below 1% and fiber volume higher than 56%. More chemical test results are reported in the teardown inspection sub-section of Section 5.

A closeup of a typical frame/stiffener intersection corner is shown in Figure 4.19. Excellent consolidation and radius definition is evident. Part quality around the shear tie (discernible as a darker portion of the hat stiffener to the inside of the frame) which consists of the outer plies of the frame web cocured on the hat stiffener webs is also very high with accurate placement and contour definition. Aluminum doublers 0.5 in. thick and 3.0 in. wide were fastened on three-ply graphite/epoxy doublers that were cocured with the specimen. The aluminum doublers formed a picture frame fixture for introducing pure shear load into the specimens.

The finite element model used to analyze the panel is shown in Figure 4.20. One specimen end is loaded in tension (along a diagonal) and the opposite end is fixed. MSC NASTRAN SOL 66 geometric nonlinear solution was used to determine the buckling load and post buckling behavior of the panel. The model consists of 606 grid points, 576 QUAD elements, and 3601 degrees of freedom.

#### **4.2.6.1 COMPARISON OF TEST RESULTS TO FINITE ELEMENT PREDICTIONS**

The strain gage data obtained from the frame-stiffener intersection specimens was compensated for gage transverse sensitivity and percent reinforcement (resulting from gage bagging and adhesive material) following procedures recommended by the gage manufacturer (Micro-Measurements Division, Measurement Group Inc.) and reference 15.

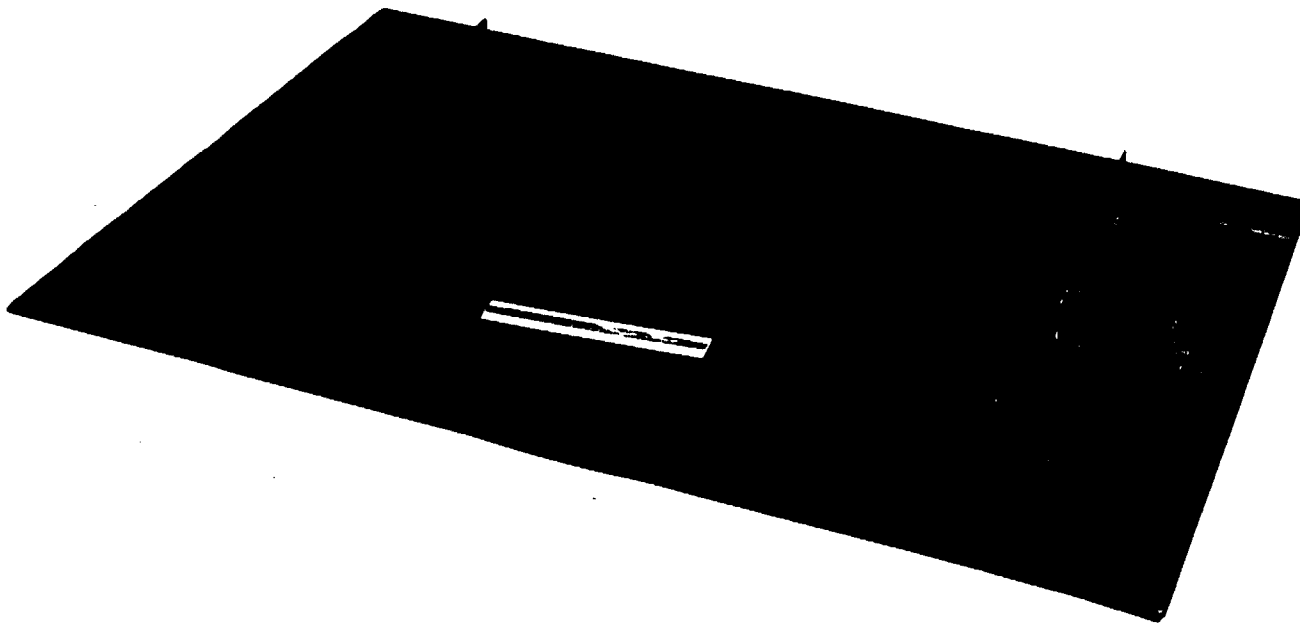


FIGURE 4.18. FRAME-STIFFENER INTERSECTION SPECIMEN

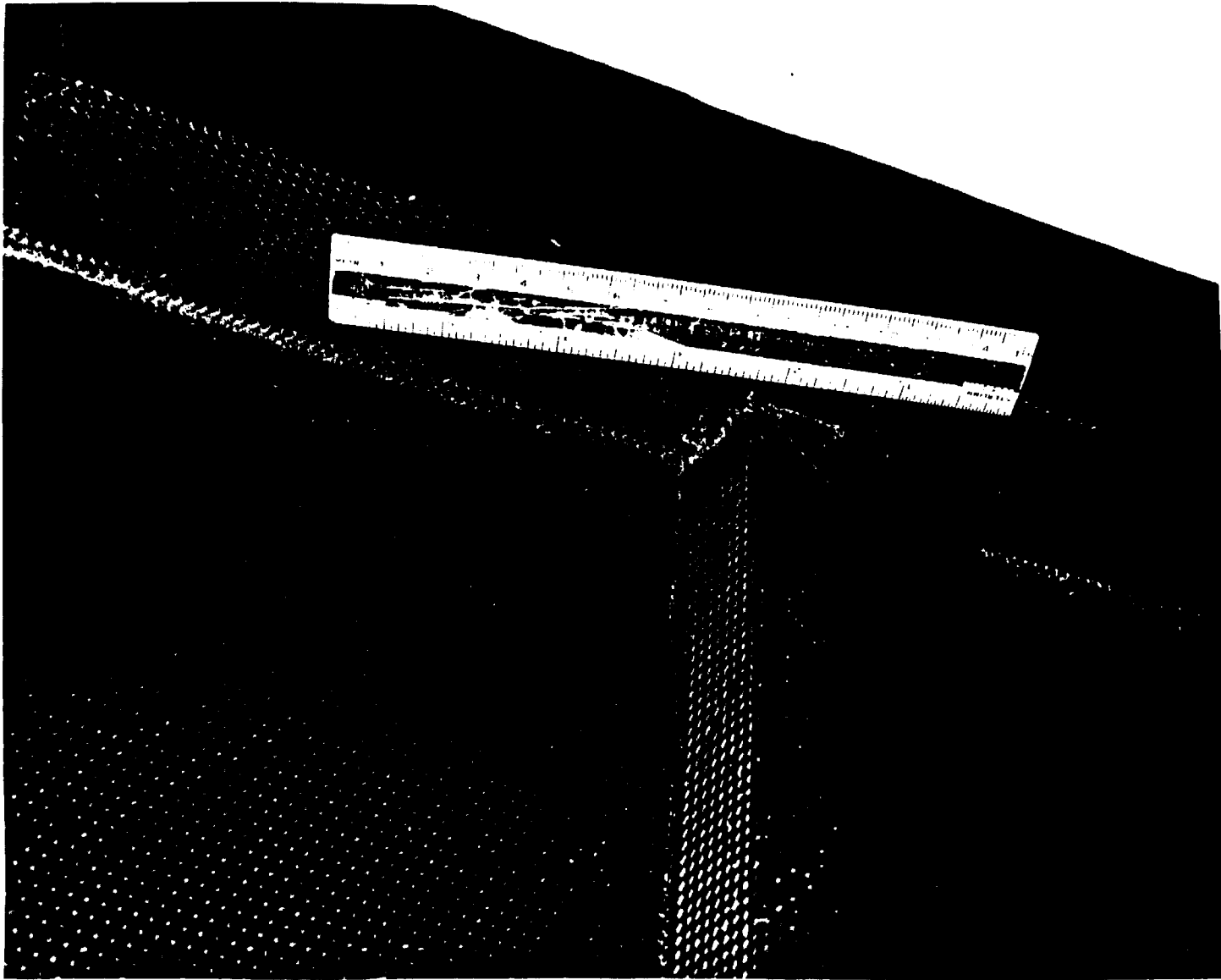


FIGURE 4.19. FRAME-STIFFENER INTERSECTION DETAIL



FIGURE 4.19. (CONT'D) FRAME-STIFFENER INTERSECTION DETAIL

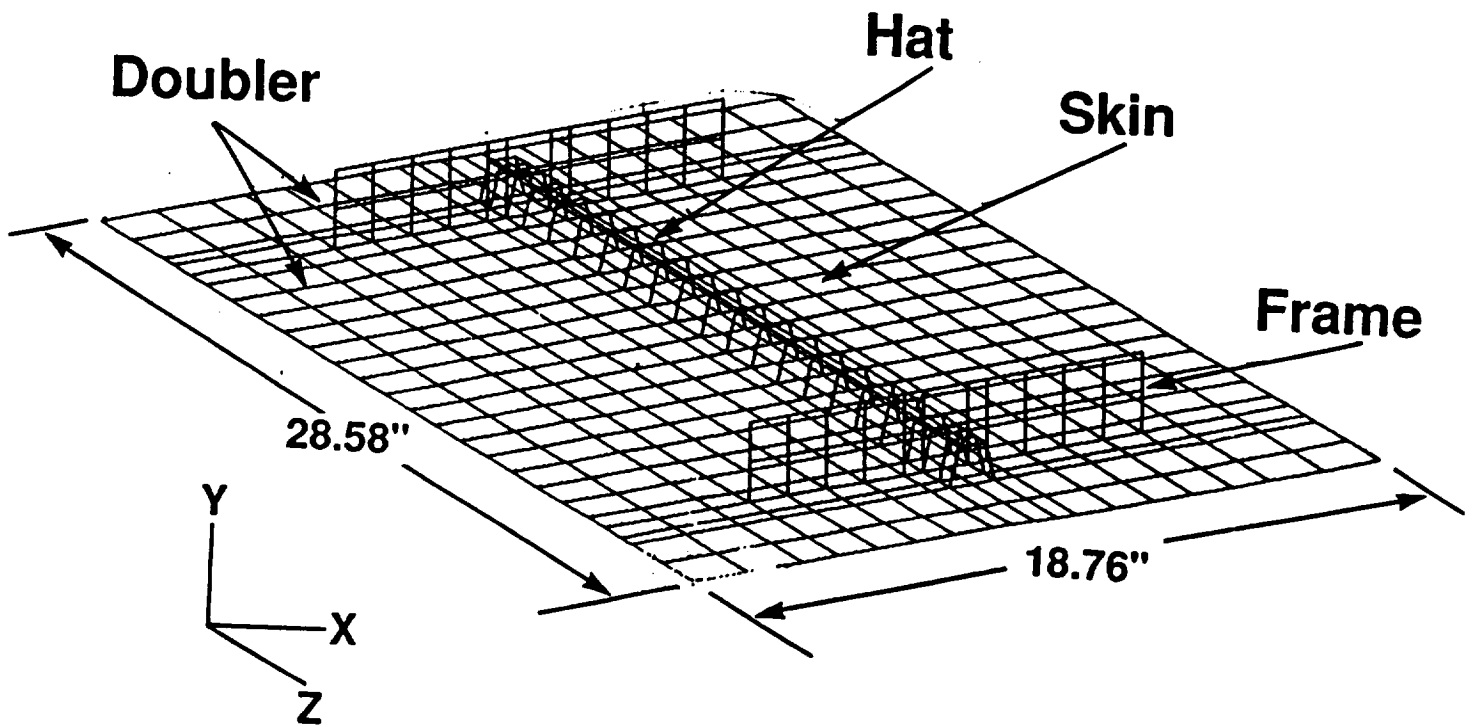


FIGURE 4.20. FINITE ELEMENT MESH FOR FRAME-STIFFENER INTERSECTION SPECIMEN

For the type of gages used (CEA-03-063UR-350) the transverse gage sensitivity is insignificant (only 1% change to the apparent strain). The percent reinforcement effect however, for the materials and layups used, ranges from 0.6% to 15.8% (depending on the gage installation such as back-to-back or single face, laminate thickness, and open face versus encapsulated gage configuration). The results reported below have this correction included wherever it is considered significant (more than 5%).

The strain gage locations (total of 18 rosettes) were chosen to give a detailed strain distribution throughout the specimen and in particular at skin bays and near the frame-stiffener intersections (see Figure 4.32). Finite element predicted surface strains are compared to test results at various panel locations and load levels in Figures 4.21 through 4.24. The locations are: (1) Hat Stiffener Center (Figure 4.21), (2) Frame-Stiffener Intersection Corner (Figure 4.22), (3) Bay Quarter Point (Figure 4.23), and (4) Bay Center (Figure 4.24). At low applied loads (except for the frame-stiffener intersection location) and high loads close to the failure load (in all cases) the finite element predictions are in very good agreement with the experimental results. At intermediate loads the correlation ranges from poor (bay center and frame stiffener intersection corner) to excellent (hat stiffener center and bay quarter point).

The shadow moire method was used to monitor the out-of-plane displacements of the panel during the test. The first moire fringe pattern appeared at an applied load of 2600 lbs and is shown in Figure 4.25. The postbuckling mode shape just before the panel failure load of 20000 lbs is shown in Figure 4.26.

Using the moire fringe patterns, the out-of-plane deflections of the skin can be calculated. Typical experimental and analytical results for the out-of-plane displacement along the panel skin bay at the applied load of 16000 lbs are shown in Figure 4.27. The moire measured amplitude correlates well with the finite element prediction. However, the wavelength of the deflection mode shape is less than the finite element prediction. The discrepancy between finite elements and moire pattern data is attributed to local eccentricities of the specimen and resulting differences in load transfer.

#### **4.2.6.2 FAILURE MODE AND PREDICTION OF FRAME-STIFFENER INTERSECTION SPECIMEN**

Failures of stiffened panels occur, in general, very rapidly and consist of multiple branching cracks, stiffener pull-off, and stiffener crippling. Because of this multiplicity of events, it is very hard to determine the actual detailed failure scenario and sequence of events during post mortem examination of specimens. A lot of information can be obtained from moire interferometry but that is also limited to events that change the out-of-plane deflection of the panel.



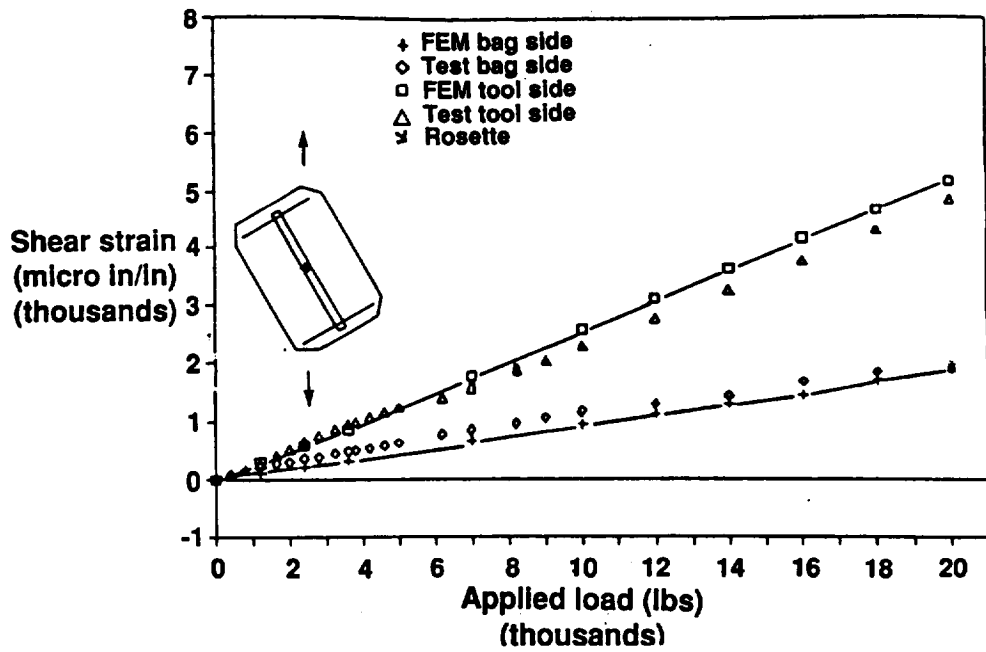


FIGURE 4.21. COMPARISON OF FINITE ELEMENT PREDICTIONS TO TEST RESULTS AT HAT STIFFENER CENTER (SHEAR STRAINS)

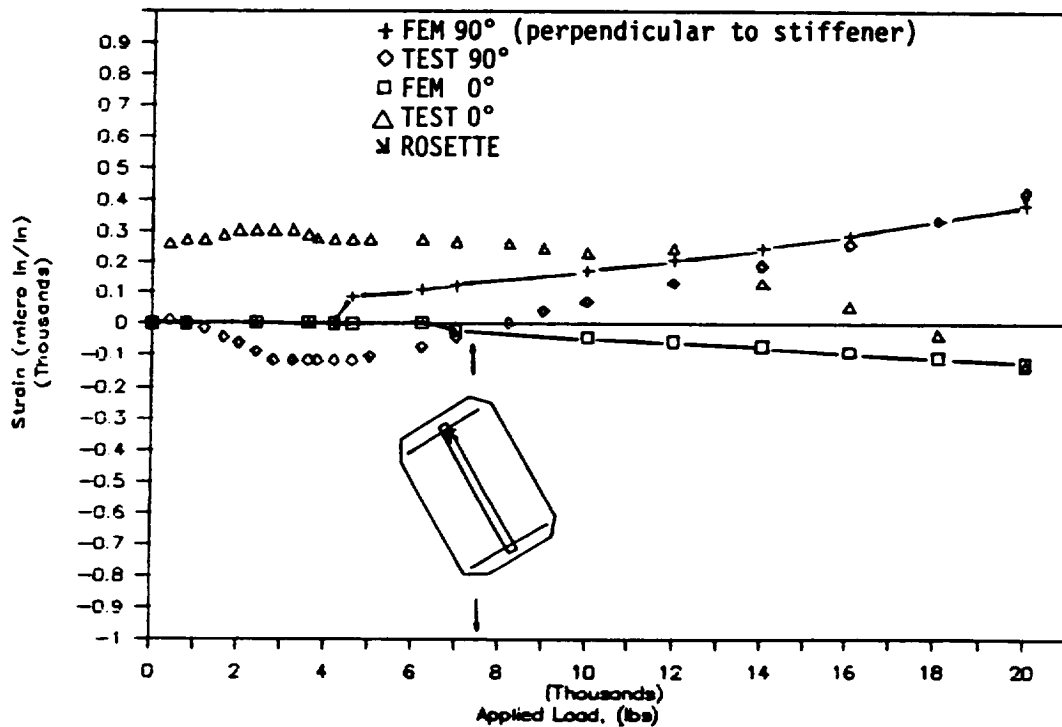


FIGURE 4.22. COMPARISON OF FINITE ELEMENT PREDICTIONS TO TEST RESULTS AT FRAME-STIFFENER INTERSECTION CORNER

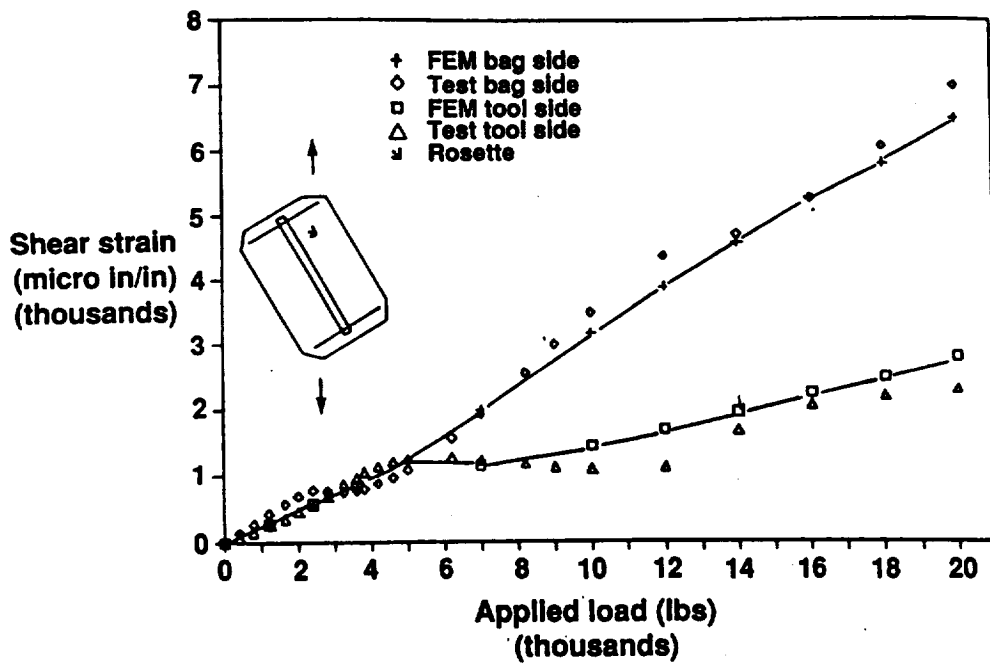


FIGURE 4.23. COMPARISON OF FINITE ELEMENT PREDICTIONS TO TEST RESULTS AT BAY QUARTER POINT (SHEAR STRAINS)

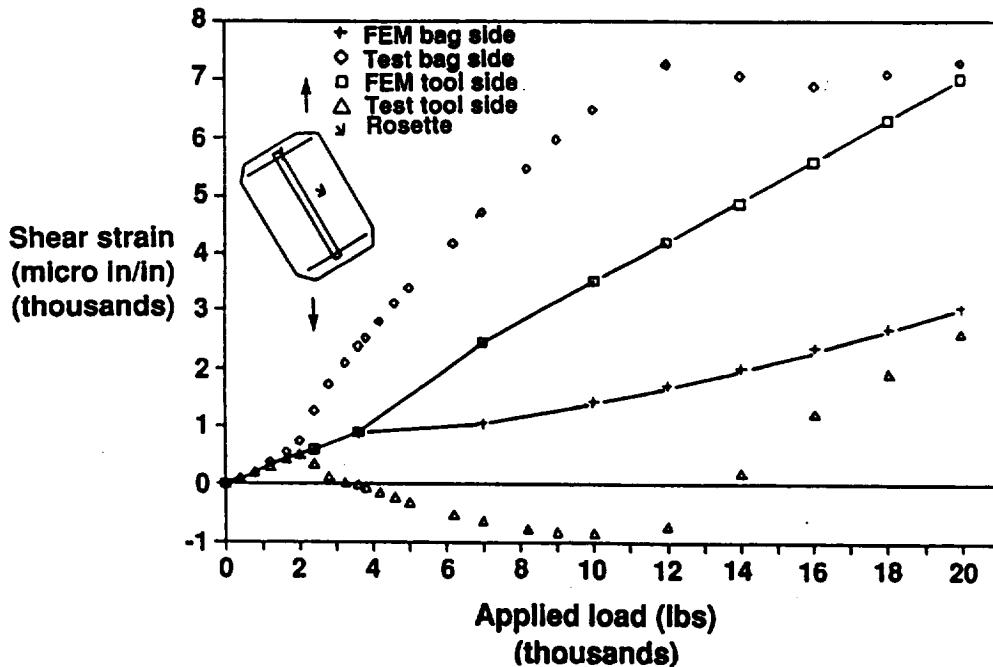


FIGURE 4.24. COMPARISON OF FINITE ELEMENT PREDICTIONS TO TEST RESULTS AT BAY CENTER (SHEAR STRAINS)



FIGURE 4.25. FIRST SHADOW MOIRE FRINGES ON FRAME-STIFFENER INTERSECTION SPECIMEN (2600 LBS OF APPLIED LOAD)



FIGURE 4.26. SHADOW MOIRE FRINGES NEAR FAILURE OF FRAME-STIFFENER INTERSECTION SPECIMEN (20000 LBS)

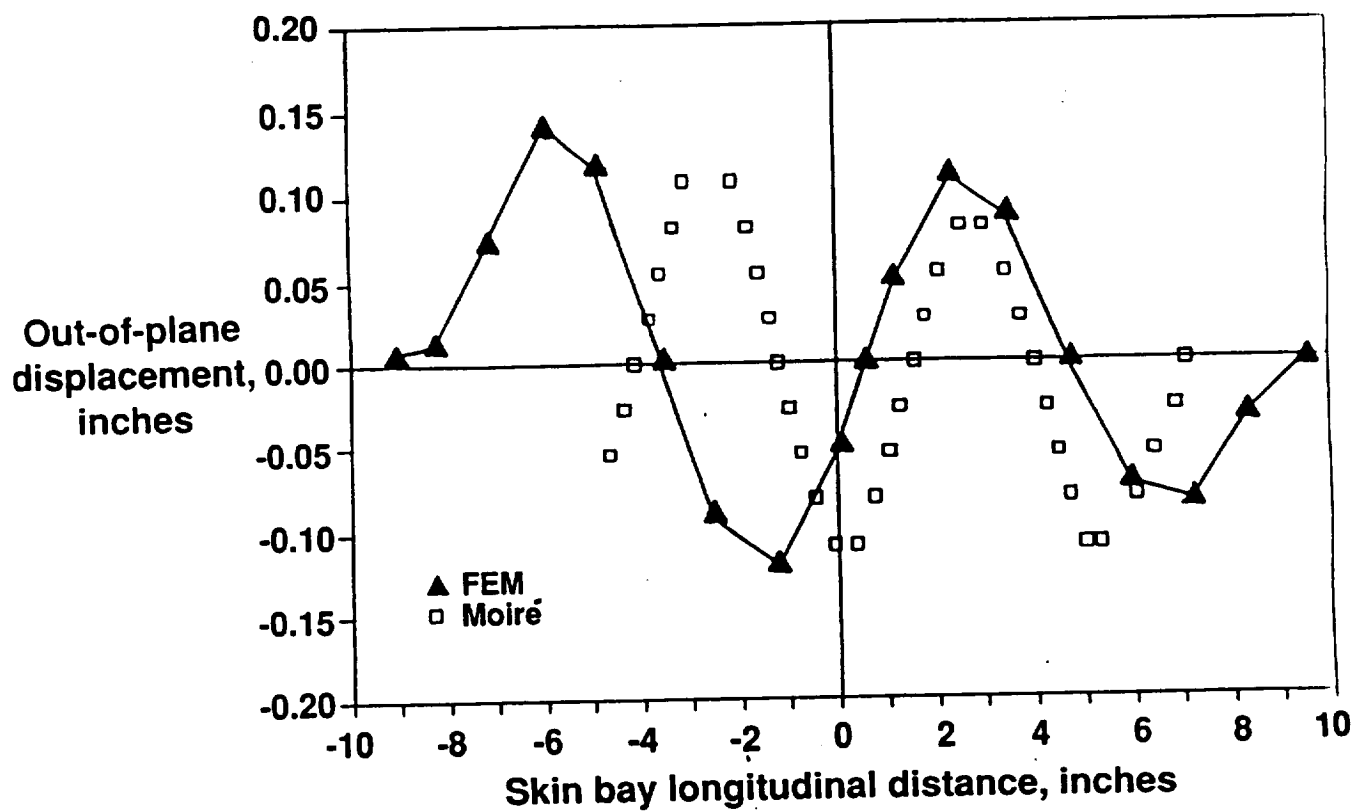


FIGURE 4.27. COMPARISON OF OUT-OF-PLANE DEFLECTION SHAPE AT BAY CENTER PARALLEL TO STIFFENER AXIS

An effort was made during the first frame-stiffener intersection specimen test to stop the test right at the beginning of final failure in order to determine which part of the panel fails first and in what failure mode. This had the additional advantage of keeping parts of the panel relatively intact thus making possible subsequent impact testing in order to determine threshold of visibility impact levels to be used on the third frame-stiffener intersection specimen that was tested in shear after impact.

For the first frame-stiffener intersection specimen the onset of failure was determined by the first significant load drop, and massive cracking noise emanating from the specimen. This happened when the applied load reached 20,000 lbs during test. The panel was then removed and inspected. Inspection revealed a crack 3.5 inches long starting at the upper bay corner next to the loaded specimen end. This is shown in Figure 4.28 along with the onset of failure location as predicted by finite elements as the element with the highest shear strain. Very good agreement between the finite element prediction and test result is observed. C-scans of the specimen showed no other defects other than the starting crack and delamination in its vicinity.

The failure mode for the second frame-stiffener intersection specimen is shown schematically in Figure 4.29. A crack is shown in the same location as for the first specimen. Massive delamination and cracking are present throughout the specimen. The failure load was 22,000 lbs (643 lb/in). Of interest is the damage on the hat web near one of the frame/stiffener intersection corners. It should be recalled that the failure mode of the crippling specimens included damage in the hat webs (see section 4.2.3).

The failure prediction for these specimens was obtained by determining the most highly loaded element in the finite element model and using the forces and moments on that element as input in a first ply failure criterion. That element coincided with the location where a crack initiated (near the bay corner) during testing.

Using mean material strength values the predicted failure load, using a stress interaction criterion [16], is 26000 lbs. The corresponding predicted B-Basis failure load was 22,950 lbs. The test failure load (average of two specimens) is 21000 lbs (614 lbs/in). The failure predictions, based on material strength values for conventionally manufactured parts, (since the building block approach to this point showed the parts had essentially properties equivalent to autoclave tooled parts) were unconservative by 9 to 24% (B-Basis versus mean allowable predictions). Two reasons are presented for the discrepancy: (1) Loading of the first test specimen was stopped when the first cracks developed (at 20000 lbs) in order to see where failure started. The load capability may have been significantly higher as is indicated by the failure load for the second specimen (22000 lbs). Thus, the average test failure load of 21000 lbs may be conservative. (2) Based on post-test visual examination and comparison to moire fringe data, final failure was determined not to result from corner cracking (which was observed in all specimens) but rather from high local strains in the vicinity of the root of the hat stiffener (near the frame/stiffener intersection) due to the buckled shape. This is verified by the shadow moire fringes (Figure 4.26),

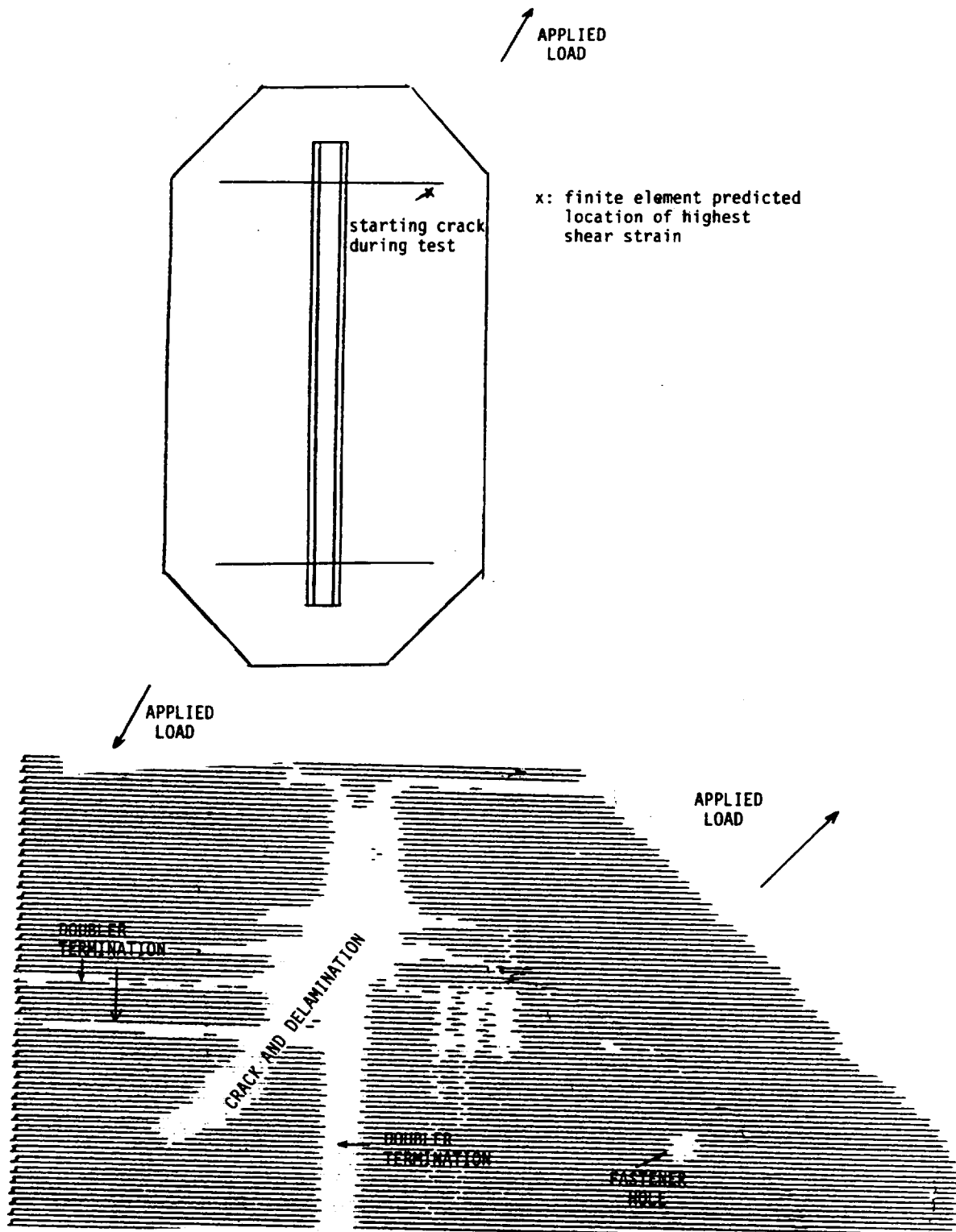


FIGURE 4.28. ONSET OF FAILURE LOCATION - FINITE ELEMENTS VERSUS TEST

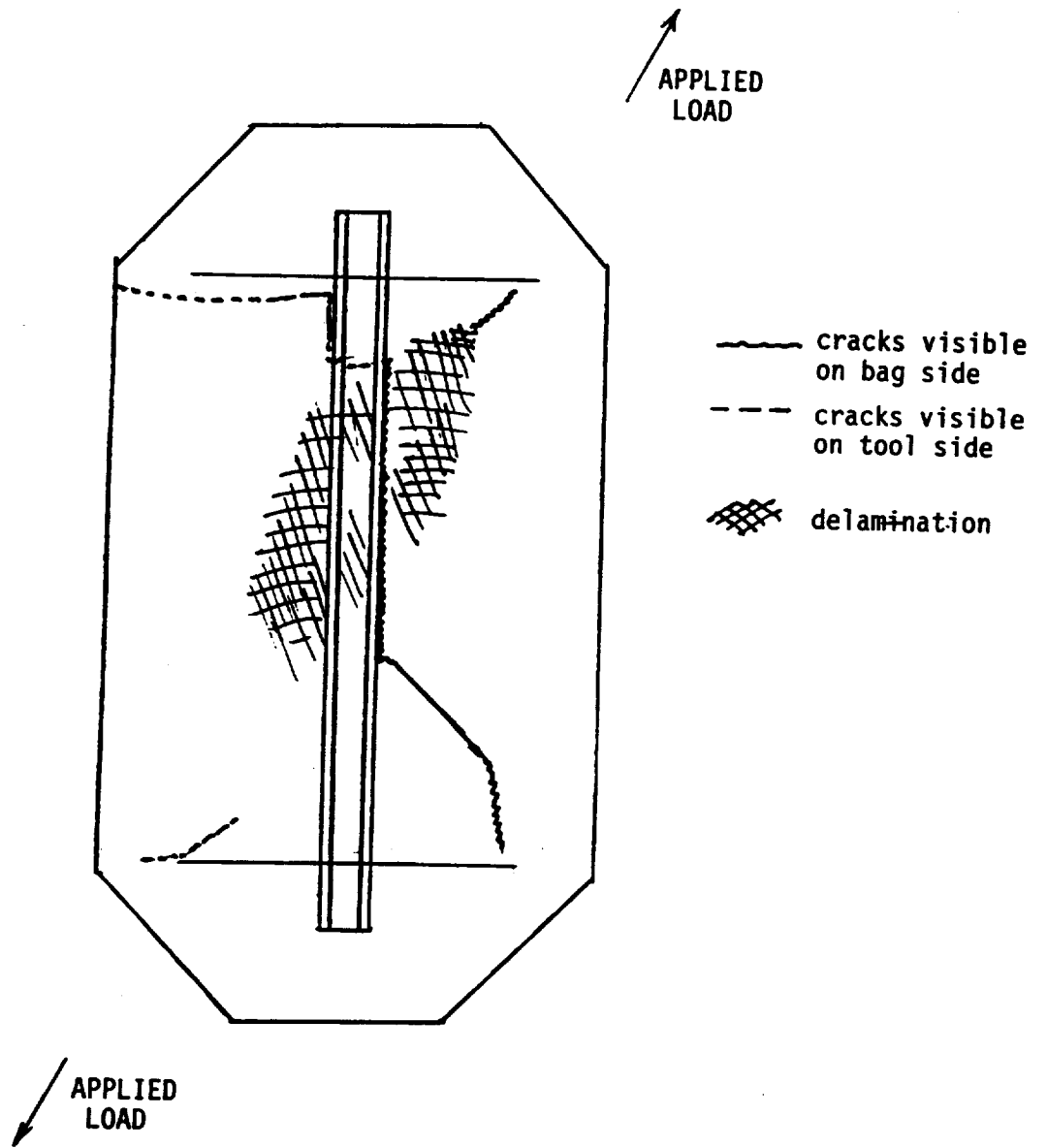


FIGURE 4.29. SCHEMATIC FAILURE MODE OF FRAME-STIFFENER INTERSECTION SPECIMEN



which do not cross the centerline of the specimen but stop where the stiffener webs meet the skin. The fringes, which indicate out-of-plane deflection, tend to come close together in the vicinity of the stiffener. This implies a large displacement gradient was present in this area and the associated high bending moments precipitated final failure. The existence and location of this high strain area was confirmed by the finite element analysis. However, the mesh density was not high enough to permit accurate failure prediction at this location.

The damage present in the hat stiffener webs should also be noted. It is unclear from examining the failed specimens whether it initiated failure or it is a secondary failure precipitated by the large rotations of the hat stiffener once the skin near the stiffener-frame corner failed.

#### 4.2.6.3 DAMAGE TOLERANCE OF FRAME-STIFFENER INTERSECTION SPECIMENS

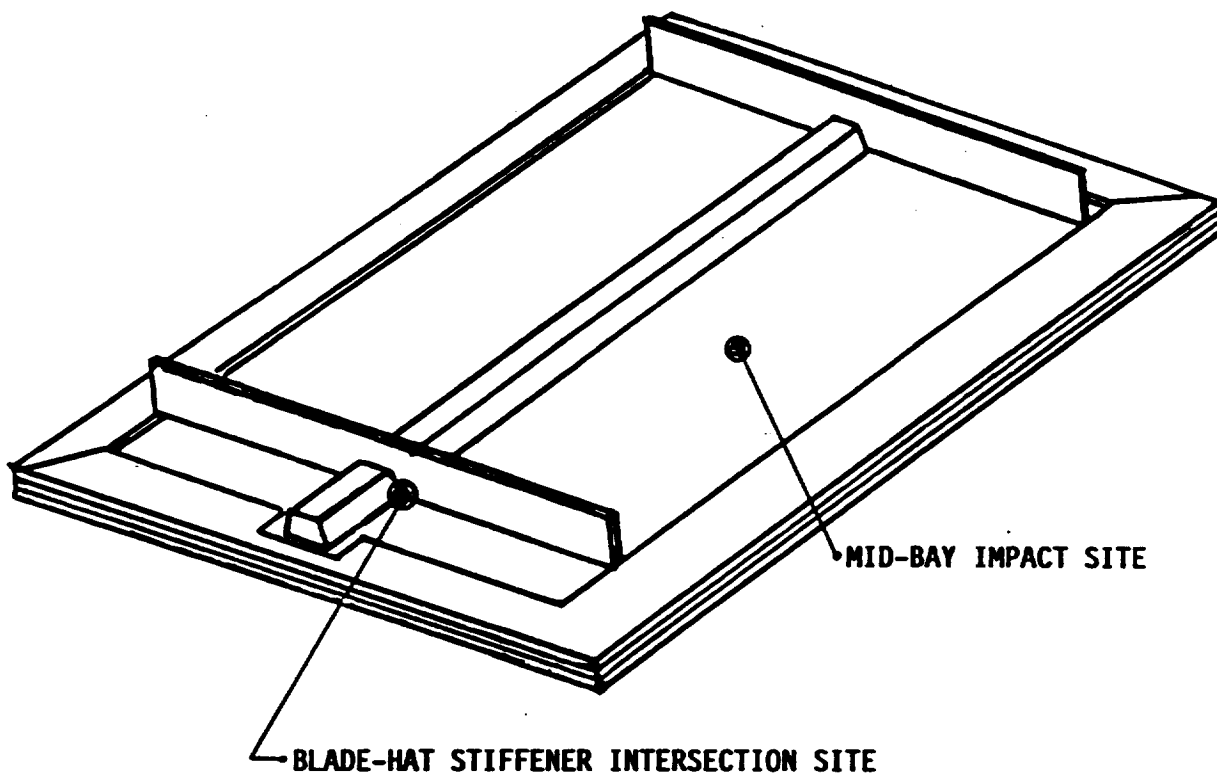
The third Frame-Stiffener Intersection Specimen was used to obtain information on the damage tolerance capabilities of the configuration and manufacturing process. Two sites were selected for impact. The first was at the center of a bay and the second was at a frame-stiffener intersection, at the point where the hat stiffener web intersects the skin and the frame.

Impact energy levels (using a drop weight impactor), sufficient to produce "Threshold of Visibility" (TOV) damage at the two locations shown in Figure 4.30, were determined by incrementally varying impact energy from levels producing damage clearly below to levels producing damage clearly above the threshold of visibility. Consistent with Sikorsky Aircraft experience with large scale structures, TOV damage was defined as barely discernible damage when inspected with the unaided eye from a distance of five feet [17].

The first frame/stiffener intersection specimen, which had been tested previously, was used to establish an impact energy-TOV correlation. Prior to impact, an ultrasonic C-scan of this specimen revealed only localized internal damage resulting from the initial static test, (Figure 4.28). Since this damage was far from the present locations of interest, it was judged not to affect the incremental impact energy tests subsequently performed.

Impact damage was generated using a 5.33 lb cylindrical weight with a 0.5" diameter hemispherical striking tip dropped from different heights to produce specific impact energies. During the impact events the specimen was supported along its edges in the picture frame shear fixture used for static tests. Since the specimen was attached to the picture frame using through-bolts and two 0.5" thick aluminum plates around all edges, the support conditions were assumed to be clamped.

Impact tests at the frame/hat stiffener intersection were conducted at 15 and 16 ft-lbs impact energy. Internal damage identified by C-scan is shown in Figure 4.31. The internal damage is almost completely obscured by the hollow hat



**Note: Impact damage delivered to unstiffened side of specimen**

**FIGURE 4.30. TWO IMPACT LOCATIONS FOR THE FRAME-STIFFENER INTERSECTION SPECIMEN NO. 3**

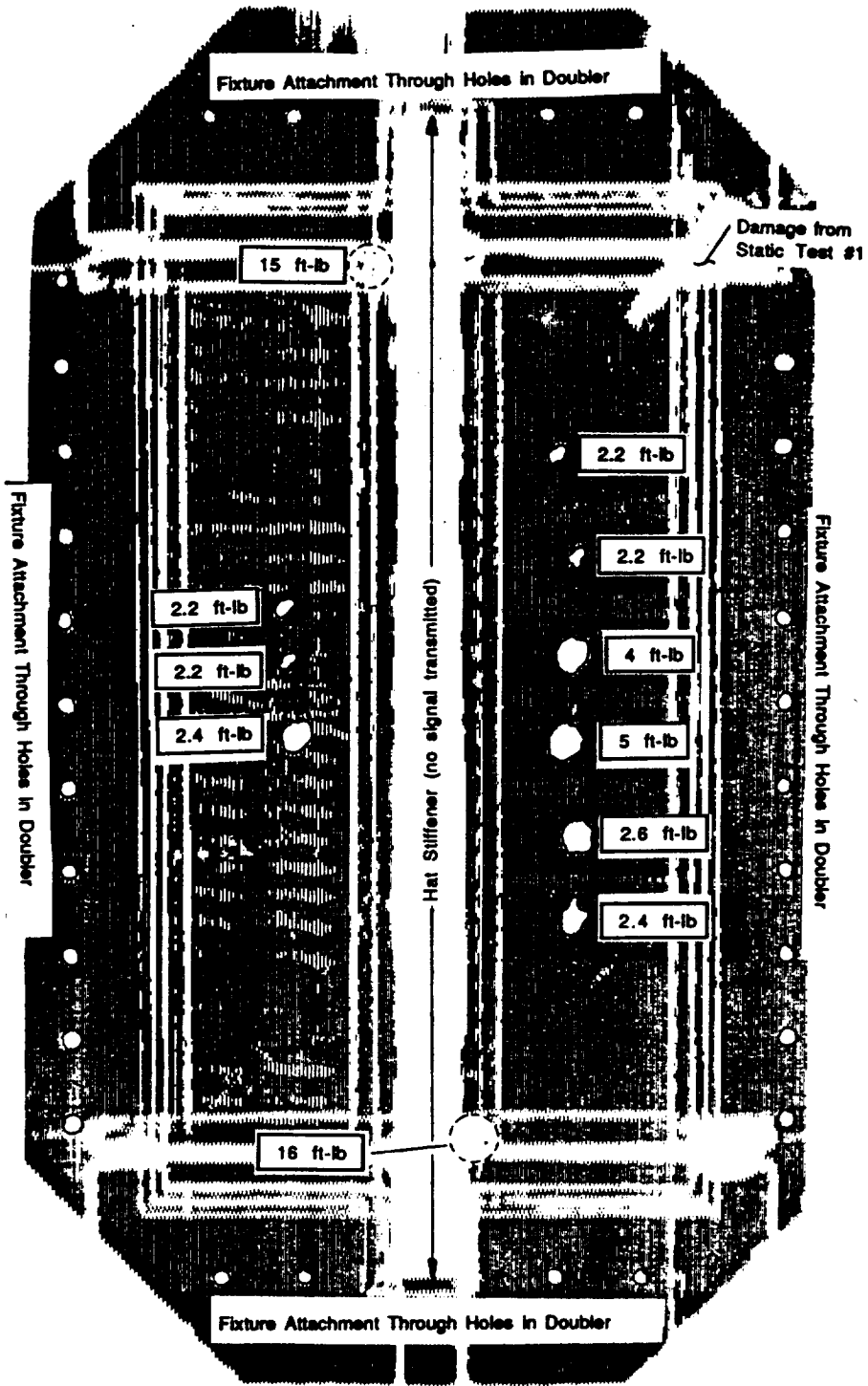


FIGURE 4.31. INTERNAL DAMAGE PRODUCED BY VARYING LEVELS OF IMPACT ENERGY

stiffener and frame intersection, but its extent is suggested by the hashed circles. A summary of the measured indentation at the point of impact is provided in Table 4.9. Based on visual evaluation of damage caused at various energy levels, 15 ft-lb was selected as the TOV damage level.

Table 4.9  
Damage Measurements at Impact Locations

Impact Energy (ft-lb)	Indentation at Point of Impact (in)	Damage Area from C-Scan (square inches)	Part Thickness at Point of Impact (inches)
<b>Frame/Stiffener Intersection</b>			
15	0.038	---*	---*
16	0.045	---*	---*
<b>Bay Center</b>			
5.0	Penetration	0.20	0.03
4.0	Penetration	0.20	0.03
2.6	0.051	0.17	0.03
2.4+	0.037	0.13	0.03
2.2++	<0.005	0.05	0.03

- \* Total damage area obscured by part geometry
- + Average of two impact sites
- ++ Average of four impact sites

Mid-bay impact test results are shown in Figure 4.31 and Table 4.9. Interestingly, 2.2 ft-lb impacts cause indentations estimated to be less than 0.005 inches deep while still producing measurable internal damage averaging 0.05 square inches. The internal damage is approximately equal to a circular flaw of 0.25 inches diameter. The "Threshold of Visibility" damage level was selected to be 2.4 ft-lb.

The TOV damage levels identified for this specimen, summarized by indentation measured at the point of impact, were noted to be in good agreement with Sikorsky Aircraft experience when applied to impact damage in thin laminates [17]. Since the composite parts in reference 17 were manufactured using conventional fabrication procedures, this similarity suggests that parts made with the THERM-X® process exhibit similar damage resistance (where damage resistance is defined as the ability of a part to withstand or contain damage).

The last building block test specimen, Frame/Stiffener Intersection No. 3, was C-scanned and the quality of the panel was judged to be very good with no ultrasonic indications recorded.

"Threshold of Visibility" damage (15 ft-lb) was inflicted on the unstiffened side of the specimen at the point of intersection of the hat stiffener web with the frame using the same impactor weight, tip diameter, and support conditions discussed earlier. Indentation measured at the point of impact was 0.040". The specimen was inspected using pulse echo ultrasonic techniques to determine the extent of internal damage due to impact. The specimen was instrumented with 18 strain gage rosettes (Figure 4.32) and tested to the design limit load (167 lb/in edge shear flow). No audible acoustic emissions were noted. The specimen was unloaded, removed from the fixture, and pulse-echo inspected. Pulse-echo inspection indicated that no damage growth resulted from the limit load test.

After the last inspection, the specimen was reinstalled in the picture frame fixture and impacted at Location B of Figure 4.33 with 2.4 ft-lb of impact energy. Indentation at the point of impact was measured to be 0.042". Pulse-echo inspection revealed a circular damage area of 0.15 square inches, or 0.437 inches in diameter. C-scans could not be taken at this stage due to the presence of the 54 strain gage wires which blocked the ultrasound signal. The specimen was tested statically to a failure load of 19000 pounds (557 lb/in edge shear). This result, when compared to the undamaged specimen average ultimate load (644 lb/in edge shear), represented a 14% reduction in failure load. The failure mode observed in the damaged specimen test was identical to that observed for undamaged specimens. Close visual monitoring of both impact sites during the ultimate test indicated the damage had no readily apparent influence on failure load. The path of final failure did not initiate at or pass through impact damage at the frame/stiffener intersection, but did propagate through the mid-bay damage site upon final failure. There were no indications failure initiated at the mid-bay impact point.

To predict this failure, direct application of thick specimen Shear-After-Impact strength results (see section 4.2.4) to the mid-bay impact site was done. Since the frame/stiffener intersection impact did not contribute to the failure in any marked manner, it was neglected. Using the internal damage area for the Threshold of Visibility damage level documented in Table 2.1 (0.13 square inches), in conjunction with Figure 4.34 below, the estimated strength reduction is less than 2%. Indentation at the point of mid-bay impact can be utilized in much the same way, see Figure 4.35. Estimated shear strength reduction due to a 0.042" indentation is approximately 25%. When compared to the observed 14% strength reduction, it is judged that indentation at the point of impact produces a more accurate prediction than that of internal damage area.

#### **4.2.6.4 CONCLUSIONS FROM FRAME-STIFFENER INTERSECTION TESTS AND ANALYSIS**

The intersection corner with the shear tie performed very well and did not fail during the test. The embedded flange concept performed very well since no frames or stiffeners separated from the skin during the test. Failure occurred at a postbuckling factor of almost 6. This gives confidence in the design of the full-scale article and in the large postbuckling capability of composite stiffened structure under shear loads. Failure starts at the specimen corner

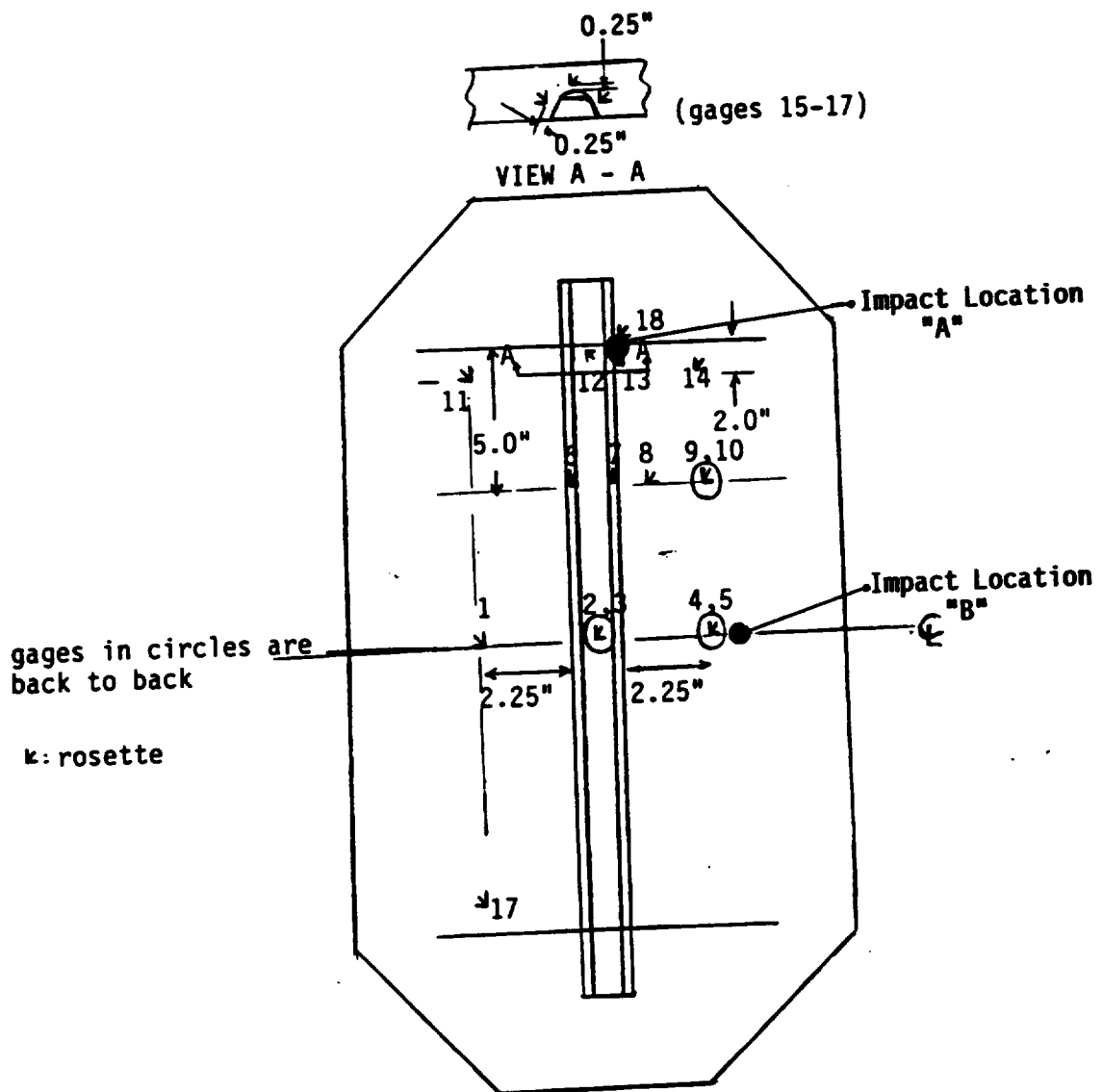


FIGURE 4.32. IMPACT DAMAGED SPECIMEN STRAIN GAGE LOCATIONS

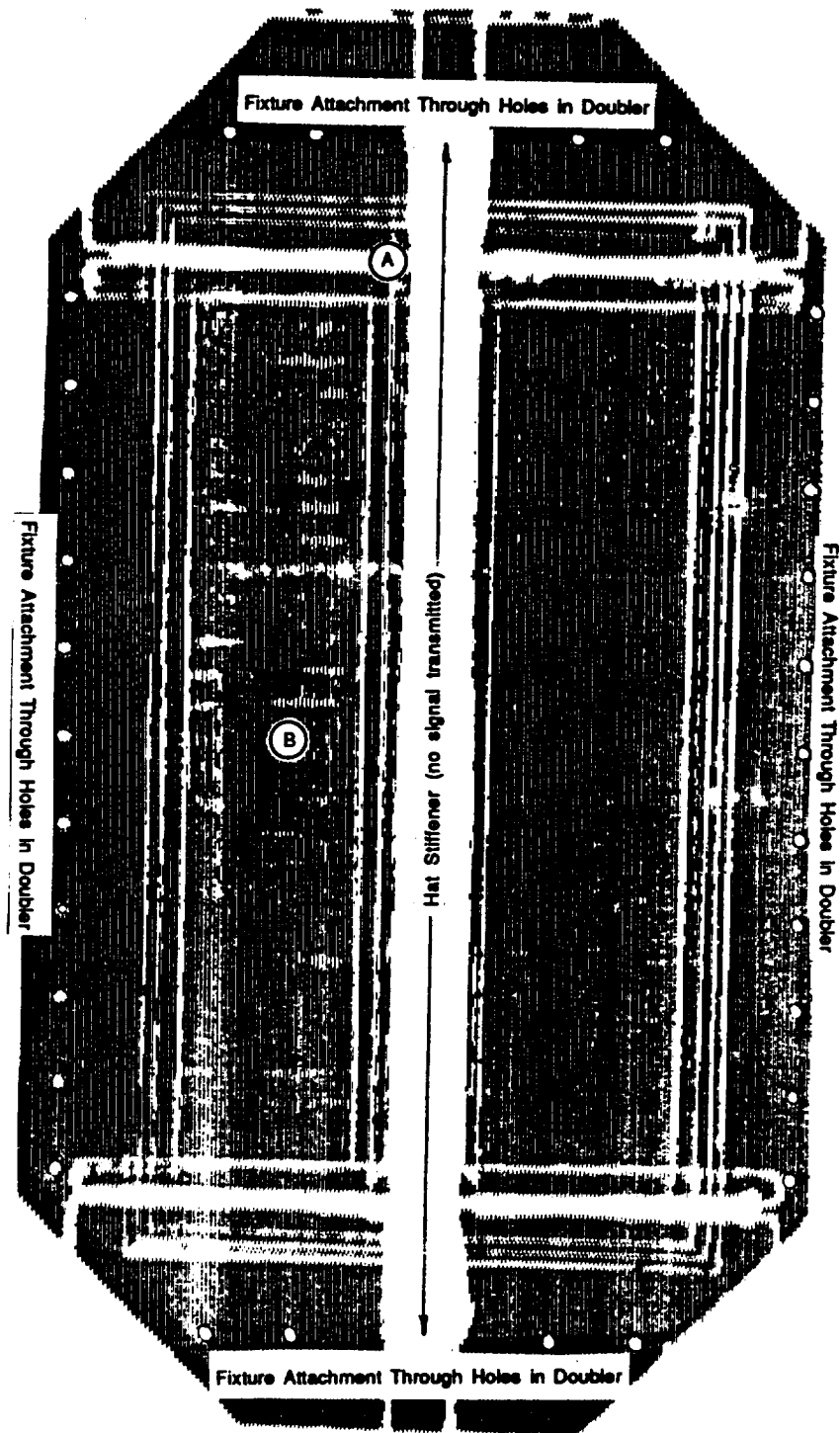


FIGURE 4.33. IMPACT SITES ON FRAME-STIFFENER INTERSECTION SPECIMEN NO. 3

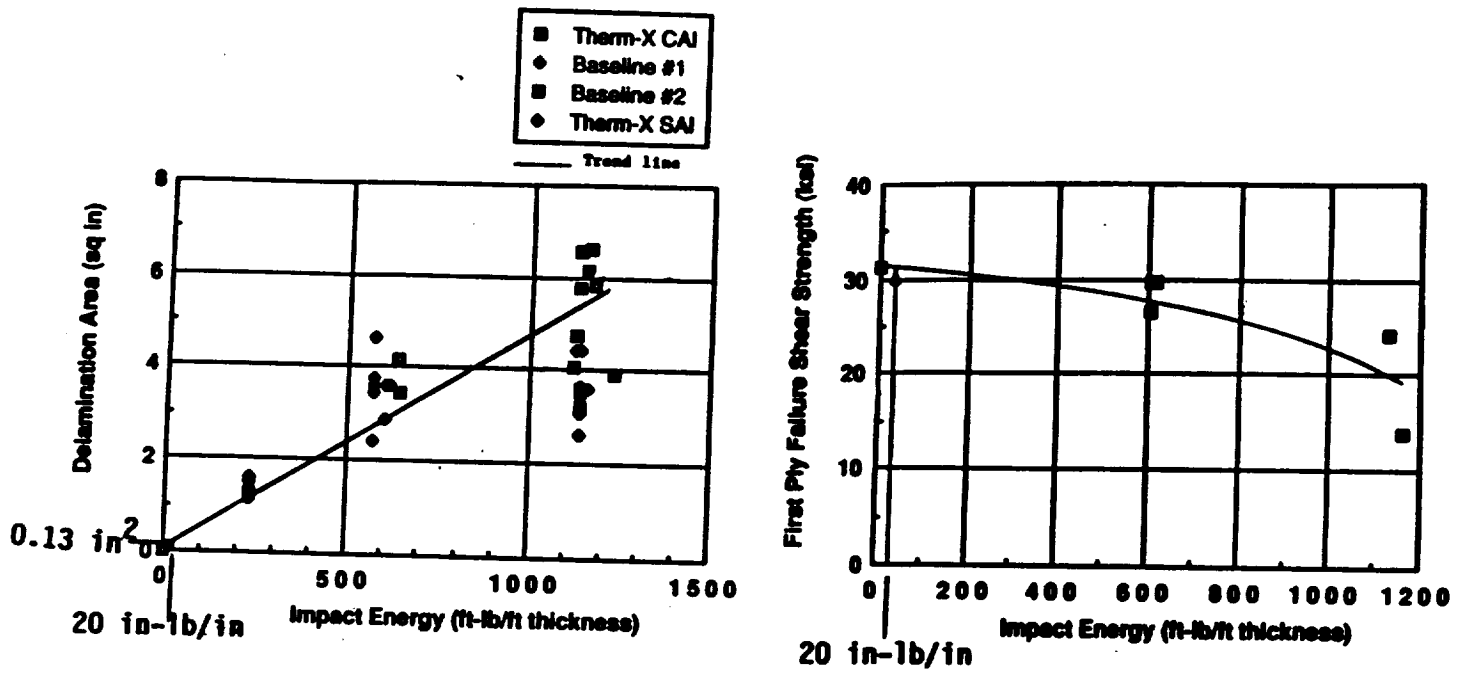


FIGURE 4.34. DELAMINATION AREA PREDICTION OF RESIDUAL SHEAR STRENGTH

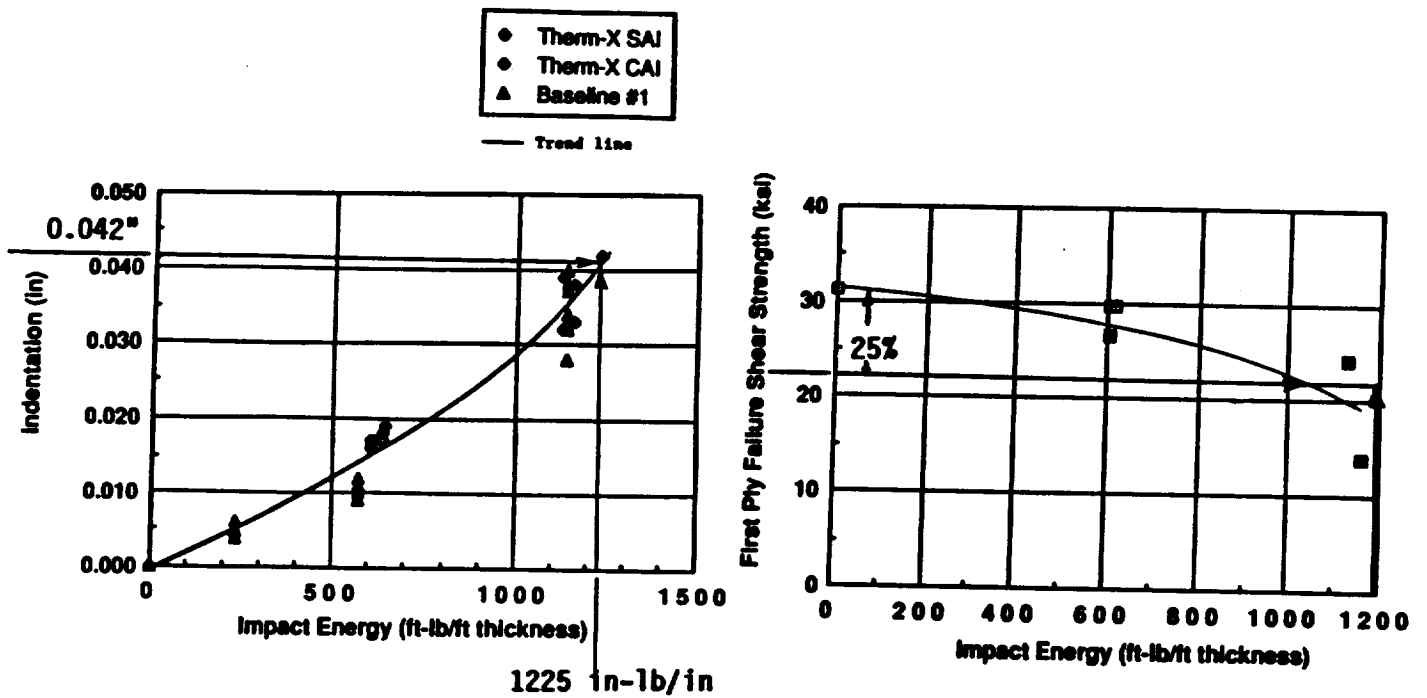


FIGURE 4.35. INDENTATION PREDICTION OF RESIDUAL SHEAR STRENGTH



but once the pinching stresses are relieved, the specimen can withstand significantly higher load until the skin and hat webs near the frame-stiffener intersection corner fail. Massive delamination was evident in the failed specimen. The shear after impact strength of the specimens is 14% lower than the undamaged strength. This is a smaller knockdown than with compression loading and is in agreement with the findings of section 4.2.4 on thicker specimens.

The finite element strain predictions are in good agreement with the experimental results for loads up to buckling and loads beyond three times the buckling load; predicted strains at failure are less than 5% off the experimentally measured values. Failure predictions based on finite elements are somewhat unconservative (26000 lb mean, 22950 lb B-Basis versus 21000 lbs from test results). For damaged specimens, failure predictions can be based on indentation depth cross-correlated to residual strength. They are more accurate than predictions based on damage area but still about 11% off.

#### 4.3 SUMMARY OF LABOR HOURS NEEDED FOR SPECIMENS MADE WITH THE THERM-X PROCESS

The labor hour content of the specimens used in the building block evaluation are given in Table 4.10. Tooling hours are included for the frame stiffener intersection specimen since it was the only one that required significant tooling to manufacture the steps for the doublers on the aluminum plate that served as the tool bottom, to machine the two cross members that served as the locators and supports for the two frames and to fabricate the aluminum walls of the tool box into which the pressure medium was poured.

Table 4.10  
Labor Hours Required to Manufacture Building Block Specimens

Task	±45 Coupons	Skin-Stiff'nr Separation	Stiffener Crippling	CAI & SAI	Skin Tearing	Inter-sectn
(No of specim.)	(8)	(5)	(6)	(15)	(8)	(3)
Tooling	0.3	0.3	0.3	0.3	0.3	45.0
Cut Material	4.0	6.0	8.0	8.0	1.5	87.5
Layup and Bag	1.0	3.0	3.5	2.0	1.0	207.5
Strip and Trim	1.0	4.0	1.5	2.0	1.0	40.5
Cut Specimens and Pot	3.5	29.0	5.0	10.5	3.5	0.0
Totals	9.8	42.3	18.3	22.8	7.3	380.5

## 4.4 CONCLUSIONS FROM BUILDING BLOCK EVALUATION

### 4.4.1 FLAT PARTS

As the  $\pm 45$  coupon and skin tearing tests showed, the THERM-X<sup>®</sup> process is very successful in making flat parts. Micrographs and section cuts revealed excellent consolidation. Chemical tests showed very low void contents well within the Sikorsky acceptance requirements. Mechanical tests showed strength and stiffness values comparable, if not slightly higher, than those obtained from specimens made with conventional layup. Data scatter was very low indicating specimen uniformity. Thus, at this level of complexity, THERM-X<sup>®</sup> processing is equivalent to conventional manufacturing methods. The shear and tension strength values obtained from these tests could be used to predict skin failure in the postbuckling regime during testing of the full-scale article.

### 4.4.2 COMPLEX CO-CURED PARTS

The results of the stiffener crippling and skin/stiffener separation tests showed that the specimens performed very satisfactorily. It is felt that the specimen design was successful in isolating the failure modes of interest and accurately depicting failure progress. Strain gage plots (see Figure 4.36) for the crippling specimen for example, show very uniform loading of the angled webs of the hat stiffener (gages 2 and 7 are very close to one another) up to failure. The failure values for the crippling specimens compare well with analysis predictions made assuming THERM-X processed parts to have the same structural properties as autoclave tooled parts. This validates the assumption made in the analysis that parts made with the THERM-X<sup>®</sup> process have the same compression stiffness and strength as parts made with conventional manufacturing methods.

Wrinkles and increased voids found in the crippling and separation specimens were traced to the bagging procedure which was altered for the the frame-stiffener intersection and the full-scale panel. These modifications are discussed in section 4.4.5.

The frame-stiffener intersection specimens showed excellent quality in particular around the intersection corners where the skin, hat stiffener and frames meet. The radii were well defined with no wrinkles or resin rich or poor regions. This suggested that the THERM-X<sup>®</sup> process would be very successful in fabricating the full-scale panel with minimum tooling at the intersection corners. This reduced tooling and ensuing savings in tooling fabrication and vacuum bagging time became evident in the full scale panel.

The Frame-Stiffener Intersection specimen tested in shear after impact showed only moderate strength reduction due to impact damage. This implied that the full-scale panel should be quite damage tolerant under repeated shear loading (see Section 5 on fatigue of the full-scale panel).

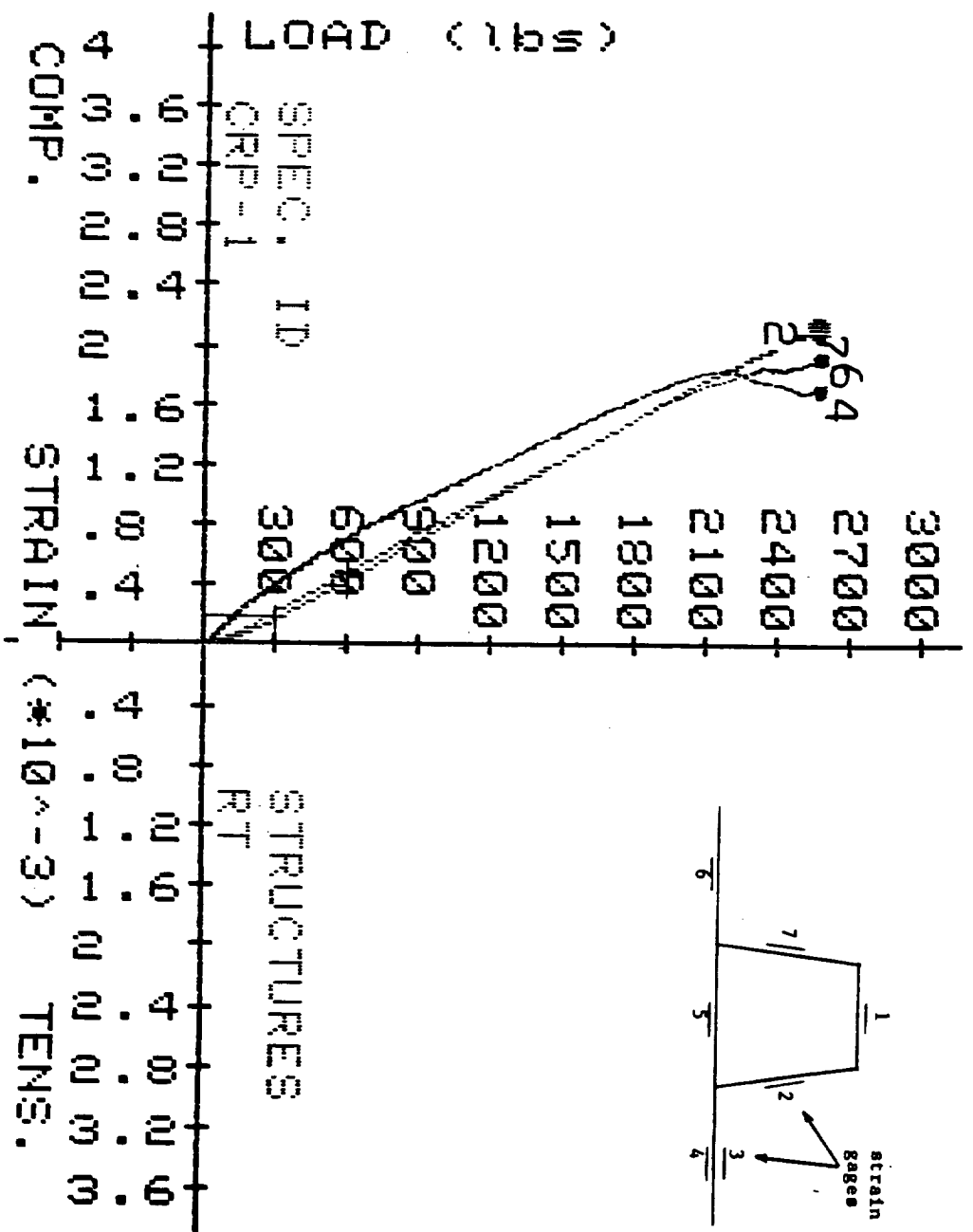


FIGURE 4.36. STRAIN GAGE PLOTS FOR CRIPPLING SPECIMEN CRP-1

### **4.4.3 EFFECTIVENESS OF THE EMBEDDED FLANGE**

The Crippling, Skin/Stiffener Separation, and Frame/Stiffener Intersection specimens used the embedded flange concept where one of the skin plies is used to cover the stiffener and frame flanges as illustrated in Figure 4.37. The failure modes and loads observed in these specimens showed that the flange/skin interface is no longer the weakest link of such configurations. In particular, the skin/stiffener separation failure loads are approximately three times higher than the pull-off loads obtained with specimens with no embedded flanges in other Sikorsky programs.

This increase in strength results from the fact that the high stress location shifts from the edge of the flange to the root of the flange when the flange is embedded in the skin (Figure 4.38). The radius at the flange root reduces the stress concentration and the peak stresses are not as high as at the flange edge when the flange is not embedded. This increases the out-of-plane load carrying capacity of the configuration.

It is felt that this increased strength justifies the small increase in manufacturing cost associated with cutting the top skin plies to fit in each of the bays of the panel. The embedded flange was, as a result, used extensively in the full-scale test article and permitted high postbuckling ratios that otherwise would have been limited by peeling off of the stiffeners and/or frames from the skin during testing as was the case in cocured configurations without the embedded flange [18].

### **4.4.4 EFFECTIVENESS OF THE SHEAR TIE**

The failure modes of the Frame-Stiffener Intersection with and without impact damage showed no damage of the frame-stiffener intersection. The shear tie connecting the frames with the stiffeners was intact indicating uninterrupted load transfer between the two members all the way through the failure load. This gave confidence in the shear tie design and suggested that the failure mode for the full scale panel should not involve the shear tie and the intersection corner.

### **4.4.5 WRINKLES AND VOIDS AT RADIUS REGIONS**

The Stiffener Crippling and Skin-Stiffener Separation specimens showed some voids and wrinkles in the vicinity of corners (see sections 4.2.2 and 4.2.3). This problem was traced to the use of FEP stretchable sheet to separate the part to be cured from the pressure medium (see Figure 4.39). By splicing and overlapping this sheet, the problem was eliminated in the Frame-Stiffener Intersection and Full-Scale specimens. Further, concerns about interaction of the pressure medium with the part are no longer an issue and in future programs the FEP sheet will not be necessary. It is important to note that this splicing (Figure 4.39b) would not be possible with conventional vacuum bagging and is an advantage of the THERM-X® process. In addition to splicing, tape material was inserted at the stiffener corners where the webs intersected the skin to avoid the creation of voids.

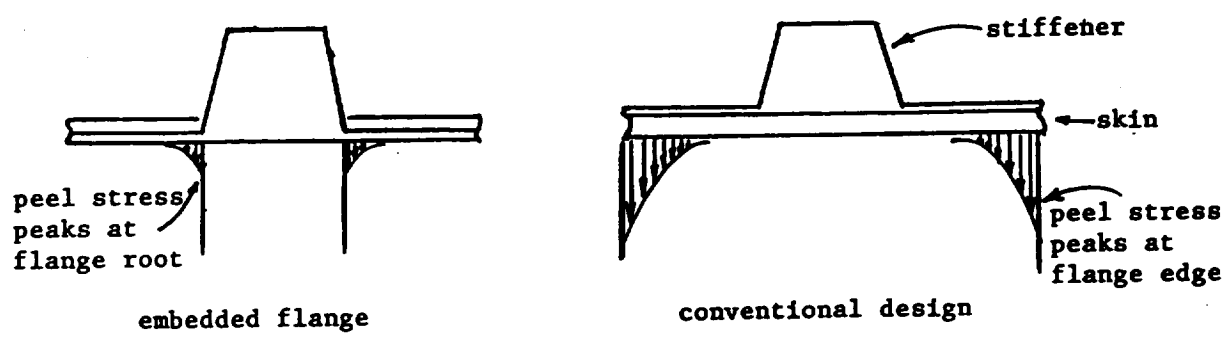
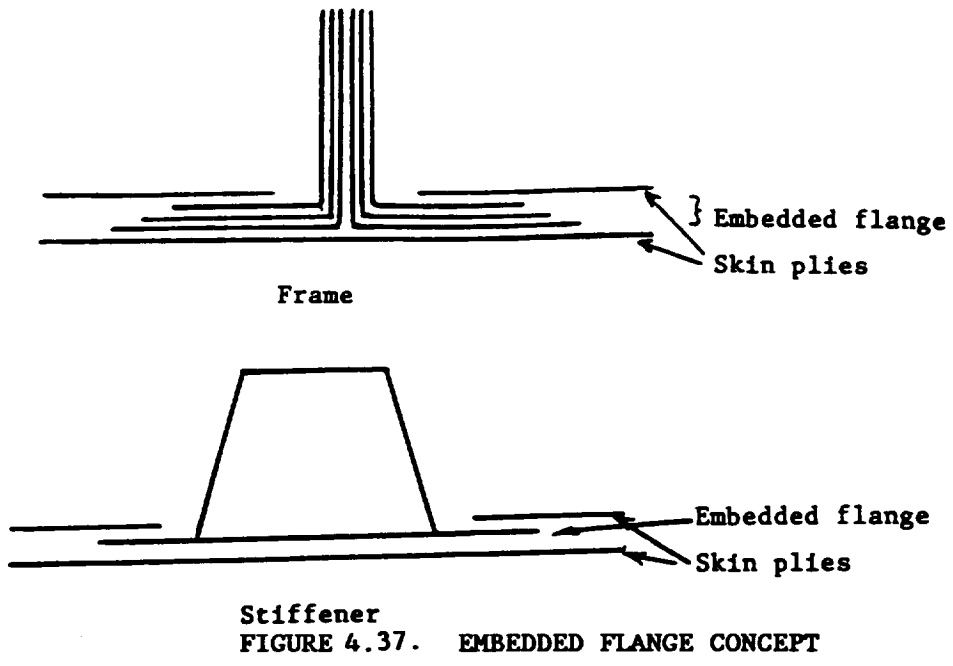


FIGURE 4.38. STRESS CONCENTRATIONS FOR EMBEDDED AND NON-EMBEDDED FLANGE DESIGNS

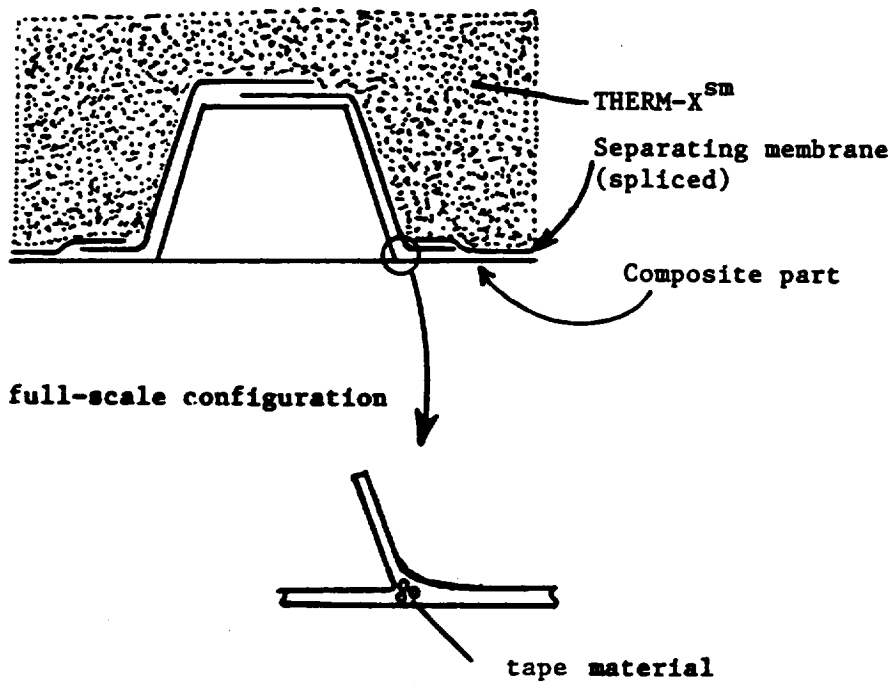
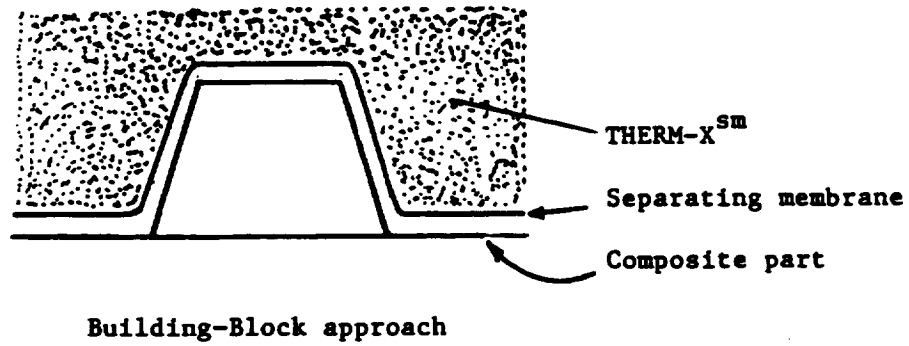


FIGURE 4.39. SEPARATION OF PRESSURE MEDIUM FROM PART TO BE CURED

## 5.0 FULL-SCALE PANEL

The full-scale panel is shown in Figure 5.1. The building block tests and the portions of the full-scale panel they represent are also shown. A detailed drawing of the full-scale panel is given in the Appendix. The full-scale panel configuration was the one resulting from the optimization method of Section 3.

The optimization method defined the skin thickness (about 0.03 inches) the frame and stiffener spacing (20 inches and 6.5 inches respectively) and the ratios  $A_s/d_s$  and  $A_f/d_f$  where  $A_s$  and  $A_f$  are stiffener and frame cross sectional areas for the stiffener and frame respectively and  $d_s$  and  $d_f$  are stiffener and frame spacings. The cross sections selected for the frames and stiffeners were such that the  $A_s/d_s$  and  $A_f/d_f$  ratios of the optimization process were matched and the bending stiffnesses were close to the bending stiffnesses of the rectangular configurations assumed in the optimization program. Hat stiffeners and inverted "tees" (blades) were used.

A concurrent engineering approach was used for the design, fabrication, testing and analysis of the full-scale panel. Representatives of all groups involved, design, analysis, testing, fabrication, tooling, weights, and cost accounting met at the beginning of the program and at regular update intervals to discuss and evaluate options, alternative configurations and approaches and anticipate problems with the manufacture, testing, and analysis of the full-scale panel.

### 5.1 TOOLING

Several options were considered for the main tool. The simplest and least labor intensive would be an aluminum sheet rolled at the required radius of curvature (40 inches) and supported by a truss-like structure. This concept presented problems since, under autoclave pressure, the deflection of the tool in some locations would be unacceptable unless the supporting structure was made very rigid and the supports were closely spaced. The tooling cost would then be similar to machining a solid block of aluminum to the desired radius. Such a configuration would have no curvature change during curing caused by autoclave pressure. To minimize the impact of machining errors, it was decided to machine 3 inch wide aluminum blocks and then match them together to form the tool for the 30 inch by 30 inch specimen. Issues that received special consideration were surface smoothness and the elimination of gaps between matched tool parts. The tool resulting from this process (shown in Figure 5.2) performed very well and was used to manufacture one tool proof skin (no stiffeners) and all four full-scale parts without any problems or needed modifications.

No tooling was necessary for the hat stiffeners other than inner mandrels machined out of solid Teflon (shown in Figure 5.2). To facilitate removal of the Teflon mandrels, thin aluminum strips covered with porous Teflon were installed at the bottom of the Teflon mandrels. They helped keep the Teflon mandrels from creating a pool of resin around their base thus trapping it in the stiffeners and provided an additional heat source at the hat stiffener base.

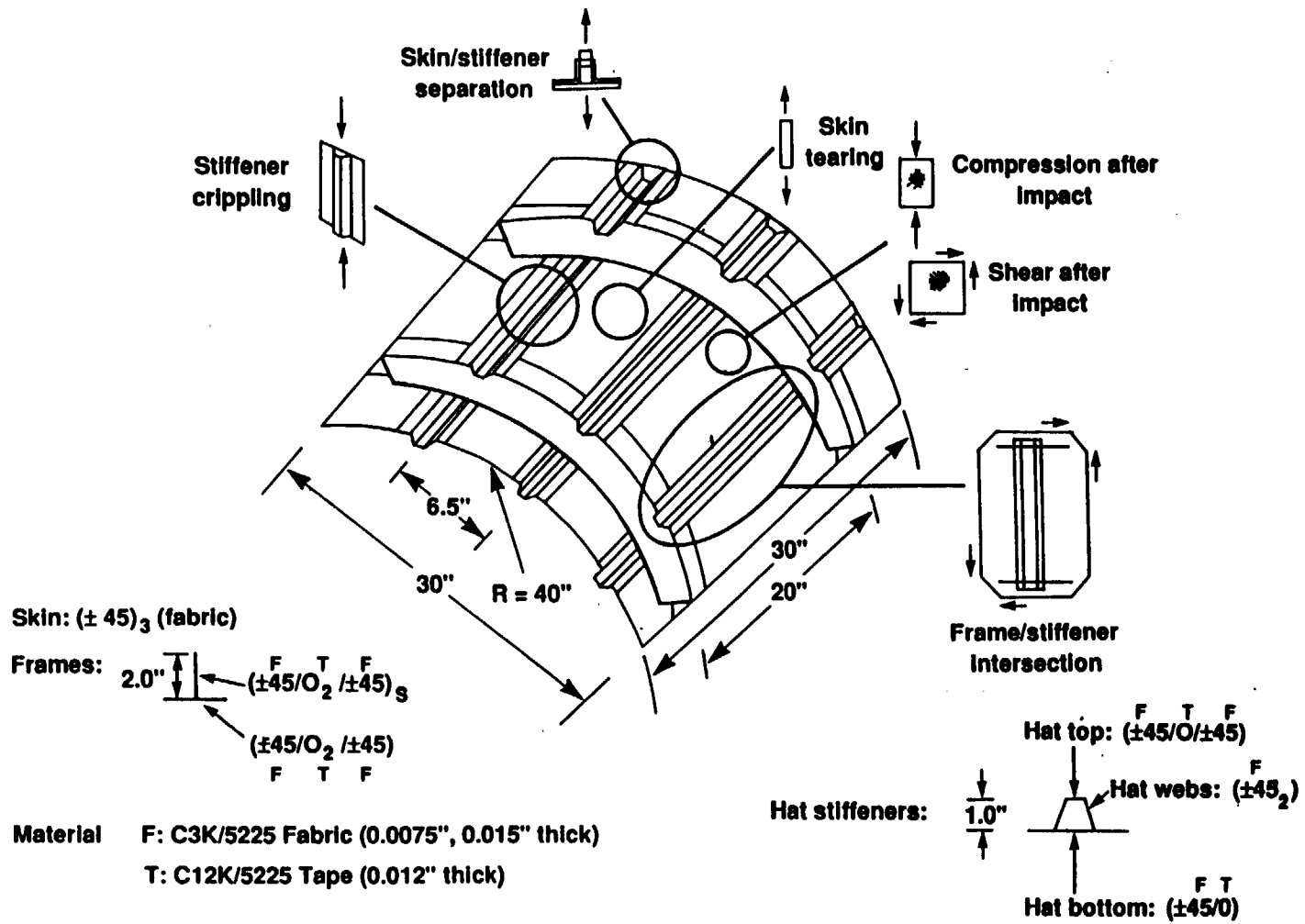


FIGURE 5.1. FULL-SCALE PANEL AND BUILDING BLOCK TEST SPECIMENS



ORIGINAL PAGE  
BLACK AND WHITE PHOTOGRAPH

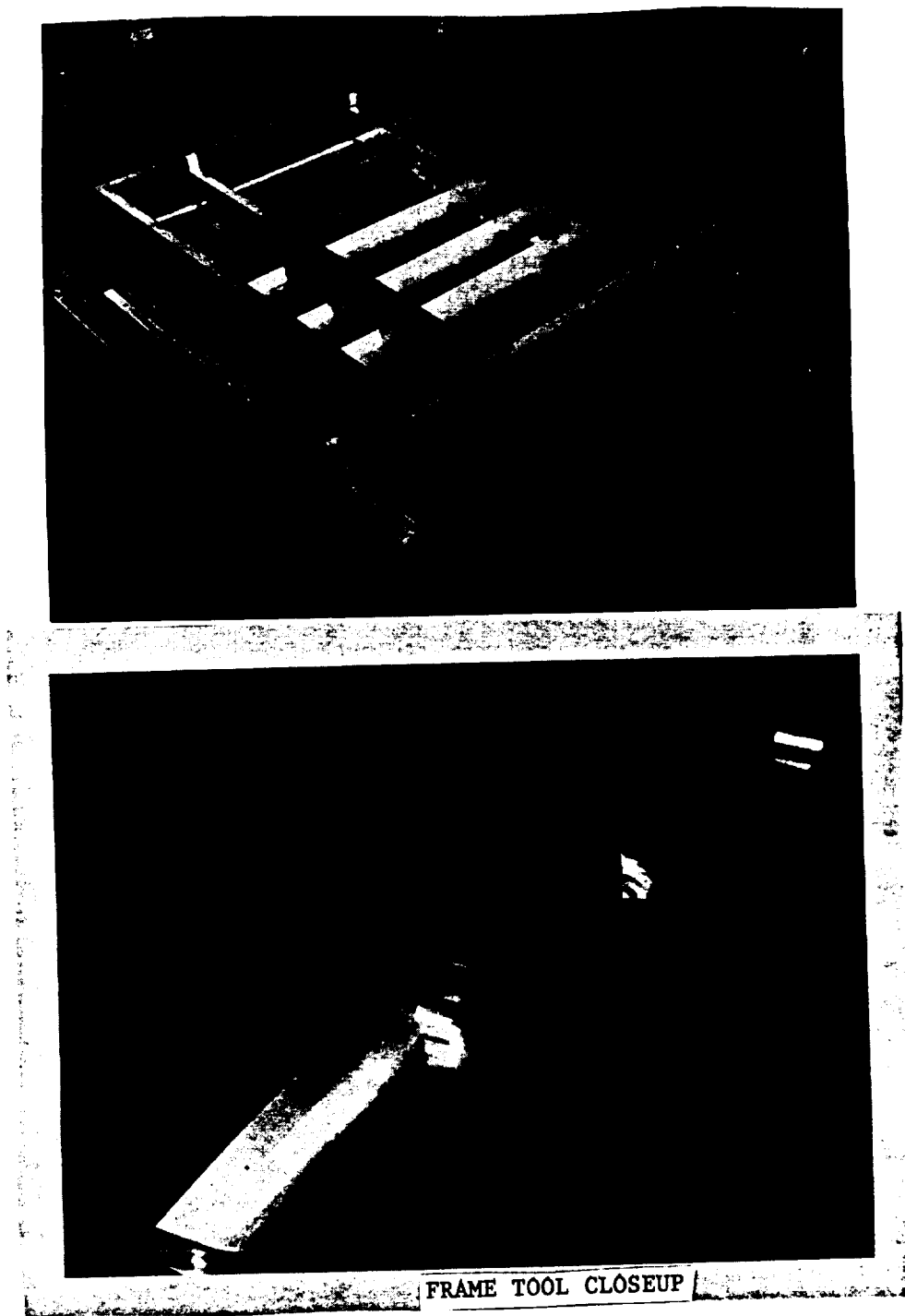


FIGURE 5.2. ALUMINUM TOOL FOR FULL-SCALE ARTICLE

Care was taken to make sure the Teflon mandrel and aluminum strip matched as closely as possible the inside shape of the hat stiffener.

The only tools used for the frames were two 0.5 inch thick aluminum cross members (shown in Figure 5.2) one for each frame. They acted as locators and supports for the frame webs. Holes were machined at their bottom to allow for the hat stiffeners.

For quality consolidation in the radius and transition regions of the curved stiffened panel, 0.25 inch gaps (with one inch radius) between the frame tools and the hat stiffeners going through them were machined to allow THERM-X to "flow" over the hat stiffeners at the frame/stiffener intersections. For the same reason, pressure transfer at radius regions, the frame tool did not touch the skin plies but was raised to leave a 0.25 inch gap. This facilitated pressure medium access to the radius region at the flange/web region of the frame. In addition, this provided the room necessary for laying up the top skin ply that covered the frame and stiffener flanges (embedded flanges).

The specimen doublers on the bag side of the part were cocured on the skin when the whole panel was cured. The doublers on the tool side were laid up separately on specially provided slots at the two sides of the tool (see Figure 5.2) which were machined with a radius of curvature that matched the panel radius of curvature. These doublers, with the correct radius of curvature built-in, were secondarily bonded in place after the part was cured.

The tool was surrounded with one inch thick removable walls that acted as the surrounding box that encased the pressure medium. These walls are also shown in Figure 5.2.

## **5.2 FABRICATION**

The layup procedure, shown schematically in Figure 5.3 was as follows:

- a. Skin: The first skin ply was laid up on the tool.
- b. Hat Stiffeners: The lower flange (reinforcing strip) ply was laid up flat on the first skin ply at the required locations.
- c. Skin: The second skin ply was then laid up on the tool.
- d. Hat Stiffeners: The inner ply that forms the stiffener webs and upper flange was wrapped around the Teflon/aluminum mandrels. The assembly was then positioned on the two skin plies in the tool directly above the flange plies laid up in b. The third ply (top flange insert) was laid up on the mandrels. The fourth ply was then draped over.
- e. Frames: Each half frame (4 plies) was laid up on the separate aluminum mold with the outer-most ply right next to the mold. The plies were bent at the bottom conforming to the aluminum mold corner to form one side of

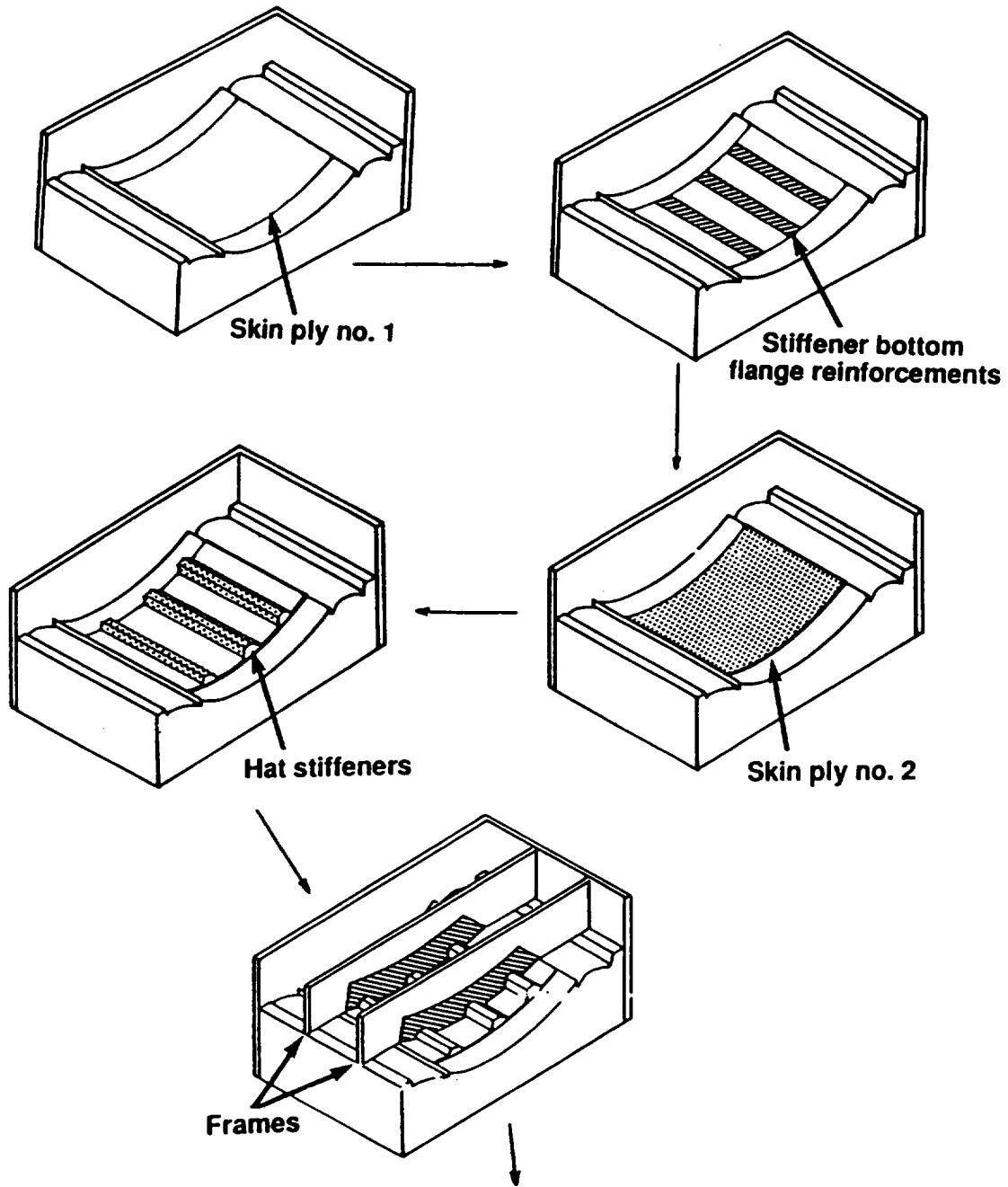


FIGURE 5.3. FULL-SCALE PANEL LAYUP PROCEDURE

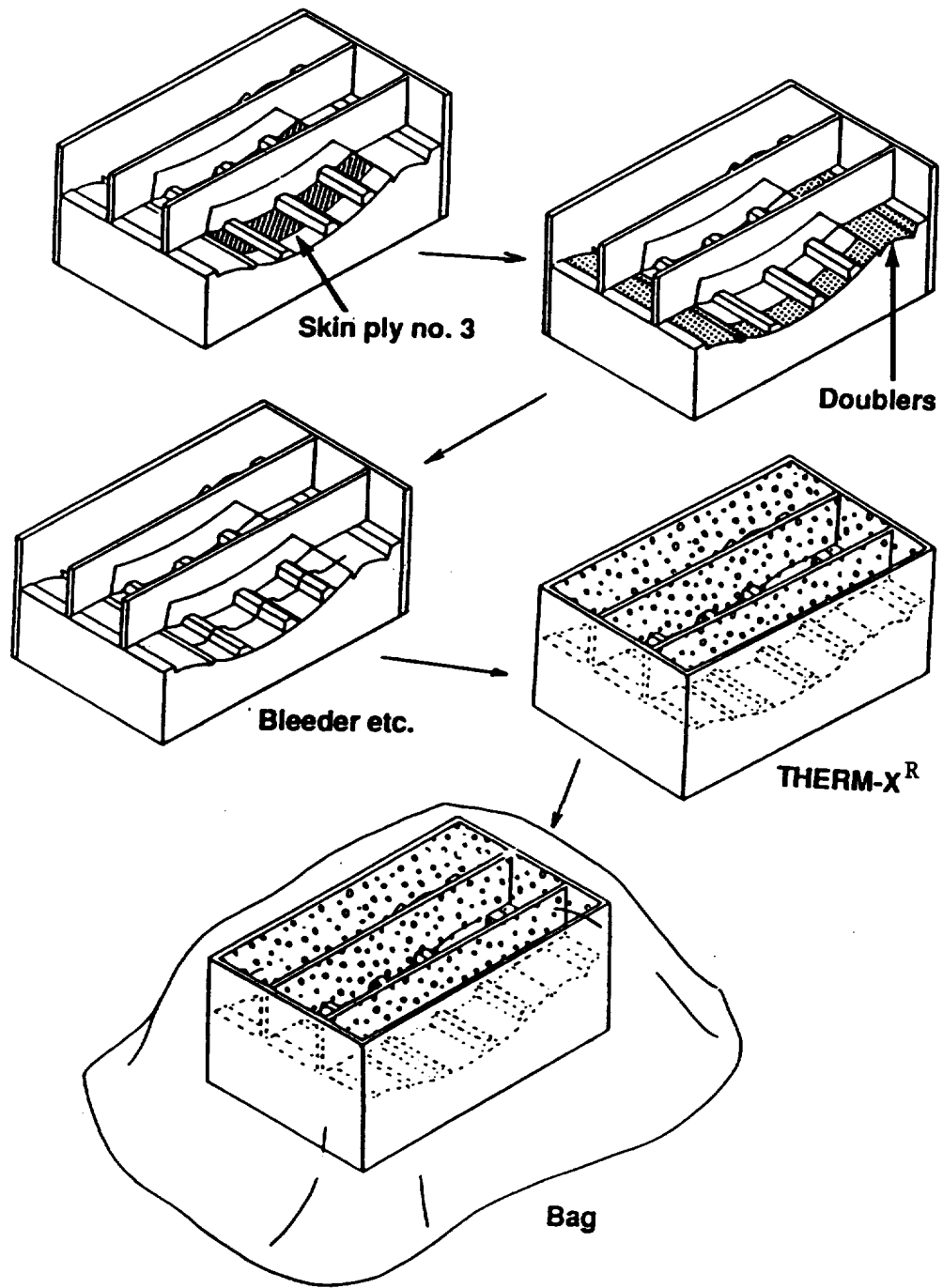


FIGURE 5.3. (cont'd) FULL-SCALE PANEL LAYUP PROCEDURE

the frame flange. The plies were cut at the mold cutouts that accommodated the hat stiffeners except for the first ply which was bent outwards through the cutout thus forming two 0.35 (approximately) inches by 1 inch flaps that were used as shear ties to tie the frames and stiffeners together (see Figure 5.4). This was done on both sides of each frame. The two half frames were mated and placed on the half inch thick frame tool and the assembly was lowered in the tool. A gap of 0.25 inches between the aluminum tool and the skin served to facilitate layup of the third skin ply (see f below) and pressure medium flow in that region for improved consolidation.

- f. Skin: The last (third) skin ply was laid up next. It was cut in pieces matching the bays formed by the frames and stiffeners and covered all flanges by at least 0.5 inches.
- g. Doublers: The doublers on the bag side were laid up next on the third skin ply. The doublers on the tool side (to be secondarily bonded) were laid up in the specially provided space in the tool and at the edges of the skin (the tool was larger than the part in order to accommodate these doublers).

With this procedure, and the cure cycle described in section 2, four full-scale panels were made. Each specimen was inspected visually and using hand-help pulse echo ultrasonic equipment. An effort to use through transmission C-scan was abandoned because of the specimen curvature making it hard to align the acoustic signal. The hand held pulse echo showed very good consolidation and no internal defects. The labor hours needed to manufacture each of the four specimens are shown in Table 5.1.

Table 5.1  
Labor Hour Breakdown for Full-Scale Panels

Task	Panel No. 1	Panel No. 2	Panel No. 3	Panel No. 4
Cut Mat'l	16 (1)	3	3	3.5
Layup	16	20	18	20
Bag/THERM-X	29.5 (2)	16	13	14
Strip & Trim	21 (2)	10	10	10
<b>TOTAL</b>	<b>82.5</b>	<b>49</b>	<b>44</b>	<b>47.5</b>

- Notes (1) Includes making templates  
 (2) Part had to be stripped and rebagged because the vacuum bag broke during cold pressure check.

Overall specimen quality was very good especially in traditionally difficult corner and intersection areas. An overview of one of the specimens is shown in Figure 5.5. The three hat stiffeners are shown with the white Teflon mandrels still in place. No flanges (for either the stiffeners or the frames) can be

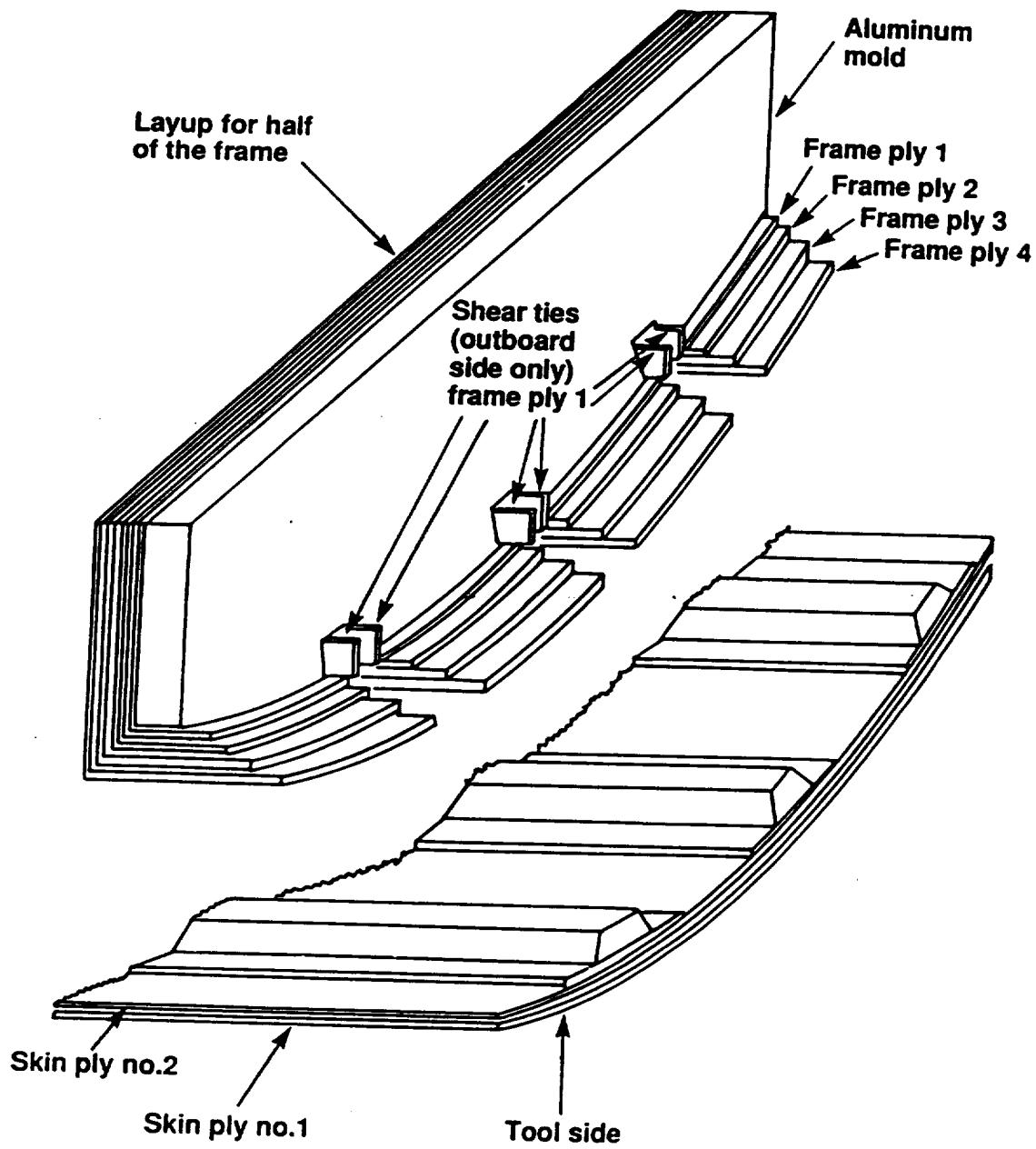


FIGURE 5.4. DETAIL OF ASSEMBLY DURING LAYUP OF FULL-SCALE PANEL.

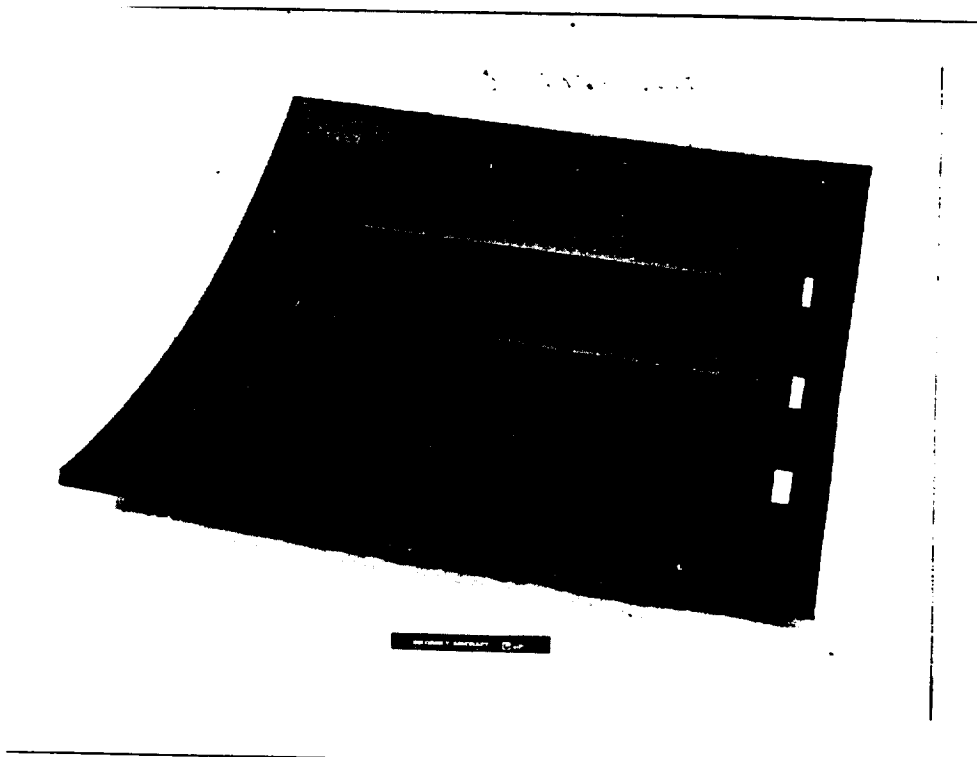


FIGURE 5.5. FULL SCALE PANEL NO. 1

seen because they are covered by the top skin ply (embedded flange). A detail of the hat stiffener web and skin is shown in Figure 5.6. The radius between the web and skin is very well defined. Similar radius definition high quality is evident at the frame-stiffener intersection corners shown in Figure 5.7. No voids, wrinkles, or resin starved locations were found. High part quality was consistent in all four full-scale panels manufactured. The THERM-X® process was proved to be very effective in fabricating cocured parts of high complexity with minimum tooling. Part-to-part consistency indicated that the risk factor associated with cocuring large parts is significantly reduced. For larger parts, a fabrication error or process problem can be very costly since larger parts may have to be scrapped. The THERM-X® process is not dependent on an individual's bagging practices from part-to-part or from detail-to-detail within the same part and thus the probability of bag bridging or insufficient pressure transfer, which is a major cause for fabrication problems, is reduced.

Some wrinkles were present at the ends of the frames in the radius region where the web transitioned into the flange (see Figure 5.8). This was the only area with visible manufacturing discrepancies for the first full-scale panel. An increased number of wrinkles appeared in the frame-skin intersection of the third full-scale panel. These wrinkles were caused by relative movement of the aluminum cross member used to locate and support the frames. For the fourth full-scale panel, the cross member was shimmed to eliminate movement and was lowered closer to the skin (0.125 inch gap) to increase the level of support in this area. As a result of these changes, the wrinkles were eliminated in the fourth full-scale panel.

Void content and fiber volume measurements of specimens cut off the corners of the skin and frames showed excellent part quality with void content less than 0.6% and fiber volumes at approximately 58%.

## **5.3 TEST**

### **5.3.1 STATIC TEST**

The first three specimens were tested in shear using a picture frame fixture. The steel fixture consisted of I-beams with aluminum angles bolted on the webs. The angles served as doublers fastened to the specimen. A dummy skin specimen was tested first to verify the fixture and data acquisition equipment. The fixture performed very well during all tests.

Up to 18 strain gage rosettes (54 legs) were used with each specimen to monitor strains at the skin center and quarter points within various bays, at the frame-stiffener intersection corners (rosettes were placed on the stiffener webs, the hat tops, and the frame webs), and near the doublers to verify uniform shear loading and load transfer.



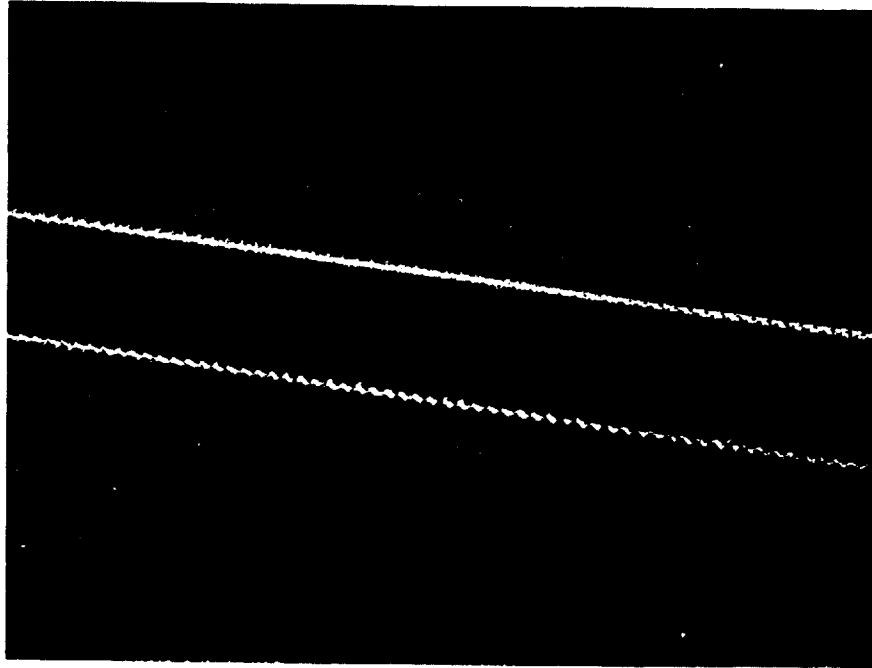
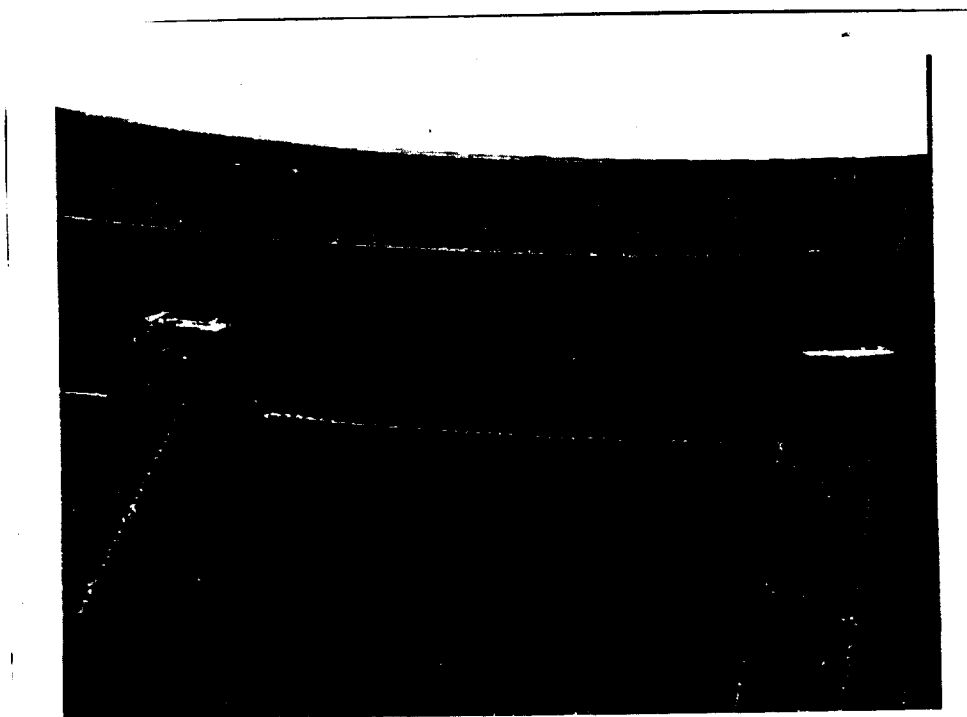


FIGURE 5.6. FULL-SCALE PANEL NO. 1 - HAT STIFFENER DETAIL



**FIGURE 5.7. FULL-SCALE PANEL NO. 1 - FRAME-STIFFENER INTERSECTON CORNERS**



FIGURE 5.8. FULL-SCALE PANEL NO. 1 - FRAME END

A deflection gage was attached to the specimen to measure out-of-plane deflection at the center of one bay. Acoustic emission equipment with 8 transducers located near the intersection corners, at the loaded specimen corners and the bay centers was used to monitor damage initiation and growth during testing.

Shadow moire techniques were used to monitor out of plane deflections of the specimens. Due to the specimen curvature, a shadow pattern was present before applying load. Photographic records of the pattern were taken and used to subtract the initial curvature from the pattern on the specimen under load.

A typical test sequence follows. At an applied load of 4000 lbs, buckling occurred. It was accompanied by noise indicating snap-through of the skin in the center bays and a pattern change in the shadow moire. Further increases in load led to higher deflections in the postbuckled pattern until, between 6000 and 9000 lbs (141 and 212 lbs/in) another snap-through occurred also accompanied by noise suggesting another bifurcation.

A specimen is shown under 12000 lbs (283 lbs/in shear flow) of applied load in Figure 5.9. No visible damage can be found other than the two pinching cracks at the top and bottom (loading) corners which were caused during the first time this particular specimen was tested (see below). At this load, postbuckling factor of 3, the buckled pattern is clearly discernible in each bay as alternating areas of light and shadow. Four halfwaves (two towards and two away from the reader) can be seen in each bay. The buckles in the two center bays are at an (approximate) angle of 33 degrees with the stiffener axis. The orientation of the buckles in the lower two bays and the fact that they have no out-of-plane displacement next to the lower hat stiffener suggest that the stiffener still acts as a panel breaker (see Figure 5.12 for a change in this pattern).

Visible cracks appeared at the loaded corners of the specimen at an applied load of 17000 lbs (400 lbs/in shear flow) and grew to a size of 3 inches at a load of 18000 lbs (424 lbs/in). These are pinching cracks, caused by test fixture corner stress concentrations common to picture frame shear tests. They did not grow any more beyond that load. Testing of the third full-scale specimen was stopped at 18000 lbs of applied load (424 lb/in shear flow) for non-destructive inspection (NDI). At that point, the only visible damage consisted of the two pinching cracks at the two loading corners of the specimen. Hand-held pulse echo inspection of the specimen in the vicinity of the frame stiffener intersection corners showed no damage. NDI did verify the two visible pinching cracks and indicated their size to be very close to their visible size (no cracks or delaminations below the specimen surface were found ahead of the visible crack tip). It should be noted that acoustic emission equipment picked up damage at around 10000 lbs (234 lb/in shear flow) in the vicinity of the frame/stiffener intersection corners. The fact that NDI did not document this damage suggests that the damage was at the radius regions or under the hat stiffener caps where the NDI equipment could not inspect. In addition, the damage size was probably too small since it was not found by detailed visual inspection.



FIGURE 5.9. FULL-SCALE TEST NO. 3. APPLIED LOAD: 12000 LBS (283 LBS/IN)

ORIGINAL PAGE  
BLACK AND WHITE PHOTOGRAPH

The postbuckled pattern of the specimen at an applied load of 20680 lbs (487 lbs/in) is shown in Figure 5.10. The load corresponds to a postbuckling factor of 5.1. A crack has now appeared on the web of the lower hat stiffener halfway along the stiffener and having a length of about 5 inches. The crack is mostly at the center of the web halfway between the cap and the skin. This crack was observed in all full scale specimens and the two flat frame-stiffener intersection specimens when they were examined after failure. It should be pointed out that the hat webs consist of only two fabric plies (at 45 degrees to the stiffener axis) while the caps and flanges of the stiffeners had additional tape and fabric plies. This crack is in agreement with the location of damage in the crippling tests during the building block evaluation (section 4.2.3) that showed that the hat stiffener webs were among the weakest parts of the specimen. No other damage is observed in the specimen other than the already existing pinching cracks which had not grown.

The specimen is shown under an applied load of 23000 lbs (542 lbs/in) in Figure 5.11. The crack in the stiffener web has extended to about 6 inches and now one end has reached the web/skin interface. No damage is visible at any of the stiffener or frame flanges and the pinching cracks at the specimen corners have not changed. The change in the buckling pattern can be seen in the upper middle bay where there now appear 5-6 halfwaves (depending on how the shadowy region at the bottom of the bay is interpreted). This modal change was documented by shadow moire.

A slight increase in applied load causes drastic changes in the damage pattern. This is shown in Figure 5.12 where the specimen is under an applied load of 23500 lbs (554 lbs/in shear flow). The crack in the stiffener web has grown to about 7 inches along the web/skin interface. An additional crack has appeared in the top middle bay emanating from the top frame/stiffener intersection corner and extending to a length of 7-8 inches at an angle following the angle of the buckles in the bay. This crack was also seen in the other full-scale tests but rather than following the angle of the buckles (full-scale specimen No 3) it extended along the hat stiffener at the web/skin interface and caused the final failure (separation) of the specimen (full-scale specimen Nos 1 and 2). The angle of the buckles has changed from 33 degrees at a load of 12000 lbs to 36 degrees at this load level. In addition, the point where the top buckle in the lower middle bay meets the middle stiffener has moved down by 1-2 inches (see vertex of measured angle in Figures 5.12 and 5.9). The damage in the lower stiffener has reduced its bending stiffness to the point that it does not act as a panel breaker anymore. The buckles that terminated near the cracked web have now aligned themselves and the skin deflection where they meet the lower hat stiffener is not zero any more. The pinching cracks at the specimen corners are unchanged.

A failed specimen, still in the testing machine is shown in Figure 5.13. Failure occurred at an applied load of 25925 lbs (611 lbs/in shear flow or a postbuckling factor of 6.5). Final failure occurred at the two lower edges of the specimen where the skin cracked along the edge of the lower bay and parallel to the lower frame. The cracks in the lower hat stiffener and the corner of the upper bay (see Figures 5.10 and 5.12) did not precipitate final failure. It appears though that these two cracks redistributed the load to the edges of the

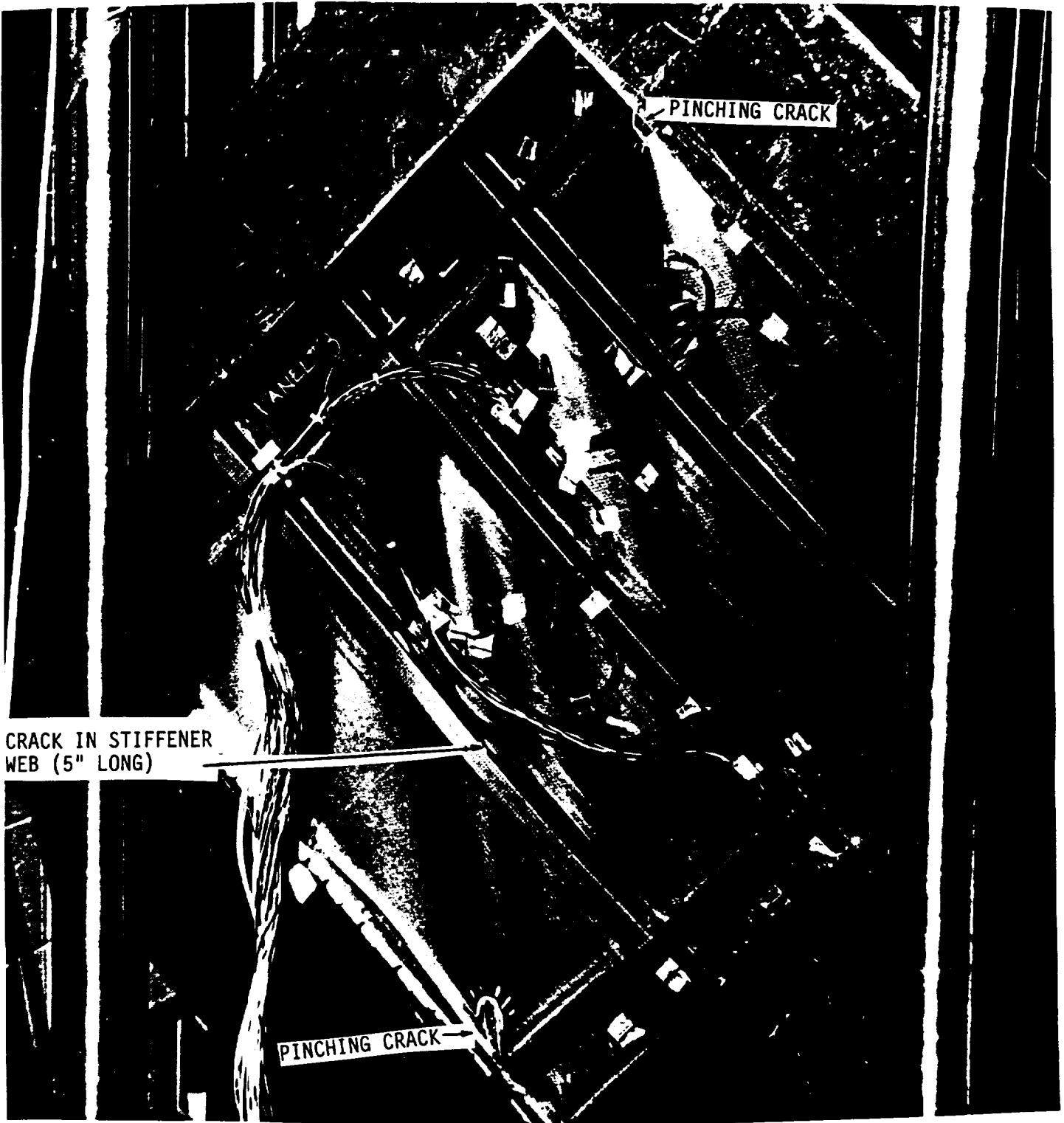


FIGURE 5.10. FULL-SCALE TEST NO. 3. APPLIED LOAD: 20680 LBS (487 LBS/IN)



FIGURE 5.11. FULL-SCALE TEST NO. 3. APPLIED LOAD: 23000 LBS (542 LBS/IN)





FIGURE 5.12. FULL-SCALE TEST NO. 3. APPLIED LOAD: 23500 LBS (554 LBS/IN)

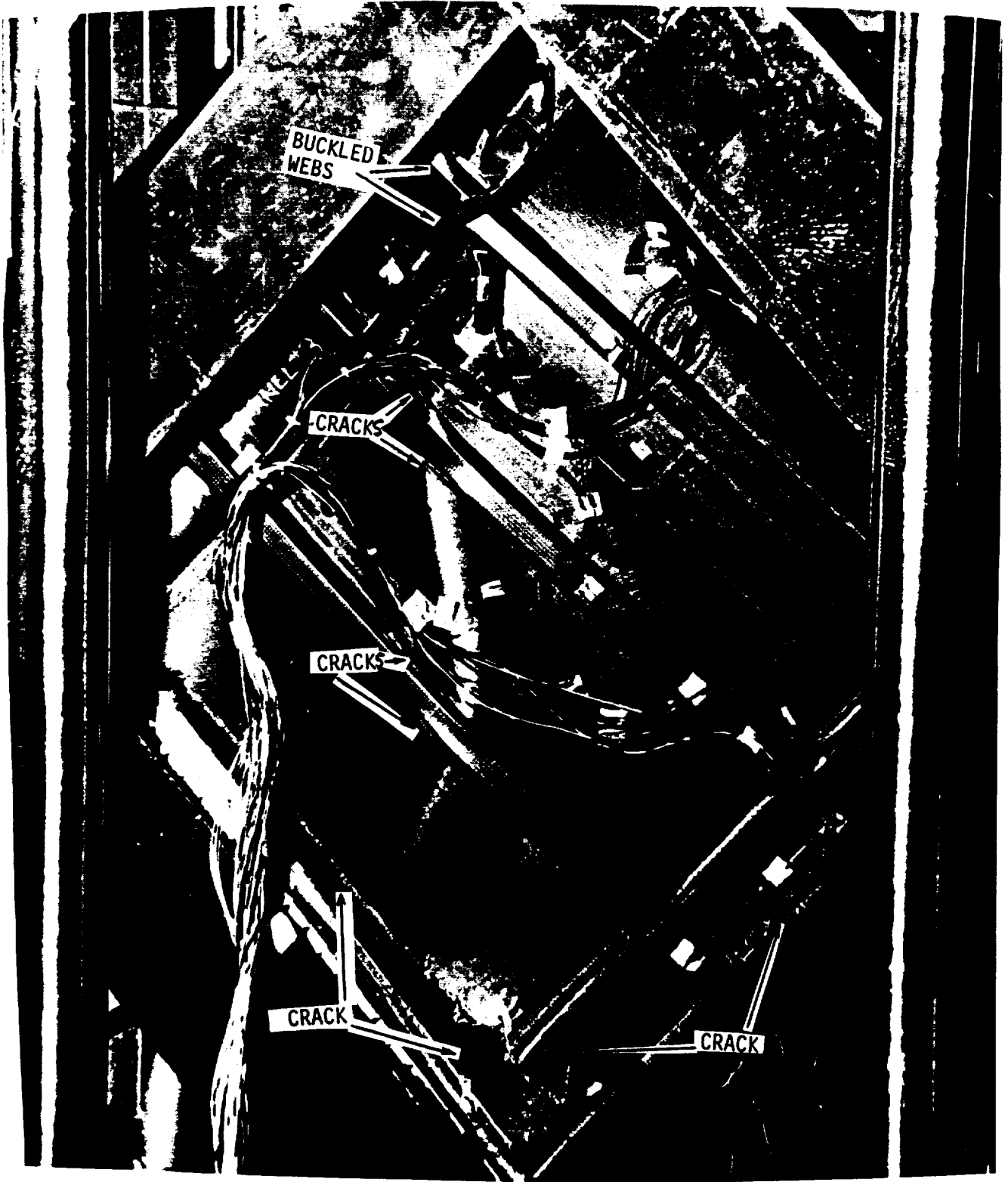


FIGURE 5.13. FULL-SCALE TEST NO. 3. FAILURE AT 25925 LBS (622 LBS/IN)

specimen since they softened the skin and the stiffeners at the center. It should be noted that the first two static tests failed by separation at the center of the specimen caused by the second crack noted during this test (see Figure 5.12). The failed specimens 1 and 2 are shown in Figure 5.14. As is shown in this test specimen, significant cracking was present on both sides of the middle hat stiffener and the frame and stiffener webs were buckled at the upper frame-stiffener intersection corner. As was the case in the first two static tests, the shear ties held in place and did not separate, nor did the stiffener and frame flanges from the skin. The cracks observed were through the skin and flanges at the stiffener web/skin interfaces. As was anticipated from the building block evaluation (Skin Stiffener Separation and Frame-Stiffener Intersection specimens) the built-in shear tie and the embedded flange design were very effective in suppressing their associated failure modes.

To obtain sufficient data to reconstruct the sequence of failure events during testing of full-scale panels, acoustic emission was used to monitor the third specimen during testing. An IBM 386 based Physical Acoustics Corporation system was used with 8 transducers attached to the bag side of the specimen at various locations as shown in Figure 5.15.

Previous experience with the C3K/5225 and C12K/5225 material systems has shown that signal data below 50 db corresponds to matrix damage (microcracking for example). Signal data between 50 db and 75 db corresponds to delamination related phenomena (growth, buckling). Any db level higher than 75 db corresponds to breaking of fibers. The threshold values of 50 and 75 db should not be viewed as absolute as they are mostly based on qualitative correlation and some of the failure events will overlap. In addition, as signals travel through the panel they attenuate and thus recorded data may correspond to higher db levels depending on the relative location of the transducer and the failure site.

Acoustic emission data is reported in terms of energy stored in the signal and signal amplitude. Total energy (throughout the test) versus channel is shown in Figure 5.16. Channel 1 malfunctioned during test. Figure 5.16 indicates that most damage activity was in the vicinity of transducers 2 and 5. This is corroborated by the amplitude versus channel plot shown in Figure 5.17. For each channel the signal amplitudes are recorded throughout the test on a vertical line. So different data points correspond to different points during the test. The highest amplitudes are recorded by transducers 2, 5, 6, and 7. This suggests that failure initiates in the vicinity of these areas. Referring to Figure 5.15, transducers 2, 5, and 6 correspond to frame-stiffener intersection corners while transducer 7 corresponds to either a frame-stiffener corner or the top of the specimen where pinching may cause some local failures.

These results suggest that failure initiates in the vicinity of one of these three corners. The progression of events at one of these corners (corresponding to transducer number 5) is shown in Figure 5.18. There appear to be no signals below 50 db so no matrix related failures are present. Since matrix cracks, which would correspond to signals below 50 db, are not recorded, this acoustic emission result is viewed with some suspicion as failure initiation in such

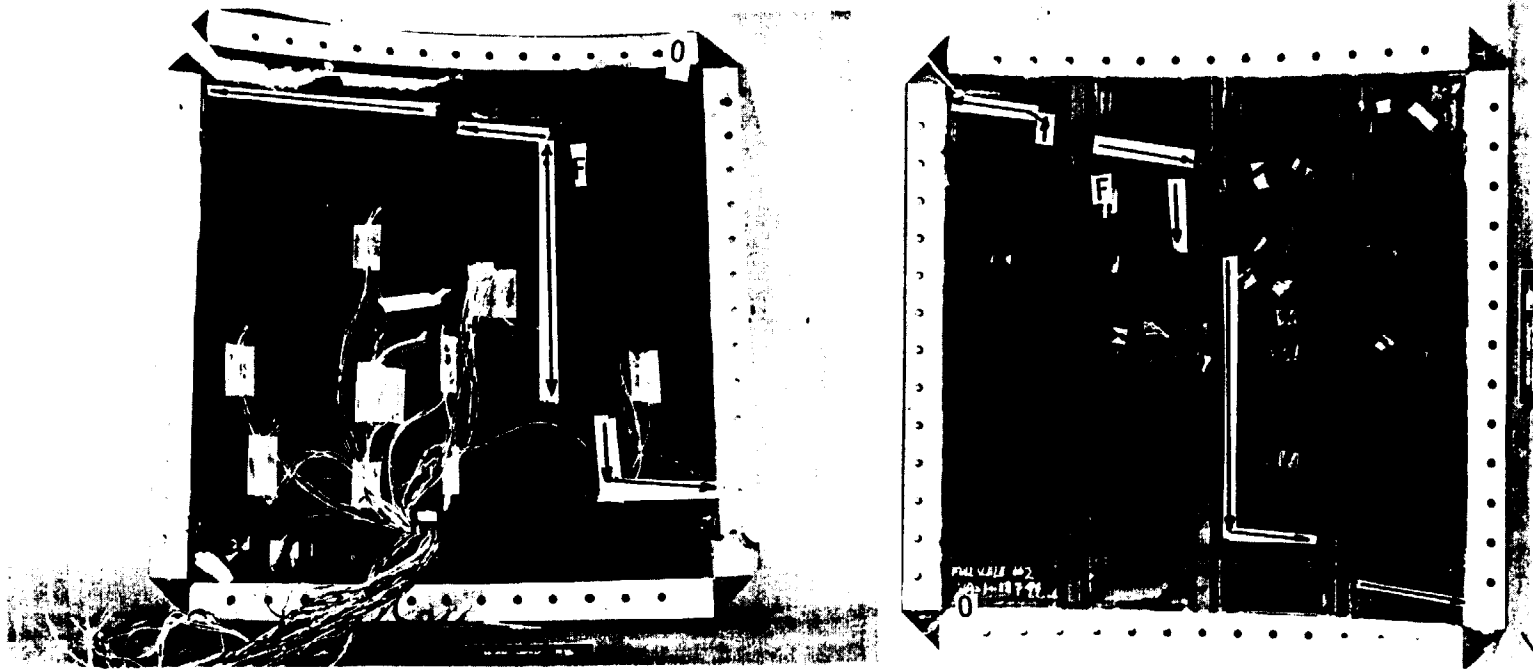


FIGURE 5.14. FAILED FULL-SCALE SPECIMENS 1 AND 2

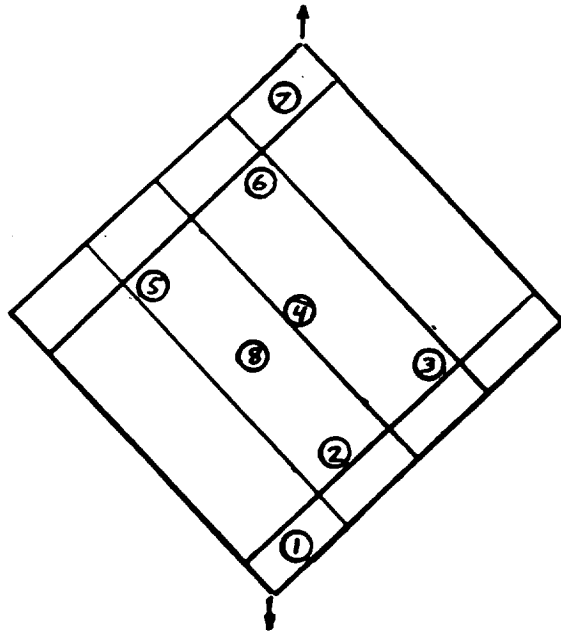


FIGURE 5.15. TRANSDUCER LOCATIONS FOR COLLECTING ACOUSTIC EMISSION DATA

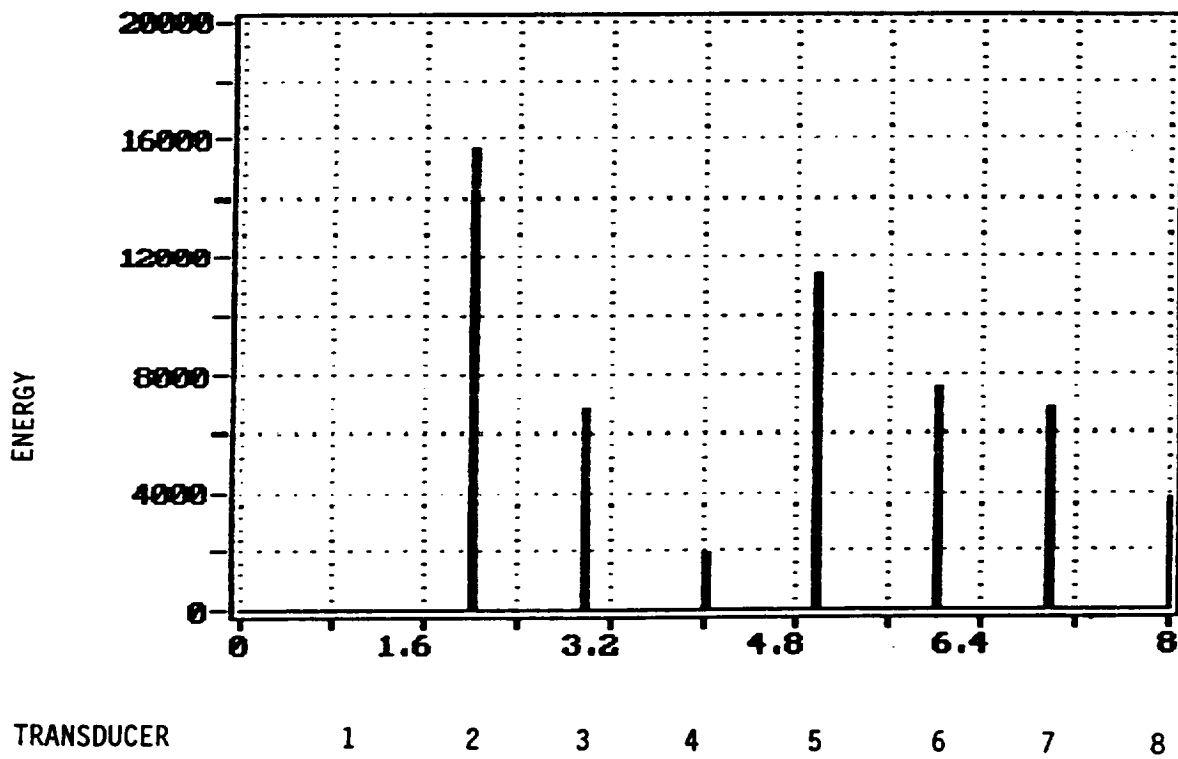


FIGURE 5.16. ACOUSTIC EMISSION ENERGY VERSUS CHANNEL (TRANSDUCER)

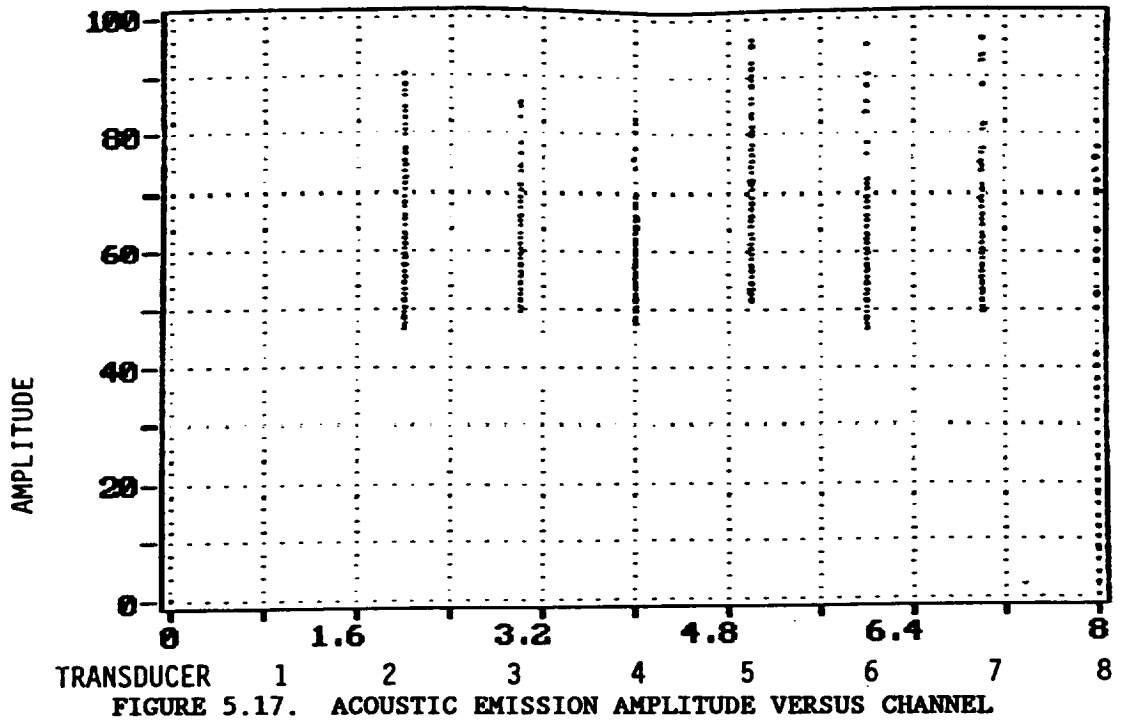


FIGURE 5.17. ACOUSTIC EMISSION AMPLITUDE VERSUS CHANNEL

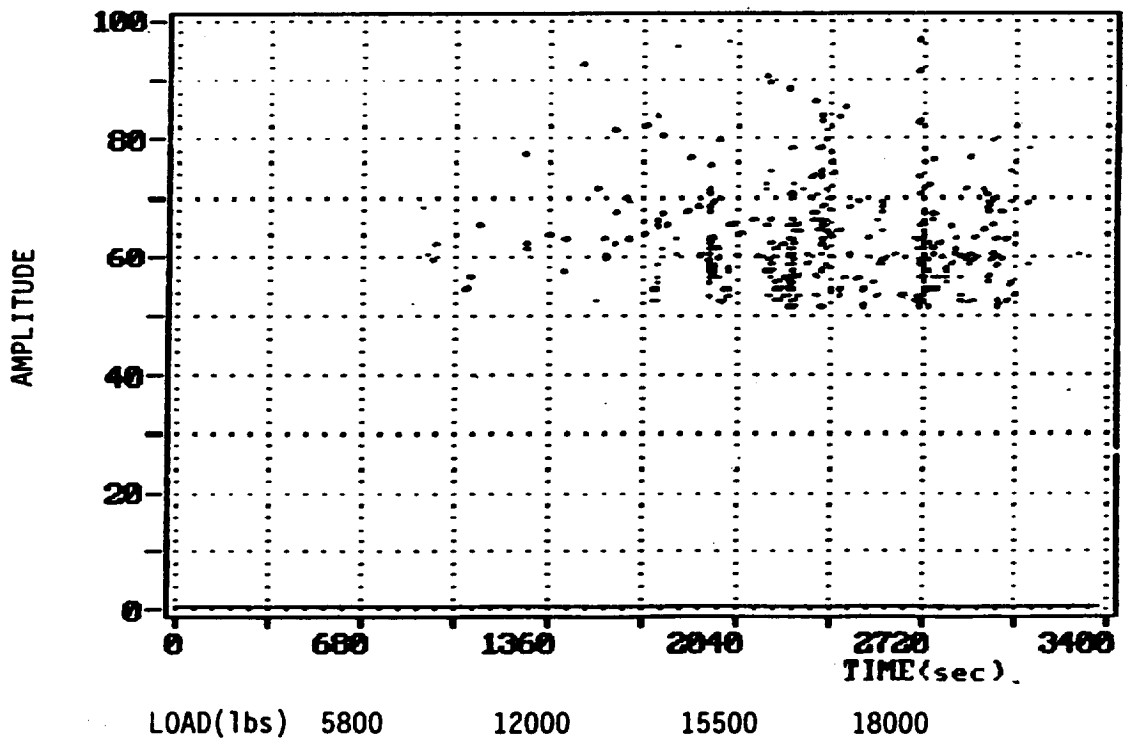


FIGURE 5.18. ACOUSTIC EMISSION AMPLITUDE VERSUS LOAD FOR TRANSDUCER NO. 5

panels always contains matrix cracks. Damage initiates around 10000 lbs (236 lbs/in) and starts to increase rapidly (as suggested by increase in signals recorded) around 15000 lbs (353 lbs/in) of applied load. This damage initiation around 10000 lbs might partly explain why the finite element predictions start deviating from the test results at that load (see section 5.4): the finite element model designed to capture the overall panel behavior rather than local details of the load transfer, does not model this damage. A local model in an area of interest was constructed later to predict failure (see Section 5.4.3). The db level for the damage suggests some delamination and fiber breaking are taking place. As this damage was not picked up by NDI (see above discussion on NDI) it must correspond either to sizes very small (smaller than 0.25 inch in diameter) or to locations that NDI could not inspect (corners, intersections, hat webs).

The exact location of failure onset can be inferred by examining the buckling pattern and the failed specimens. The buckling pattern of the specimen under load (12000 lbs or a postbuckling factor of 3) is shown in Figure 5.9. The halfwaves in each bay are readily visible as alternating light and shadow regions. It can be seen that there are halfwaves terminating near the frame/stiffener intersection corners. At these locations of low radius of curvature, there will be increased bending moments that are expected to initiate failure. This failure manifested itself as cracks in the hat stiffener webs which as already pointed out were among the weakest structural details of the specimen.

The failure loads for the three static full-scale tests are shown in Table 5.2. The average load of 24608 lbs corresponds to a postbuckling factor of 6.1.

Table 5.2  
Full-Scale Test Failure Loads

Specimen No	Failure Load (lbs)	Failure Load (lbs/in)
1	24000	566
2	23900	563
3	25925	611
Average	24608	580

### 5.3.2 FATIGUE TEST

There were two main considerations driving the selection of fatigue loads. The first was that, in order to gain more information and insight on the material behavior, it would be advantageous to select loads that would cause some damage in the specimen. Thus, damage initiation and growth could be studied during the test and any effects of the manufacturing process could be inferred by comparing to similar tests done in the past with specimens fabricated with conventional manufacturing methods. The second was that for simplicity in performing the test, interpreting the results, and comparing with tests in the literature most

of which are done at constant amplitude, a constant amplitude test should be selected. For typical helicopter tailcone spectrum loading, tests of the full-scale panel would almost certainly show no damage since the static test results showed the panel was capable of carrying loads much higher (by a factor of 6 or more) than the typical loads included in a spectrum loading fatigue test.

The original design for the full-scale panel accounted for TOV impact damage by assuming a knockdown factor of 50% (based on compression after impact data) and requiring that the panel sustain ultimate load with such a damage present. For an ultimate load of 250 lb/in of shear flow (typical of S-76 helicopter tailcone) the undamaged failure strength of the panel should be twice that value (500 lb/in) to account for TOV impact damage. The panel was designed with these requirements in mind. The undamaged ultimate strength of 580 lb/in that resulted from the static tests indicates the original design is consistent with the final test results.

An aggressive load level of 70% of static limit load was selected that was expected to show some damage during the test and provide meaningful trends in damage progression.

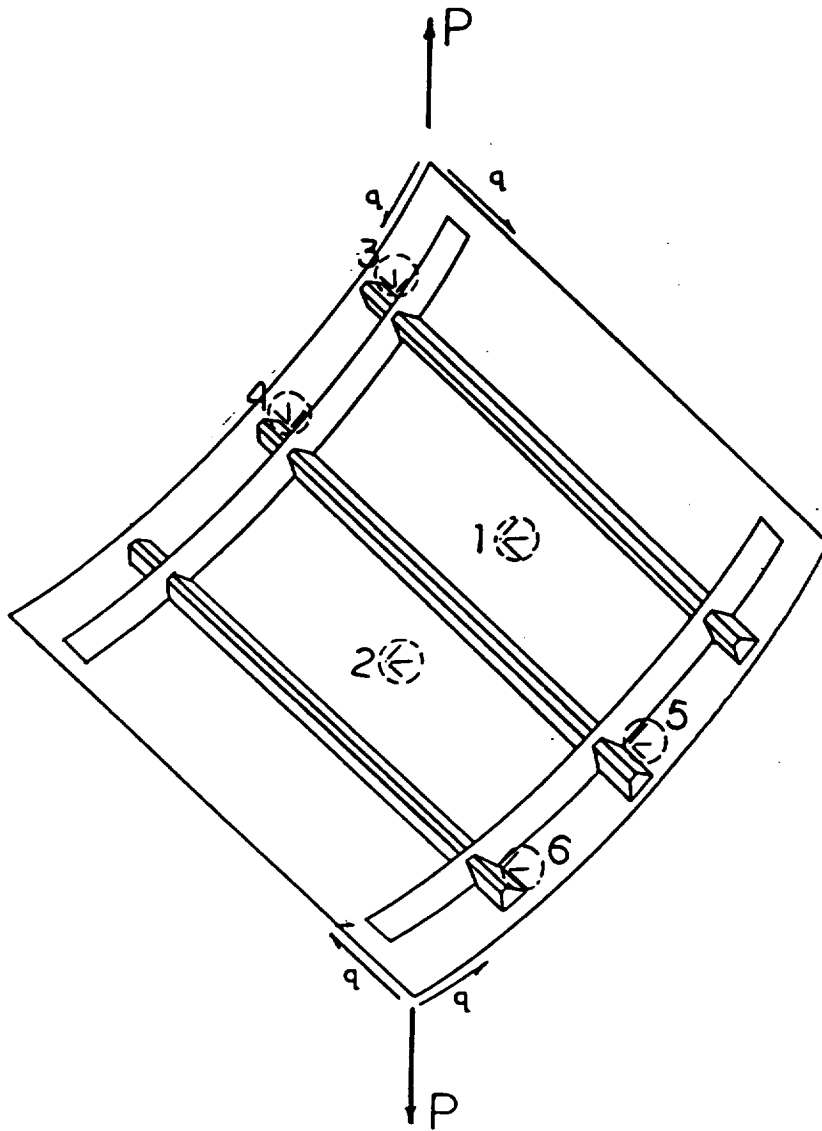
The shear after impact tests on the flat frame-stiffener intersection specimen however, showed a knockdown factor of only 14% (see section 4.2.4 above) which suggests that the current design should sustain loads significantly higher than the design ultimate load of 250 lb/in. A 14% knockdown factor on the undamaged static test average of 580 lb/in suggests an ultimate load carrying capability (including TOV impact damage) of  $580/1.14 = 509$  lb/in. This corresponds to a limit load of  $509/1.5 = 339$  lb/in. As originally specified, the constant amplitude test would be at 70% of limit load or at  $0.7 \times 339 = 237$  lb/in. This would substantiate room temperature dry parts (with an aggressive loading as already mentioned). To account for environmental effects and fatigue life scatter, a load enhancement factor of 1.2 (similar to what is suggested in reference 19) was applied. The resulting load is  $1.2 \times 235 = 284$  lb/in.

The load of 284 lb/in determined above translates to 12068 lbs of applied load along the specimen diagonal. Static test results however suggested that damage initiation (beyond the first acoustic emission indications at 10000 lbs) occurred after the applied load reached 12000 lbs. Thus, to select some load that is likely to cause damage during testing, a load higher than the arrived at value of 12068 lbs and the documented value of 12000 for damage initiation load should be used. As such, 14000 lbs load was selected which corresponds to 57% of the static ultimate load and a postbuckling factor of 3.5.

The test parameters selected, i.e. maximum load, R-ratio, and test frequency, are summarized in Figure 5.19. Also presented in Figure 5.19 are strain gage locations which were monitored throughout the duration of the test.

Testing was done using the same MTS 458 machine with hydraulic grips and the same test fixture that was used for static testing. Limits were set on the machine stroke and load ( $\pm 1\%$  of maximum 20000 lbs on load and  $\pm 10\%$  of maximum 5





$P_{max} = 14,000 \text{ lbs}$  ( $q = 330 \text{ lbs/in}$  shear flow)  
 $P_{min} = 1,400 \text{ lbs}$  ( $q = 33 \text{ lbs/in}$  shear flow)  
 Test Frequency = 0.3 to 0.6 Hz

FIGURE 5.19. FATIGUE TEST PANEL - TEST PARAMETERS INFORMATION

inches on stroke). If these limits were reached, significant load redistribution would have taken place suggesting damage generation. The machine would then automatically shut down and the specimen be inspected. Inspections were originally planned for every decade (after cycles 1, 10, 100, 1000, 10000 etc). If damage developed in between, additional inspections would take place as necessary. Inspection was visual, tap test, and hand-held pulse-echo.

An illustration of the buckled shape of the panel during the first loading cycle is shown in Figure 5.20. The hat stiffeners again acted as buckled waveform breakers across which buckling patterns were not continuous. This is very similar to the buckling pattern observed during static test (see Figure 5.9 for example). Buckling of the panel was clearly visible once the load went over 5000 lbs. In fact, in agreement with the conjecture of the existence of two bifurcation points at two different buckling loads (see section 5.3.1) two snapping sounds were audible as the specimen load increased and two similar sounds were audible as the load decreased to almost zero in each cycle as the specimen went through the reverse modal change.

The extension of several visible cracks, denoted A, B, C, and D, during the first 10,000 cycles is highlighted in Figure 5.21. Based on experience gained during static testing, these cracks mainly provided relief of local stress concentrations due to the picture-frame shear loading configuration and did not influence the fatigue life of the panel. This assumption was supported by the fact that growth of these cracks was arrested for a long time prior to final failure of the specimen. Ultrasonic inspection of the entire panel during the planned inspections yielded no indications of nonvisible damage. The hand-held ultrasonic pulse-echo equipment used during the inspections was set to detect damage larger than or equal to 0.25 inches in diameter.

The test was continued until further damage was noted, see Figure 5.22. Once again, these delaminations were judged to relieve local stress concentrations due to the loading configuration and therefore not adversely affect the total life of the part. No visible or nonvisible damage in addition to that shown in Figures 5.20, 5.21, and 5.22 was found.

The first significant failure occurred at 69,200 cycles. This failure initiated in the webs of one of the outer hat stiffeners as shown in Figures 5.23 and 5.24. The cracks were easily visible with the unaided eye and were located approximately halfway between the root and tip of the web aligned with the stiffener axis. Extension of the cracks to the sizes shown and branching to the root of the web occurred in a single cycle. Ultrasonic inspection found no new nonvisible damage. The buckled shape of the panel after the first significant failure is presented in Figure 5.25. Note that while the two undamaged hat stiffeners continued to function as panel breakers, the failed stiffener did not.

Immediately following failure of the hat stiffener, the decision was made to quasi-statically test the panel to a limit load of 381 lbs/in shear flow (16174 lbs of applied load along the diagonal). This test established limit load capability of the damage panel and serves to certify the panel up to that load level and equivalent service flight hours. The reasoning is based on the fact

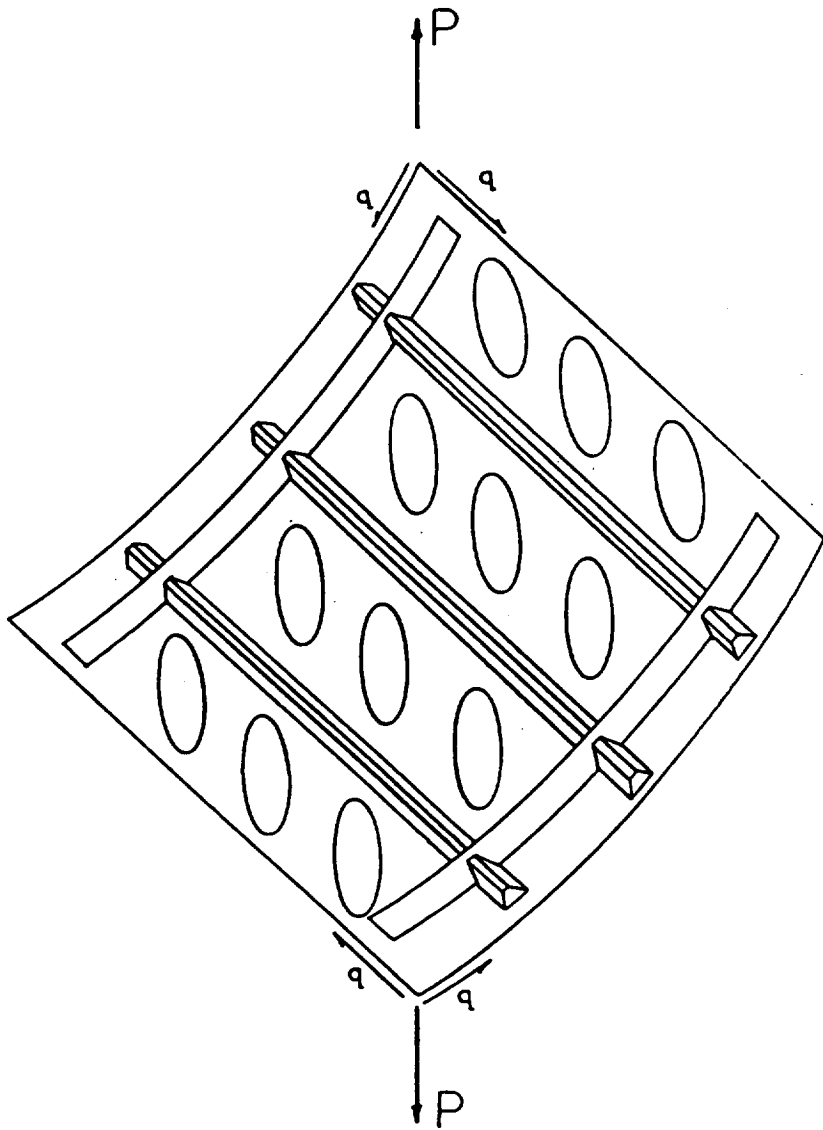
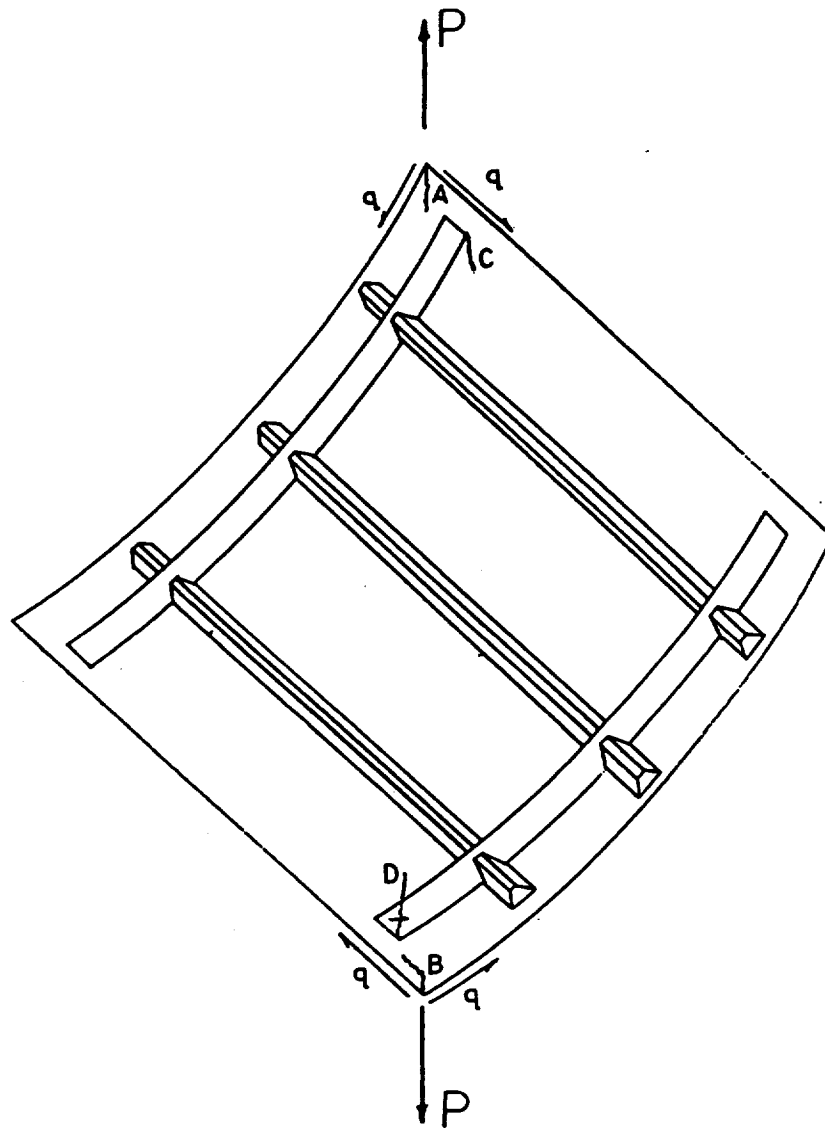


FIGURE 5.20. BUCKLED SHAPE DURING FIRST LOADING CYCLE



Crack	Crack Length [in]				
	1 cycle	10 cycles	100 cycles	1,000 cycles	10,000 cycles
A	1.50	1.50	2.75	2.75	2.75
B	1.50	1.50	1.50	2.50	2.50
C	----	0.75	0.75	2.00	2.00
D	----	----	0.50	0.50	2.50

FIGURE 5.21. FIRST DAMAGE - DATA UP TO 10000 CYCLES

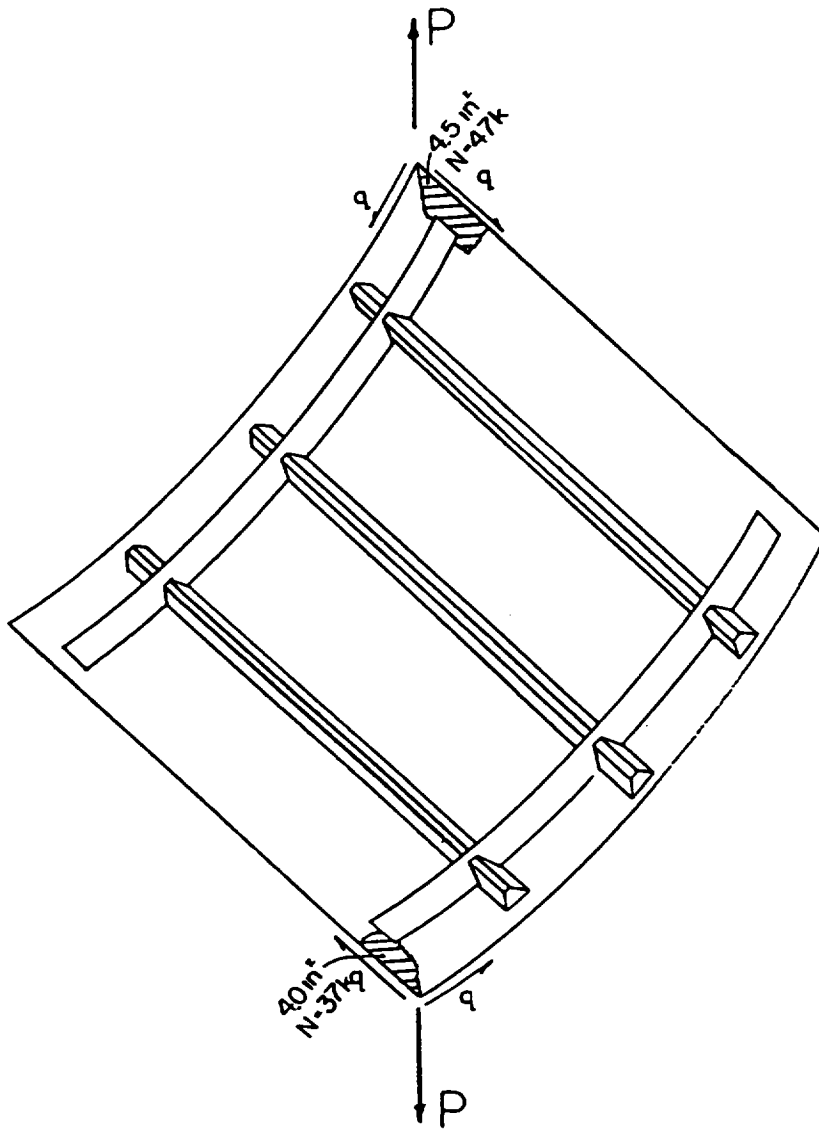


FIGURE 5.22. CORNER DELAMINATIONS AT 37000 AND 47000 CYCLES

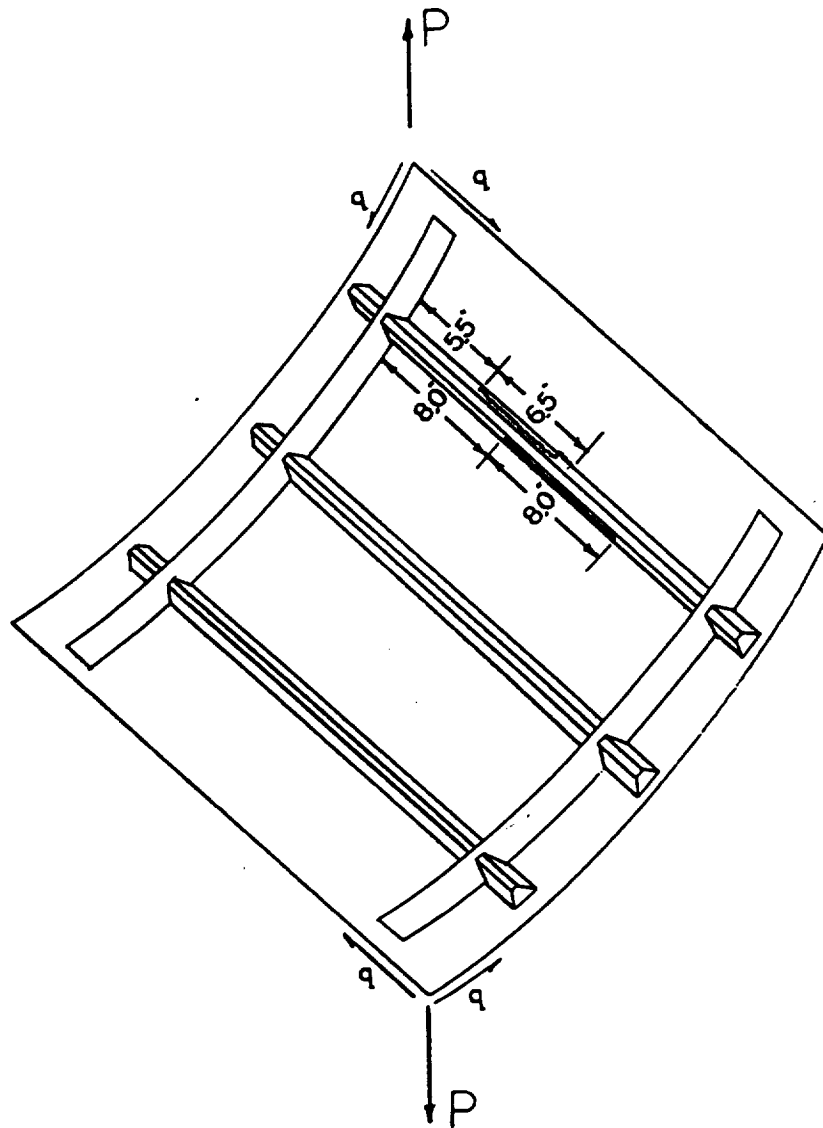


FIGURE 5.23. STIFFENER WEB FAILURE - 69200 CYCLES (SCHEMATIC)

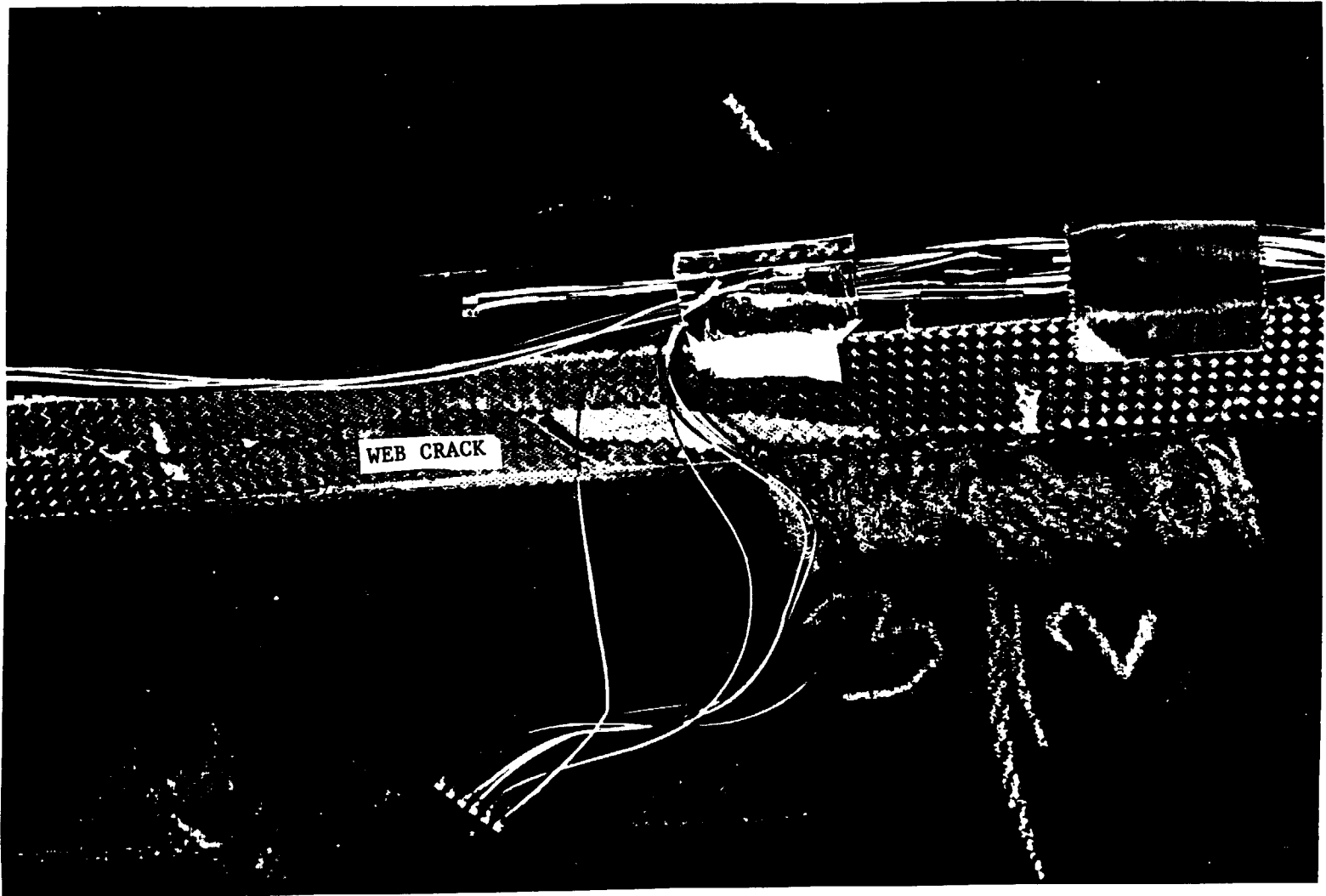


FIGURE 5.24. STIFFENER WEB FAILURE - 69200 CYCLES (PHOTOGRAPH)

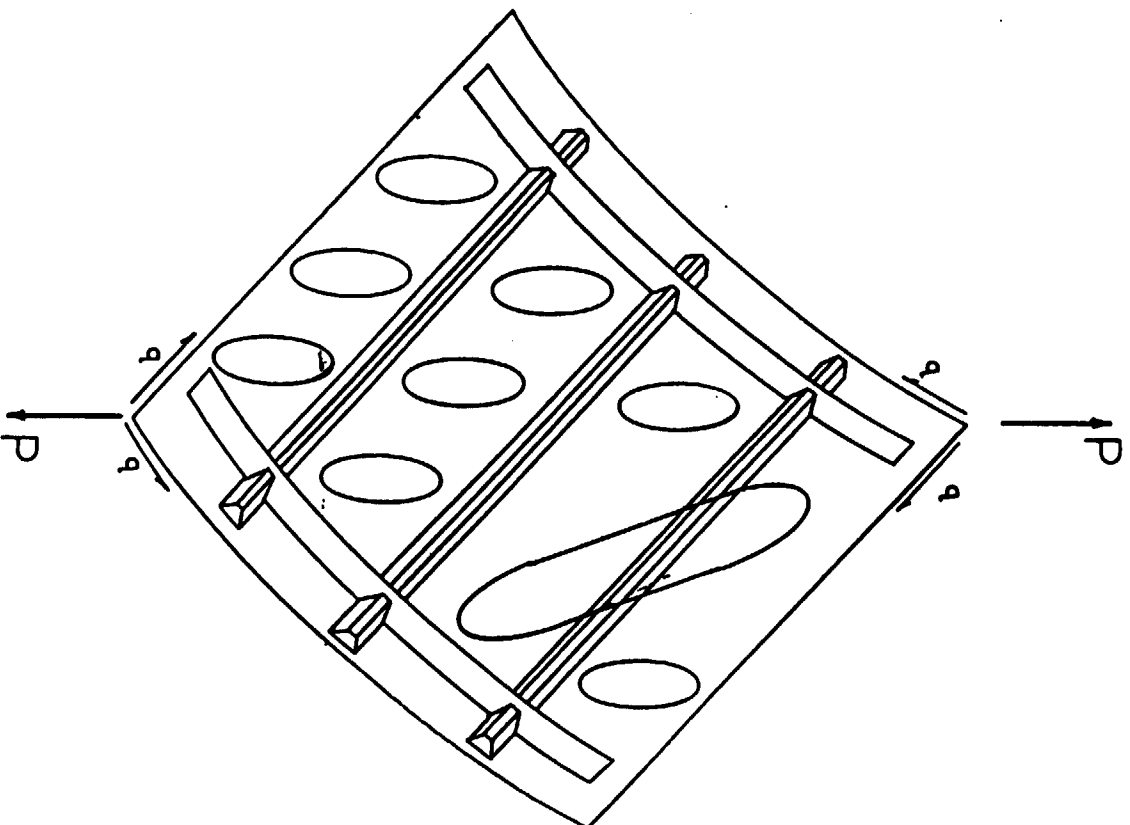


FIGURE 5.25. BUCKLED PATTERN AT 69200 CYCLES



that FAA certification requires a residual strength test after fatigue testing that proves limit load capability. It is advisable, therefore, to include limit load cycles at regular intervals during fatigue testing as a risk reduction measure. That way, if failure occurs during one of these intervals, the structure can still be certified to the cycle level at the end of the previous interval when the last limit load cycle was applied.

Limit load was assumed to be 66 per cent of the average failure load established during static testing (P-24608 pounds or 580 lb/in shear flow). During the quasi-static limit load test a second hat stiffener failed at 16,100 pounds, or 99.5% of the empirical limit load. The location of this failure initiated in the webs of the central hat stiffener at the frame-stiffener intersection corner and grew unstably to the dimensions shown in Figure 5.26. Nonvisible delamination areas also shown in Figure 5.26 at the flanges of the two damaged stiffeners were found using pulse echo techniques. All previously existing cracks, which were theorized to be stress relief cracks only and not life limiting cracks, did not extend during this test. Since the panel essentially passed limit load prior to the second failure, the lower bound on residual shear strength of the fatigue damaged specimen was assigned to be 66% of the experimentally determined ultimate load after 69,200 cycles.

The buckled shape of the panel after failure at limit load is shown in Figure 5.27. Note that the central hat stiffener is no longer entirely effective as a waveform breaker but the intact stiffener remains effective.

Further cycling of the panel to 200,000 cycles was started immediately following the limit load test. Additional nonvisible damage resulting from this cycling is shown in Figure 5.28. No new visible cracks initiated during this interval.

Based on the results of quasi-static strain surveys performed at specific cyclic intervals, the decision to stop the test was made at this point. Refer to Figure 5.19 and note strain gage rosettes number 1-6. Throughout the fatigue test, maximum shear strain during the load cycle was measured at each location, see Figure 5.29 (shear strains are normalized to the shear strain values of the first cycle). Presumably due to the high strain range, rosette 1 malfunctioned at some point between cycle 1000 and cycle 10,000 and gave no more readings. Rosette 2 stopped recording after the 100th cycle and before the 10,000 cycle mark was reached. During inspection after 200,000 cycles, new rosettes were placed on locations 1 and 2 in order to take the final strain survey.

Note that rosettes 3-6 demonstrated significant increases of up to 80% in measured shear strain before and after the limit load test (abscissa = 69,200 cycles). Rosettes 1 and 2 were inactive over this interval but they do show a gradual decrease in strain after 1,000 cycles to a 80% reduction after 200,000 cycles. The jumps in measured strain were interpreted to represent a significant redistribution of load through the specimen which occurred as a result of the damage in the two hat stiffeners. The fact that the strain readings for gages 1 and 2 after 200,000 cycles are 20 to 40% of the values during the first cycle, suggests that very little load goes through the center areas of the specimen. Rather, the primary path for load transfer after the

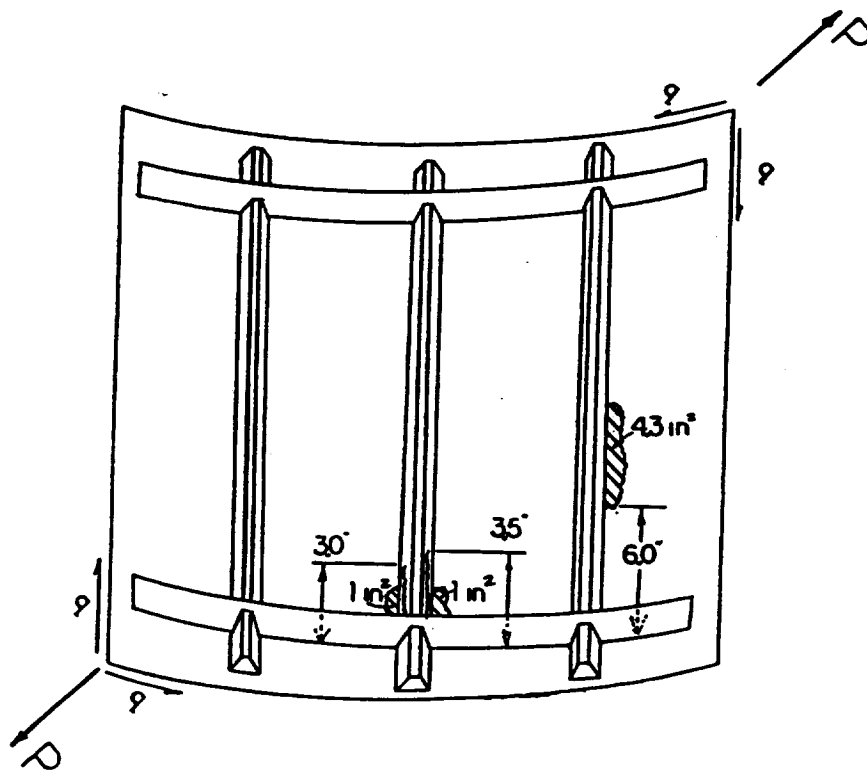


FIGURE 5.26. DAMAGE DURING LIMIT LOAD CYCLE AFTER 69200 CYCLES

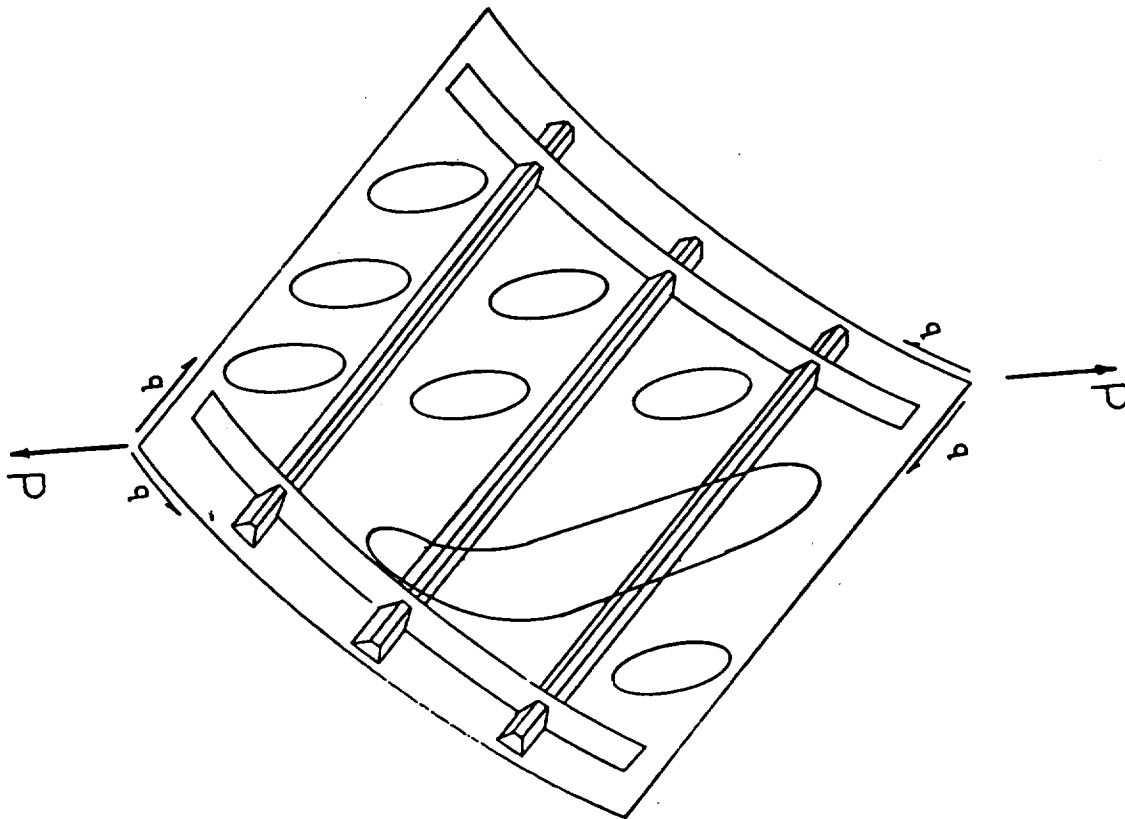
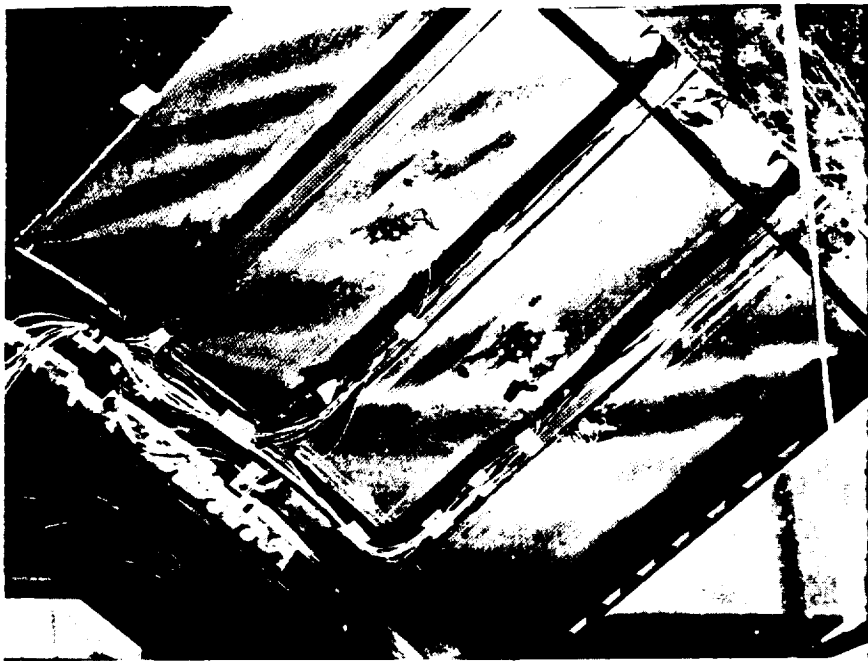


FIGURE 5.27. BUCKLED PATTERN DURING LIMIT LOAD CYCLE

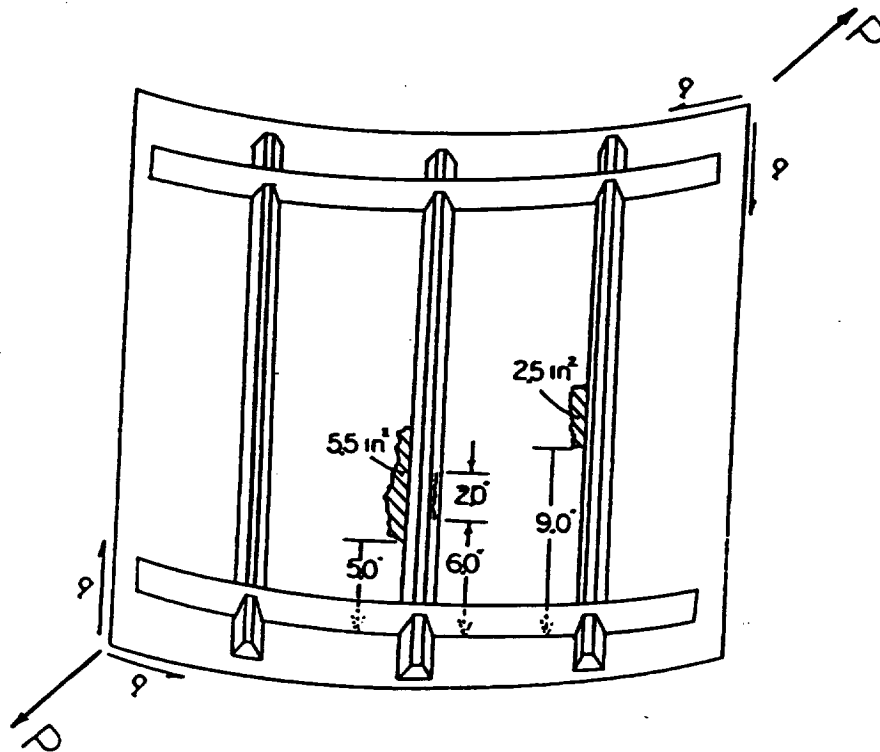


FIGURE 5.28. DAMAGE AFTER 200000 CYCLES

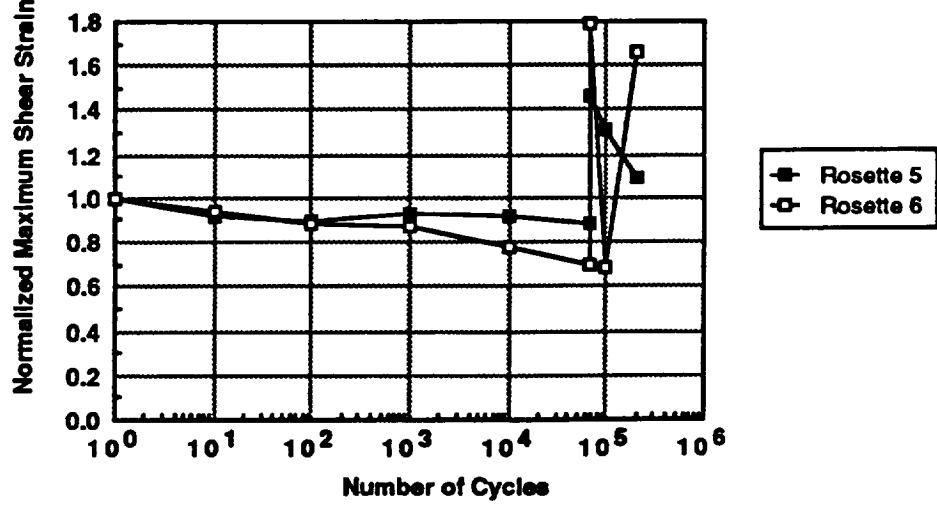
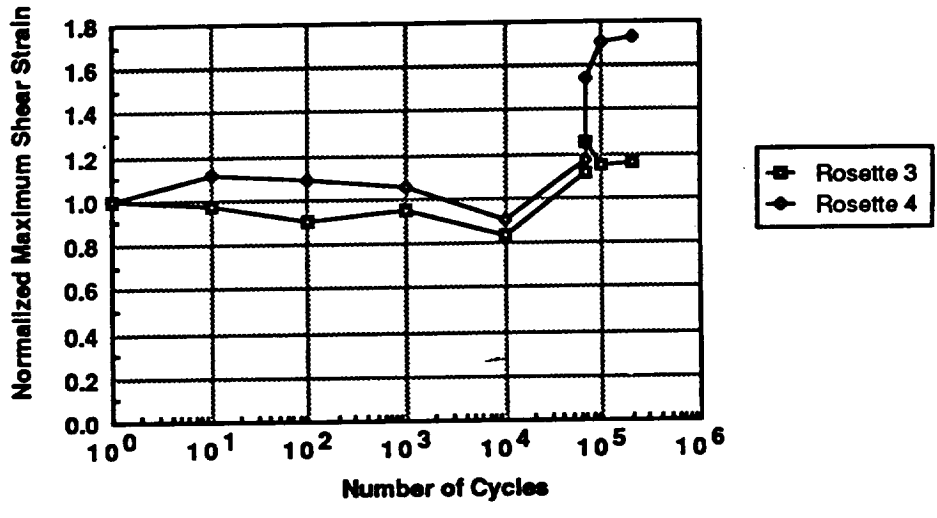
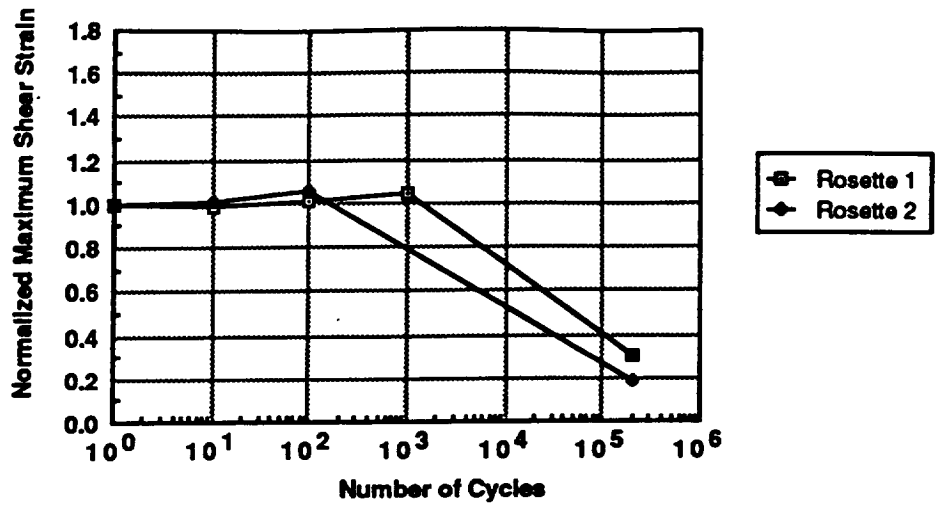


FIGURE 5.29. SHEAR STRAINS AT VARIOUS CYCLE LEVELS

limit load test was around the perimeter of the specimen and the amount of load transfer to the specimen edges increased with cycles as the damage at the center of the specimen increased. Since this load path no longer worked the gage section of the specimen, no useful information on panel performance would be obtained by continuing the test, and thus, the test was discontinued at 200,000 cycles.

The results of the fatigue test are summarized for convenience in Figure 5.30.

## **5.4 CORRELATION OF TEST RESULTS WITH ANALYSIS PREDICTIONS**

Two approaches were used to model the full-scale panel behavior. A nonlinear finite element model, and a modified diagonal tension analysis.

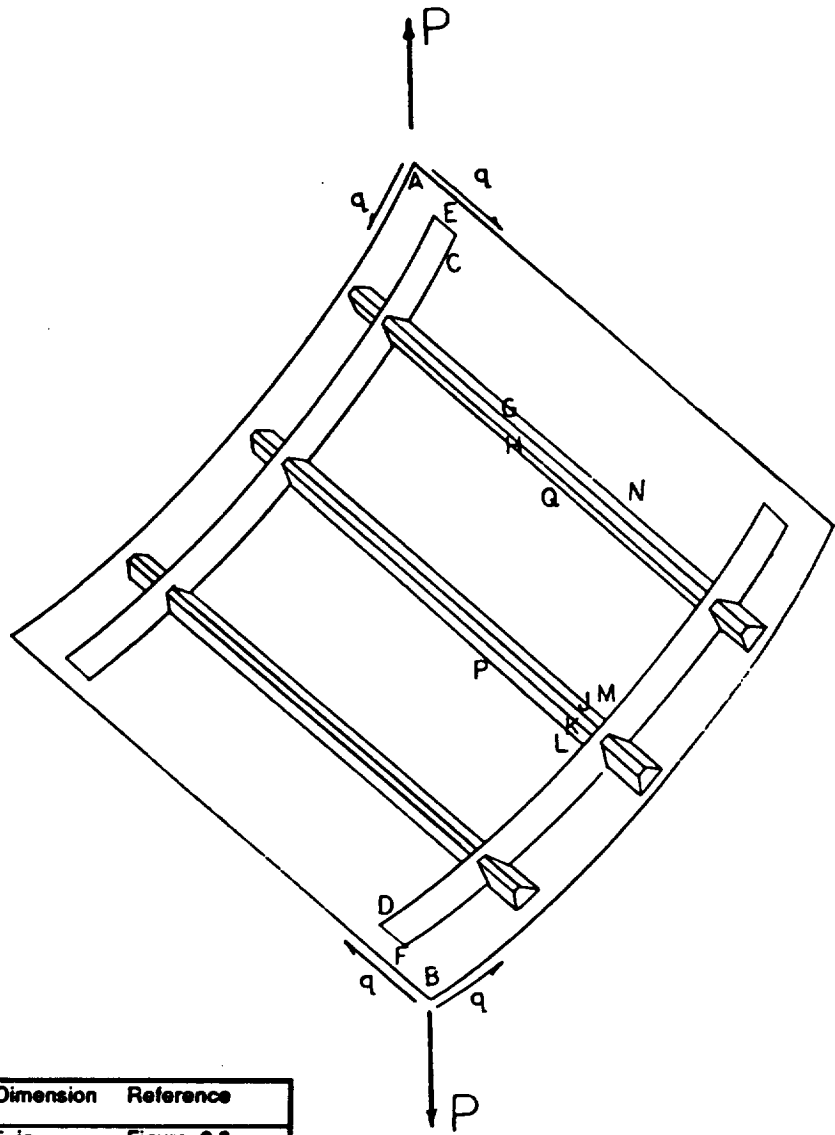
### **5.4.1 FINITE ELEMENT ANALYSIS AND COMPARISON WITH TEST RESULTS**

A refined mesh finite element model was generated using MSC NASTRAN (version 65E, solution 66). The model contains 3365 node points (10095 degrees of freedom) 3152 CQUAD4 elements and 339 CBEAM elements. This mesh gives 60 elements per bay that enable modelling the embedded flange area and capturing the postbuckled shape with accuracy. The test fixture was also included in the finite element model. The model is shown in Figure 5.31.

The picture frame fixture was constrained at one corner to react the diagonal shear load. In addition, the picture frame was constrained in the out-of-plane direction to prevent rigid body rotation of the finite element model. The hinge action of all corner pins was modelled by multiple point constraints between frame flanges which allow the fixture sections to have an in-plane rotation but not to deflect, relative to each other. An additional grid point of one corner pin was constrained along the z-direction in-plane displacement, as shown in Figure 5.31, to suppress the rigid body rotation of the model.

The NASTRAN Solution 66 non-linear finite element modelling option was used to determine the buckling and post buckling behavior of the full scale curved panel under shear load (tension along a diagonal). The basic nonlinear solution method used in NASTRAN for a geometric nonlinearity is the Newton-Raphson iteration process whereby the out-of-balance nonlinear loads are measured and iterated upon to obtain the updated stiffness matrix. The convergence of this iteration is rather time consuming. Therefore, two curved panel models and three picture frame models were built to evaluate the iteration time required for the solution to converge at each load increment without losing significant accuracy in the analysis. The most refined configuration required 339 CPU seconds on an IBM 3090 computer to reach a load approximately twice the buckling load.

A comparison of strain gage data at the center of the panel to finite element predictions is shown in Figure 5.32. The shear strain at a point inside one of the bays (quarter of the distance between the two hat stiffeners) is shown in



Damage Site	Type	Final Dimension	Reference
A	Crack	2.75 in	Figure 2.3
B	Crack	2.50 in	Figure 2.3
C	Crack	2.00 in	Figure 2.3
D	Crack	2.50 in	Figure 2.3
E	Delam	4.5 in <sup>2</sup>	Figure 2.4
F	Delam	4.0 in <sup>2</sup>	Figure 2.4
G	Crack	6.50 in	Figure 2.5
H	Crack	8.00 in	Figure 2.5
J	Crack	5.50 in	Figure 2.7,2.9
K	Crack	3.00 in	Figure 2.7
L	Delam	1.0 in <sup>2</sup>	Figure 2.7
M	Delam	1.0 in <sup>2</sup>	Figure 2.7
N	Delam	4.3 in <sup>2</sup>	Figure 2.7
P	Delam	5.5 in <sup>2</sup>	Figure 2.9
Q	Delam	2.5 in <sup>2</sup>	Figure 2.9

FIGURE 5.30. DAMAGE LOCATIONS AND EXTENT ON FULL-SCALE FATIGUE TEST PANEL

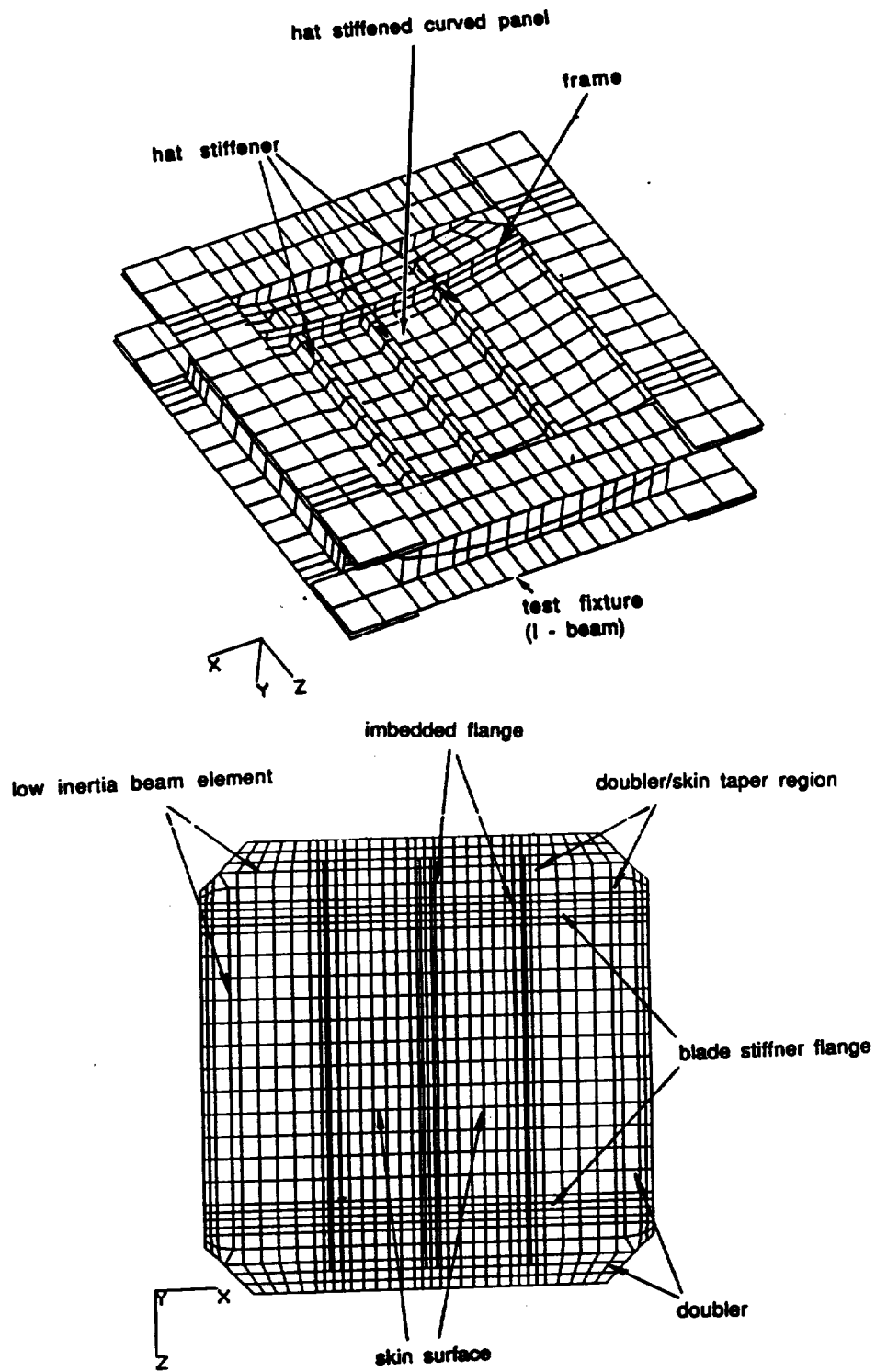


FIGURE 5.31. FULL-SCALE PANEL FINITE ELEMENT MODEL



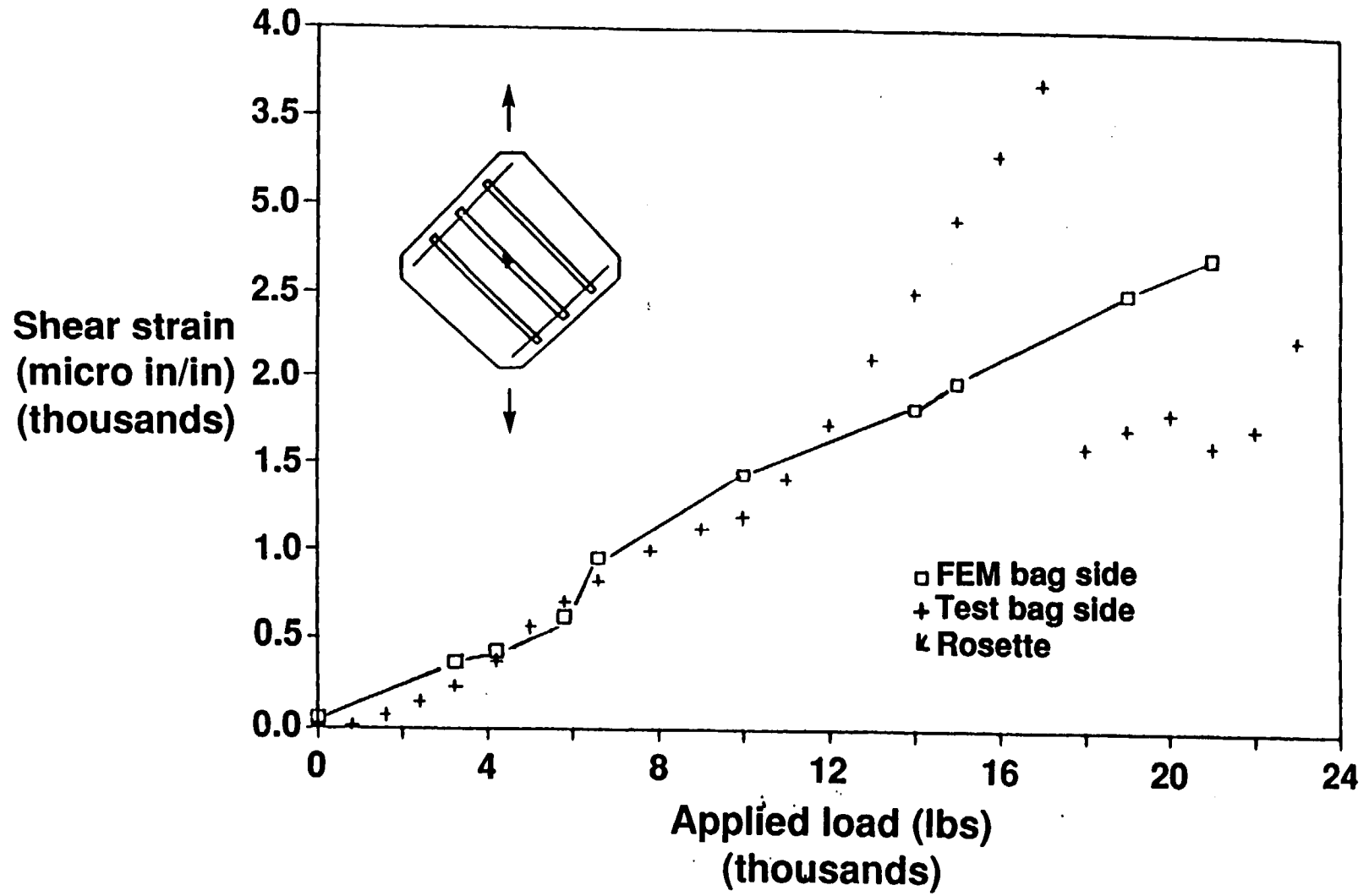


FIGURE 5.32. COMPARISON OF FINITE ELEMENT PREDICTION TO TEST RESULTS AT HAT STIFFENER CENTER (SHEAR STRAINS)

Figure 5.33. The axial strain along the frame axis at the center of one of the outer bays is shown in Figure 5.34. In all cases, test and finite element analysis are in good agreement up to 10000 to 12000 lbs of applied load (postbuckling factor of about 3). The differences at higher loads are due to local failures that occurred (manifesting themselves with loud noises and sharp increases in the deflection gage measurements) and redistributed the load. These local failures were not modelled by the finite element model.

The out-of-plane deflection measured by the deflection gage positioned at the center of one of the two center bays is compared to the finite element predictions in Figure 5.35. For the same load, the deflections predicted by finite elements are 20-30% less than test results through panel failure. The bay buckling load predicted by finite elements is in excellent agreement with the test result of 4000 lbs (94 lbs/in). A more detailed finite element analysis (up to buckling) with the same mesh but with smaller load increments showed the predicted bifurcation load to be 102 lb/in or 8% higher than the bifurcation load indicated by the deflection gage during test. It was a snap-through buckling where the skin, up to that point deflecting in the direction of the panel curvature, reversed direction with a jump in deflection of more than an order of magnitude.

#### **5.4.2 DIAGONAL TENSION ANALYSIS AND COMPARISON WITH TEST RESULTS**

The diagonal tension analysis employed was a modification of the diagonal tension analysis developed by Kuhn [10] and modified by Northrop and McDonnell recently for composite materials [20,21].

In the curved shear panel analysis developed by Kuhn, the stresses are divided into pure shear (unbuckled) and diagonal tension (totally buckled) components. The diagonal tension components are determined by assuming that the buckled web (skin) cannot take compression stresses. Typical panels will fall in between the two extremes of pure shear and diagonal tension. The diagonal tension factor  $k$  is used to indicate the degree of diagonal tension, where  $k=0$  corresponds to pure shear (unbuckled) and  $k=1$  corresponds to pure diagonal tension. This diagonal tension factor  $k$  is calculated from the postbuckling ratio ( $q/q_{cr}$ ) and the panel dimensions as:

$$k = \tanh \left[ \frac{(0.5 + 300 (t ds)/(R df)) \log (q/q_{cr})}{10} \right] \quad (5.1)$$

where  $t$  - skin thickness  
 $ds$  - stiffener spacing  
 $df$  - frame spacing  
 $R$  - panel radius  
 $q$  - applied shear flow

The geometry of the panels is shown in Figure 5.36.

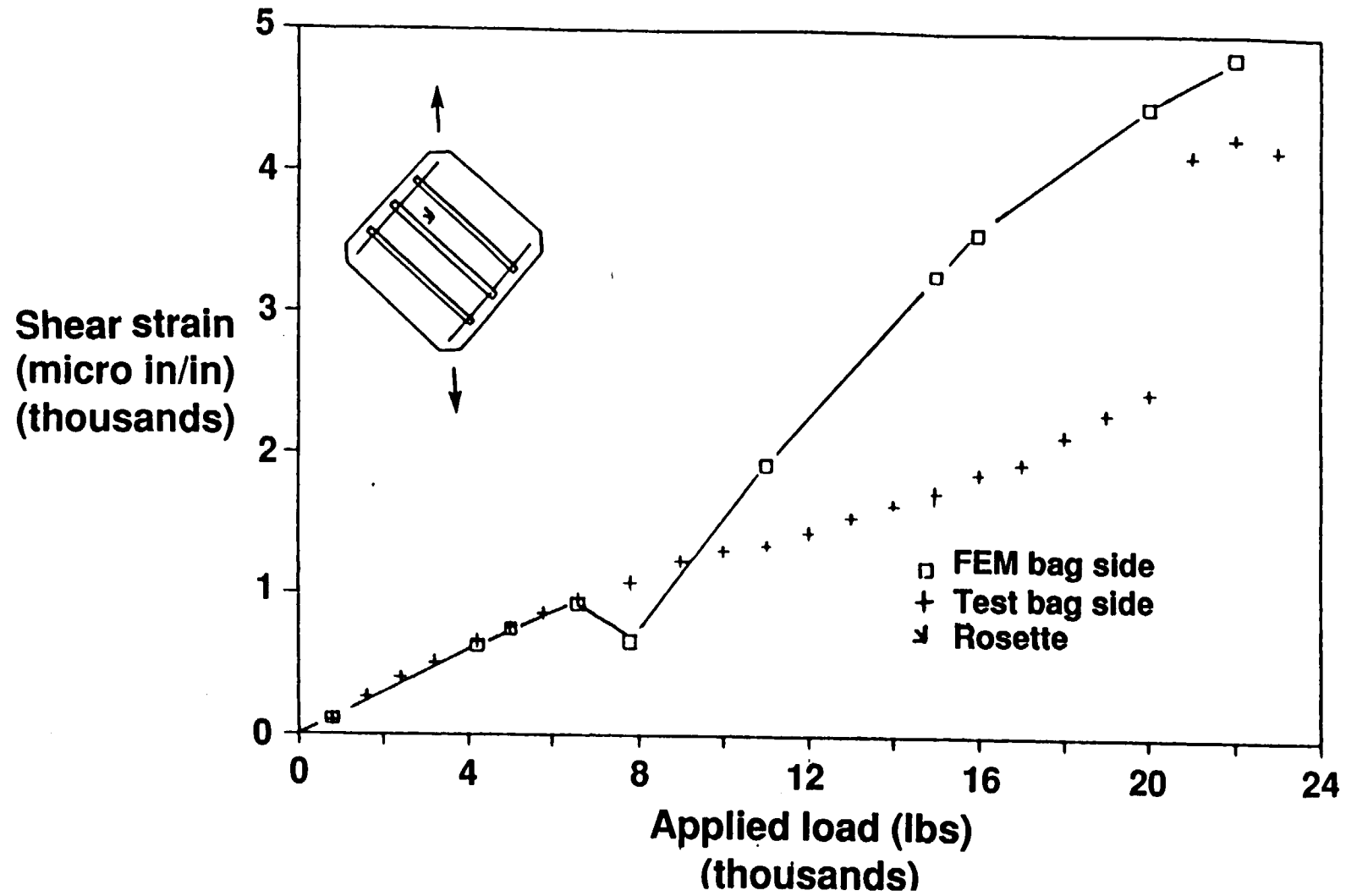


FIGURE 5.33. COMPARISON OF FINITE ELEMENT PREDICTIONS TO TEST RESULTS AT BAY QUARTER POINT (SHEAR STRAINS)

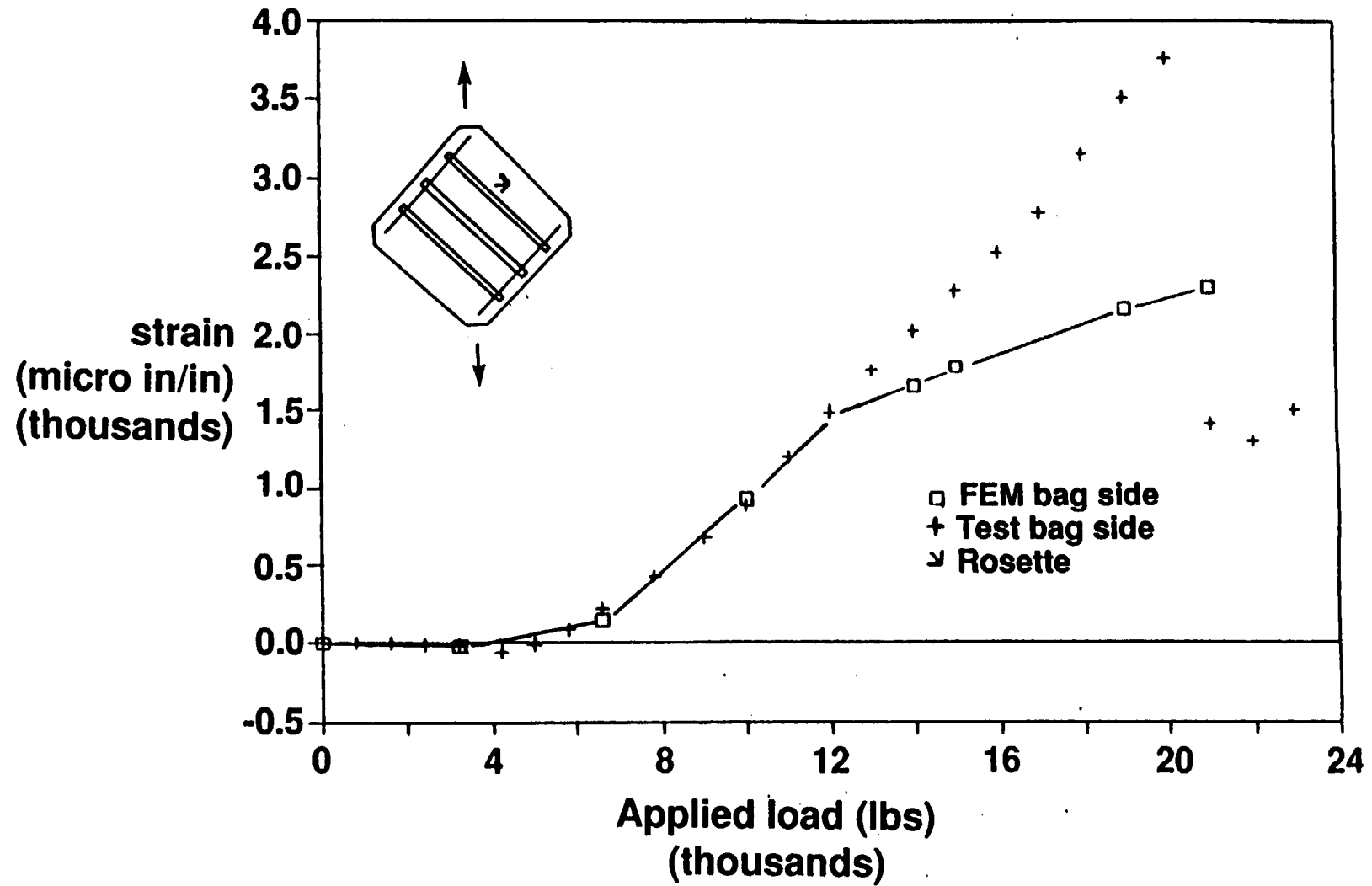


FIGURE 5.34. COMPARISON OF FINITE ELEMENT PREDICTIONS TO TEST RESULTS AT BAY CENTER (STRAIN ALONG FRAME AXIS)

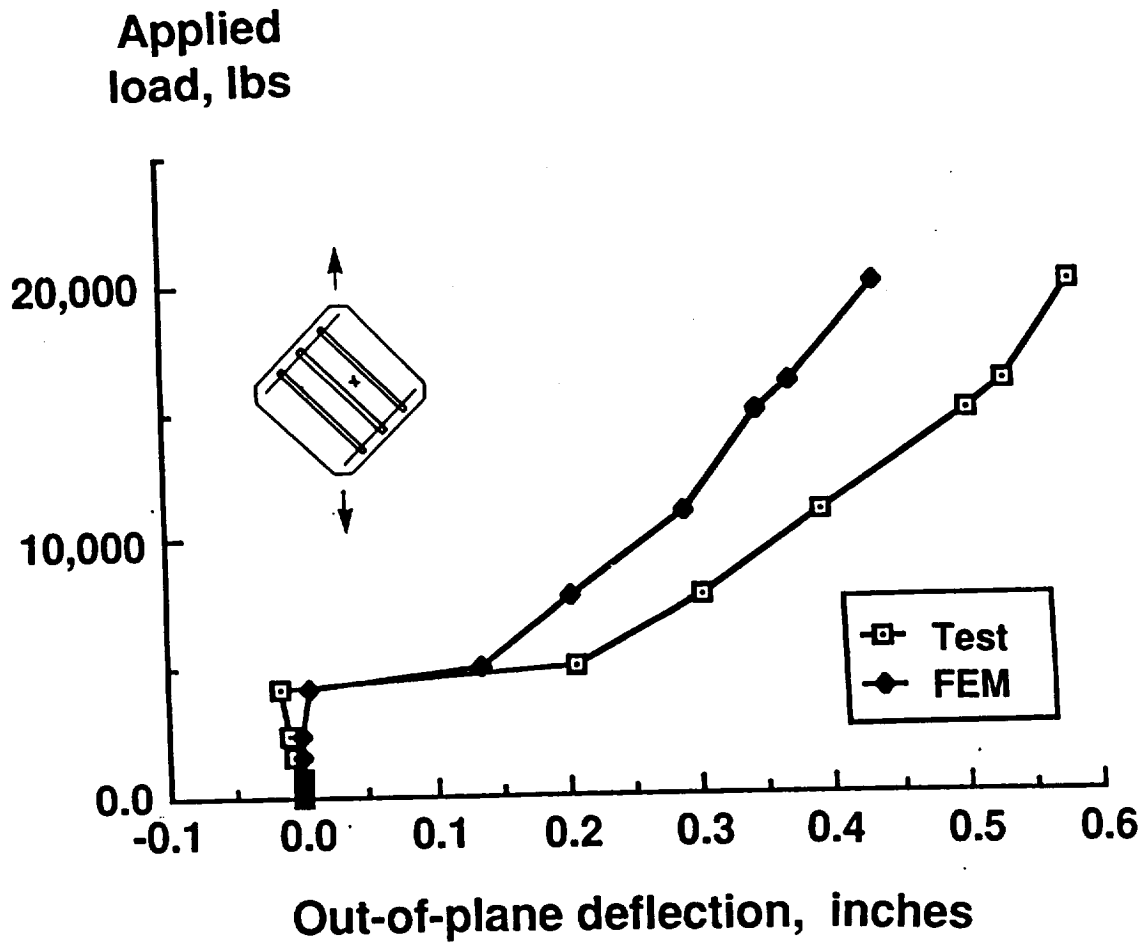


FIGURE 5.35. LOAD VERSUS DEFLECTION PLOT AT BAY CENTER (FINITE ELEMENT PREDICTION AND TEST MEASUREMENT)

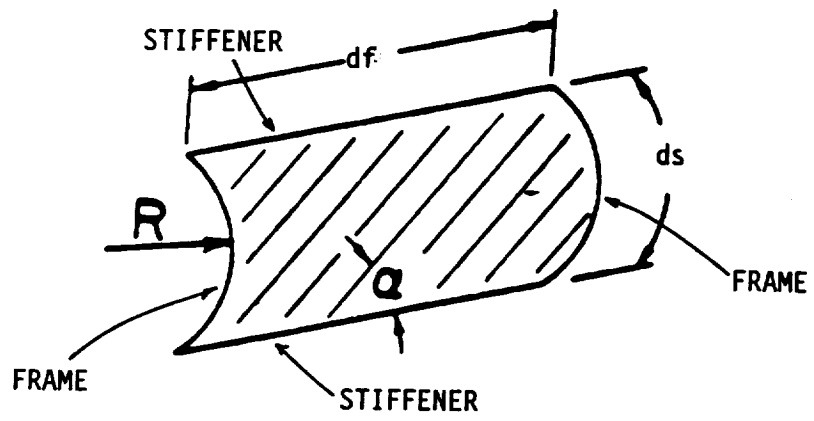


FIGURE 5.36. FULL-SCALE PANEL BAY GEOMETRY

The diagonal tension angle depends on the state of stress in the skin and the panel stiffener and frames, as given by:

$$\tan^2\alpha = \frac{e - e_s}{e - e_f + R_f} \quad (5.2)$$

with

$$R_f = (ds/R)^2 / 24 \quad \text{for } df > ds \quad (5.3)$$

$$R_f = ((df/R)^2 \tan^2\alpha) / 8 \quad \text{for } ds > df \quad (5.4)$$

$$e = \tau/E [2k/\sin 2\alpha + (1-k)(1+\nu)\sin 2\alpha] \quad (5.5)$$

$$e_s = \frac{k\tau \cot\alpha}{A_s/(ds \ t) + 0.5(1-k)} \quad (5.6)$$

$$e_f = \frac{k\tau \tan\alpha}{A_f/(df \ t) + 0.5(1-k)} \quad (5.7)$$

$E$  and  $\nu$  are the skin modulus and Poisson's ratio,  $A_s$  and  $A_f$  are the stiffener and frame cross-sectional areas,  $\tau$  is the applied shear stress, and  $ds$ ,  $df$ ,  $R$ , and  $t$  are as defined above. Strain  $e$  is the skin strain in the direction of the buckle ( $\alpha$ ), and  $e_s$  and  $e_f$  are the strains in the stiffener and frame averaged over their lengths. Equation 5.2 is solved by iteration to determine the diagonal tension angle.

These equations were modified by Northrop [20] to account for the orthotropic nature of composites as follows:

$$\tan^2\alpha = \frac{e - e_s}{e - e_f + R_f} \quad (5.8)$$

$$e = \tau/E_wa [2k/\sin 2\alpha + E_wa/2G_{rs} (1-k) \sin 2\alpha] \quad (5.9)$$

$$e_s = \frac{k\tau \cot\alpha}{\overline{E}A_s/(ds \ t) + 0.5(1-k) E_wa} \quad (5.10)$$

$$e_f = \frac{k r \tan \alpha}{\overline{E A f} / (d f t) + 0.5(1-k) E_{w f}} \quad (5.11)$$

$$\overline{E A s} = E A s \frac{E I s}{\overline{E I s}} \quad (5.12)$$

$$\overline{E A f} = E a f \frac{E I f}{\overline{E I f}} \quad (5.13)$$

where  $E_{w a}$  is the modulus of the web in the direction of the buckle  
 $E_{w s}$  and  $E_{w f}$  are the web (skin) moduli in the direction of the stiffener and frame,  
 $G_{r s}$  is the skin shear modulus,

$\overline{E A s}$  and  $\overline{E A f}$  are the effective axial stiffnesses of the stiffeners and frames at the skin line ( $E A s = E I s + E A y$ ),

$\overline{E I s}$  and  $\overline{E I f}$  are the stiffener and frame bending stiffness at the skin line.

The modulus of the web in the direction of the buckle is calculated from

$$E_{w a} = 1 / [m^4 / E_{x w} + m^2 n^2 (1 / G_{x y w} - 2 \nu_{x y} / E_{y w}) + n^4 / E_{y w}] \quad (5.14)$$

with  $m = \cos \alpha$ ,  $n = \sin \alpha$ ,  $m^2 = m^2$ ,  $m^4 = m^4$ , etc

The average strains in the stiffener and frame, accounting for eccentricity, are:

$$e_{s \text{ ave}} = e_s \frac{\overline{E A s}}{E A s} \quad (5.15)$$

$$e_{f \text{ ave}} = e_f \frac{\overline{E A f}}{E A f} \quad (5.16)$$



The maximum strains in the stiffener and frame (on the skin surface) are:

$$e_{s \max} = e_s [1 + 0.775 (1-k) (1-0.8 AR)] \quad (5.17)$$

$$e_{f \max} = e_f [1 + 0.775 (1-k) (1-0.8 AR)] \quad (5.18)$$

where  $AR = ds/df$  if  $ds < df$ , and  $AR = df/ds$  if  $ds > df$

The bending moment induced in the stiffeners and frames due to the radius of the panel is

$$M_{st} = k q ds df^2 \tan \alpha / (24R) \quad (\text{clamped ends}) \quad (5.19)$$

$$M_{st} = k q ds df^2 \tan \alpha / (12R) \quad (\text{simply supported ends}) \quad (5.20)$$

$$M_{fr} = k q df ds^2 \tan \alpha / (12R) \quad (5.21)$$

Equation 5.19 is used when the stiffeners are continuous, as for a typical airframe fuselage where there is a fixed end moment at the ends of the stiffener. Equation 5.20 is used when the stiffeners are not continuous, as for our picture frame shear tests, where the moment at the end of the stiffener is zero or near zero.

The analysis procedure described above was implemented in a computer code (CWEB) and used to analyze the full-scale test panel for this program. The properties used in this analysis are given in Table 5.3. The results are given in Table 5.4 for a shear flow of 514 lb/in, which corresponds to a panel load of 22000 lbs. All of the curved panels failed at loads between 22000 and 26000 lbs.

The average diagonal tension strain is predicted to be 2900 microstrain for an applied shear flow of 514 lb/in. This average strain is not strictly comparable to the strains measured during testing since it does not consider bending strains due to the diagonal tension buckles. For a direct comparison, the bending effects from the test strain readings should be removed.

The test strain gage measurements for the first two full-scale tests are shown in Table 5.5. The locations of the strain gages are shown in Figure 5.37. Gages 12 and 13 are back to back on the skin at the bay quarter point. Gages 14 and 15 are back to back gages on the skin at the middle of the bay.

Table 5.3  
Full-Scale Panel Properties Used in the Analysis

Configuration	df = 20 in. ds = 6.5 in. R = 40 in.
Skin Properties	t = 0.030 in. Ex = Ey = 2.7E6 psi Gxy = 4.54E6 psi $\nu_{xy}$ = 0.73
Stiffener Prop.	As = 0.1749 in Es = 4.85E6 psi Is = 0.0329 in ys = 0.286 in EAs = 848000  EAs = 590000 EIs = 159000
Frame Properties	Af = 0.3457 in Ef = 8.36E6 psi If = .1535 in yf = 0.684 in Eaf = 2890000  Eaf = 1407000 EIf = 1283000

Table 5.4  
Analysis Results for Full-Scale Panel

applied shear flow	= 514 lb/in
k	= 0.552
$\alpha$	= 42.17 degrees
qcr	= 115 lb/in
Ewa	= 9.36E6 psi
q/qcr	= 4.47
avg diagonal tens strain e	= 0.0029
stiffener strain es	= -0.0029
frame strain ef	= -0.0029
avg stiffener strain esav	= -0.0020
avg frame strain efav	= -0.0014
max stiffener strain esmax	= -0.0036
max frame strain efmax	= -0.0037
stiff'r bending moment Mst	= 1410 in-lb

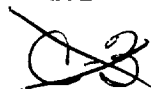


Table 5.5  
Measured Strains from Curved Panel Tests  
(Applied Load 22000 lbs)

PANEL NO	GAGE NO	0 LEG	45 LEG	90 LEG	45 MIDPLANE	
<b>SKIN GAGES</b>						
1	12	11100	3700	1400		
	13	5500	2200	-11000	2950	
	14	8000	4500	2000		
	15	5200	2500	-7800	3500	
	2	12	5900	3400	1700	
	13	3200	2300	-6800	2850	
	14	4400	2900	-5800		
	15	6600	3900	200	3400	
<b>STIFFENER GAGES</b>						
1	9(cap)	6900				
	10(skin)	-1900		Moment - 1403 in-lb		
2	9(cap)	6300				
	10(skin)	-600		Moment - 1100 in-lb		

Averaging the 45 degree gages on the top and bottom of the skin to remove bending effects gives the diagonal tension strain at the skin midplane (last column in Table 5.5) for comparison with analysis (average diagonal tension strain in Table 5.4). The range of measured values (2850 to 3500 microstrain) compares well with the theoretical prediction of 2900 microstrain especially considering that only two skin locations were sampled.

Using the strain gage reading from gages 9 and 10 on the top and bottom of the stiffener to calculate the moment gives a range of values between 1400 and 1100 in-lb (Table 5.5 moment values). These values compare very well with the predicted moment value of 1410 in-lb (last entry in Table 5.4 calculated from equation 5.20).

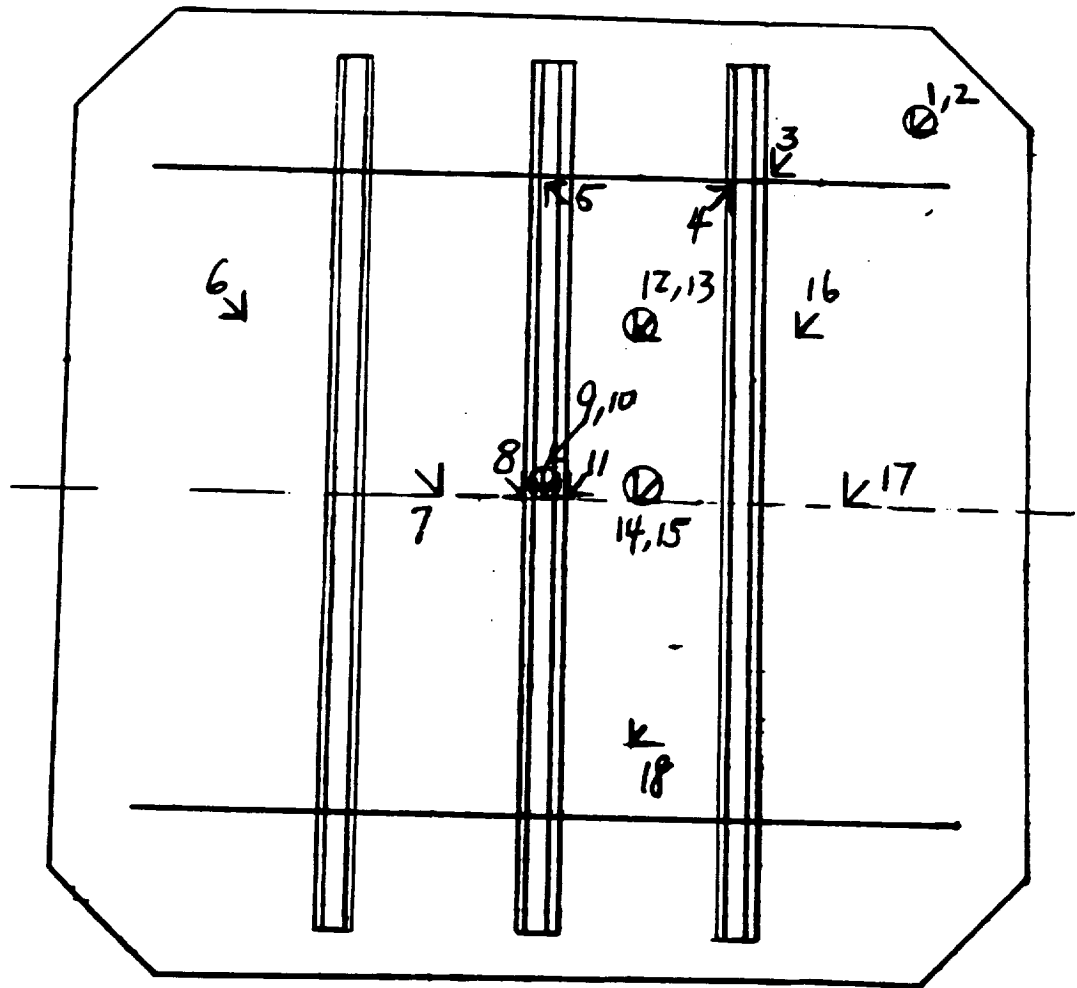


FIGURE 5.37. STRAIN GAGE LOCATIONS IN FULL-SCALE STATIC TESTS

These good correlations show that the modified diagonal tension method can be used successfully for the analysis of curved composite panels. More testing with panels of different configurations is needed to ensure that the method is applicable over the range of panel designs used in industry. With the applicability of the diagonal tension method established, the use of expensive and complex nonlinear finite element analyses is not required for production stress analysis, although finite elements should be used for research studies to gain further insight into the phenomenon. In addition, as is shown from the results of the next section, finite elements are invaluable in predicting failure especially when local phenomena such as web buckling are involved.

### **5.4.3 FAILURE PREDICTIONS**

The results of the building block evaluation showed that the common failure modes expected in stiffened panels such as frame-stiffener intersection failure, and skin stiffener separation should be suppressed in the full-scale panel since the panel design with the built-in shear tie and embedded flange had either very high failure loads (Skin-Stiffener Separation Specimen) or did not show that failure mode at all (Frame-Stiffener Intersection Specimen). The remaining failure modes of skin tearing and stiffener crippling were examined and the failure loads compared to the finite element predicted loads in the skin and hat stiffener. The loads in the panel were found to be too low to cause failure of the corresponding members assuming a failure load equal to the failure load for the corresponding mode as measured during the building block evaluation. This agrees with the failure mode observed for the full-scale panel (see section 5.3.1) which consisted of cracks that started near the hat stiffeners or in the hat stiffener webs and were caused by high bending and twisting moments due to the large postbuckling deflections. This failure mode was very similar to that of the frame-stiffener intersection specimen.

As a first approximation, failure of the full-scale panels was predicted using the results of the flat frame-stiffener intersection specimens which showed a very similar failure mode (see Section 4.2.6). As is shown in Figure 5.38, the shear strains at the bay center for the two specimens are very close to each other up to a load of 12000 lbs. At that point, the full-scale panel diverges probably due to a change in the mode shape or local buckling of the hat stiffener webs (see below). It is believed that the strains at the location where final failure started for both flat and curved specimens are similar and thus the loads (in lbs/in of shear) at which internal strains reach the material allowables should be the same for both types of specimen. The failure load for the flat specimen then should be a reasonable approximation to the full-scale article failure load. As already mentioned, the failure load for the full-scale article was 580 lbs/in (Table 5.2) which is 6% lower than the value of 614 lbs/in that the flat specimen failure would predict.

To gain more insight in the failure mechanism, the finite element model was revisited in light of observations made during (and after) static and fatigue testing of the full-scale panels.

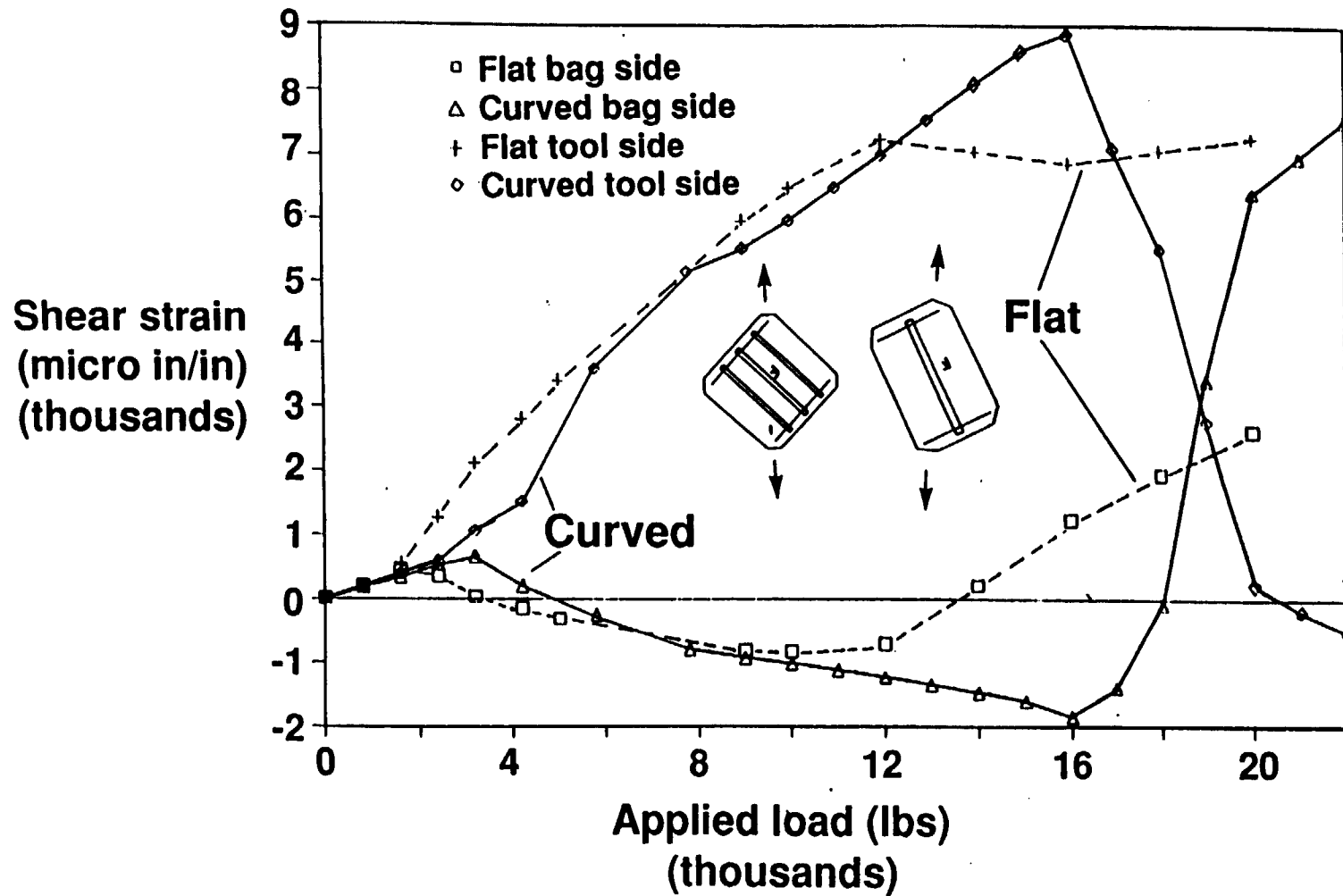


FIGURE 5.38. SHEAR STRAIN COMPARISON FOR INTERSECTION AND FULL-SCALE TESTS (BAY CENTER)

Observations during fatigue testing indicated that the hat stiffener webs were buckling during loading in a short wavelength (along the web axis) pattern. Examination of the failed static specimens showed cracks in these webs. It was decided to revisit the analysis model in that area and perform a local model of the hat stiffener web using the global full-scale model results as input to the local model.

The global and local regions considered are those denoted as hat stiffener #1 and shown in Figure 5.39. Since the height of the web in the global model was modelled with only one element, the admissible displacement field (linear between nodes) of the web could not adequately reflect buckling-type deformations between the base and the cap of the hat stiffener. Strength analysis using the results of the global model yielded a minimum margin of safety equal to 2.37 for element 7004. It was proposed that a more refined finite element mesh would allow both the buckled shape and failure point of the web to be identified.

The first local finite element model included the area of web elements with the minimum margin of safety (Nos 7001 to 7005), (Figure 5.40). Boundary conditions around the highlighted perimeter of elements 7001 through 7005 were applied by means of specified nodal displacements (Degrees Of Freedom 1-3) and rotations (DOFs 4-6) at nodes of the local model with exact correspondence to nodes of the global model. Linear interpolation of all six boundary conditions was used for local boundary nodes in between those boundary nodes with correspondence. The total displacements and rotations associated with a load of 24100 lb (568 lb/in) which is very close to the average failure load, were extracted from the global model and incrementally applied to the boundary of the local model in forty equal increments using the NASTRAN nonlinear finite element solution sequence 66. The nonlinear nature of SOL 66 allows the buckled configuration of the web to be captured numerically.

At boundary conditions associated with 24100 lb, the deflected shape obtained using the first local model is shown in Figure 5.41. This result was viewed in a critical light because of the abrupt termination of the buckled waveform near the right edge of the model. It was suspected that the forced linear variation of boundary conditions along this edge, a kinematic constraint, produced an artificial stiffening by not allowing nodes between the cap and the base of the web to take on a buckled configuration. Several different iterative schemes, varying the displacement increments, were used in an attempt to rectify the improper deformed shape, however, all schemes which were tried yielded the same final shape.

The existence of the artificial stiffening was verified by examining margins of safety for each ply calculated by classical laminated plate theory. In this study the Hoffman failure criterion [22] was used. The form of the criterion allows unequal values of tension and compression strength in the material directions and was defined as the Hoffman Failure Number (HFN):

$$\text{HFN} = 1 - (S_{11} * S_{11} / X_t * X_c) - (S_{22} * S_{22} / Y_t * Y_c) + (S_{11} * S_{22}) / X_t * X_c - (X_c - X_t) * S_{11} / X_t * X_c - (Y_c - Y_t) * S_{22} / Y_t * Y_c - (S_{12} * S_{12}) / T * T$$

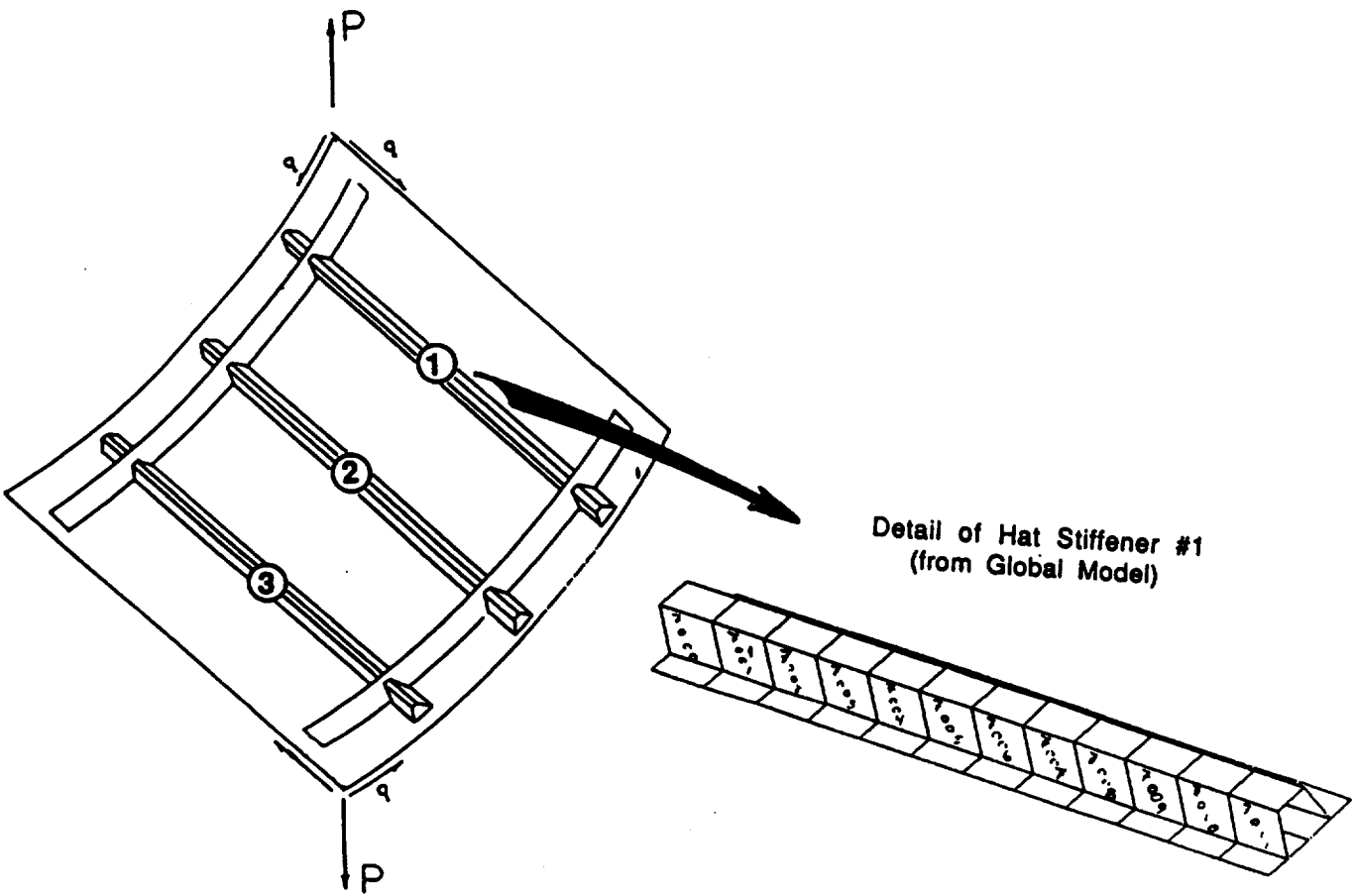


FIGURE 5.39. GLOBAL FINITE ELEMENT MODEL AND LOCAL REGION OF INTEREST



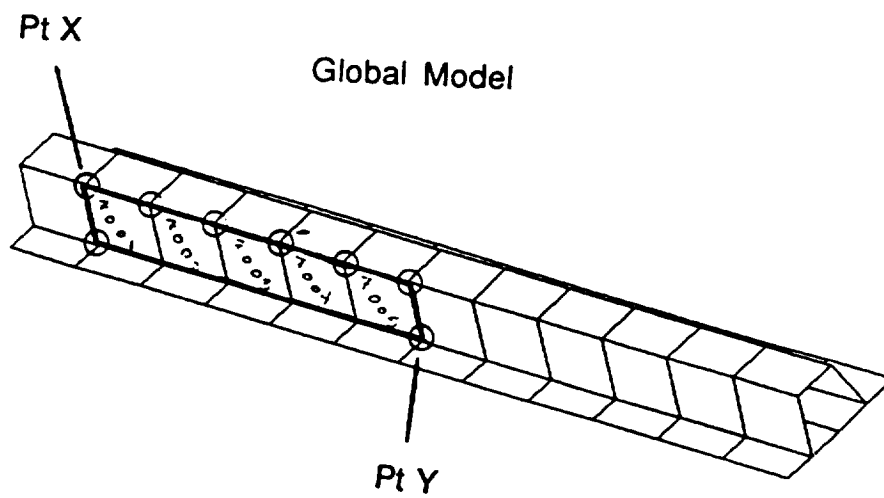
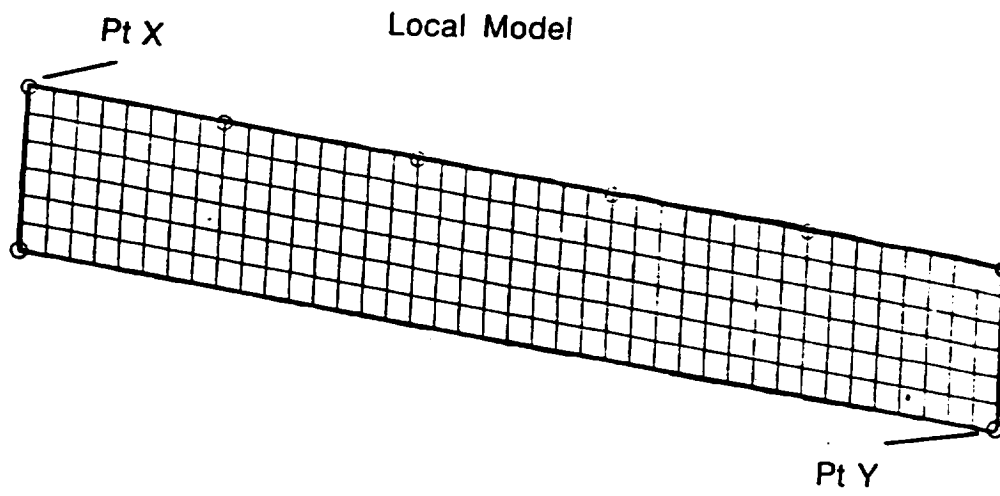


FIGURE 5.40. LOCAL FINITE ELEMENT MODEL #1

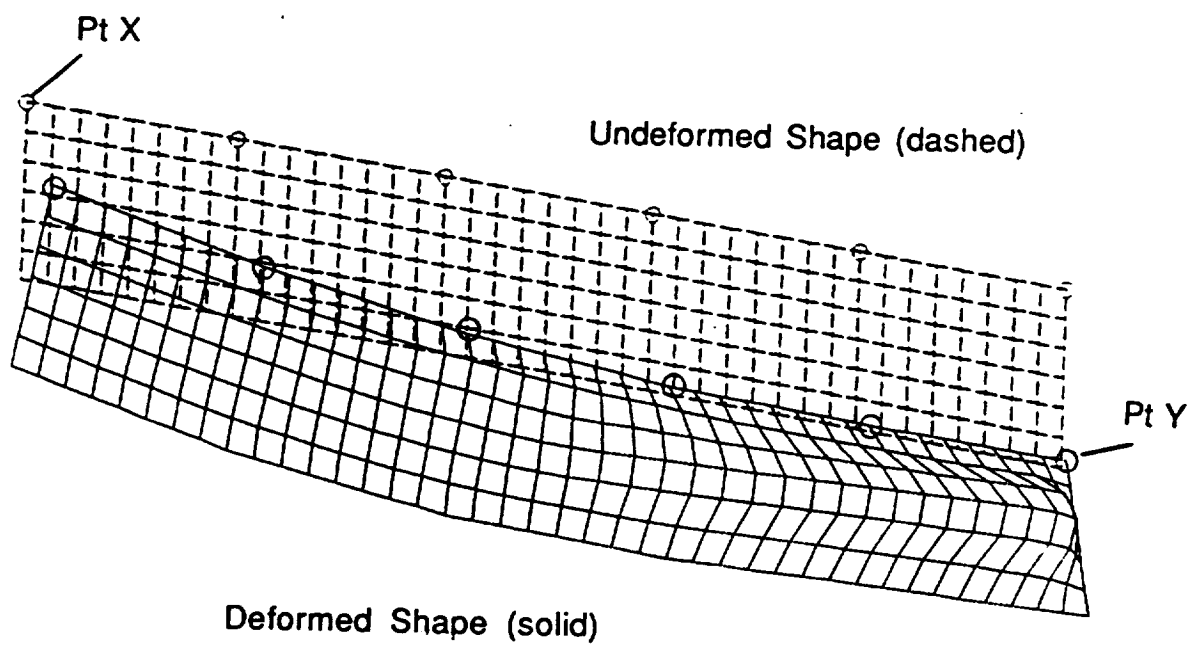


FIGURE 5.41. DEFORMED SHAPE OF LOCAL MODEL #1 AT 24100 LB OF APPLIED LOAD

when  $HFN > 0$ , no failure of ply,  
when  $HFN \leq 0$ , failure of ply,

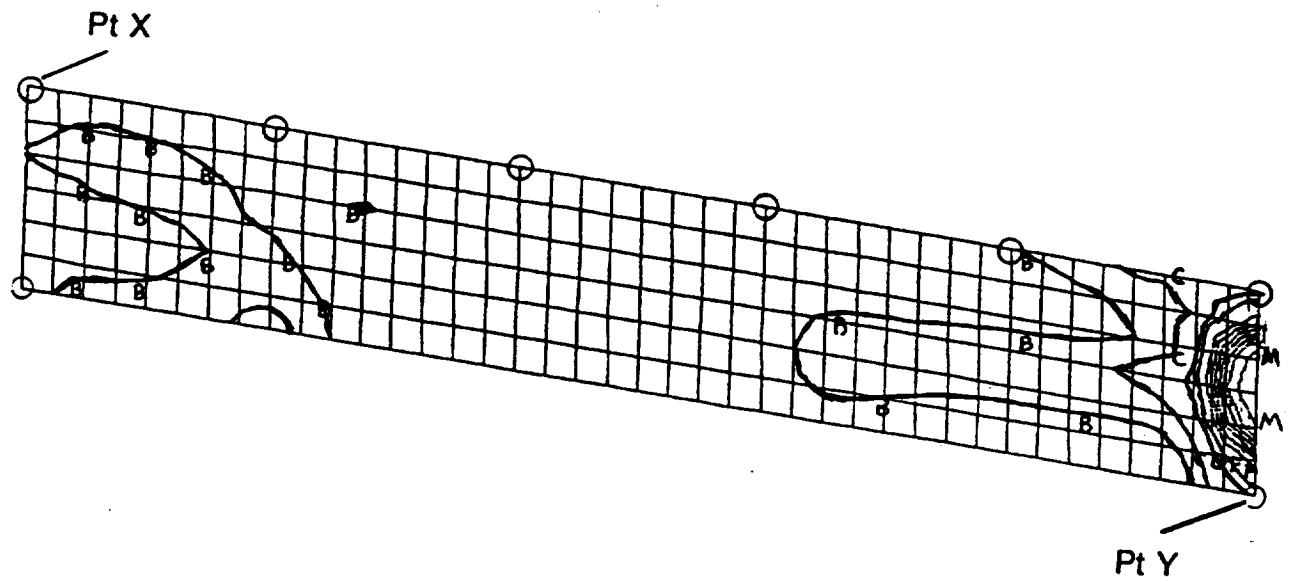
where  $S_{11}$  = calculated stress in fiber (or warp) direction,  
 $S_{22}$  = calculated stress in transverse (or fill) direction,  
 $S_{12}$  = calculated in-plane shear stress,  
 $X_t, X_c$  = tension, compression strength in fiber direction,  
 $Y_t, Y_c$  = tension, compression strength in transverse direction,  
 $T$  = in-plane shear strength

An automated routine to postprocess NASTRAN CQUAD4 element results (i.e. in-plane normal, shear, bending, and twisting loads) was written to calculate the HFN for each element and graphically present the results. A contour plot of HFN calculated for local model #1 and mean material strength allowables is shown in Figure 5.42. As hypothesized above, a large amount of load has been transferred to the artificially stiffened right end as evidenced by the cluster of contour lines near the rightmost edge. Since the very close grouping of contours was not indicated by the global model, the results of model #1 were judged to be a function of boundary condition overconstraint and therefore not useful for analysis.

To overcome the problem of boundary overconstraint, another local model was constructed wherein the linear variation of edge boundary conditions was more realistic. This second model, shown in Figure 5.43, was of the entire length of the hat stiffener web between the solid inverted-T frames which served as circumferential stiffeners. The solid frames ( $t=0.072$ " ) were expected to sufficiently constrain the web to follow the linear shape of the mousehole (cutout) in that area and, thus, provide end conditions for the web ( $t=0.015$ " ) reasonably approximated by linear variation. The shear ties linking the ends of the webs to the solid frames provided additional support.

The deformed shape of local model #2 at applied displacements and rotations associated with 24100 lb (568 lbs/in) is shown in Figure 5.44. The twisting undulations of the web from the leftmost to the rightmost edge were noted during both static and fatigue testing. Hoffman Failure Numbers for mean strength allowables are presented graphically in Figure 5.45a. The detailed contour output shows the lowest margin lies between contours N and O, the exact value being 0.072. Assuming stresses to scale linearly with load, an acceptable approximation at this point of the postbuckled analysis, the percent error between the analysis and the applied load which was very close to the average test result is +7.2%. In order to get an idea of where the test results lie with respect to anticipated material variability, a local analysis was performed using B-basis allowables and produced a minimum margin of safety in the same location (results not shown) but equal to -0.033, a -3.3% error thus bracketing the test results.

A photograph of the exact same location highlighted in Figure 5.45a is shown in Figure 5.45b. It was taken from full-scale panel No 3 after failure. The distance of the crack, evident in the hat stiffener web, from the frame-stiffener intersection corner is the same as the location of minimum margin in Figure 5.45a. Only the location across the web is different (by 0.6 inches).



Contour Letter	Hoffman Failure Number (Mean)	Contour Letter	Hoffman Failure Number (Mean)
A	1.000	I	-1.000
B	0.750	J	-1.250
C	0.500	K	-1.500
D	0.250	L	-1.750
E	0.000	M	-2.000
F	-0.250	N	-2.500
G	-0.500	O	-3.450
H	-0.750		

FIGURE 5.42. HOFFMAN FAILURE NUMBERS OF LOCAL MODEL #1 AT 24100 LB OF APPLIED LOAD

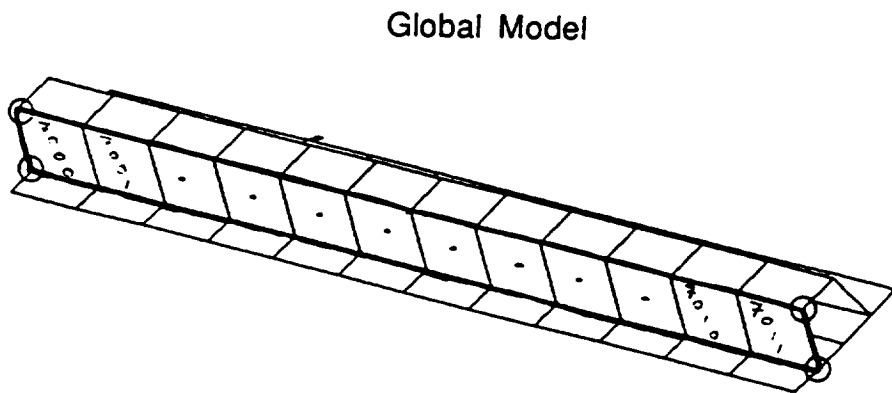
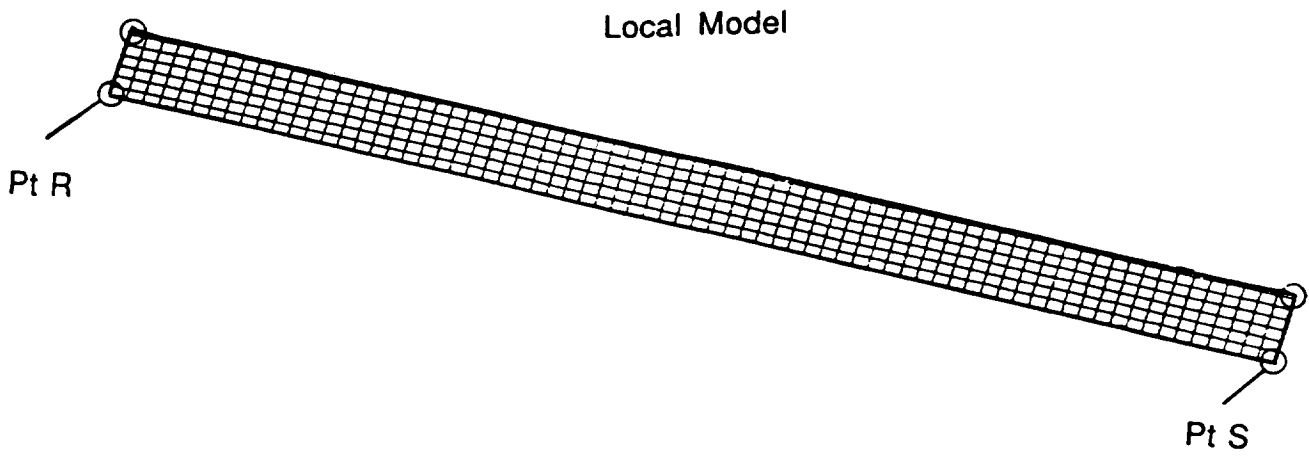


FIGURE 5.43. LOCAL FINITE ELEMENT MODEL #2

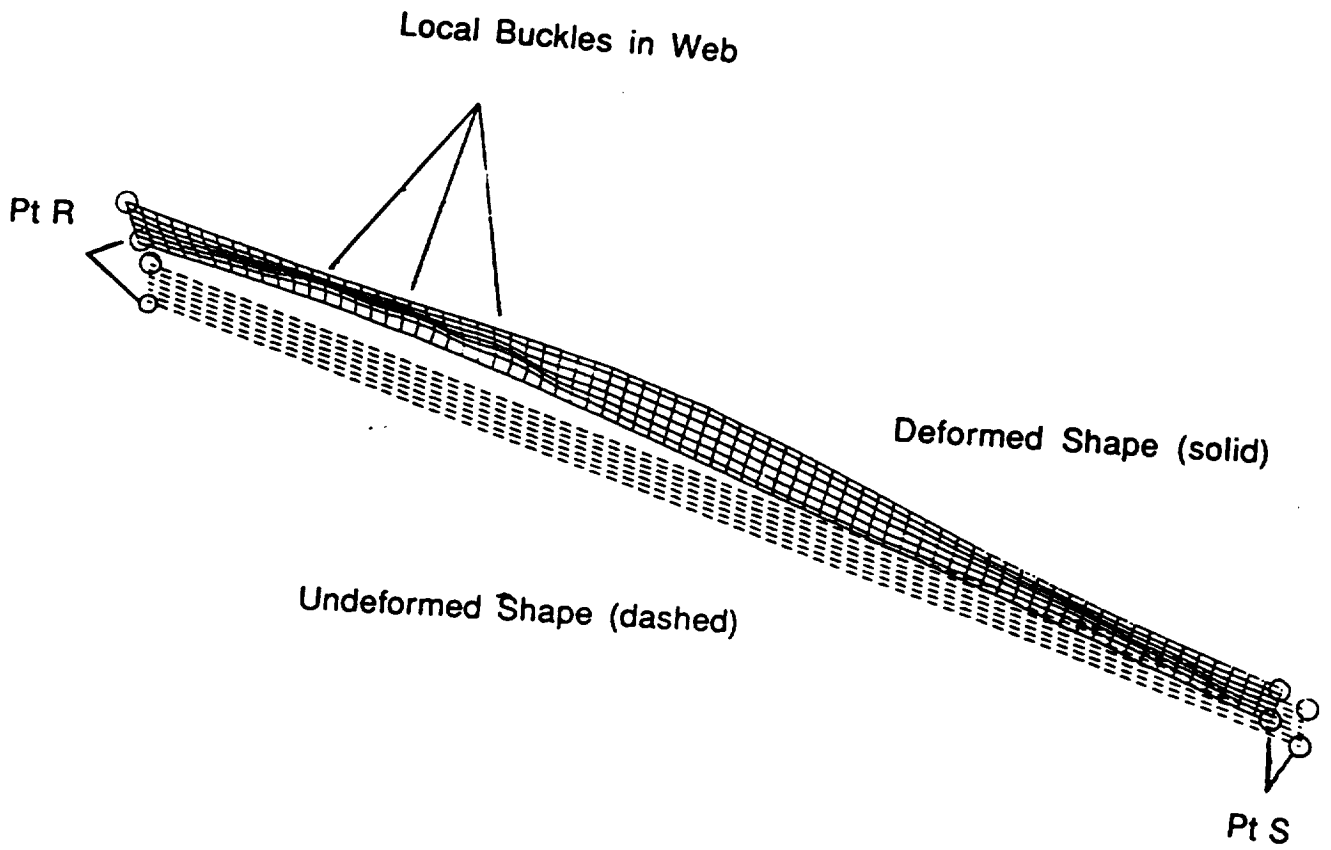
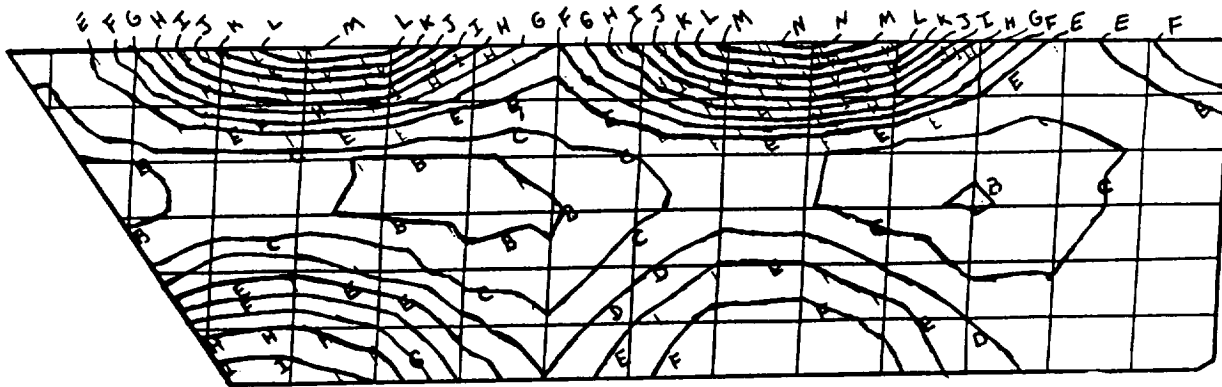
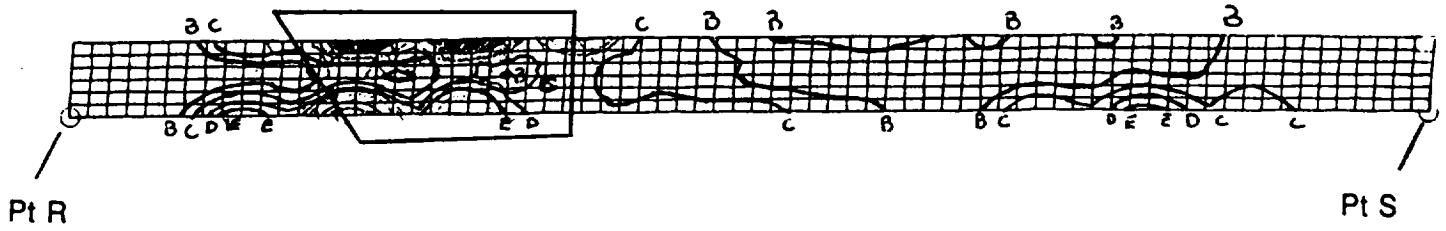


FIGURE 5.44. DEFORMED SHAPE OF LOCAL MODEL #2 AT 24100 LB OF APPLIED LOAD



(detail)

Contour Letter	Hoffman Failure Number (Mean)	Contour Letter	Hoffman Failure Number (Mean)
A	1.000	I	0.467
B	0.933	J	0.400
C	0.867	K	0.333
D	0.800	L	0.267
E	0.733	M	0.200
F	0.667	N	0.133
G	0.600	O	0.067
H	0.533		

FIGURE 5.45a. HOFFMAN FAILURE NUMBERS OF LOCAL MODEL #2 AT 24100 OF APPLIED LOAD AND TEST SPECIMEN SNAPSHOT



**FIGURE 5.45b. (CONT'D) HOFFMAN FAILURE NUMBERS OF LOCAL MODEL #2 AT 24100 OF APPLIED LOAD AND TEST SPECIMEN SNAPSHOT**



The prediction in Figure 5.45a is at the top of the web while the observed crack was toward the bottom. This discrepancy is probably due to the applied deflections at the top of the hat web in the local model which may be stiffening the structure too much in that area.

These results are in excellent agreement with the test failure loads and modes and complete the analysis of the full-scale panel. It should be noted that the second snap-through buckling sounds recorded during static and fatigue testing (sections 5.3.1 and 5.3.2) originally attributed to a change in buckling mode of the whole panel, are now believed to correspond to the local buckling of the hat stiffener web just discussed.

## **5.5 TEARDOWN INSPECTION**

### **5.5.1 VOID CONTENT AND FIBER VOLUME MEASUREMENTS**

Void content and fiber volume measurements were taken at various stages during the program both during the building block approach and the full scale phase to verify part quality. Results of these tests were already mentioned when the respective parts were first introduced. A more comprehensive set of measurements taken as part of the teardown inspection is presented in this section.

Void content and fiber volume measurements were taken from various locations of the full-scale panel No 2 and the flat frame-stiffener intersection specimen No 2. The test samples for the full scale panel were cut from the hat stiffener webs and top along one hat stiffener between the two frames, and from the skin at the center of a bay next to that stiffener. The test samples for the flat frame-stiffener intersection specimen were cut from similar locations. These locations are shown in Figures 5.46 and 5.47. The specific specimens that were cut out for teardown evaluation correspond to the markings on the specimens (for example F1R, C21L etc).

The variation of void content with location along the rightmost hat stiffener is shown in Figure 5.48. The cutoff value of 2% void content is marked as a straight horizontal line. The symbols on each of the plotted lines correspond to locations where the actual measurements were taken. All the hat top measurements are below the 2% cutoff value. The skin values are below 2% except in the vicinity of the frame stiffener intersection where a value of 4.13% was recorded. The hat webs (right side web in Figure 5.46) were higher than 2%. While near the two stiffener ends the void content was very close to 2%, the values at the center of the hat stiffener were between 4.4% and 7.4%. Of all these measurements, the values of some concern are the hat web values above 4%. The remaining values are quite good considering the complexity of the part.

The fiber volume values at the same locations as void contents are shown in Figure 5.49. The lowest acceptable value for production at Sikorsky is 55%. The hat top and skin values meet that requirement (with one exception that is just below 55%). The side webs show fiber volumes as low as 51.5% approximately

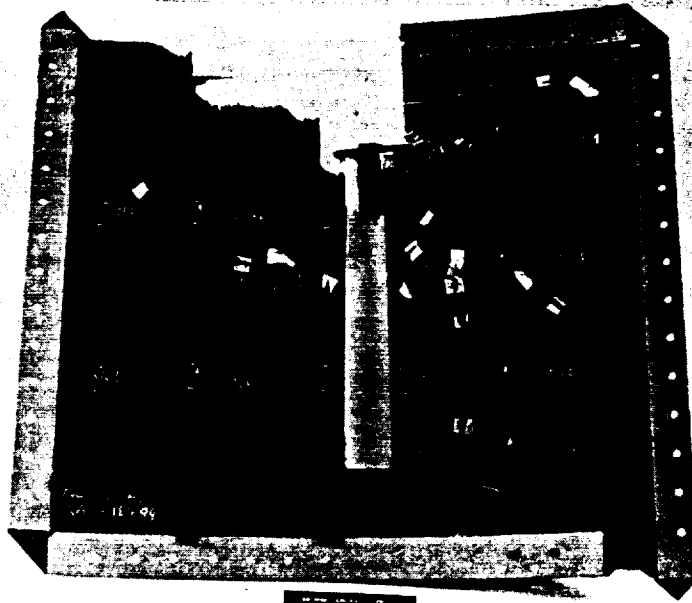


FIGURE 5.46. SPECIMENS USED FOR TEARDOWN INSPECTION (FULL-SCALE PANEL)



FIGURE 5.47. SPECIMENS USED FOR TEARDOWN INSPECTION  
(FRAME-STIFFENER INTERSECTION SPECIMEN)

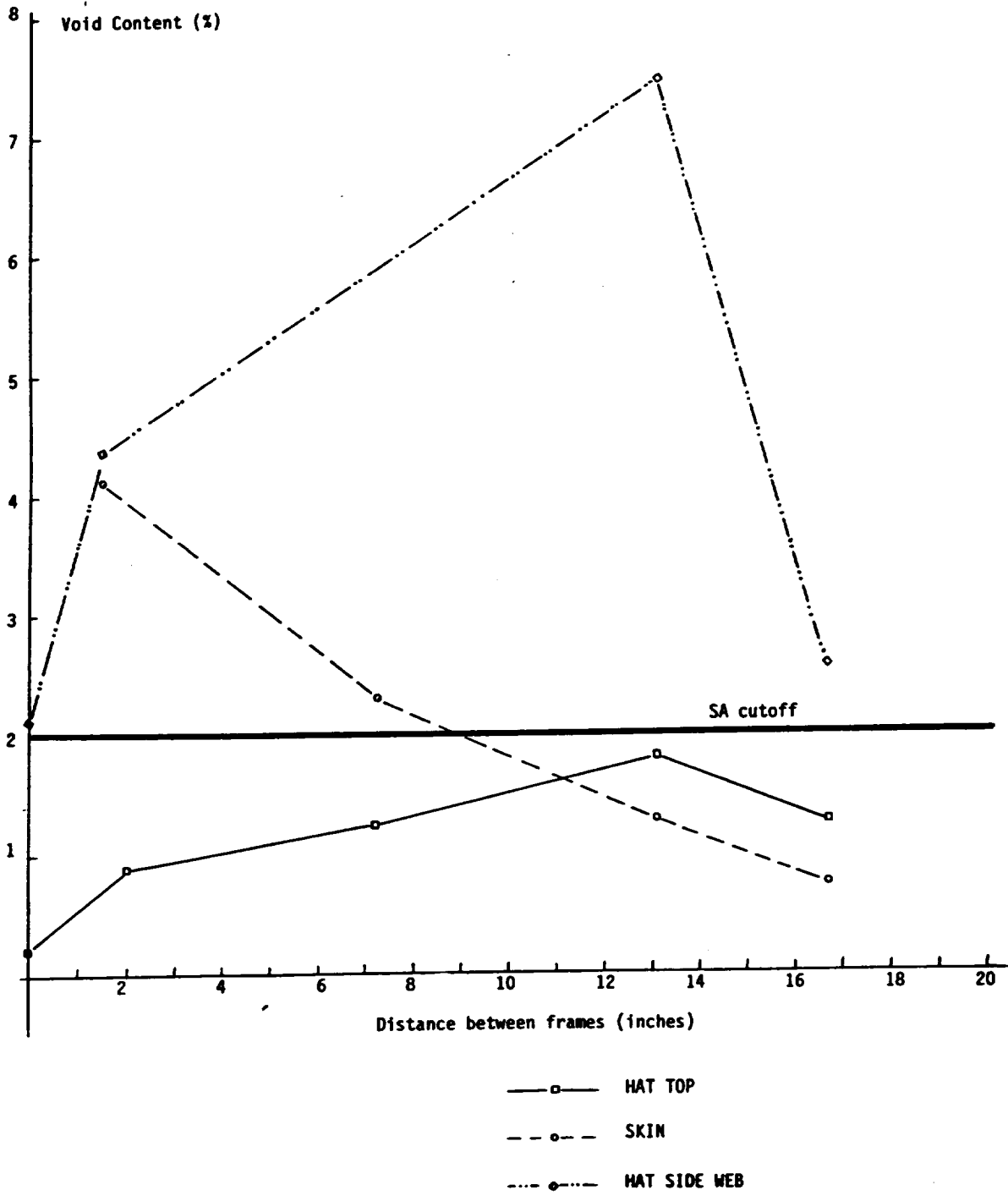


FIGURE 5.48. VOID CONTENT VALUES FOR FULL-SCALE PANEL NO. 2

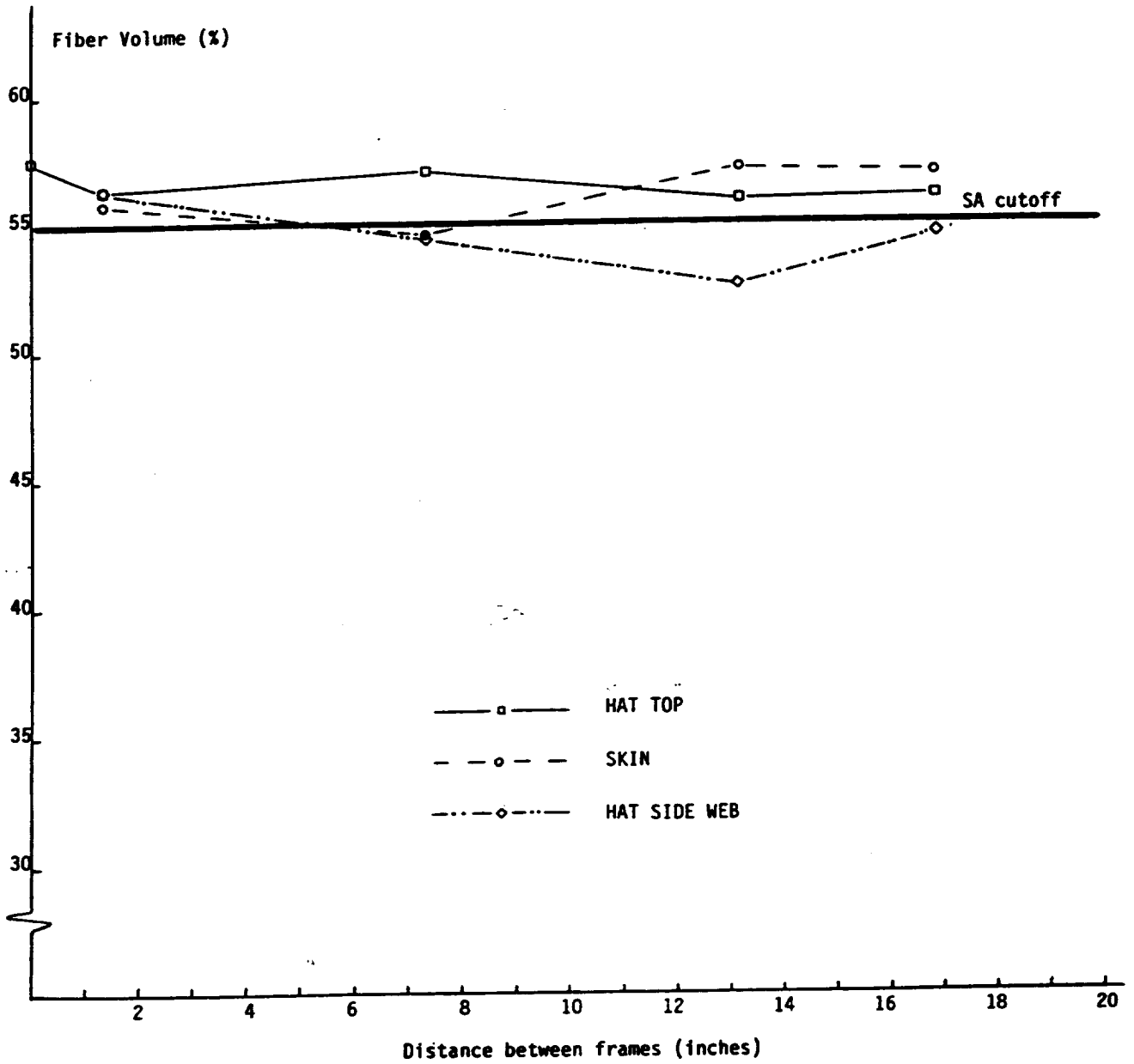


FIGURE 5.49. FIBER VOLUME VALUES FOR FULL-SCALE PANEL NO. 2

halfway between the frames. These low values for the hat webs in conjunction with the increased void contents in the same area suggest pressure control and heat transfer during curing may not have been adequate in that area (the highest void content and lowest fiber volume occur at the same location). The remaining measurements are quite satisfactory.

Perhaps the area of most interest, from the point of view of part quality and degree of consolidation, is the frame/stiffener intersection corner. Void content and fiber volume values for the hat webs (including the shear tie), hat top, frame web, and panel skin at an intersection corner of the full-scale panel are shown in Figure 5.50. The values are excellent with void content well below 1% except for the hat webs again where the values were 2.14% and 4.0%. The fiber volumes are all very good, higher than the cutoff value of 55%.

Void content values for the flat frame-stiffener intersection specimen (skin locations in the right bay of Figure 5.47) are shown in Figure 5.51 at three locations between the two frames. The void content values both at the thin and thick portions of the skin are excellent well below 1%. The corresponding fiber volume values are shown in Figure 5.52. Even though some of the values are relatively low, close to 54%, they are not considered to be a cause for concern.

The somewhat high void contents for the full-scale panel raised the question of whether this was particular to that specimen or a consistent problem associated with the tooling used and, possibly, the THERM-X® process. Additional teardown tests were done on the full scale panel No 1 with specimens taken from approximately the same locations. The void contents were very close to 0% (all below 2%) and the fiber volumes were higher than 55% suggesting excellent compaction. The higher void values reported in Figure 5.48 seem to be specific to this part (full-scale panel No 2). The tendency of the hat stiffener webs to have higher void contents than the top or the bottom cap was also present in the specimens from the full-scale panel No 1. It is possible that the Teflon insert may not have provided sufficient support on the pressure medium and thus the voids in the hat webs were not all driven out.

Small specimens (typically .75 in. long by 0.5 in. wide) were cut from the full-scale and the frame-stiffener intersection specimens, polished and mounted on a stand for observation under the microscope. These micrographs give additional information on the quality of the parts, their degree of consolidation and the presence of voids in them.

Portions of the skin of the flat frame-stiffener intersection specimen No 2 are shown in Figure 5.53. Very good quality is evident in Figure 5.53a. The fibers appear to be evenly distributed throughout the thickness of the specimen. Hairline cracks can be seen in the top ply. As this is a specimen that had already failed during static testing and the specimen was taken from the vicinity of the 45 degree crack shown in Figure 5.47, these cracks are assumed to have been the result of specimen failure. The Kevlar tracer fibers can also be seen in Figure 5.53a. Increased resin concentration can be seen around them.

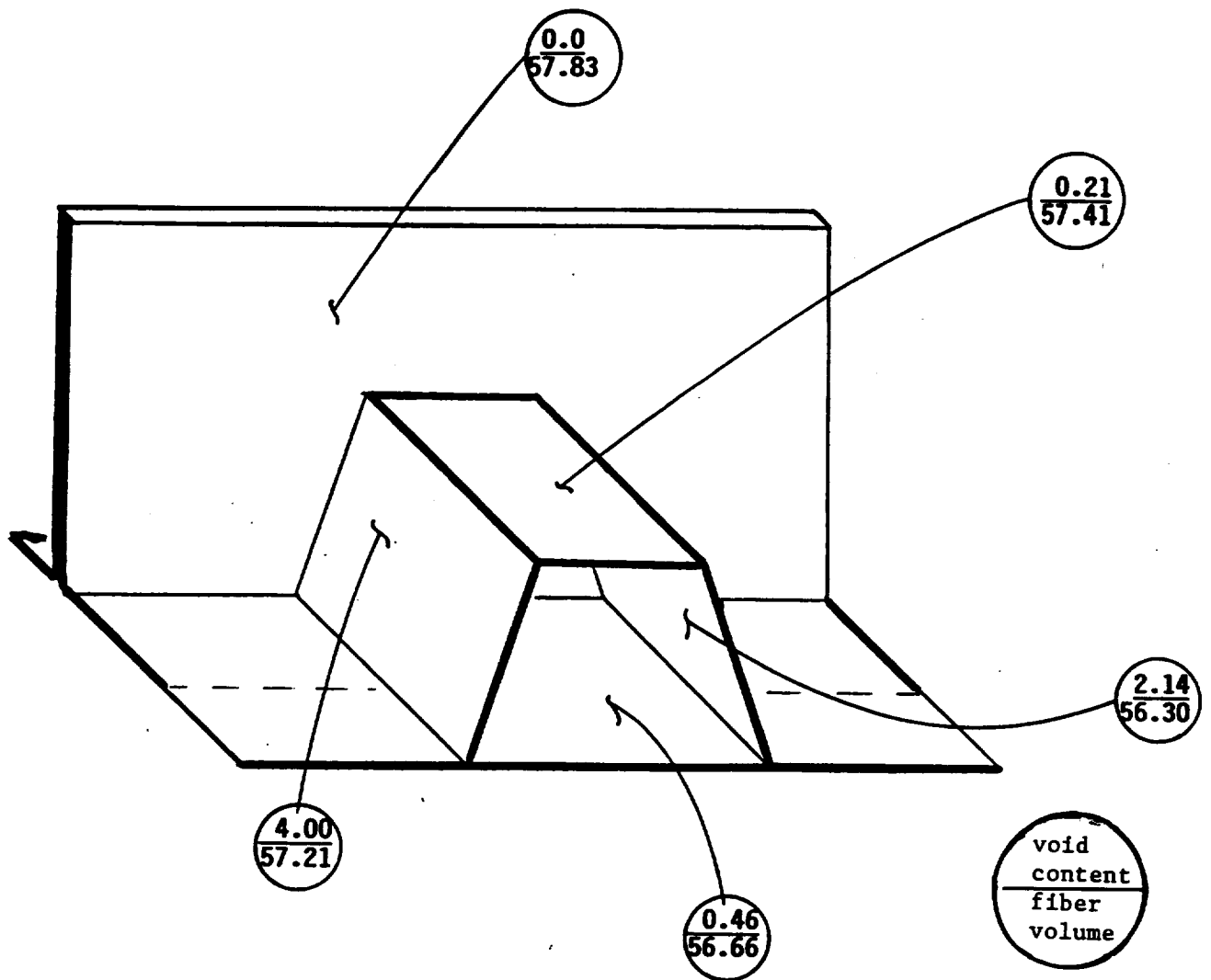


FIGURE 5.50. VOID CONTENT AND FIBER VOLUME VALUES AT FRAME-STIFFENER INTERSECTION CORNER OF FULL-SCALE PANEL NO. 2

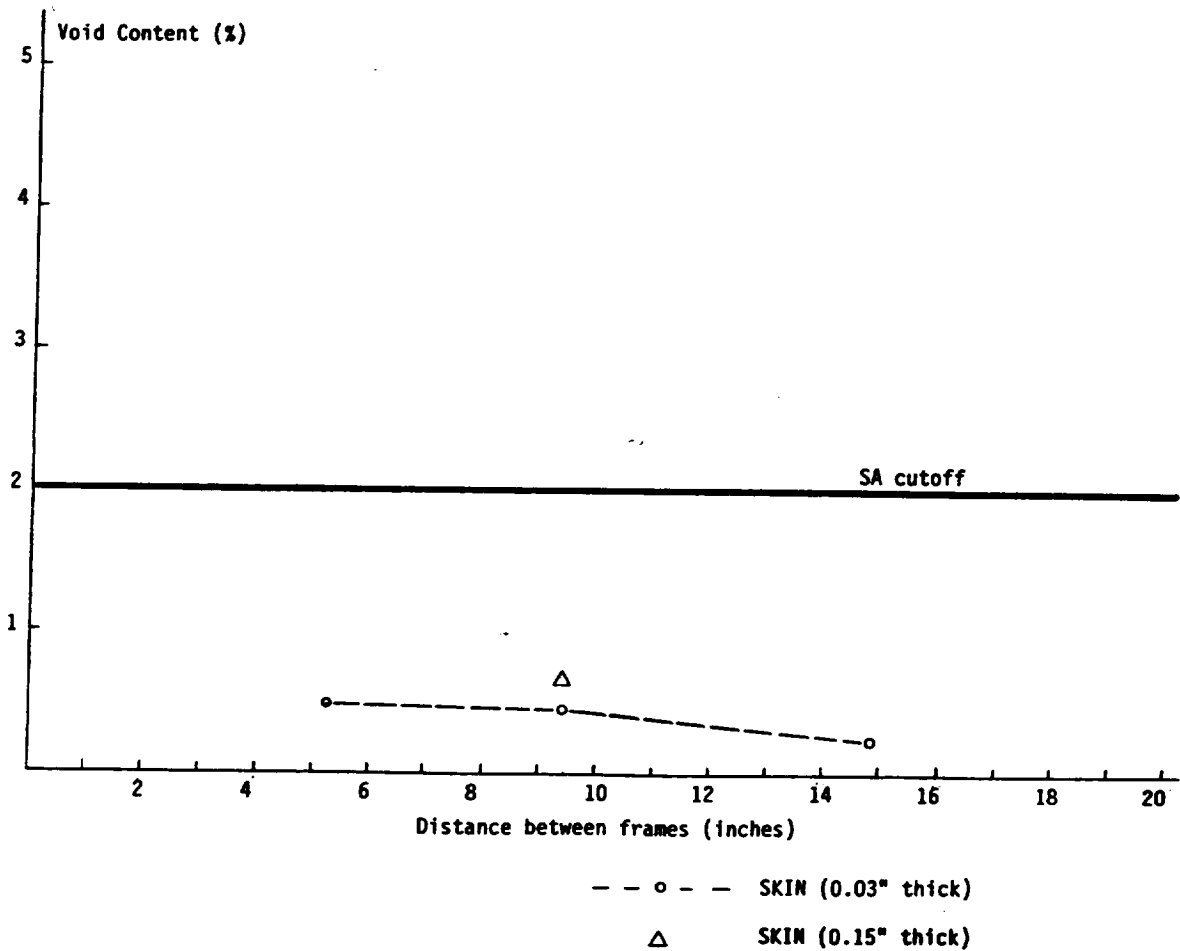


FIGURE 5.51. VOID CONTENT VALUES FOR FRAME STIFFENER INTERSECTION SPECIMEN NO. 2

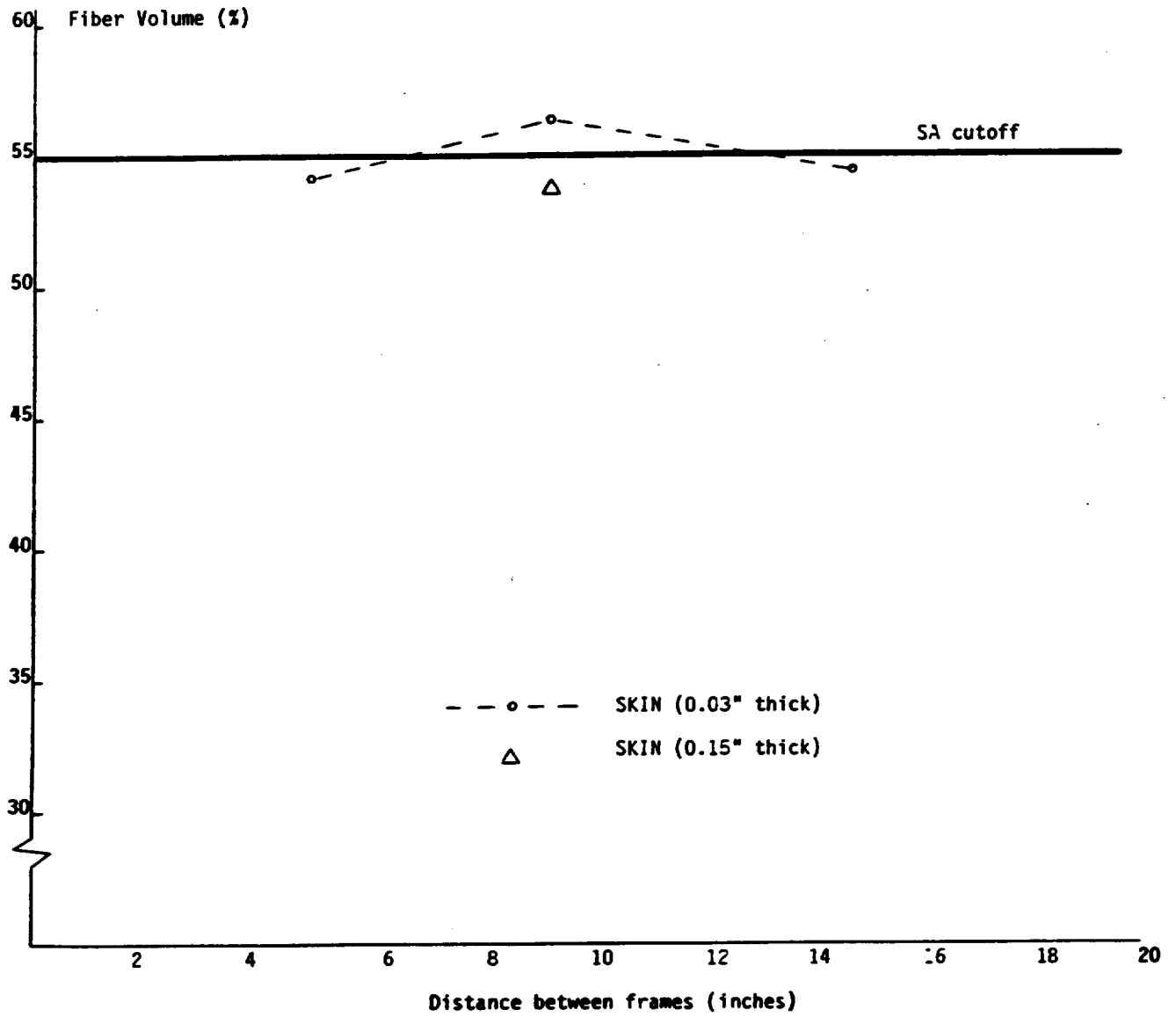
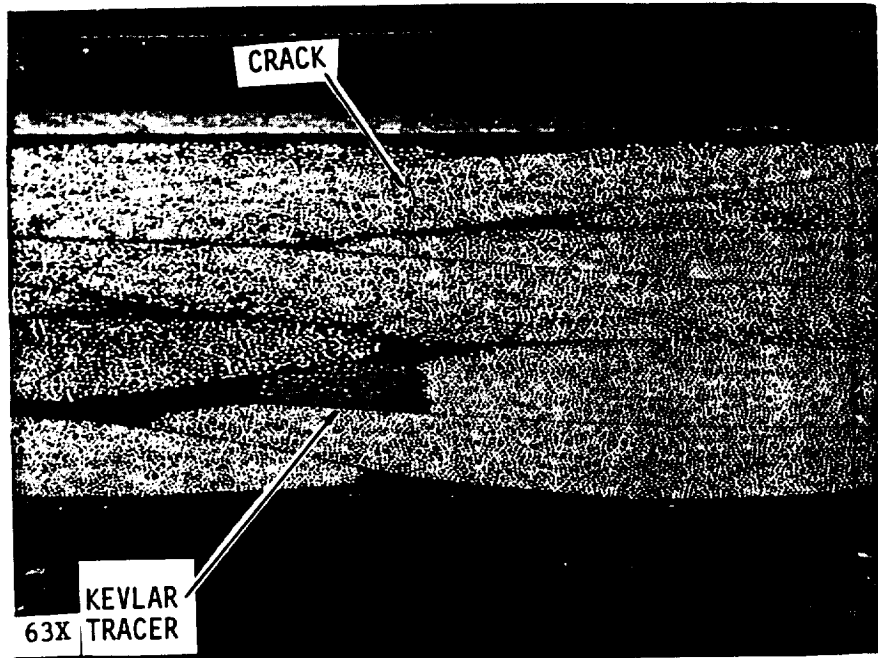
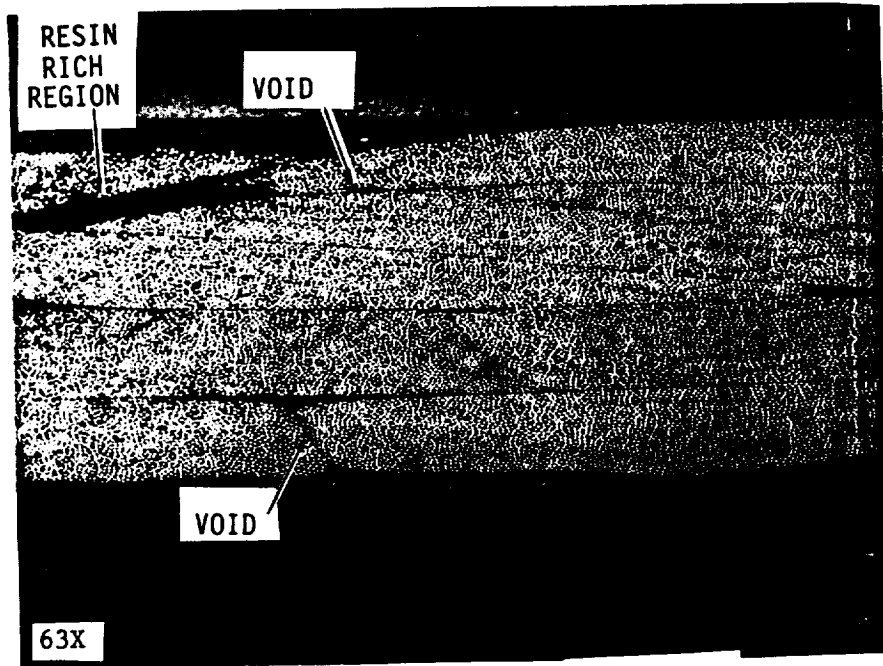


FIGURE 5.52. FIBER VOLUME VALUES FOR FRAME STIFFENER INTERSECTION SPECIMEN NO. 2





SPECIMEN F1L



SPECIMEN F3L

FIGURE 5.53. SKIN MICROGRAPHS FROM FRAME STIFFENER INTERSECTION SPECIMEN

This is typical and is a result of the fact that the tracer fibers have larger diameter and they are concentrated in a confined spot through the specimen thickness. Similar good quality is evident in Figure 5.53b. Minor voids and some areas of increased resin concentration can be seen.

Two local cross sections from the skin of the full-scale panel No 2 are shown in Figures 5.54 and 5.55. Small voids are present in the cross-section shown in Figure 5.55 in particular in between tows. It should be pointed out that these voids are shown under 63X magnification so are actually very small (no more than 0.004 in. diameter). That is why they were not picked up by NDI when the specimens were inspected prior to testing (NDI equipment was set to inspect for voids larger than or equal to 0.25 inches in diameter).

Typical cross sections of the hat stiffener from the frame-stiffener intersection specimen No 2 are shown in Figure 5.56. The cross-section in Figure 5.56a was cut away from the failure region and the hat stiffener is intact. Overall quality is good especially at the corners where the canted hat webs meet the skin. No filler material was used at these corners. A resin pocket has been created in that region without any voids. The geometry definition in the vicinity of all corners is very good and no wrinkles are seen. It should be noted that the top of the hat is thicker than the canted webs on either side because an additional tape ply (fibers along stiffener axis) was laid up in the hat top as a stiffening reinforcement.

The cross-section in Figure 5.56b was cut next to the failure region. Cracks and delaminations caused by specimen failure can be seen across the hat top, along the hat webs and extending into the skin. The delaminations in the hat top are on either side of the the zero degree tape reinforcement. The delamination and associated fiber fractures in the vicinity of the web/skin intersection are under the outer web ply which extends in between the skin plies. Since this is an embedded flange design, the upper skin ply is above the outer web ply.

A cross section of the "tee" frame near the frame/stiffener intersection of Frame/Stiffener Intersection specimen No 2 is shown in Figure 5.57. Thin tape strips were used as filler material in these areas of the panel. The quality and compaction is very good except for the wrinkle on the right side of the point where the web meets the skin. It is unclear whether there was relative movement during cure that caused the wrinkle or the plies were laid up with an overlap which during cure under THERM-X® pressure resulted in a wrinkle. No voids and no excess resin are evident.

Cross sections of hat stiffener corners near the same frame/stiffener intersection are shown in Figure 5.58 (Frame/stiffener intersection specimen No 2). These were close to the failure region. Delaminations caused during specimen failure are seen between the web plies and failed skin plies. The hat top and webs are intact except one of the two web/skin intersection corners. A well defined resin pocket without any voids can be seen in the left corner. No filler material was used in these corners. This shows that the pressure medium is effective in transmitting enough pressure at corners to achieve a high degree of compaction.

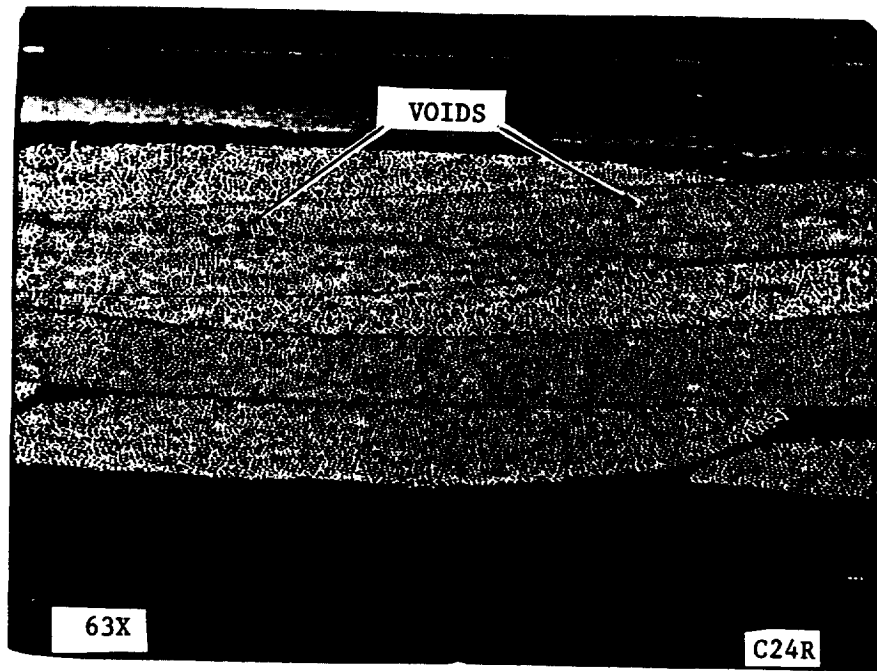
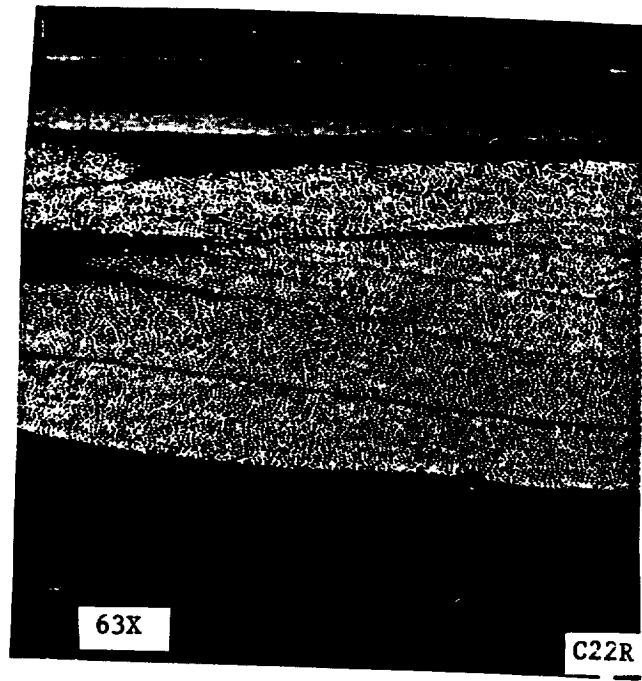
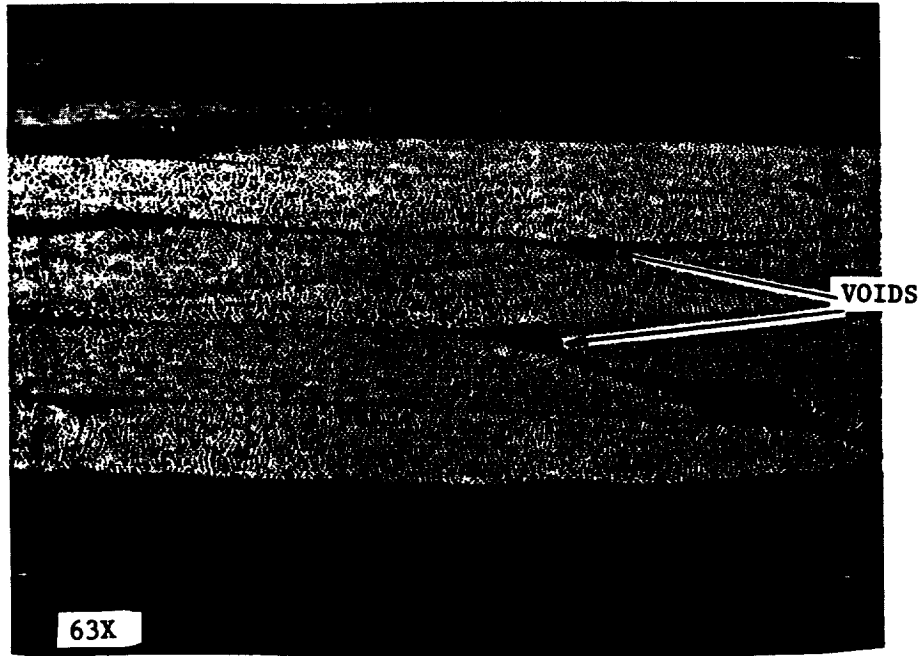
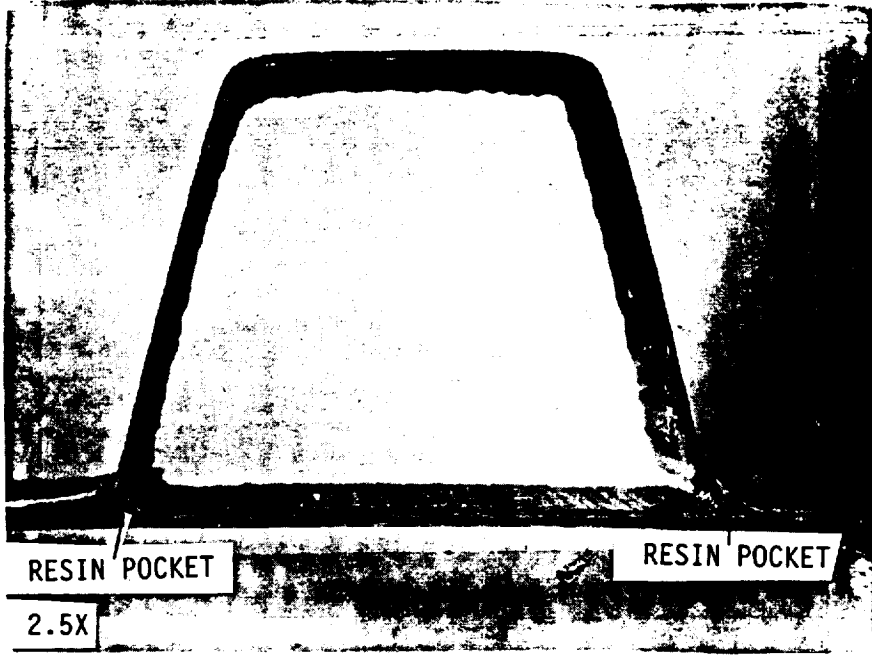


FIGURE 5.54. SKIN MICROGRAPHS FROM FULL-SCALE SPECIMEN



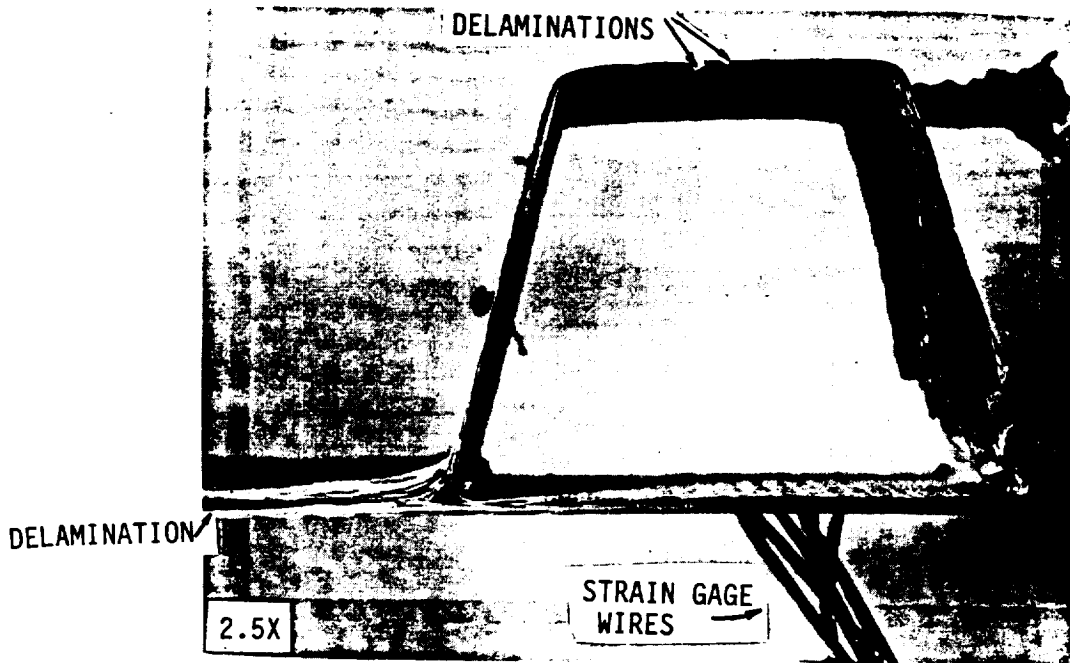
SPECIMEN C26R

FIGURE 5.55. SKIN MICROGRAPH FROM FULL-SCALE SPECIMEN (LEFT MIDDLE BAY)



a.

SPECIMEN F1C



b.

SPECIMEN F2C

FIGURE 5.56. HAT STIFFENER CROSS-SECTION (FRAME STIFFENER INTERSECTION SPECIMEN)

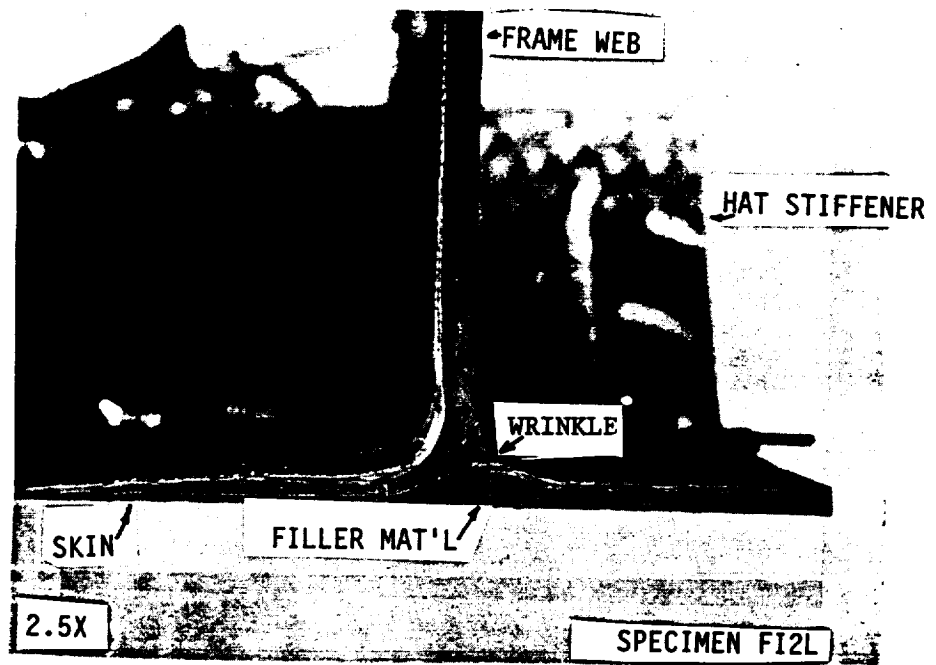


FIGURE 5.57. FRAME CROSS-SECTION (FRAME STIFFENER INTERSECTION SPECIMEN)

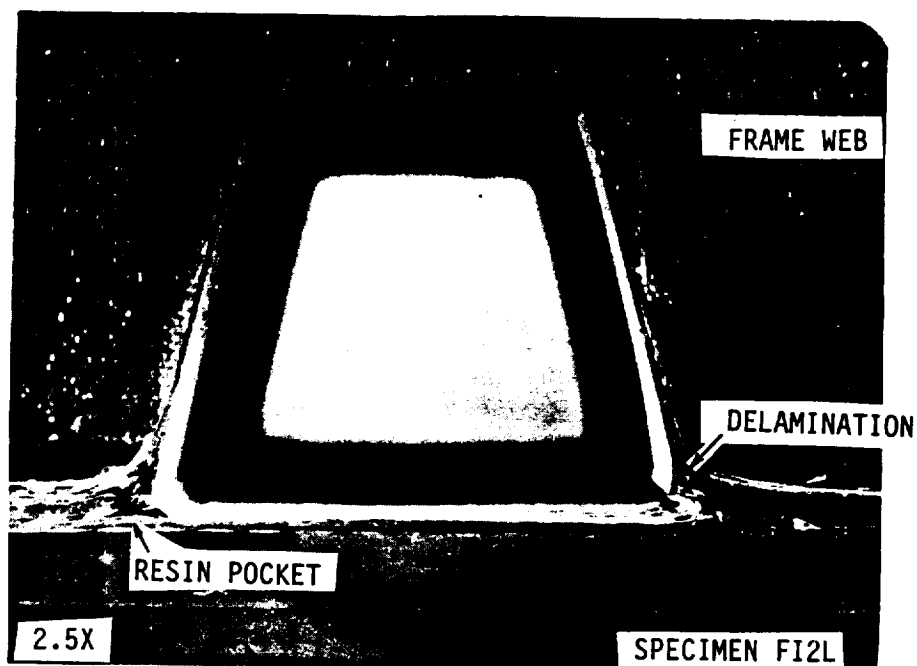


FIGURE 5.58. HAT STIFFENER CROSS SECTIONS NEAR FRAME STIFFENER INTERSECTION CORNERS

ORIGIN PAGE  
BLACK AND WHITE PHOTOGRAPH

Cross sections of the frame and hat stiffener near a frame/stiffener intersection corner of the full scale article are shown in Figure 5.59. A small void can be seen in the frame (Figure 5.59a). Similar small voids are seen at the two web/skin intersection corners in Figure 5.59b. No filler material was used in these corners. Comparison of Figure 5.59 to 5.58 suggests that THERM-X cannot entirely eliminate problems in these corners without using some filler material. It may be possible to improve the quality further by using higher autoclave pressures during cure if that is permissible by the material cure cycle.

Similar hat stiffener cross sections from the full-scale specimen are shown in Figure 5.60. These were at regions away from the frame/stiffener intersection corner. Small voids are present in one of the web/skin intersection corners. The rest of the cross-section indicates a quality part.

In summary, the teardown inspection showed very good part definition and good consolidation. Radius regions were very well defined and, even without filler material, there were very few voids and wrinkles at the corners of intersecting members. The THERM-X® process was successful in curing complex parts with minimum tooling. Few areas of increased void content were observed, specific to one part. They can be improved with minor tooling modifications (closer tolerance machining of the hat stiffener mandrels).

## 5.6 LABOR HOURS COMPARISON-THERM-X TOOLING VERSUS CONVENTIONAL LAYUP

In this section, a comparison of labor hour requirements for THERM-X® processed parts and parts fabricated using conventional hand layup is done. For this comparison the parts made during the Advanced Composite Airframe Program (ACAP) and the UH-60 (BlackHawk) Composite Rear Fuselage are used. The first comparison is done with the assembly time excluded from the labor hour content. In that way, the parts used are parts of varying complexity and size but the labor hours reported do not include time to put them together into subassemblies. A plot of labor hours per part weight as a function of part weight is shown in Figure 5.61. It is a (natural) log-log plot. There are 180 ACAP parts shown in this plot and their weight ranges from 0.01 to 38 lbs.

There is some scatter in the data but a decreasing trend is well defined. This suggests that larger parts have smaller labor hours per pound content because assembly time is reduced when parts are cocured and because labor intensive structural details become a smaller percentage of the total for a larger part. The correlation coefficient for the straight line in Figure 5.61 is  $R=0.74$  which means that half ( $0.74 \times 0.74$ ) of the variation of labor hour content is due to the size effects discussed. The other half is due to other factors believed to be related to part complexity. The plot in Figure 5.61 does not differentiate parts on the basis of their complexity. It should be noted that this dependence of labor hours on part weight was first observed and reported by Gutowski et al [23].



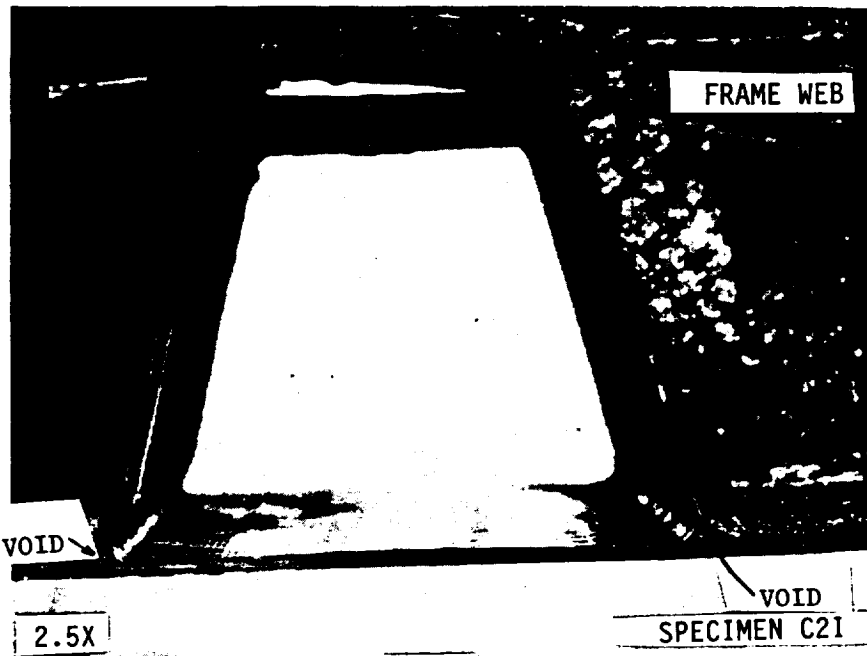
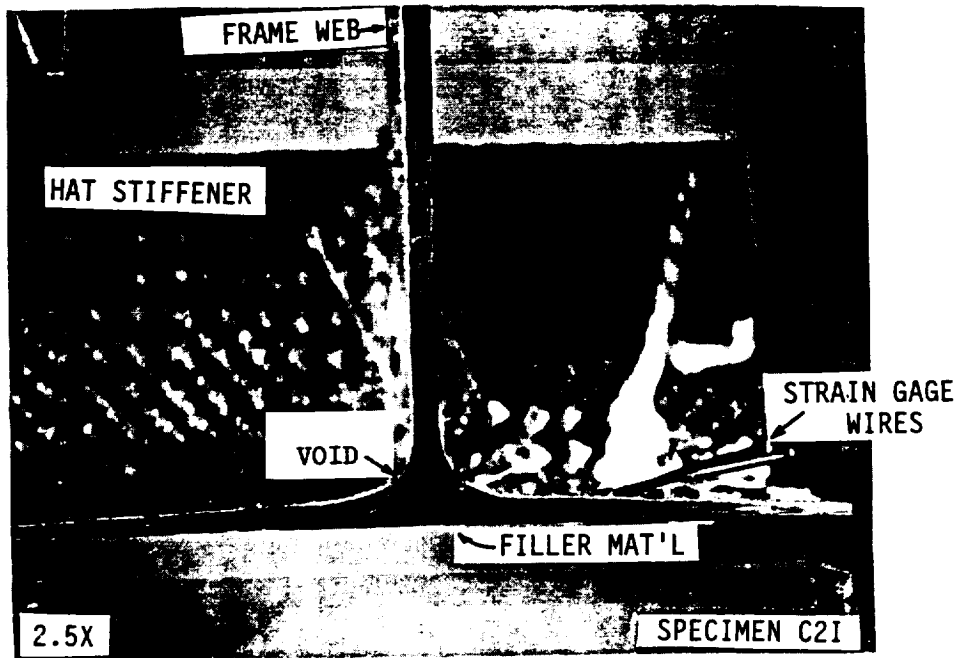


FIGURE 5.59. FRAME AND STIFFENER CROSS-SECTIONS NEAR FRAME STIFFENER INTERSECTION CORNERS (FULL-SCALE SPECIMEN)

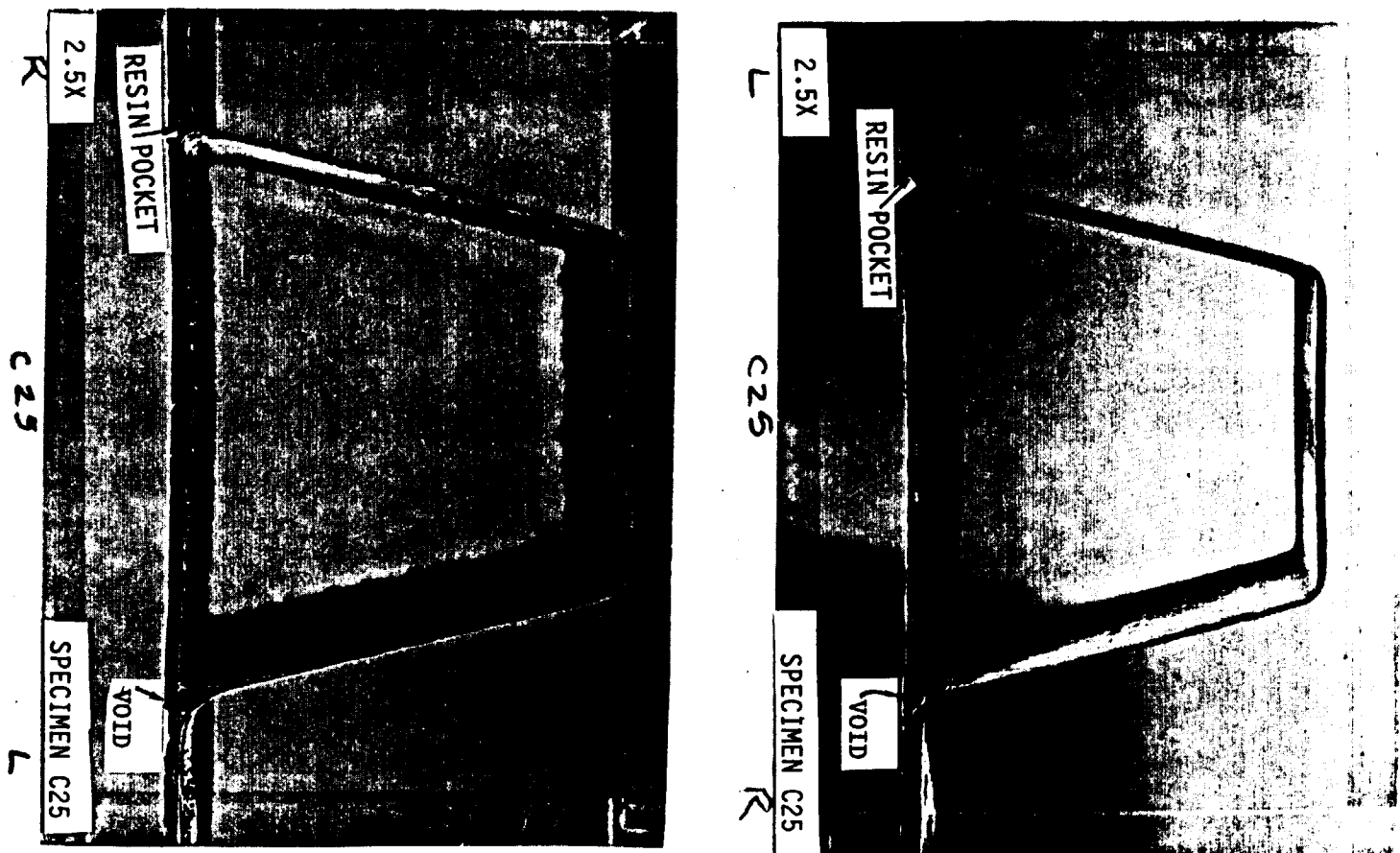


FIGURE 5.60. STIFFENER CROSS SECTIONS FROM FULL-SCALE SPECIMEN

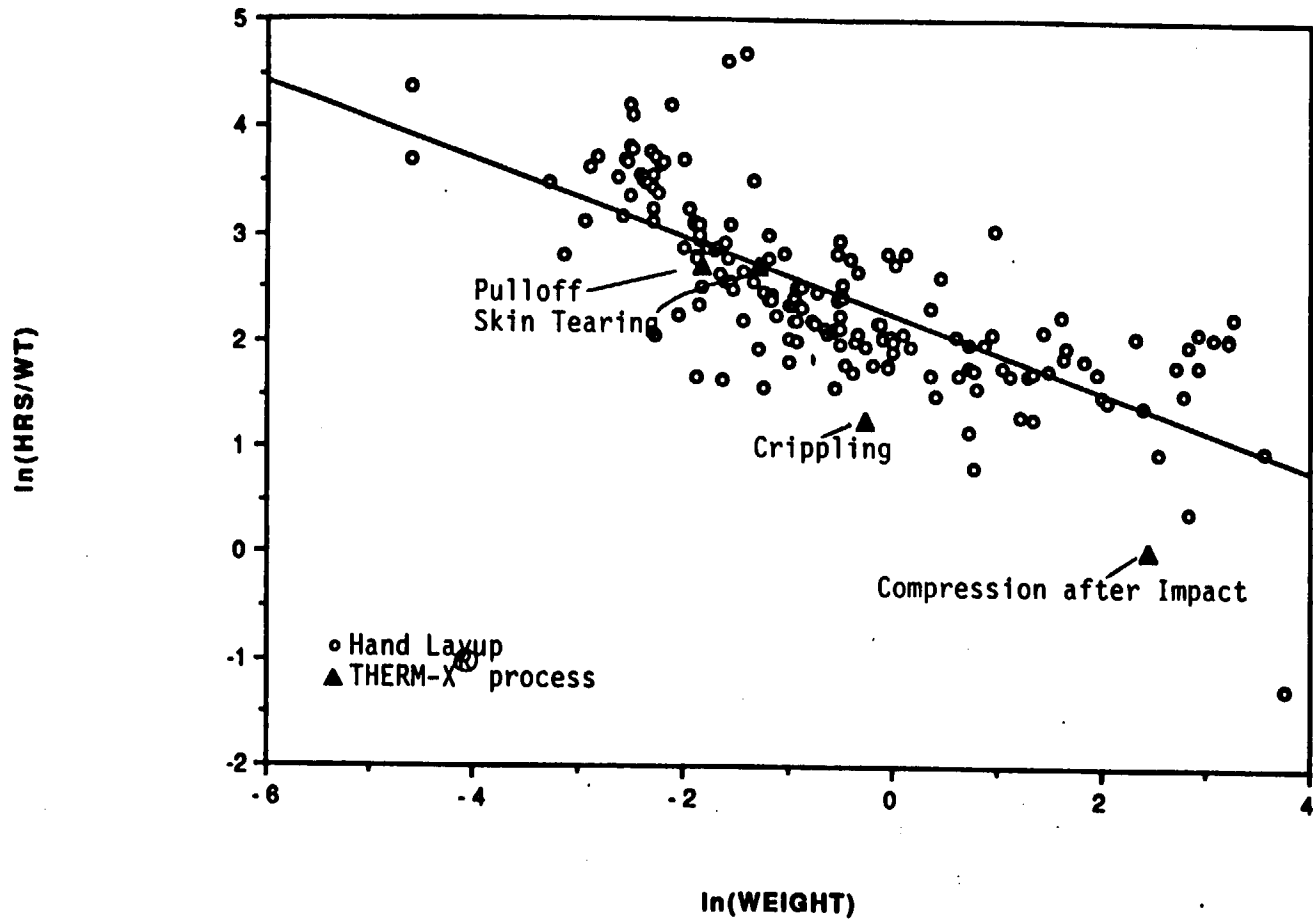


FIGURE 5.61. LABOR HOURS AS A FUNCTION OF PART WEIGHT FOR HAND LAID UP AND THERM-X<sup>®</sup> PROCESSED PARTS (NO ASSEMBLY)

Four of the parts made using the THERM-X® process are included in Figure 5.61 (filled triangles) for comparison. These are (1) the Skin-Stiffener Separation (Pulloff) Specimen, (2) the Skin Tearing Specimen, (3) The Crippling Specimen and (4) Compression after Impact Panel. These are compared to the best fit trend line in Figure 5.61. The full scale panel is not included in this comparison because it is more complex than the hand laid up parts included in Figure 5.61 and would correspond to parts that involve some assembly (secondarily bonding or fastening frames or stiffeners on the skin). The frame-stiffener intersection specimen is not included either because the labor hour content includes additional bagging cycles (rebagging one of the parts because of bag failure and double bagging another).

The Compression after Impact Panel shows the largest savings (almost 50%) but this result is misleading since it is a flat part compared to more complex hand laid up parts. The crippling specimen is more representative (many of the hand laid up parts in Figure 5.61 were similar) and shows about 23% savings. The Skin Tearing specimen and the Pulloff specimen are parts that did not benefit from using the THERM-X® process because the tooling was the same with equivalent hand laid up parts. Thus, they are seen to fall very close to the best fit line for the hand laid up data.

For the full-scale panel, two comparisons were made. A one-to-one comparison with a similar ACAP part and a general comparison to ACAP and CRF parts of high complexity that involved some assembly. No parts for which manufacturing data are available had the exact same configuration and size as the full-scale panel in this program.

The part chosen for the one-to-one comparison is the crew floor of the ACAP. It consists of a curved skin (three ply Kevlar) with reinforcing stiffeners of sandwich construction with graphite faces spaced approximately every 6 inches which is very close to the stiffener spacing (6.5 inches) in the current program. Unlike the current program, the ACAP crew floor had no frames. Approximate dimensions for the 0.03 inch thick skin (same thickness as the full scale panel in the current program) were 150 inches long, by 50 inches wide (radius of curvature about 100 inches). Three panels were made. The finished panel weights were 26.1, 26.5, and 26.2 lbs, and required, respectively, 291.4, 311.5, and 311.5 hours to complete. It should be noted that most of the manufacturing time was taken up by assembling and curing the various parts that comprised the crew floor.

For comparison to the full-scale panel, the full scale panels 2 through 4 will be used. The labor data for the first panel are not used because the part had to be bagged twice after the bag failed the pressure leak test. The time required to bond the doublers and prepare for secondarily bonding them on the skin tool side is not included in the calculation since the part in a production line would not require the doublers. The results and comparison are given in Table 5.6.

Table 5.6  
Labor Hours Comparison - THERM-X Versus Hand Layup

	Weight (lbs)	Manuf. Hours	Hours/lb	Hours/lb (avg of 3)
THERM-X	*	40	10.2	
Full-Scale	3.91	33	8.4	9.5
	*	38.5	9.8	
Conv. Layup	26.1	291.4	11.2	
(ACAP Crew Floor)	26.5	311.5	11.8	11.6
	26.2	311.5	11.9	

\* (no weight measurement possible because aluminum doublers were added)

The average values of labor hours per pound in the last column give an indication of THERM-X® processed parts savings over conventional hand layup. The THERM-X® processed full scale panels for this program show, on the average, 18.1% savings over conventional manufacturing. It should be noted that the full scale panel in this program had frames that the ACAP Crew Floor did not have. The frames add to the complexity of the full scale panel and thus, the 18% savings value is a lower bound. If the parts compared were identical, the savings realized by THERM-X® processing would be larger. In addition, the hourly values above do not include any tooling costs. Using THERM-X usually requires simplified tooling as pressure transfer is successfully done through the pressure medium without any need of significant hard tooling. Additional savings would result if tooling cost were included in the above calculation. This was not possible in this case since the parts compared are not identical. Finally, if, as this program has shown, the quality of THERM-X® parts is such that no rework (or negligible rework) is necessary compared to conventional hand layup, additional cost savings would be incurred by using the THERM-X® process.

The last comparison involves ACAP and CRF parts including assembly time. This comparison involves the parts of Figure 5.61 once they are assembled to sub-assemblies. A total of thirty three such subassemblies were included made of graphite, glass, and kevlar parts of various degrees of complexity and geometry and their weight varied from a few tenths of a pound to 200 pounds. The hours per pound required to make these parts are plotted as a function of their weight in Figure 5.62.

There is large scatter in the data because of the varying materials and degree of complexity of the parts pooled (R value for the straight line fit is 0.384) but a downward trend is evident. This trend can be more accurately defined if the parts were separated by material, assembly means, and complexity. In a manner similar to the trend of Figure 5.61, it suggests that the labor hours per pound decrease as the part size increases. This is because the assembly required decreases as the part size increases and the effect of labor intensive details is less pronounced for large parts.

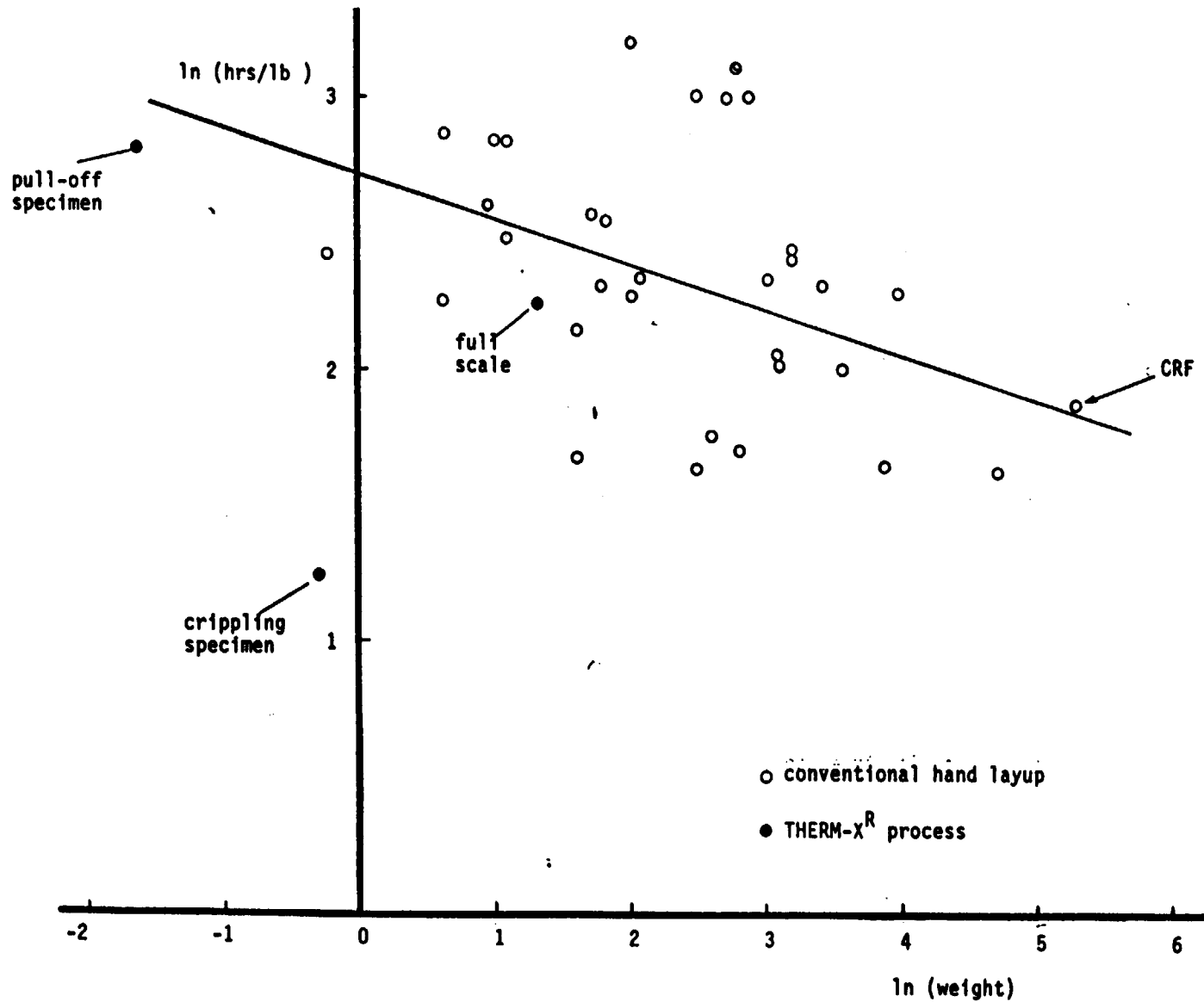


FIGURE 5.62. VARIATION OF LABOR HOURS WITH PART WEIGHT  
(ASSEMBLY INCLUDED)

The full scale panel, the crippling specimen and the stiffener pull-off specimen have also been plotted in Figure 5.62. They all lie below the best fit line to the data showing significant savings of the THERM-X® process for various part weights. Of special interest is the full scale panel. The difference from the best fit line corresponds to a  $\ln(\text{hrs/lb})$  difference of 0.25 which translates to 22% savings of the THERM-X® process over conventional layup. Again, additional savings due to simplified tooling and possible reduced rework are, at this point not quantified.

In conclusion, the comparisons show significant savings (18%-22%) over the conventional hand layup and these values are lower limits as additional savings in tooling and rework are not included. The savings of the THERM-X® process reported here are due to simplified vacuum bagging and the fact that complex parts can be cocured inexpensively without needing secondary assembly. It should be noted that the quantified savings of 22% are in-line with the original estimate of 28% of Section 3.2 (Table 3.14).

## 6.0 CONCLUSIONS AND RECOMMENDATIONS

### 6.1 CONCLUSIONS

1. The autoclave THERM-X® tooling process can be used effectively to manufacture cocured high quality parts of high complexity with minimum tooling. Isolated defects such as wrinkles or void contents can be traced to errors in the fabrication procedure and can be easily corrected to give defect-free parts. The THERM-X® processed parts showed comparable structural properties as parts fabricated with conventional autoclave tooling.
2. Parts made with the THERM-X® process show savings of 18 to 22% due to reduced vacuum bagging time. Additional savings due to reduced tooling and rework for defective parts are anticipated.
3. THERM-X® tooling can generate consistent parts almost independent of the operator doing the fabrication. The risk of defect occurrence in larger parts is reduced and the savings of cocuring larger parts rather than assembling smaller parts can be realized.
4. The embedded flange concept while marginally more labor intensive was found to increase the failure load for the skin stiffener separation mode (by a factor of 3 in this program) to the point that this failure mode is suppressed.
5. The built-in shear tie connecting frames and stiffeners at intersections improved load transfer. No failures in that area for any of the specimens in the program verified its effectiveness. The concept is simple to use and, to some extent, eliminates the need for separately laying up and curing clips.
6. The building block approach was successful in isolating and quantifying possible failure modes and pointing to the strengths and weaknesses of the full-scale panel prior to fabrication. This made design changes possible that improved the full-scale panel performance.
7. The full-scale panel design performed very well, meeting and surpassing the design ultimate load of 250 lbs/in. Valuable information on the onset and growth of damage was collected during the static and fatigue tests. First damage was observed at a load of 280 lbs/in (exceeding the design ultimate load). The picture frame shear fixture performed well even though corner pinching cracks developed (but did not grow) during the test.
8. Test results and a combination of global-local nonlinear finite element analyses defined the failure of the full-scale panel as initiating in the hat stiffener webs close to intersection corners and progressing to the skin of the panel. The failure was caused by high loads present near nodes of the skin postbuckled pattern at the intersection line between the outer hat stiffeners and the skin.



## 6.2 RECOMMENDATIONS

1. It is recommended to splice any separating or bleeder material that is used over regions with sharp geometry changes to avoid bridging. The splicing need not guarantee vacuum isolation as the vacuum bag is placed on top of the pressure medium and is not spliced.
2. A relation of part size and labor hour content is apparent. It is recommended that this relation be examined further in particular in order to understand the effect of part complexity on manufacturing labor hours.
3. An optimization procedure for stiffened panels was developed. It is recommended that methods that incorporate structural requirements and manufacturing information be integrated in a procedure such as the one developed in this program to obtain reliable cost estimates and permit quick accurate trade-off studies.
4. Throughout the program good agreement between analysis and test results was observed. In particular the strain predictions for the intersection specimen and the failure prediction for the full-scale panel were in excellent agreement with the test results. Nonlinear finite element analyses should be used when analyzing postbuckled panels if a detailed understanding of the load distribution and failure mode is necessary. For sizing of structure, standard diagonal tension procedures (not involving finite elements) are more than adequate.

## REFERENCES

1. Stover, D., "The Outlook for Composites Use in Future Commercial Transports", *Advanced Composites*, May/June, 1989, pp 49-58.
2. Jane's, All the World's Aircraft, 1988, pp 107-110.
3. Young, W.C., Roark's Formulas for Stress and Strain, 6th Ed., McGraw-Hill Book Co, 1989.
4. Sikorsky Aircraft TEM-88-V2-7769, 1988, pp 3-39.
5. Timoshenko, S., and Woinowsky-Krieger, S., *Theory of Plates and Shells*, McGraw Hill, 1959, chapter 11.
6. Rivello, R.M., Theory and Analysis of Flight Structures, McGraw Hill, 1969, chapter 8-5.
7. DOD/NASA Advanced Composites Design Guide, vol 2, July 1983, chapter 2.2.
8. Libove, C., "Buckle Pattern of Biaxially Compressed Simply Supported Orthotropic Rectangular Plates", *J. Composite Materials*, vol 17, 1983, pp 45-49.
9. Bruhn, E.F., Analysis and Design of Flight Vehicle Structures, S.R. Jacobs and Associates, Inc., Indianapolis Indiana, 1973, chapters C5.9-C5.12.
10. Kuhn, P., Peterson, J.P., and Levin, L.R., "A Summary of Diagonal Tension Part I - Methods of Analysis", NACA Technical Note, 2661, May 1952.
11. "Design, Fabrication, Test, and Analysis of Hat-Stiffened, Graphite/Epoxy Postbuckled Shear Panels", Sikorsky Engineering Report 510268, June 30, 1988.
12. "Testing, Analysis and Preliminary Design of Graphite/Epoxy Hat Section Stiffeners Subjected to Static and Fatigue Compression Loads", Sikorsky Engineering Report 510257, January 1987.
13. ACEE Composites Project Office, Compiler, "ST-1: Specification for Compression After Impact Test", *Standard Tests for Toughened Resin Composites - Revised Edition*, NASA Reference Publication 1092, July, 1993, pp. 1-5.
14. Morton, J., and Godwin, E.W., "Impact Response of Tough Carbon Fibre Composites", *Composite Structures*, vol 13, 1989, pp 1-19.
15. "Error Due to Transverse Sensitivity in Strain Gages", M-M Technical Note TN-509, MicroMeasurements Division, Measurement Group, Inc., Raleigh NC, 1982.
16. Tsai, S.W., "Strength Characteristics of Composite Materials", NASA CR-224, April 1965.

17. "Impact Damage Tolerance of the MH-53E Composite Sponson", Sikorsky Engineering Report 13899, March 1990.
18. Rouse, M., "Postbuckling and Failure Characteristics of Stiffened Graphite-Epoxy Shear Webs", 28th SDM Conference, Monterey CA, April 1987, AIAA paper 87-0733.
19. Whitehead, R.S., Kan, H.P., Cordero, R., and Saether, E.S., "Certification Methodology for Composite Structure", vol II - Methodology Development, Final Report, N62269-84-C-0243, October 1986.
20. Deo, R., Agarwal, B., and Madenci, E., "Design Methodology and Life Analysis of Postbuckled Metal and Composite Panels", AFWAL-TR-85-3096, vol 1, Northrop Corp, 1985.
21. Ogonowski, J.M., and Sanger, K.B., "Postbuckling of Curved and Flat Stiffened Composite Panels Under Combined Loads", NADC-81097-60, McDonnell Douglas Corporation, December 1984.
22. Vinson, J.R., and Sierakowski, R.L, The Behavior of Structures Composed of Composite Materials, Martinus Nijhoff Publishers, 1987.
23. Gutowski, T., Henderson, R., and Shipp, C., "Manufacturing Costs for Advanced Composites Aerospace Parts", SAMPE Journal, vol 27, No. 3, May/June 1991, pp 37-43.

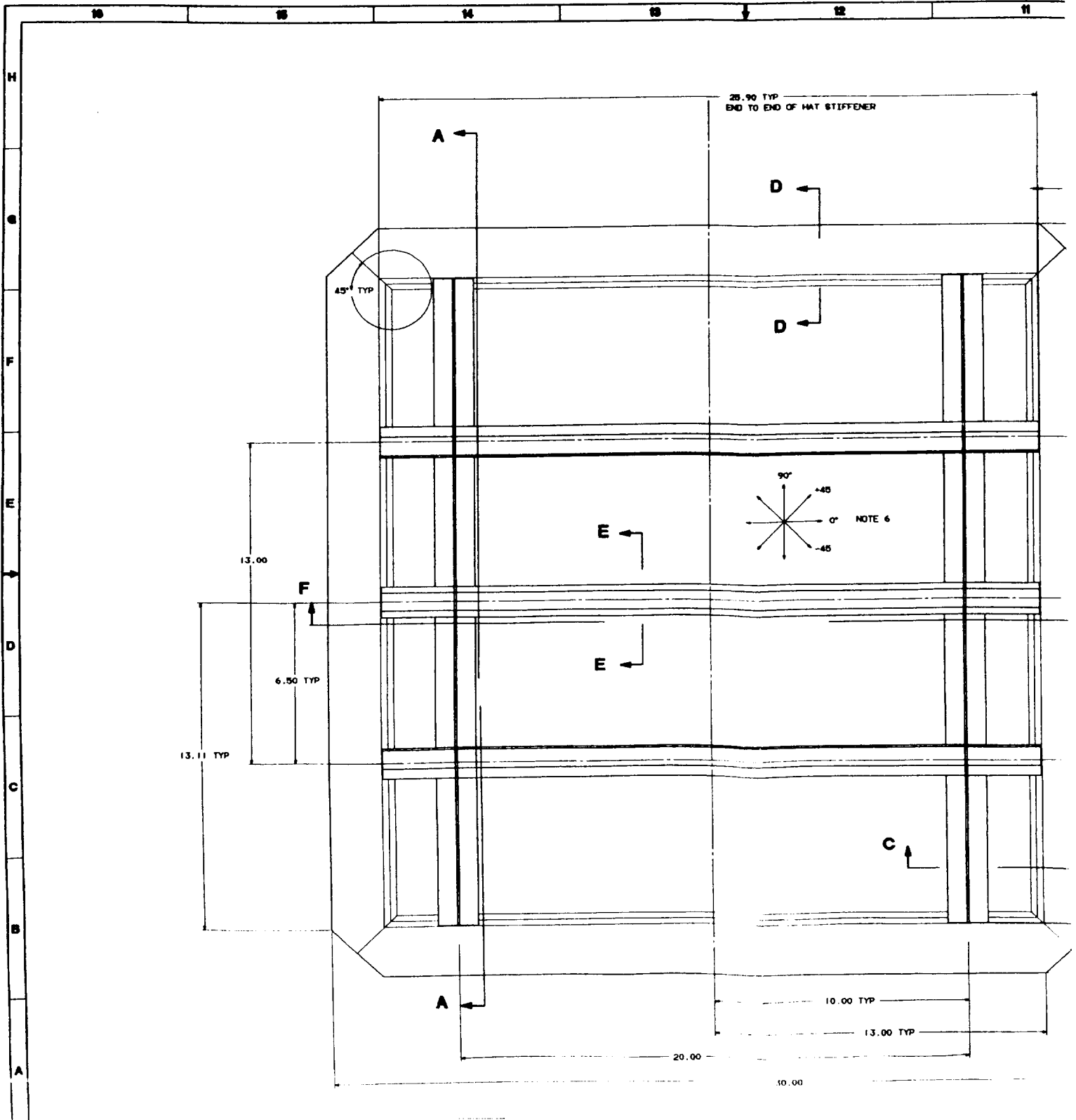
## APPENDIX

This Appendix includes a detailed drawing of the full-scale panel.





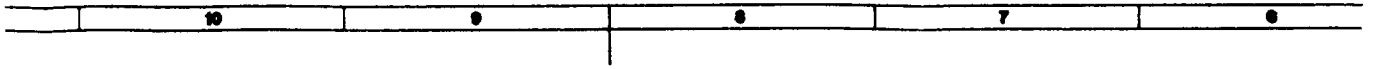
# FOLDOUT FRAME



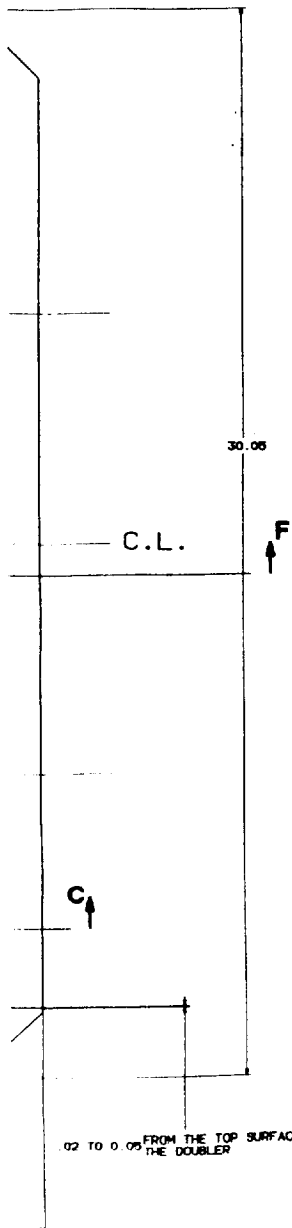




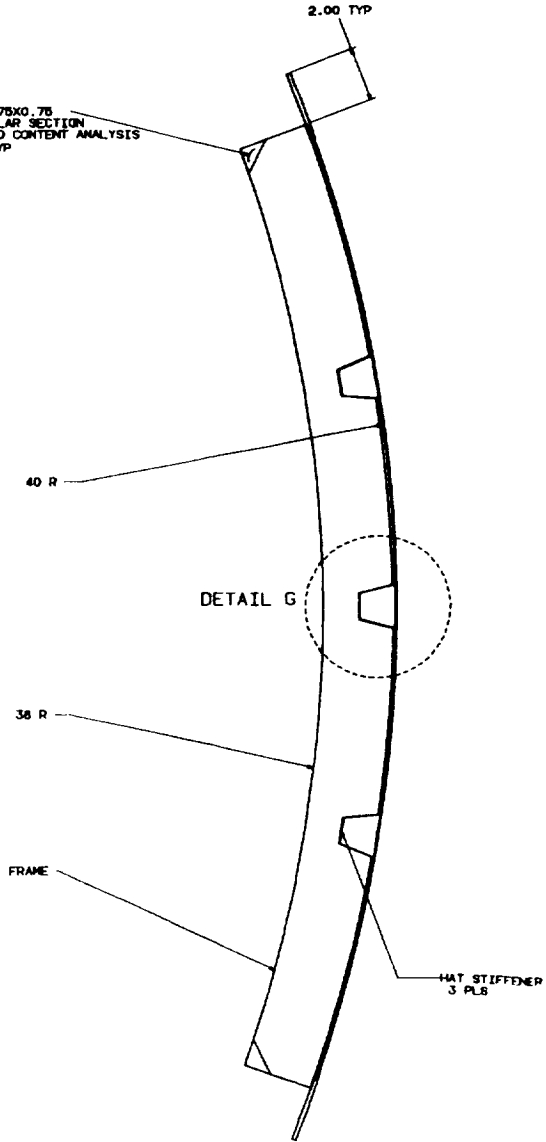
2.  
FOLDOUT FRAME



.02 TO 0.05 TYP FROM THE TOP SURFACE OF THE DOUBLER

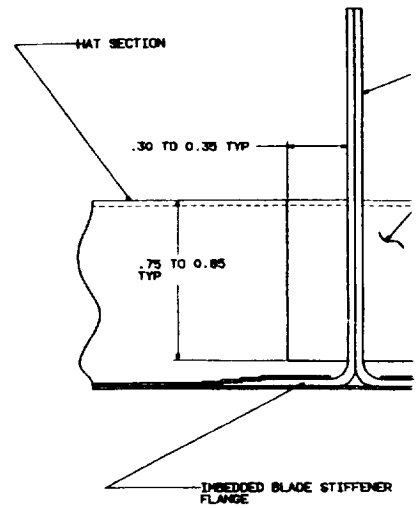
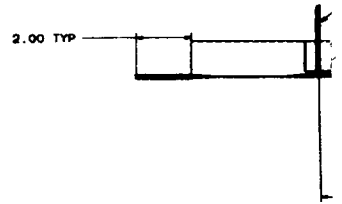


TRIM 0.75X0.75 TRIANGULAR SECTION FOR VOID CONTENT ANALYSIS 2 PLS TYP



SECT A-A  
SCALE 3/4

2.00 TYP



DETAIL L  
SCALE 4/1

.02 TO 0.05 TYP FROM THE TOP SURFACE OF THE DOUBLER

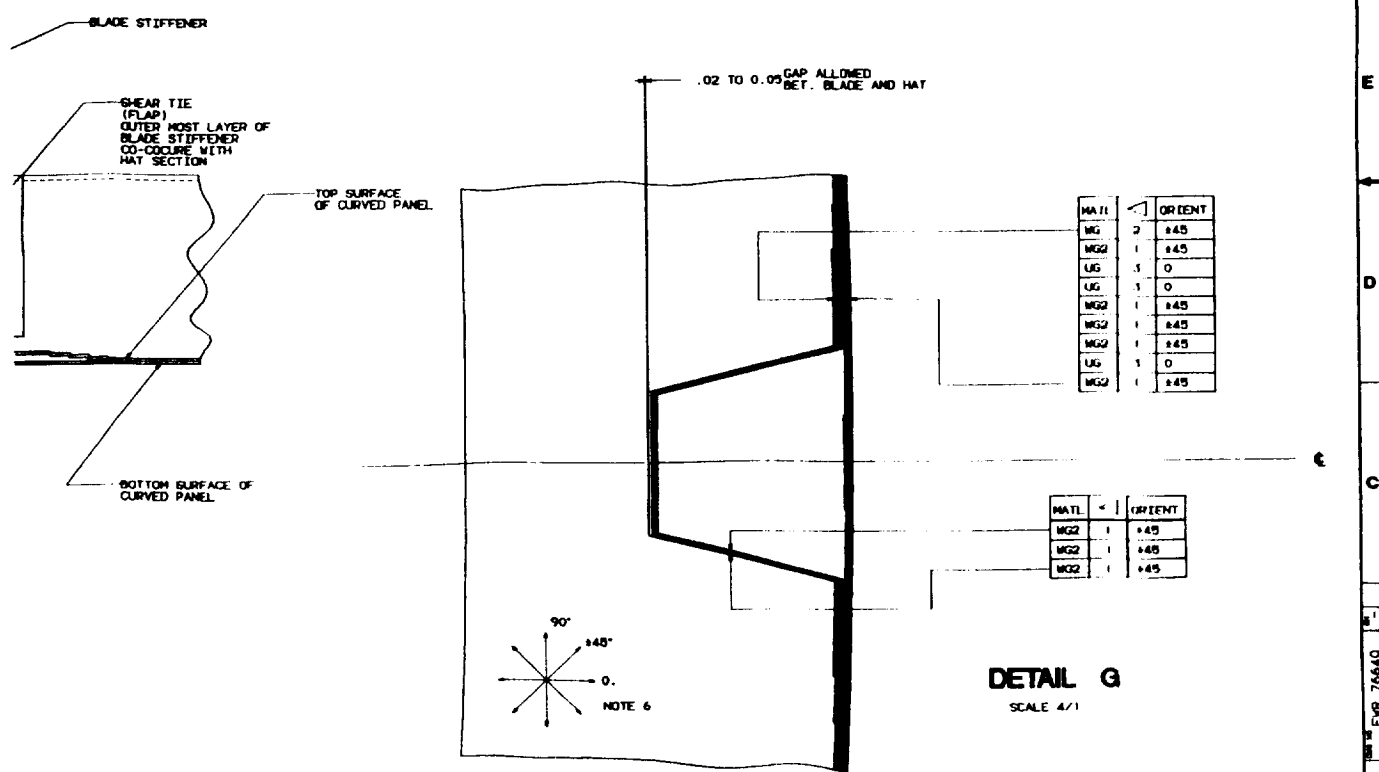
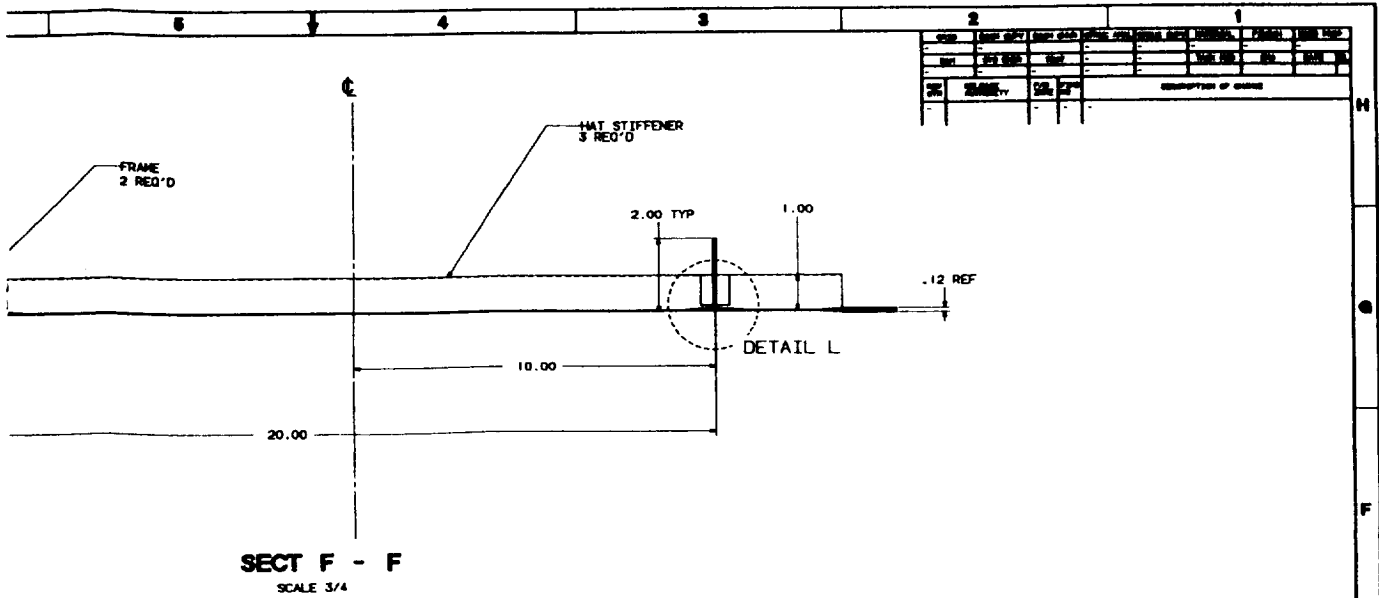
76640

NO.	DESCRIPTION	DATE	BY	CHKD.	APP'D.
1	ISSUED FOR FABRICATION				
2	REVISION				
3	REVISION				
4	REVISION				
5	REVISION				
6	REVISION				
7	REVISION				
8	REVISION				
9	REVISION				
10	REVISION				



3.

# FOLDOUT FRAME



REV	DATE	DESCRIPTION
1		
2		
3		
4		
5		
6		
7		
8		
9		
10		

REV	DATE	DESCRIPTION
1		
2		
3		
4		
5		
6		
7		
8		
9		
10		

REV	DATE	DESCRIPTION
1		
2		
3		
4		
5		
6		
7		
8		
9		
10		

NO CHANGE MAY BE MADE TO THIS DRAWING SHEET EXCEPT BY INPUT TO CAD/CAM FILE		DATE	
DESIGNED BY		DATE	
CHECKED BY		DATE	
RELEASE AUTHORITY		DATE	
DATE		DATE	
DATE		DATE	
DATE		DATE	

#1 SEPARATE PARTS LIST	
REVISED TITLE	DATE
FULL SCALE CURVED STIFFENED PANEL	
(40" x 6")	
PART NO.	QUANTITY
J 76288	EWR 76640
REV	XX

EWR 76640

10/10/10

10/10/10

# REPORT DOCUMENTATION PAGE

Form Approved  
OMB No. 0704-0188

Public reporting burden for this collection of information is estimated to average 1 hour per response, including the time for reviewing instructions, searching existing data sources, gathering and maintaining the data needed, and completing and reviewing the collection of information. Send comments regarding this burden estimate or any other aspect of this collection of information, including suggestions for reducing this burden, to Washington Headquarters Services, Directorate for Information Operations and Reports, 1215 Jefferson Davis Highway, Suite 1204, Arlington, VA 22202-4302, and to the Office of Management and Budget, Paperwork Reduction Project (0704-0188), Washington, DC 20503.

1. AGENCY USE ONLY (Leave blank)		2. REPORT DATE February 1992	3. REPORT TYPE AND DATES COVERED Contractor Report	
4. TITLE AND SUBTITLE Innovative Fabrication Processing of Advanced Composite Materials Concepts for Primary Aircraft Structures			5. FUNDING NUMBERS C NAS1-18799 WU 510-02-11	
6. AUTHOR(S) Christos Kassapoglou, Al DiNicola and Jack Chou			8. PERFORMING ORGANIZATION REPORT NUMBER	
7. PERFORMING ORGANIZATION NAME(S) AND ADDRESS(ES) United Technologies Sikorsky Aircraft Division 6900 Main Street Stratford, CT 06601			10. SPONSORING / MONITORING AGENCY REPORT NUMBER NASA CR-189558	
9. SPONSORING / MONITORING AGENCY NAME(S) AND ADDRESS(ES) National Aeronautics and Space Administration Langley Research Center Hampton, VA 23665-5225				
11. SUPPLEMENTARY NOTES Langley Technical Monitor: Jerry W. Deaton Final Report				
12a. DISTRIBUTION / AVAILABILITY STATEMENT FEDD Subject Category 24			12b. DISTRIBUTION CODE	
13. ABSTRACT (Maximum 200 words)  The autoclave-based THERM-X <sup>R</sup> process was evaluated by cocuring complex curved panels with frames and stiffeners. The process was shown to result in composite parts of high quality with good compaction at sharp radius regions and corners of intersecting parts. The structural properties of the postbuckled panels fabricated were found to be equivalent to those of conventionally tooled hand laid-up parts. Significant savings in bagging time over conventional tooling were documented. Structural details such as cocured shear ties and embedded stiffener flanges in the skin were found to suppress failure modes such as failure at corners of intersecting members and skin stiffener separation.				
14. SUBJECT TERMS THERM-X <sup>R</sup> process, postbuckled panels, cocuring, skin-stiffener separation			15. NUMBER OF PAGES 236	
			16. PRICE CODE	
17. SECURITY CLASSIFICATION OF REPORT Unclassified	18. SECURITY CLASSIFICATION OF THIS PAGE Unclassified	19. SECURITY CLASSIFICATION OF ABSTRACT Unclassified	20. LIMITATION OF ABSTRACT 